NON - SYNCHRONOUS OPERATION OF A HYSTERESIS MACHINE

A thesis submitted for the degree of

DOCTOR OF PHILOSOPHY

SURESH CHANDRA BHARGAVA

THE UNIVERSITY OF ASTON IN BIRMINGHAM

September 1972

SUMMARY

A detailed study is made of the field distribution in a hysteresis machine, having a mechanically rotated magnetic field, for non-synchronous speeds. A qualitative theory of operation is developed and the Poynting vector concept of nett power flow used to predict the torque-excitation characteristic.

Constructional details of the experimental machine are given and the tests performed for the measurement of torque and magnetic flux density are described. A comprehensive interpretation of the magnetic flux density waveforms is given, with special regard to those obtained in the non-magnetic regions. To demonstrate the significance of the low relative permeability of the rotor active material alone, experiments with a non-metallic, non-magnetic rotor and on analogue models are conducted, and verified analytically. In the light of these results, the spatial hysteresis effect of the rotor on the field distribution is discussed.

The qualitative theory brings out clearly the physical operation of the machine. It establishes a new concept of 'independent' rotor magnetisation, derived from the permanent magnet properties of the rotor, as the connecting link between the rotating magnetic field and the production of torque. The spatial hysteresis effect on the airgap magnetic field is explained by reference to this rotor magnetisation.

Poynting's theorem is applied to calculate the power flow in the machine. The developed torque is obtained as the difference between the nett power flow in the airgap and arbor regions of the rotor. This eliminates the necessity of measuring the magnetic field components within the rotor magnetic material. The calculated torque-excitation curve shows satisfactory correlation with the measured characteristic.

CONTENTS

CHAPTER I

THE HYSTERESIS MOTOR

CHAPTER I

THE HYSTERESIS MOTOR

1.1 Historical Review

Hysteresis (in Greek ὑστερέω meaning "lag - behind"), a widely known phenomenon in the modern sciences, was first associated with magnetic materials in research by Warburg[1*] - and simultaneously by Ewing[2] - about the year 1879. Until then, the use of 'iron', the most common example of magnetic material in those days, in electric machines and apparatus was based on the assumption of single-valued relationship between magnetising force and induced magnetism[3], and perhaps the importance of residual magnetism was not fully realized. Ewing showed that the induced magnetism lagged behind the applied magnetomotive force (m.m.f.) and named this property the 'hysteresis effect'[4]. Cyclic variation of the m.m.f. resulted in a closed hysteresis loop and again this was demonstrated on a 'theoretical basis' by Ewing[5] with the help of various models using small permanent magnets pivoted on needle-supports.

The physical meaning and importance of the loop was explained by Warburg[1]. It was established by further research[6,7] that the area of the hysteresis loop for a magnetic material

---

*Numbers show references listed at the end of the thesis.

represented the energy lost as heat in taking a material through one complete cycle of magnetisation.

1.1.1 Alternating and rotational hysteresis

Two types of hysteresis are known to occur in magnetic materials. The remarks of Section 1.1 apply to 'alternating hysteresis' in which the cycle of magnetisation consists of increasing the magnetising force in one direction to a maximum value, reducing it to zero, and followed by similar variation in the opposite direction. 'Rotational hysteresis' which results from the rotation of a magnetic material, say a disc, through one cycle in an applied magnetising force of constant magnitude, was predicted by Swinburne in 1890[8] and confirmed by Baily in 1894[9]. When used with reference to early development of hysteresis motors, it is the alternating hysteresis which is assumed to give rise to torque.

1.1.2 Origin of hysteresis motor

Although no clear evidence is available, the origin of the 'hysteresis motor' can be traced back to 1886-87. In one of the well-known researches described in "The Electrodynamic Rotation Produced by Alternating Currents"[10,11], Ferraris used a laminated iron cylinder and a rotating magnetic field. The torque that was developed in the cylinder could not be explained completely as eddy currents and was stated by Ferraris to result principally from hysteresis effect. This elementary device, which he called a 'motor', can be considered as the original hysteresis motor. According to Ferraris, such a motor would be

of little industrial use because of the low value of the developed torque and yet might have some useful applications because of its special properties*.

Parallel to the time of the 'accidental invention' of the motor by Ferraris was the development of an instrument by Ewing[12] of historical importance. This instrument, called the 'hysteresis tester', was devised to measure the hysteretic quality of a laminated magnetic material in terms of the angle of hysteretic advance. Torque was produced by the action of the field of an electromagnet on a mechanically rotated sample, and was clearly due to hysteresis effect (in the absence of eddy currents). On the basis of torque production, Ewing's hysteresis tester can be regarded as another form of an early hysteresis machine and, if the electromagnet is allowed to rotate, as the first hysteresis coupling.

1.1.3 Steinmetz's theory

A theory of the hysteresis motor was attempted first by Steinmetz around 1896-97[13,14]. He derived the expressions for the torque and efficiency of the motor based on alternating hysteresis, the machine being treated as an ideal model. The principal features of his theory can be summarised as follows:

(a) The developed torque is proportional to hysteresis loss in the rotor material and hence to the area of the

---

*A self-starting synchronous motor, with a sub-synchronous torque which, ideally, is independent of speed.

hysteresis loop

(b) Assuming a sinusoidal m.m.f. distribution, the efficiency is proportional to the angle of hysteretic advance

(c) During asynchronous operation, the electric power supplied to the rotor divides in two parts: a part, proportional to slip, supplies the hysteresis loss and is dissipated as heat; the remainder, proportional to speed, supplies the mechanical power at the shaft.

The theory forms a basis for approximate calculation of torque in hysteresis machines, but does not provide a rigorous framework for analysing the machine performance. Also, the operation at synchronous speed is not very clear from Steinmetz's description.

1.1.4 Progress during the first-half century

1.1.4.1 Developments following Steinmetz's work

Hysteresis motors attracted little attention during the early years of this century since their practical use was very much limited in comparison to other contemporary motors. However, the effect of hysteresis in rotors of polyphase induction motors, in modifying characteristics or affecting the performance, was widely reported[15,16,17]. It was noticed that the operation of an induction motor near synchronous speed or "passing through synchronism" was influenced by the hysteretic torque, probably because this was comparable to that due to normal 'induction-motor-action' at very low values of slip.

The fact that hysteresis in the rotor of an induction motor could give rise to useful torque was first noted by Smith[18] and then specifically reported by Robertson in 1911[19] who stated that if only the hysteresis could be made large enough the motor would run without slip (i.e. at synchronous speed). There would still be the undesirable hysteresis loss due to high - frequency pulsations in the teeth, but this could be minimised by using closed or partially closed rotor slots. The economical advantage of hysteretic torque in induction motors was therefore in the possible use of the "cheapest brand" of iron for the rotors (high hysteresis loss) and a "low-loss brand" for the stators. Also, the slip at load in such motors would be low.

The possibility of a pure hysteresis motor on a commercial scale was discussed by Robertson and, on the basis of the high-hysteresis loss materials then available, was proved to be impracticable*. As shown by a simple phasor diagram, the power factor in these motors would be invariably low and input current relatively high, resulting in poor efficiency.

In spite of these drawbacks, hysteresis motors in small sizes found increasing use in special applications requiring self-starting, constant torque drives, such as electric clocks, timers and record players. An account of such

---

*For example, a motor with one horse-power output (746 W) would require from 700 to 1000 cubic-inch (1.15×10^{-2} - 1.64×10^{-2} m^3) of rotor iron at a flux density in rotor of 1 T and supply frequency of 50 Hz.

applications is given by Holmes and Grundy[20]. Even at low outputs (approx. 1.1 W to 2.8 W) the motors operated at very poor efficiency ($< 1.0\,\%$) and the performance was far from satisfactory.

Commercially, therefore, the motor could not be deemed a success, and was not manufactured on a large scale. The low output/unit rotor volume was due to lack of suitable magnetic materials. No detailed theoretical treatments appear to have been published during this period, and the electrical design of the machine was based on the application of Steinmetz's simple theory[20] and empirical formulae.

1.1.4.2 Teare's theoretical approach

Teare's paper in 1940[21] was a new attempt to develop a detailed theory for hysteresis motor torque. This was based on the principle of virtual work, and a general expression for torque was derived in which components of rotor flux density in all three space directions were taken into account. A simplified torque equation for a thin rotor was obtained, which supported Steinmetz's theory. For this Teare assumed that the radial component of flux density would not contribute noticeably to the torque. Experimental verification was made with a 'circumferential - flux' type hysteresis motor; a term normally used to describe a machine with rotor having non-magnetic arbor*.

---

*A machine with a magnetic arbor of relatively high permeability is referred to as a 'radial - flux' type hysteresis motor.

A valuable part of Teare's theory is the treatment of the operation at synchronous speed, with particular reference to varying load conditions and the effect of space harmonics. It is shown that the latter modify the fundamental hysteresis loop and result in a reduction of the developed torque. Changes in load requirements at the shaft are explained by adjusting the width of hysteresis loop in order to change its area. The effects of magnetic saturation and hysteresis in the stator are not discussed.

When applied to the study of an experimental motor, the theory is simplified by a number of assumptions: for example, a two-dimensional magnetic field, the absence of eddy currents, constant permeability and an elliptic hysteresis loop. These linearize the problem and do give satisfactory correlation, between theory and practice, for a machine with an enlarged airgap and for low values of flux density. However, they are not valid for practical motors and hence, apart from providing a qualitative interpretation of the synchronous operation, the simplified theory does not contribute quantitatively to the understanding of the motor performance.

An analysis of the radial type motor was presented by Jaeschke[22], based on the assumptions of sinusoidal m.m.f. distribution in the airgap and infinite permeability for the stator material and the rotor core. The expression for the "slip force" and driving torque (shown to be independent of speed) are derived in terms of the rotor flux density (obtained by applying a sinusoidal magnetising force to the B - H loop and considering the fundamental component of the

resulting flux density waveform) and the applied m.m.f. Harmonics are completely ignored, except for their effect in modifying the speed-torque characteristic, by giving rise to eddy current torques.

The latter part of his paper discusses the results obtained from the experimental models using the theory and it is shown that, by considering an elliptic cycle in comparison to an actual loop, the error in the torque would not exceed 7%.

1.1.4.3 Commercial improvements

The development of improved hard magnetic materials with a higher hysteresis loss/unit volume revived interest in the commercial manufacture of hysteresis motors on a large scale. Notwithstanding the use of new materials, the efficiency of the machine was still low and efforts were made to improve the performance by modifying the constructional features, notably by 'Smith & Sons' in 1943[23] and Roters in 1947[24]. The former used magnetic sleeves to bridge the slots in order to reduce the undesirable effects of stator-slot-flux undulations in the airgap. The sleeves were cylindrical and inserted into the pre-wound stator.

Modifications on a similar line were reported by Roters[24] who discussed the effects of open slots in detail. The reason for low efficiency was attributed to the undulation of the space distribution of the rotor flux density relative to the rotating magnetic field, resulting in "spurious loss" which could be of the order of from one to three times the power output of the rotor. Reduction of this loss was achieved by

using a large number of closed slots on the stator and typical efficiencies of 80 per cent. were claimed. Fractional horse power motors could thus be manufactured economically. To speed-up the production, "back-winding"* of the stator was used.

In a machine with a high permeability rotor, closed slots result in increased magnetising current and low power factor, because of the shunting action of the slot bridges. So that in the hysteresis motor, where the average permeability of the rotor material is much lower, these effects are inevitable. Nevertheless, it appears that in the construction used by Rotors, the increased stator loss was considerably less than the 'parasitic' loss resulting from the variation of airgap permeance. The closed-slot construction for the stator thus gave improved performance.

Roters' work was qualitative (relevent to manufacture of motors) and does not appear to have been used in any subsequent published electrical designs. Indeed, examination of machines currently manufactured by the English Electric and Stovold companies shows that the open stator slot construction is still favoured. The manufacturing difficulties are overcome in the external rotor construction[25], where a magnetic sleeve can be pressed over the pre-wound rotor or steel bonding-wire used.

The use of hysteresis drag devices in textile and wire

---

*Inserting the wound coils from the back of the stator and making-up the yoke portion by fitting an external cylindrical magnetic sleeve over the pre-wound stack of laminations.

industries was reported by Parker[26]. Here a constant tension, independent of speed, is required and therefore hysteresis machines make an excellent drive.

1.2 Further Theoretical Investigations

Since Teare's and Jaeschke's publications, many theories have been advanced to explain hysteresis motor performance at both sub-synchronous and synchronous speeds. These theoretical investigations are based on different approaches and governed by various assumptions and approximations to account for the non-linearity of the rotor active material. Detailed studies of such aspects as derivation of torque equation of the machine, development of an 'equivalent circuit' and approximate design considerations are available in a number of published papers. Since a rigorous analysis is not yet obtainable, a general discussion of the topics covered by these papers, with particular reference to the assumptions made and their implications, is given in the following sections.

1.2.1 Assumptions and approximations

The B - H relationship of the material used in the construction of the rotor is naturally non-linear and multivalued. In Steinmetz's theory each particle is assumed to trace a simple loop. However, in practice the hysteresis loop is modified by minor and recoil loops because of harmonics in the stator m.m.f. and other effects[24].

A necessary requirement therefore in all theoretical

analyses has been assumptions regarding the relative permeability of the rotor material, and nature of the hysteresis loop.

1.2.1.1 Constant relative permeability

The most common assumption is that of constant relative permeability. This treats the B - H relationship as a straight line between the commencing point and the operating point on the actual magnetisation curve. Since many of the theories have used the 'variables-separable' solution of Laplace's equation to give expressions for the flux density in the rotor material, this assumption becomes essential. In a few cases, two constant values of permeability have been used, when approximating the hysteresis loop by a parallelogram[27,28], thus making it possible to differentiate between linear and saturation portions of the B - H curve. A different approach has been adopted by Larionov[29] where a constant value of permeability is related to the angle of hysteretic advance. Yet another approach is the assumption of a complex permeability by Miyairi and Kataoka[30].

Although the assumption of constant relative permeability must be unrealistic in practice, the error involved may not be serious if the operation of the motor is restricted to a limited range of magnetising force; this is certainly dependent on the shape of the B - H curve or, in other words, on the material used for the rotor. In practical machines, operating at synchronous speed, the input current is nearly constant and hence the 'average' permeability, corresponding to an undistorted fundamental hysteresis loop, will be constant. However, the assumption is not justified in the case of hysteresis machines

required in variable-torque drives where the torque is controlled by varying the excitation current. The relative permeability in such cases may typically vary from about 10 to 40 or more.

1.2.1.2 Hysteresis loop approximations

Various geometrical shapes have been used to approximate the hysteresis loop. These have been generally used for loops obtained by ballistic methods and assumed to apply to the fundamental component of the stator m.m.f. - and then extended to the high order harmonics.

A parallelogram approximation has been used by Copeland and Slemon[27,28], which is modified to a rectangular shape, to represent the steeply rising part and saturation stage of the B - H curve. The advantages claimed by the authors are analytic simplification and the feasibility of deriving an equivalent circuit for the machine. An obvious limitation is that the flux distribution will still contain large number of harmonics even when the applied m.m.f. is assumed to be sinusoidal. The approximation has not been noted in any other published research.

Other approximations include representing the loop by an inclined ellipse[30,31,32,33,34] for a sinusoidal variation of flux density and fundamental component of applied m.m.f., a parabola[35] or a rectangular hyperbola[36]. The elliptic hysteresis loop, inclined to the m.m.f. axis, permits inclusion of the angle of hysteretic advance consistently in the analysis, based on the solution of Laplace's equation[34]. The analysis thus becomes relatively simple. At low magnetising forces, hysteresis

loops formed by displaced parabolas have a close resemblance to the actual loops, and provide an accurate means to calculate the alternating hysteresis loss analytically[37]. The displaced rectangular hyperbola shape, on the other hand, is seen to be a more appropriate approximation for loops having the $\hat{B}$, $\hat{H}$ point near 'knee' portion of the B - H curve.

A source of inaccuracy in the elliptic loop approach arises from the assumption of a similar variation for higher order space harmonics in the applied m.m.f., and the subsequent superposition in the analysis. Since the harmonics rotate at different speeds relative to the fundamental, these do not necessarily form closed loops of elliptical shape and the loops may not be repeatable.

1.2.1.3 Miscellaneous assumptions

The miscellaneous additional assumptions made in connection with the theoretical analyses[27 - 41] are:

(i) Infinite permeability of the stator magnetic circuit

Since the relative permeability of rotor is very low compared to the high grade laminated steel normally used for the stator, this assumption is justifiable. Some 'localized' saturation occurs in the teeth which results in increased effects of permeance variation in the airgap due to reduction in stator permeability.

(ii) Uniform airgap

Unless a closed-slot construction is used for the stator, the airgap is never uniform in practical motors. The variation of airgap permeance gives rise to a modified field

distribution which has not yet been reported on the basis of measured flux density waveforms during operation of the machine, though it has been discussed qualitatively[24]. The effect of a slotted stator is usually taken into account by increasing the airgap length, based on Weber's approach[31,34], thus making the solution of Laplace's equation possible. Machines with an enlarged airgap are used for experimental verification of the results[21,32]. Clearly, with small number of slots per pole, the 'equivalent', increased airgap may be unrealistic and an alternative analysis, replacing the toothed region by an anisotropic one, may be more accurate[42].

(iii) Negligible eddy currents in the rotor

This assumption is only partially true for commercial motors, or the experimental machines described in some of the papers. With the use of a much higher resistivity for rotor hysteresis material, the eddy currents in it may be neglected, especially at synchronous speed (at this speed, high frequency space harmonics of m.m.f. may still induce e.m.f.s in the rotor), but the operation at sub-synchronous speeds and the starting torque are greatly influenced by induced eddy currents in other parts of the machine (such as ventilating fans) arising from the leakage flux which is more pronounced in hysteresis motors than in other electrical machines. The torque-speed characteristic is consequently far from the ideal in commercial motors.

(iv) Negligible magnetic field in the arbor

The use of permeable cylinders to screen equipment from the influence of magnetic fields is well known (from as early

as 1897[43]), and has been assumed to apply to the hysteresis motors (circumferential-flux machines) notwithstanding the poor permeability of the rotor material. The field distribution in the non-magnetic arbor is therefore usually assumed to be negligible as this has the advantage of limiting the solution of Laplace's equation to two regions only: the airgap and the rotor annulus. No attempt appears to have been made so far to establish the validity of this assumption, e.g., by suitable experimental measurements, although an analytical treatment using linear theory is available[41]. Obviously, any flux crossing the arbor region of the rotor can greatly affect the machine performance as the arbor is normally made of aluminium. Paradoxically, it appears that manufacturers are aware of this phenomenon and use the eddy current torque to modify the motor characteristic.

(v) Sinusoidal distribution of stator conductors

This is a highly idealizing and impracticable assumption. A distributed polyphase winding requires a finite number of slots, having a fixed number of turns per slot per phase. Hence the m.m.f. distribution is never sinusoidal and contains a large number of space harmonics. By suitable design, only certain order harmonics may be eliminated or reduced in amplitude. The assumption appears to rely on the torque due to these harmonics to be a small percentage of that due to the fundamental.

(vi) Negligible radial component of flux density in the annulus of circumferential-flux machines

The radial component of flux density is in some cases

neglected for a thin rotor. However, 'thinness' of the rotor annulus is a relative term and depends on its mean diameter and the number of pole pairs. Theoretically, the radial flux density can never be zero over the entire circumference and the only assumption that can be made usefully is with regard to its effects. Sufficient emphasis is not placed on this point in the published works.

A study of these assumptions reveals the extent to which theoretical analyses must be idealized. This limits their usefulness for the quantitative assessment of machine performance. However, they do permit the operating characteristics of commercial machines to be predicted qualitatively. The inadequacy is further discussed in Section 1.2.5.

1.2.2 Torque expressions

The simplest method of deducing the torque expression has been used by Miyairi and Kataoka[30]. The applied m.m.f. is assumed sinusoidal and the torque is obtained by dividing the total hysteresis loss at supply frequency by the rotor speed, in direct accordance to Steinmetz's theory. Copeland and Slemon's approach[27,28] consists of first deriving the "equivalent" induced e.m.f. and "load" current expressions for the machine and then calculating the torque as the power crossing into the rotor at standstill per unit angular speed of the rotating magnetic field. In the other cases[31,32,34] the power equivalent to torque at the shaft is derived, using the magnetic field components as $\int_V \bar{B}.d\bar{H}$, and then converted to torque at the appropriate rotor speed.

The effect of m.m.f. harmonics, in modifying the

fundamental torque expression, has been discussed in a few papers on the basis of the superposition of harmonic torques. The assumptions used to simplify the analyses are taken to be applicable to harmonics as well, and the reduction in torque due to these is shown. An exclusive treatment of parasitic loss* due to various types of harmonic is given in a paper by Rahman et. al.[38] and good agreement between the measured and calculated loss figures is claimed. It is not clear, however, how the losses were measured in the experimental machine.

The torque arising from radial component of flux density in the rotor has been considered in detail by Larionov[29] who uses a constant permeability 'matrix' to inter-relate the radial and tangential components of magnetising force with the angle of hysteretic advance, to account for the 'load' conditions of the motor. A limitation of Larionov's theory is that it is inapplicable to higher harmonics of the m.m.f. waveform. An approach on similar lines is that by Robertson and Zaky[34], to be discussed later.

An analytical treatment of eddy-current effects, at sub-synchronous speeds and for sinusoidal applied m.m.f., has been presented by Miyairi and Kataoka[32]. End effects are neglected and experimental results verified using a motor with end copper rings and a large airgap. The field distribution in

---

*The parasitic loss is the term used in the paper to define the loss associated with the minor loops, caused by various harmonics, which arises mainly from the eddy-current effects. See also the paper by Roters[24].

the non-magnetic arbor has been assumed negligible, although this must contribute some torque due to eddy currents*. In fact, the measured eddy current torque is greater than the calculated values and the authors have considered a 'correction factor' to allow for the error.

1.2.3 'Equivalent circuits'

Many of the published papers[27,28,29,30,32,34] give undue importance to the concept of an equivalent circuit for a hysteresis motor on the lines of other common electric machines. Thus, Copeland and Slemon[27,28] have derived a circuit by replacing each of the reluctances in the idealized machine by an 'equivalent' reactance, and making the rectangular magnetisation loop represent a cyclically varying magnetic source. The source is assumed, in effect, equivalent to a 'flat-top' flux waveform due to sinusoidal stator m.m.f. This gives rise to an induced e.m.f., which is split into a fundamental and harmonics by Fourier analysis. The approach used by Miyairi and Kataoka[30] consists of obtaining expressions for components of $\bar{H}$ and $\bar{B}$ in the rotor annulus in terms of the applied m.m.f. and the corresponding components in the airgap. The stator m.m.f. is viewed as two currents equivalent, respectively, to the m.m.f.s for the airgap and the rotor (and related to the maximum flux density and the angle of

---

*Even if the field distribution in the arbor is weak, the torque due to eddy currents can be comparable to that in the rotor owing to the low resistivity of the arbor material.

hysteretic advance in the latter). The radial airgap flux density gives rise to an induced e.m.f. and this when divided by the two current components gives the reactance of the airgap and the "impedance of the rotor ring" or annulus. The resistance part of the rotor impedance corresponds to the hysteresis loss and the mechanical power.

The concept cannot be valid for the complete range of operation because of the complex nature of the non-linear elements. Such circuits may have some use when derived experimentally for a prototype motor to study qualitatively the effects of varying design parameters, but are meaningless when arrived at analytically based on quasi-linear theory.

1.2.4 Studies based on magnetic field distribution in the airgap

Unlike other electrical machines, the m.m.f. distribution in the hysteresis machines is greatly influenced by the physical dimensions of the rotor active material, and to a lesser extent by the airgap length. A major proportion of applied m.m.f. supplies the magnetising force for the rotor, with only a small amount for the airgap. The field distribution in the airgap thus depends on the magnetic properties and physical dimensions of the rotor and studies of this distribution give an indication of that within the rotor.

A description of airgap flux density distribution in a hysteresis motor has been given by Miyairi and Kataoka[39] and the calculated and measured waveforms show the effect of low rotor permeability and stator slots. The analysis is based on a linear

theory, and the measured waveforms in the test machine are obtained by supplying one of the stator phases with alternating current at rated frequency, the magnitude of the current being such as to avoid saturation in the rotor. The flux density values are calculated from the output of a search coil mounted on the rotor surface. Since the polyphase rotating field was replaced by a pulsating one, it is doubtful if the results give the true airgap flux density variation during normal running of the motor.

The airgap field distribution has been treated by Robertson and Zaky[34] in detail, who modified the usual potential expression for the airgap to include the space phase displacement between the rotor magnetising force and the resulting flux density variation. One of the two potential functions used is due to the given potential on the stator surface while the other is equivalent to hysteresis effect of the rotor in space. Both the radial and tangential components of the rotor flux density are included. Although constant permeability and an elliptical hysteresis loop are assumed, the analysis has the advantage of consistently accounting for the angle of hysteretic advance, as in Larionov's theory[29], instead of using a simple modification of the torque equation in the final stage[31]. The analysis is extended to space harmonics with similar assumptions and superposition gives the resultant torque expression.

The calculation of rotor input power for a motor running at synchronous speed has been reported by Takahashi[40], and the effect of a non-sinusoidal airgap magnetic field on the starting torque has been analysed by Stoma[33]. The treatments again depend on many assumptions.

1.2.5 General comments

A few other papers deal with some miscellaneous aspects of the hysteresis motor. For example, general design problems are discussed by Nakamura et.al.[36] and optimum design conditions by Wakui[41]. The latter illustrates by means of graphs the suitability of the rotor magnetic characteristic for torque output and efficiency, and the effect of the stator winding arrangement and mechanical dimensions on the output. These provide useful guidelines for the design of small motors, upto about 20 W output. Again, the effect of rotational hysteresis on starting torque has been considered by Lommel[44] and extended to the synchronous operation in a recent paper by Wakui[45].

The brief survey pinpoints the main assumptions and areas of the theoretical research published in the past two decades. Perhaps the most important assumption concerns the approximation of the hysteresis loop of the rotor material. An elliptic loop permits the reduction of Maxwell's equations to Laplace's equation, which simplifies the analytical treatment and also allows the 'load conditions' (i.e. inclusion of the angle of hysteretic advance) at synchronous speed to be taken into account. The main disadvantage is that true saturation in the rotor is not allowed for: the B - H relationship is certainly non-linear, but the slope of the loop at the extremity of the major axis becomes infinite and then negative. Whatever approximation is made, it can be justified only with reference to magnetic characteristics of the rotor material, i.e., the maximum point on the B - H curve and actual hysteresis loop, and not with reference to the terminal characteristics of the actual

machine.

From the available published work, comprehensive, theoretical design details are still not available to improve the performance of commercial motors which continue to have poor charactristics. This naturally reflects on the operating cost of machines which is very high per unit power output.

An important limitation of linearized theories is the failure to account for various harmonics conclusively. The parasitic loss (see foot-note on page 18), emphasised by Roters[24] as the main reason for low efficiency of the motor, appears to have lost its significance because of the availability of better hard magnetic materials and the fact that these losses can be minimised by using enlarged airgap; this would avoid some of the technical difficulties encountered by adopting closed stator slots and back-winding process.

Theoretical investigations considering eddy-current effects are also incomplete since the assumptions made are not appropriate to commercial motors.

1.3 Object of this Thesis

The foregoing review discloses that, in spite of many papers developing the assumptions and approximations necessary to make the problem of predicting the performance tractable, a clear picture of the physical aspects of hysteresis machine operation is not available. For example, although the magnetic field distribution in the non-magnetic regions of the machine is reasonably documented, no attempt seems to have been made to relate it to operating conditions.

In this thesis an investigation is made of these hysteresis machine topics:

(i) Magnetic field distribution – To make a comprehensive experimental study of the flux density distribution in the airgap, the rotor annulus and the rotor arbor*, with emphasis on the non-magnetic regions to highlight the role of hysteresis, and support the results with analysis where possible.

(ii) Physical operation – To study the relation between the developed torque, the applied m.m.f. and the rotor magnetisation, and to develop a qualitative theory of operation based on the magnetic field distribution.

(iii) Torque calculation – With the knowledge of the magnetic field distribution in the air spaces adjacent to the rotor annulus, to apply Poynting's theorem to obtain the power flow and hence the developed torque in the machine.

Because of the complexity of the modern hysteresis motor, the investigation makes use of a hysteresis coupling, and a further simplification is introduced with a two-dimensional analysis of the magnetic fields. No detailed consideration is given to the standstill operation of the coupling, which would correspond to the synchronous operation of a conventional motor.

---

*A circumferential-flux type machine is considered, with a non-magnetic arbor.

1.4 Introduction to the Chapters

1.4.1 The experimental machine

The machine used for the experimental study is described in Chapter II. A conventional hysteresis motor is not suitable for measurement of the flux density distribution; the chief disadvantage being the presence of space m.m.f. harmonics which make it extremely difficult to record the measured waveforms consistently. This problem is avoided in the experimental machine by using a mechanically rotated magnetic field, excited by direct current. This causes the harmonics to be "locked" in space to each other and the waveforms become repeatable in time.

The chapter discusses other salient features which result in a machine completely different in appearance to a practical hysteresis motor. In general terms, it is referred to as a hysteresis machine - specifically the operation corresponds to a coupling.

The later part of the chapter describes the schemes used for the measurement of torque, speed (of the field system), and search coil induced e.m.f.s. The last pose special problems in the non-magnetic regions of the machine and elaborate instrumentation becomes indispensable.

1.4.2 The magnetic field distribution

The tests performed and the special techniques used to obtain the induced e.m.f. waveforms reliably are described in Chapter III. It is explained why 'direct' measurement of an induced e.m.f. proportional to the tangential component of flux density is not possible by usual methods and why it is necessary

to adopt an 'indirect' scheme. The oscillograms of the waveforms in the three regions are given together with introductory remarks about their appearance.

A detailed interpretation of the magnetic field distribution calculated from the waveforms follows in Chapter IV. The flux density distribution in the machine is discussed with particular reference to the effect of spatial hysteresis and the effect of the field system geometry, on the shape of these waveforms. Distribution corresponding to non-hysteretic condition of the rotor is obtained using a specially constructed non-magnetic, non-metallic rotor, and this is verified analytically. These waveforms are used to illustrate approximately the effect which the low permeability of the rotor material (in the absence of spatial hysteresis) has on the variation of flux density over a pole pitch. The manner in which saturation and leakage influence the flux distribution is also discussed. These effects are illustrated further for the air regions by iron filing patterns.

1.4.3 The qualitative theory

A study of the torque developed in the machine, corresponding to different stages of magnetisation in the rotor, is considered in Chapter V and approximate expressions to calculate the torque in terms of applied excitation are derived for the experimental machine. These indicate the possibility of predicting the torque from the alternating hysteresis loss curve alone for a uniformly magnetised rotor within a certain range of excitation currents.

The main theme of Chapter V is the development of a qualitative theory of operation. This is based on the magnetic field distribution and fundamental aspects of permanent magnetism. The concept of hysteresis is related to the mechanism of torque production through 'rotor magnetisation', which emerges as the connecting link. It is shown that the spatial distribution of magnetic field strength and flux density are consistent with a conventional hysteresis loop if the above concept of rotor magnetisation is applied.

An added feature of the theory is in explaining the behaviour of machine over the high applied m.m.f. range, when the flux distribution is significantly modified.

The chapter also describes the characteristic scalar magnetic potential distribution in the airgap arising from the rotor magnetisation. This suggests a possible analytical treatment of machine performance based on the assumption of two potential distributions in the airgap and the application of a linear theory.

1.4.4 Power flow calculations

Application of Poynting's theorem to study power flow is the subject of Chapter VI. For this, the 'standard' form of the Poynting vector is used and calculations are made, in the air spaces adjacent to the rotor annulus, with the measured waveforms. The effect of space m.m.f. harmonics in the experimental machine is discussed for a typical excitation and it is shown that the torque due to the fundamental component is supplemented by higher order harmonics by as much as 50 per cent., especially by

harmonics in the range 5 - 21. This emphasises the role of higher harmonics in contributing to developed torque as well as resulting in peaky flux density waveforms.

A torque-excitation curve is derived from the calculated power flow and compared with the measured curve. The correlation is close over the working range of excitation current, but the error in the upper range is 20 - 25 per cent. The chapter discusses in detail the factors responsible for this discrepancy, the main sources of inaccuracy being the limitation of recording the flux density waveforms and human error in sampling the data from these waveforms for digital computer calculations; the difference between mechanical and 'effective' location of the active lengths of search coils used for measurement; the nett power flow equivalent to developed torque obtained as graphical difference of power flows on the external and internal rotor surfaces and the inability to account for the exchange of energy from the rotor end surfaces which calls for a three-dimensional assessment of the problem.

The results nevertheless establish the usefulness of the Poynting's theorem approach because this requires the knowledge of field distribution in the regions adjacent to the rotor and not within the rotor annulus where accurate measurements at each point are impossible. This makes the method more realistic in practice.

1.5 Application of the Study to the Hysteresis Motor

The hysteresis coupling was the model for studying an hysteresis motor operation. This would have been justified

completely, if the percentage of stator m.m.f. harmonics had been quite small, for the results would have been applicable in every respect. As it was, the presence of harmonics completely changed the characteristics and the thesis is, in reality, the study of a hysteresis coupling. Nevertheless, both coupling and motor depend on hysteretic action and, to this extent, a restricted comparison of their performances must be possible in terms of fundamental components of m.m.f. and the field vectors.
A quantitative comparison is impossible because of the non-linearity of the magnetic circuits.

The important difference in the terminal characteristics lies in the effect of harmonic torques. In the coupling these contribute as much as 50% of the shaft torque, whereas in the motor the torque is reduced by the presence of harmonics.

CHAPTER II

THE IDEALIZED MACHINE AND TEST EQUIPMENT

CHAPTER II

THE IDEALIZED MACHINE AND TEST EQUIPMENT

2.1 Chapter Outline

A description of the idealized hysteresis machine and associated test equipment used for experimental work is given in this chapter. The machine was a modified version of one used in previous research. The mechanical arrangement, stator winding and yoke were retained, other existing parts being redesigned and new features added. The overall dimensions were unchanged. Various stages in the conception of the machine are discussed and typical constructional details illustrated in drawings and sketches. These give a clear idea of the machine which, in its final form, hardly resembles a conventional hysteresis motor and has an appearance more towards a 'hysteresis coupling'[26] or a 'hysteresis clutch'[46]. Consequently, it will be referred to as a 'hysteresis machine' rather than a hysteresis motor in the remainder of this thesis.

Miscellaneous test equipment and accessories required to measure the torque and speed of rotation of the field system, and to record experimental results are described briefly, the accuracy of measurement being assessed in each case. Details of the search coils are given and salient features of the associated instrumentation are discussed.

2.2 The Idealized Machine

The main disadvantages of a conventional hysteresis motor for experimental work are:

(a) small mechanical size, which introduces problems of installing search coils,

(b) 'high hysteretic loss material' on the revolving member,

(c) winding harmonics which modify the developed torque,

(d) rotor material having a low resistivity thus allowing eddy currents during asynchronous operation, and

(e) compact multipole design (for commercial reasons) often incorporating novel features which may obscure the fundamental hysteretic operating principle.

(a) and (b) increase the difficulties of making measurements, while (c) and (d) give rise to secondary phenomena resulting in distortion of field distribution. These disadvantages (other than (c)) were avoided with the experimental machine shown in Plate 2.1 (at the end of the thesis). The main features which distinguish it from a conventional motor are discussed in the following sections.

2.2.1 The rotating magnetic field

In a conventional machine, the rotating magnetic field is produced by currents in the stator winding. The resulting m.m.f. contains space harmonics which revolve relative to the fundamental component at speeds inversely proportional to their order. This introduces difficulties in interpreting the induced e.m.f. waveforms which will not be stationary when viewed on an

oscilloscope, but continuously modified by harmonics.

This drawback is eliminated in the experimental machine by mechanically rotating a winding supplied with direct current. The rotating field structure and the resulting m.m.f. in fact resemble that used in a simple d.c. machine (or a small synchronous machine) having salient poles and a mild steel yoke.

With this arrangement the space distribution of the m.m.f. remains fixed with respect to the pole axes as the field structure is rotated. The waveform can be resolved into a fundamental and higher harmonics, but these rotate at the same speed and result in flux density waveforms which also remain fixed with respect to the stator axes.

To facilitate measurements, the rotor is locked. Hence the 'synchronous speed' of the conventional motor corresponds to standstill in the experimental machine. Clearly, generator action is not possible and, to avoid confusion, the term 'non-synchronous' is used in place of 'asynchronous' to describe the operation at speeds other than standstill.

2.2.1.1 The field system

Although the inner member of the machine was kept stationary during the tests, it will be referred to as the 'rotor' since it carried the hysteresis-loss material, and the rotating field structure referred to as 'the field system' throughout the thesis. The term 'the field system' refers to the whole structure driven mechanically and excited by direct current.

Considering the magnetic parts of the field system alone, these comprised a solid mild steel yoke and two solid

mild steel poles*. Though not a very good magnetic material by itself, mild steel was used for the poles due to availability and low cost and, particularly, to facilitate machining (to study the effect of an increased airgap and change in machine geometry). Since the average permeability of mild steel is much greater than that of the rotor material used, heat treatment of the finished poles was not considered. The choice of a two-pole construction allowed more space for installing search coils and Hall probes, and minimised the mechanical problems of alignment and adjustment of airgap length.

The exciting winding comprised 2200 turns of No. 23 SWG synthetic enamelled copper wire on each pole, connected in series. The terminals were brought out via carbon brushes and copper slip rings.

2.2.1.2 Assembly of the field system

An aluminium housing, supported on an aluminium† pedestal by means of two ball journal bearings provided the base for the rotating field system. The pedestal was firmly bolted to a bed-plate and the housing was free to rotate. A cross-sectional

---

*These were one of the modifications made on the existing machine which had Permendur poles originally.

---

†Aluminium was used for the housing and other mechanical structure to keep the weight and leakage flux to a minimum.

view of the housing is shown in Fig. 2.1.

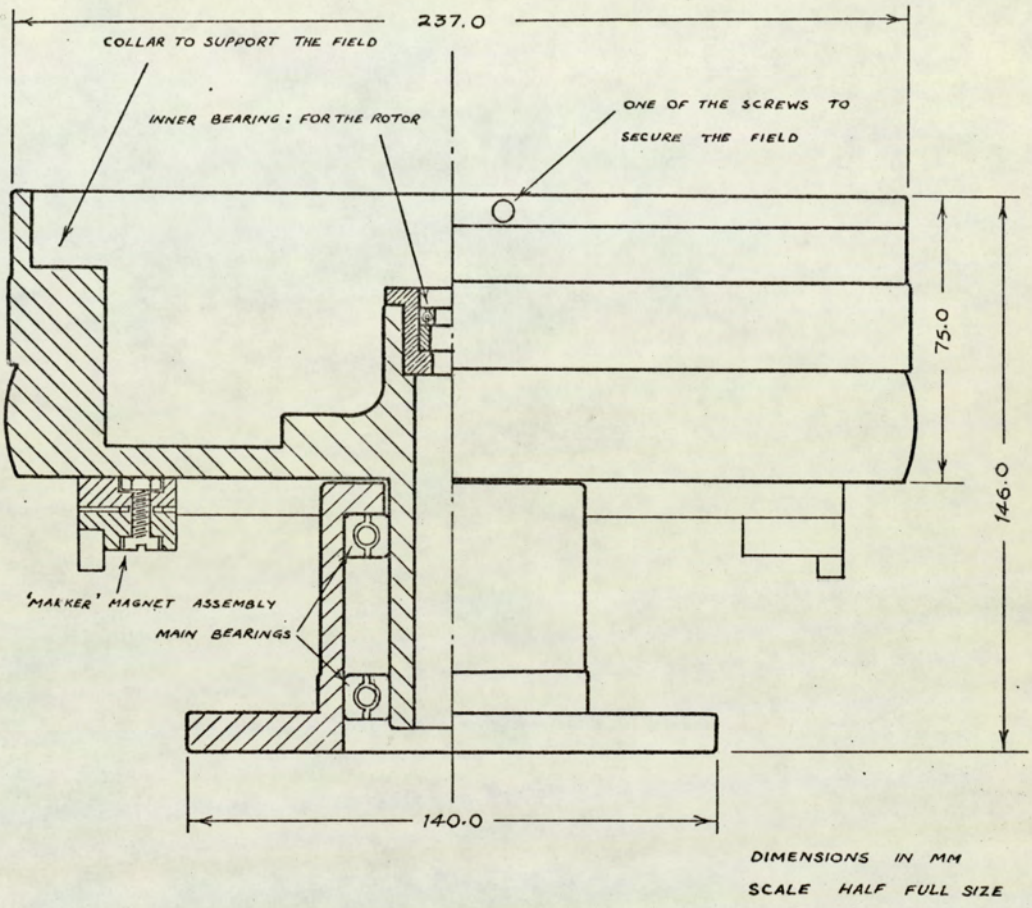

Fig. 2.1

The yoke part of the field structure rested on a shelf in the housing and being a loose fit, could be moved laterally and positioned by means of three set-screws in the side of the housing. Adjustments for concentricity were carried out while rotating the housing slowly and concentricity within ± 0.02 mm obtained.

2.2.1.3 Drive arrangements

The method used to drive the field system was required to provide smooth rotation of the field system at constant speed

during a test period, and also allow the speed to be varied gradually and smoothly from a high value down to standstill.

Both requirements were essential for reliable experimental work. During the tests, a slow, constant speed (approximately 1 rev/s) was desirable to keep the effects of eddy currents and machine vibrations to a minimum. After each set of tests, the speed was increased by about 2 ½ times and then, together with the excitation current, gradually reduced to zero to demagnetize the rotor. While eddy currents would be negligible in a rotor material of high resistivity (see Section 2.2.2.1), there might still be eddy current effects in other parts such as the rotor shaft and the supporting gantry.

These requirements were met by using a Velodyne drive motor with a split field closed loop control system (schematic diagram - Fig. 2.2) coupled by a belt to the rotatable housing.

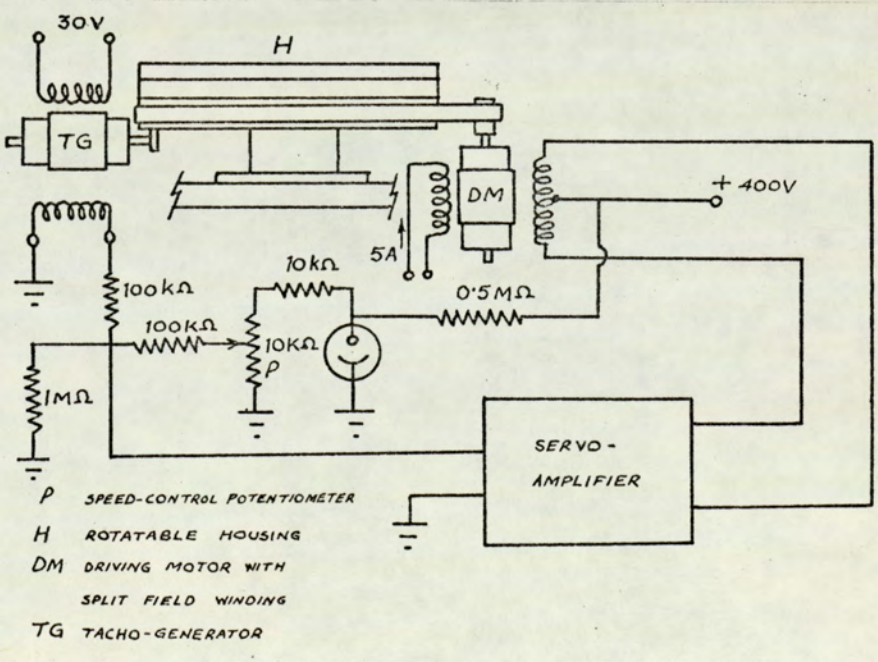

Fig. 2.2

To improve upon the voltage feed-back used for speed control, a tacho-generator, driven directly by the housing, was used instead of the usual output from the Velodyne tacho-generator.

Other methods of coupling the housing and Velodyne shaft were considered including gear and friction drives. The former cannot provide a smooth drive because of unavoidable backlash and may give rise to minor loops in the rotor magnetisation, while the latter, typified by a rubber sleeve on the motor shaft pressed against the housing, was found unreliable because of 'slip' during the tests. Belt drive proved quite satisfactory and checks during experimental work showed no noticeable variation of the instantaneous speed at any selected position of the speed-control potentiometer (Fig. 2.2). Details of field system assembly and the drive are illustrated in Plate 2.2, page 243.

2.2.1.4 Constant - current supply for field windings

While measurements were being made, it was necessary to ensure that the excitation current stayed constant at the pre-set value and did not drift, due to (say) changes in field winding resistance, since any attempt to reset the current would result in a recoil loop in the rotor magnetisation.

A simple stablized voltage source could not be used. However, it could be converted readily into a constant-current source which would hold the excitation current sufficiently constant for short time duration. The scheme used is shown in Fig. 2.3 (next page) which maintained an excitation current of 2.0 A (highest value used) to within - 0.02 A (or 1%) for

a duration of 4 - 5 minutes.

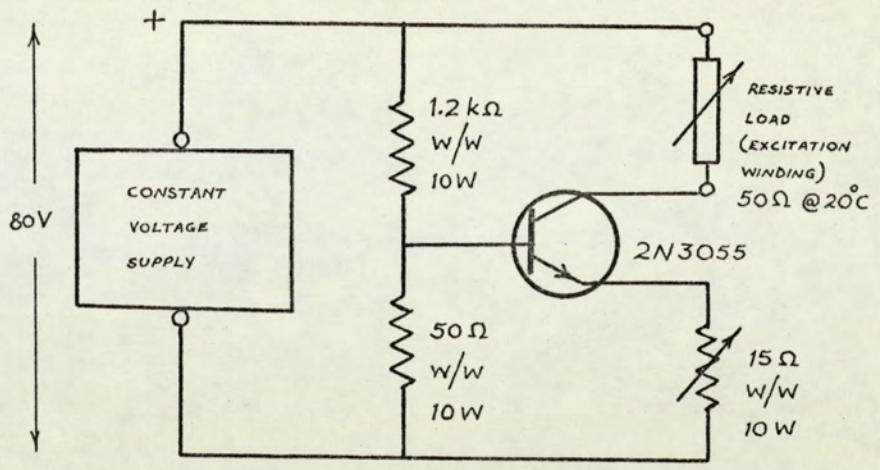

Fig. 2.3

2.2.2 Design of the rotor

The main object in the design of the rotor was to attain an almost peripheral flux density distribution. This was desirable because as a first approximation the magnetisation cycle for each point on the rotor could be assumed alternating and an assessment of the torque made on the basis of alternating hysteresis loss (see Appendix I).

In a commercial motor having a rotor with outside diameter of 82 mm (as used in the present machine), the radial thickness of the active material (considering a circumferential-flux type machine) may be typically about 5 mm, i.e., about 6% of the diameter. So that the rotor flux density distribution will contain an appreciable radial component in addition to the peripheral component.

In the experimental machine a radial thickness of 0.4 mm (i.e. about 0.5% of the diameter) was used. This represents

only $1/10$ of the rotor thickness for a commercial machine and was thought to be a practical approximation to a 'thin rotor', in which the flux density distribution would be mainly peripheral*.

2.2.2.1 Rotor material

Vicalloy I, a metal alloy of Vanadium, Iron and Cobalt, was used for the rotor active material. It has a high hysteresis loss/unit volume/cycle with a residual flux density of 0.9 T and coercivity 0.3×10^5 A/m. Although the $(BH)_{max}$ product is not high compared to other alloys such as Alnico V (Vicalloy:8000J/m^3, Alnico V:37400J/m^3), it has many qualities to support its use in an experimental machine. These include ease of machining and handling prior to heat treatment, and high resistivity (0 0.75 $\mu\Omega$ - m). The latter is of special importance as it makes the assumption of negligible eddy currents more realistic.

2.2.2.2 Rotor construction

The main constructional details of the rotor are given in Fig. 2.4 (next page). Holes were drilled in a rectangular strip of Vicalloy for search coils and it was bent into an annulus to form the rotor. After heat treatment†, the two ends were

---

*The choice of exact thickness of 0.4 mm for the rotor was dictated by the availability of the material in strip or laminated form.

---

†Ageing at 600° C ± 2° C for 2 ½ hours followed by cooling to room temperature in air.

finished to a close butt joint. Joining the ends using welding or a similar process could not be used since it would seriously affect the local magnetic properties of the alloy. Owing to the low relative permeability of Vicalloy, a butt joint was a better choice.

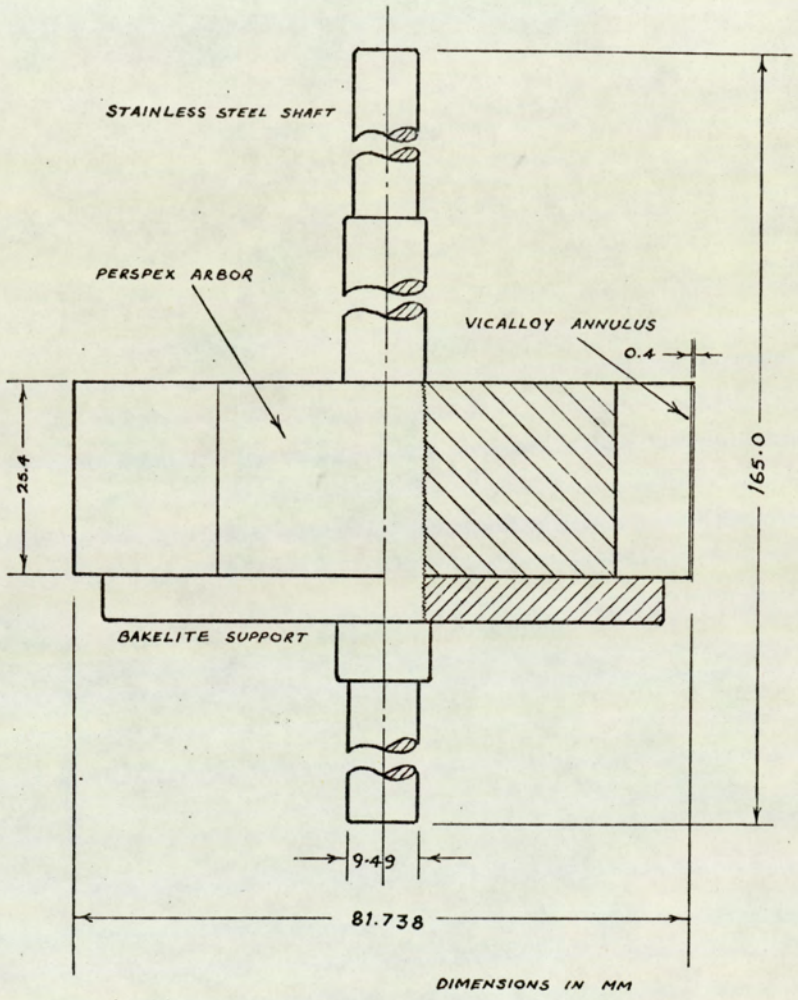

Fig. 2.4

The rotor arbor was made of perspex to avoid eddy currents. This also kept the rotor weight to a minimum resulting in negligible thrust on the supporting bearing. Concentricity of the external surface was ensured by machining the arbor and then

making the rotor annulus a close fit on it. Before the final assembly, three axial slots were machined in the arbor for search coils and a Hall probe (see Section 2.5 and Appendix I).

2.2.3 General assembly and alignment

The field system was first assembled and made concentric with the axis of the housing. The assembled rotor was placed in the machine and the airgap adjusted to within $\pm$ 0.001" (0.0254 mm), the mean airgap being 0.4 mm*.

The 'torque arm' was fitted to the rotor shaft and the top gantry plate secured. The other end of the torque arm was held in a clamp giving a knife-edge contact. Then with the field system rotating slowly (0.5 rev/s) and supplied with a low current, the alignment of the machine was trimmed so that the variation of the developed torque over a complete revolution was a minimum.

Plate 2.1 shows complete details of the machine.

2.2.4 Comment on hysteresis couplings

Less has been written about the hysteresis coupling compared with the motor, although they are commercially available. The Ewing Hysteresis Tester[12] was a historical example, more

---

*The mechanical clearance between the rotor external surface and the poles was modified by the presence of search coils in the airgap and had a minimum value of 0.07 mm.

recently details of couplings for specific applications have been described by Young[46] and Medley[47]. General design details have been discussed by Winston[48] and Yermolin[49]. Use has been made of the coupling in electromagnetic brakes - a disc version is manufactured by Ampex[50].

A machine with a similar appearance to the experimental machine but different rotor construction was described by Apperson and Hansen[51], and used for the measurement of hysteresis loss.

2.3 Torque Measurement

Accurate measurement of torque at any given excitation was an essential requirement in the context of the present thesis. From a mechanical point of view, a precision dynamometer could be used. However, the rotary motion of a dynamometer would cause the rotor to oscillate with respect to the rotating magnetic field and hence modify the magnetisation cycle. Therefore an alternative scheme for torque measurement was used in which the rotor was kept stationary.

A stainless steel bar, of rectangular cross-section and 0.31 m long, (or 'torque arm') having one end fixed to the rotor shaft through an aluminium clamp and the other held in a clamp with a V - shaped notch was used to restrain the rotor from rotating. The latter clamp was mounted on a rigid support to minimise the effect of vibration on the measured torque. Stainless steel (non-magnetic) was preferred for the torque arm to avoid mechanical hysteresis.

The principle of torque measurement was to strain the

torque arm by the developed torque and relate this strain by a suitable transducer to torque in Nm. The method did not eliminate entirely the movement of the rotor as the developed torque changed, but this was negligible.

2.3.1 Use of strain gauges

Foil type, resistance strain gauges, in standard shape were used as strain or torque transducer. The optimum location of these on the torque arm, treating it as a beam fixed at one end (the shaft) and freely supported at the other, would be towards the shaft end[52]. Since this was not possible mechanically, the gauges were located about 50 mm from the shaft-end. Four identical gauges were fixed in pairs on opposite sides of the torque arm and electrically connected as a bridge circuit.

Use of other types of strain guages, such as piezo-electric or ceramic, was considered. However, these were judged unsuitable for steady-state torque measurement and too sensitive to vibrations and stray signals for the present work.

2.3.2 Calibration of the torque arm

The strain-gauge bridge was supplied by a 1 k Hz oscillator[SC], in a commercial 'transducer meter'. The out-of-balance signal was amplified by the same equipment and, after demodulation and rectification, measured by a moving coil instrument.

To calibrate the torque arm, the rotor was held between centres in a lathe, with the arm inclined and the free end resting

on a flat support. A string wound once round the rotor, with one end fixed and the other carrying a scale-pan and gram weights, was used to strain the arm. The deflection on the meter was noted for different weights. The calibration curve obtained is given in Fig. 2.5.

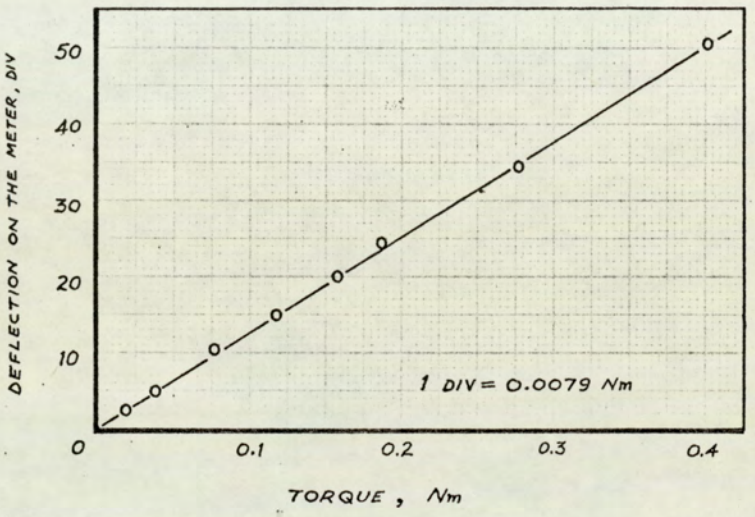

Fig. 2.5

2.3.3 Assessment of accuracy

Repeated calibrations of the torque arm showed that the torque could be measured consistently to within $\pm$ 1 % , in the range shown in Fig. 2.5, and that the mechanical hysteresis effect was un-noticeable.

The effect of frictional drag on the inner shaft bearing (see Fig. 2.1), which would result in an error torque, was checked carefully with the rotor in the machine and field system rotating at twice the normal speed, and was found to be negligible. Also, the speed of the field system during tests was high enough for stiction torque to be neglected.

2.4 Measurement of Speed

Accuracy in the measurement of speed of the field system was essential since the magnitudes of the e.m.f.s induced in the search coils were directly proportional to it. A permanent magnet and reed switch were used to produce an electric pulse at each complete revolution which triggered an electronic timer. A second pulse, produced at one-half revolution, was used to stop the timer. It was possible to measure the time interval to 0.01 second and consistency of speed measurement was observed to be within $\pm$ 2.0 % . Fig. 2.6 gives the essential details of the scheme.

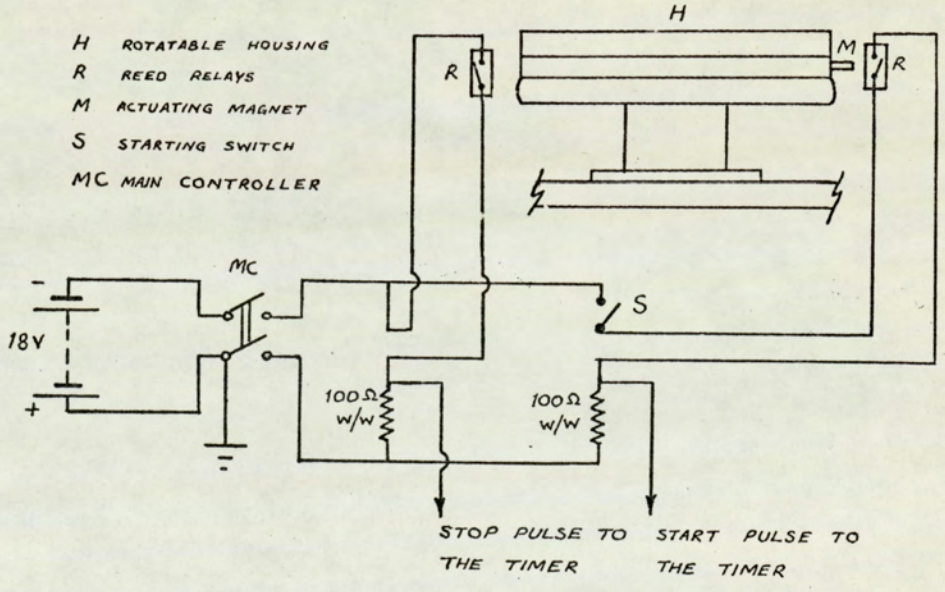

Fig. 2.6

2.5 Details of the Search Coils

The choice of a set of search coils on the rotor to determine flux density distribution was governed by various

factors discussed in detail in Chapter III. The present section describes the winding of the coils and discusses some of the practical difficulties involved.

2.5.1 Airgap search coils

The radial component of the flux density in the airgap was required at two different radii. This could be accomplished simply by winding two full pitch coils in the airgap adjacent to the external rotor surface, having their active lengths at the two desired diameters. The alternative method would have been to use one full pitch coil, giving the radial flux density at one of the radii, and a single turn coil with its plane on the same radius vector, giving an induced e.m.f. proportional to the difference of the two radial flux densities. When added algebraically to the induced e.m.f. of the first coil, this gives the radial flux density variation at other radius. The first method is more versatile because, with proper alignment of the search conductors and no stray 'pick-up', the induced e.m.f.s proportional both to the radial components as well as to the difference can be measured by simply altering the terminal connections. Hence, this scheme was adopted, the sectional details being shown in Fig. 2.7 (next page).

The main requirements for coils were mechanical alignment of the two full pitch coils on a diametrical plane, with the radial position of their active lengths accurately known, and sufficient radial distance between the coils, to simplify the mechanical construction and to give a realistic difference between the induced e.m.f.s at the two radii.

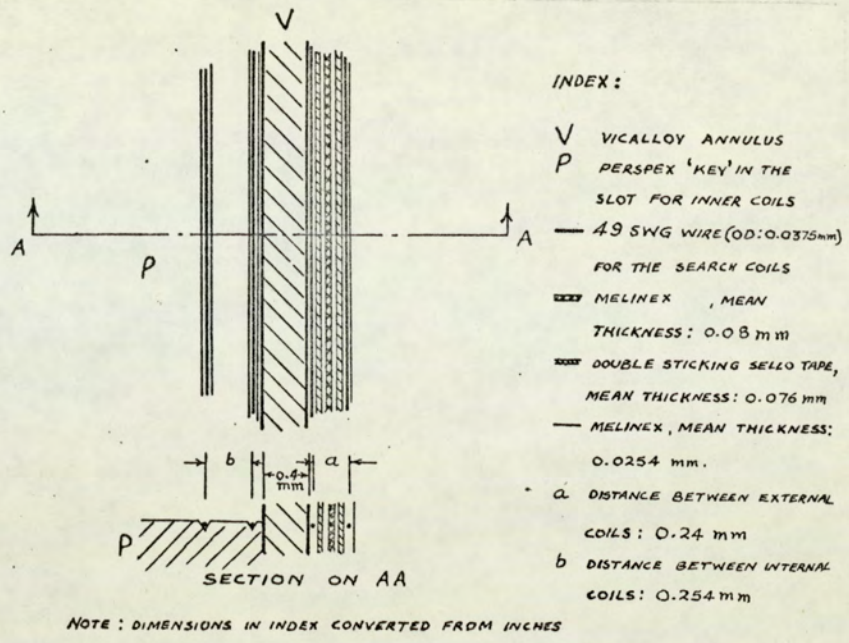

Fig. 2.7

Ideally, these requirements necessiate a long airgap. Since this was not available, very thin enamelled copper wire (49 SWG, O.D.:0.0375 mm) had to be used for the coils. This provided a sharp contour for the active coil sides. To achieve the mechanical alignment, a microscope having a magnification of 10 was used.

2.5.2 Inner search coils

Two similar full pitch search coils were wound in the arbor region adjacent to the internal rotor surface to study the magnetic field distribution on this surface. Restriction on the space requirements was unnecessary and sufficient radial distance could be allowed between the coil sides, although this could not be made too large since the magnetic field distribution away from the rotor surface changed rapidly and therefore would no longer be

wholly two-dimensional. Again, perfect mechanical alignment was essential and a special method of winding was used to align the coils to each other and to the coils on the external surface. The four full pitch coils were thus on the same diametrical plane, at four different known radii.

2.5.3 Search coils around the Vicalloy annulus

Two search coils were wound around the rotor annulus for miscellaneous tests. One was a single turn coil enclosing the full rotor section, to be used for measuring the induced e.m.f. proportional to peripheral flux density in the rotor. The other coil, of five turns, was wound through two holes (0.25 mm dia) 12.0 mm apart along the axial length of the annulus. This coil was to be used for ballistic measurements on Vicalloy as described in Appendix I.

2.5.4 Search coils on the "air-rotor"

A tufnol rotor, constructed on similar lines to the 'Vicalloy rotor' of Section 2.2.2.2 and having the same external diameter, was wound with two full pitch search coils on the outer surface. These coils were located identically to those on the Vicalloy rotor with regard to their radial position. The tufnol rotor, therefore, allowed measurement of flux density components at the same point in the machine but without spatial hysteresis. Being non-magnetic and non-metallic in construction this will be referred to as "air-rotor".

Table 2.1 (next page) summarizes the mechanical

details of all the search coils.

Table 2.1

Coil description	No. of turns	Conductor used	Size/Dimetrical distance between active sides	Remarks
4 full pitch coils on the Vicalloy rotor	one each	49 SWG, OD: 0.0015" (0.0375mm)	(i) 3.2384" (82.2554mm) (ii) 3.2195" (81.7754mm) (iii) 3.174" (80.6196mm) (iv) 3.154" (80.1116mm)	Mean diameter in order from the airgap towards the arbor. Active length : 25.4mm .
2 full pitch coils on the air-rotor	one each	Same	(i) 3.2384" (82.2554mm) (ii) 3.2195" (81.7754mm)	Active length : 25.4mm.
One coil round the Vicalloy annulus for B_θ measurement	one	48 SWG, OD: 0.0019" (0.0475mm)	25.4 mm x 0.4475 mm	Separation between the conductors : 0.4 mm (= thickness of the rotor annulus).
One coil enclosing the central portion of the annulus length	five	49 SWG, OD: 0.0015" (0.0375mm)	12.0 mm x 0.4375 mm	For ballistic measurements. Separation between the 'turns' : 0.4 mm, wound side-by-side.

2.6 Search Coil Instrumentation

2.6.1 Introduction

Measurement of the e.m.f.s induced in the search coils posed special difficulties because of their small magnitudes (the lowest being about 5 μV). The reasons for the small values were:

(i) The main search coils were placed in the airgap and the non-magnetic arbor region where the flux density was low due to the thin rotor of poor permeability.

(ii) Single turn search coils were used since accuracy of measurement of flux density at a 'point' was desired.

(iii) The speed of the field system was only 0.8 rev/s and the induced e.m.f. was proportional to this.

Therefore amplification of the e.m.f.s was necessary before measurements could be made. This was accomplished with high accuracy, wide band, direct coupled instrumentation amplifiers. These had very high input and low output impedances, thus minimizing the 'loading' effect on the search coil outputs.

The gain of the amplifiers was set at the minimum required level, precautions were taken in wiring, and the search coil leads were twisted, to avoid 'pick-up' problems. These effects were minimized also by using a differential-input scheme to the amplifiers wherever possible.

2.6.2 Recording devices

In addition to obtaining oscillograms the search coils' outputs were recorded on an Ultra Violet Recorder (UVR). The advantages of this were:

(i) Graphical analysis of the waveforms was necessary and the UVR could provide enlarged-scale, or expanded, records of several cycles of the waveforms. Naturally, a better method from this point of view would have been to use an analogue-to-digital converter, but the signals from the amplifiers were too small to consider this possibility.

(ii) Several traces could be recorded conveniently on a UVR.

(iii) UVR galvanometers, having suitable sensitivity and natural frequency of vibration, could be used to cut-down the high frequency noise from the amplifiers and other stray interference.

The UVR is not satisfactory for recording the sharp peaks, occuring near the pole tips, which are shown best by

oscillograms. This is not serious because, apart from defining the variation of the flux density, these peaks do not contribute significantly to power flow. Considering the overall accuracy of measurement (see Section 2.6.3 below), the use of a UVR was preferable to an oscilloscope.

2.6.3 Calibration of UVR galvanometers and assessment of accuracy

For calibration, each search coil was replaced by a known low voltage d.c. source, with an output comparable to the average induced e.m.f. The deflections of the UV galvanometers were recorded and mean calibration constants derived.

An assessment of the consistency of the galvanometer constants was made by repeating the calibration at regular intervals. The variation for different galvanometers was found to be from $\pm$ 0.5% to $\pm$ 1.0%. This variation was found to have negligible effect on subsequent calculations.

A galvanometer trace was used to record the instant when a particular coil side passed a given pole tip or the interpolar axis as the field system was rotated. A set of four small permanent magnets*, fixed on a Bakelite ring mounted under the aluminium housing (see Fig. 2.1), were used to actuate a reed switch and provide a rectangular pulse to the UVR. The position of these magnets was adjusted to close the switch momentarily at the correct instant.

---

*Two of these were used in conjunction with the coil around Vicalloy annulus.

2.7 General Comments

The machine is large in mechanical size considering the small power output available. This is mainly a consequence of the space requirement for the two-pole excitation winding which has sufficient ampere-turns to drive the rotor material well into magnetic saturation. The overhang parts of the winding are unavoidably large and cause a large leakage flux.

The short axial length was fixed in the original design of the machine and could not be altered. This is regarded as a serious failing and a contributory cause of error in the correlation between the two-dimensional analysis and the experimental work. Motors with similar L/D rotor proportions are in use[53], but in the majority the length and diameter are practically the same.

CHAPTER III

TESTS ON THE EXPERIMENTAL MACHINE

CHAPTER III

TESTS ON THE EXPERIMENTAL MACHINE

3.1 Chapter Outline

A detailed account is given of the tests performed on the experimental machine. These tests studied the variation of torque and flux density with applied m.m.f. (the excitation current). The flux density was deduced from the e.m.f.s induced in the search coils for both the Vicalloy rotor and the 'air-rotor'.

The aim of this chapter is to introduce the flux density waveforms obtained experimentally. The measured waveforms are illustrated as oscillograms and comments on their shape and other salient features made where necessary. The interpretation of these, and other derived waveforms, and their use in the calculation of power flow are the subjects of subsequent chapters.

The common parameter for all the tests was the applied m.m.f./pole. Each test consisted of making observations or measurements with increasing excitation current in definite steps (pertaining to the different stages of magnetisation in the rotor), and care was taken to preserve the cyclic magnetic state in the machine. If the excitation current was inadvertently set at a higher than the desired value, the machine was demagnetised and the test repeated.

3.2 Torque Measurements

3.2.1 Variation of torque with excitation

Since a major object of this research was to investigate the production of torque corresponding to different stages of magnetisation in the rotor, measurements of torque were made first at varying excitation currents. The torque-excitation curve obtained at constant speed (0.8 rev/s) is given in Fig. 3.1.

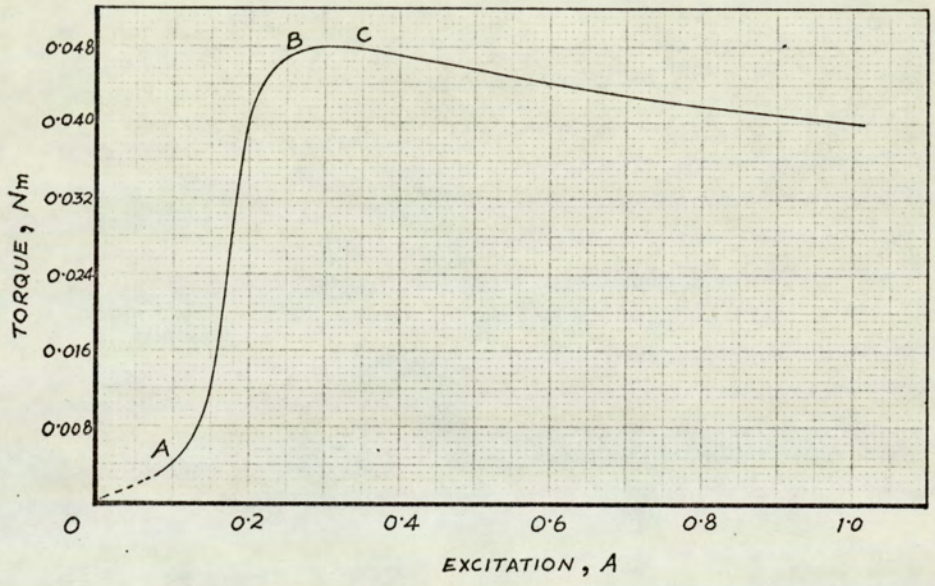

Fig. 3.1

The shape of the curve can be related approximately to the alternating-hysteresis loss curve, or indirectly to the magnetisation curve, for Vicalloy given in Appendix I. The torque for low excitation currents, upto 0.1 A (section OA in Fig. 3.1), increases slowly and corresponds to the initial portion of the B - H curve when the loss due to hysteresis is small. As the excitation is increased (section AB), the torque increases rapidly, almost linearly with current, and corresponds to the

steeply rising part of the loss curve (see Fig. A1.5, Appendix I). Finally, the torque tends to level off (section BC) in accordance with the near-saturation stage in Vicalloy, and at high excitation current (1.0 A) there is a reduction of about 17% in torque from the maximum value.

The above description is supported by the torque-excitation curve derived on the basis of pure alternating hysteresis loss and shown in Fig. A1.6, Appendix I. The derivation assumed a uniform flux distribution in the thin rotor, and a good correlation is seen between the two curves upto about 0.4 A excitation.

Further discussion of the torque-excitation curve is given in Chapters V and VI.

3.2.2 Torque measurements at varying speeds

By measuring the torque at different set speeds of the field system, the effect of any eddy currents in the Vicalloy rotor, or other metallic parts, could be ascertained. In addition, a test at standstill would show whether the operation of the coupling was similar to that of a motor at synchronous speed.

The excitation current was set at 0.3 A (corresponding to the maximum developed torque) and maintained constant during the test. The speed of rotation was gradually increased from the normal value of 0.8 rev/s to a maximum of 2.5 rev/s and a note made of the torque at several intermediate speeds. There was no noticeable difference in the values showing that the eddy-current torque could be assumed negligible. The presence of eddy currents would cause an increase in torque. At the same

time it is likely that any change in the mechanical characteristics would also cause an increase*, so that there is little possibility of the two effects cancelling.

To simulate the synchronous-speed operation of a motor, the speed was reduced gradually from its highest value of 2.5 rev/s to standstill (the slip in actual motor becoming zero). While holding it stationary in this position, the torque was observed to be the same as during 'normal' operation. The torque dropped to zero when the field system was released, the whole operation being depicted in Fig. 3.2 by the line PQ. This has the same shape as a part of the ideal torque-slip characteristic for a practical motor in the absence both of eddy currents and m.m.f. space harmonics. Harmonics are present in the experimental machine but they have a common speed and do not cause a variation in the torque-speed characteristic.

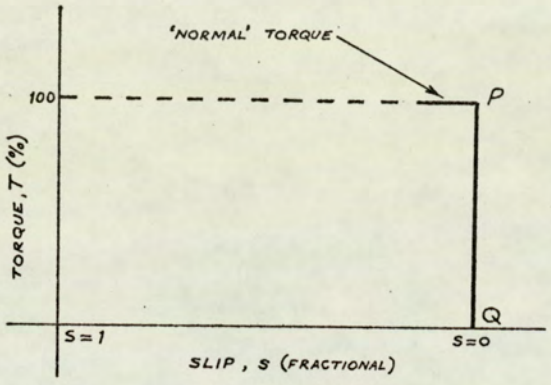

Fig. 3.2

3.3 Requirements for Magnetic Flux Density Measurements

With the assumption that any axial variation of the magnetic field could be disregarded, the study of the field distribution in the machine was confined to the radial and peripheral directions. The measurement principles involved are discussed below.

---

*Mainly the friction torque at the inner bearing (Fig. 2.1).

3.3.1 Radial magnetic flux density, B_r, distribution

The measurement of the radial component of magnetic flux density was based on the "flux-cutting" rule and made use of a full pitch search coil on the rotor. The e.m.f. induced gave either the space distribution of flux density at any instant, or the variation with respect to time for a given point on the rotor*. The advantages of using such a coil were simplicity of construction, and a measurable output. Accurate mechanical positioning of the coil conductors was essential; any 'short-pitching' would have eliminated certain order harmonics from the induced e.m.f. Careful dressing of the non-active portions of the coil was also an important factor, to avoid e.m.f.s induced due to stray flux.

3.3.2 Peripheral magnetic flux density, B_θ, distribution

3.3.2.1 Usual method of measurement

The usual method for deriving peripheral magnetic flux density in a thin magnetic material (e.g. the rotor annulus in this case) consists of using either a single- or multi-turn search coil enclosing the desired cross-section. A similar coil placed in the air region with one side in close contact with the surface is assumed to give an output proportional to the average tangential component of the magnetising force, H_θ, across the plane of the

---

*It is the former interpretation which is normally given to the various waveforms in the thesis, unless otherwise specified.

coil. The e.m.f. induced in such a coil is proportional to the time rate-of-change of the flux linking the coil (at constant speed), and therefore time integration of the coil output gives the variation of H_θ. Since the area of the coil has to be finite, the accuracy of the method depends on its width in a plane perpendicular to the rotor surface. However, the coil output has to be sufficient for realistic measurements, which necessiates either a wide coil or one having large number of turns. The latter makes it difficult to define the coil contour to calculate the 'area' of the coil* while the use of a wide coil is in contradiction to the above requirements. Therefore, a compromise must be made.

3.3.2.2 Validity of the method

The validity of the assumption that a narrow coil gives H_θ (or B_θ) on the longitudinal axis of the coil after time integration can be established by considering the induction of e.m.f.s on the basis of the flux-cutting rule applied to the radial components of flux density. With reference to Fig. 3.3 (next page), let the components of flux density at the mean radius of the coil, having coil sides at A and B, Δr apart, be B_r and B_θ. If the difference in the values of B_r at A and B is

---

*Even in a single turn coil when the physical distance between the conductors becomes comparable with the conductor diameter, the effective area of the coil can be upto 30 % greater. See Chapter VI, Section 6.5.2.1.

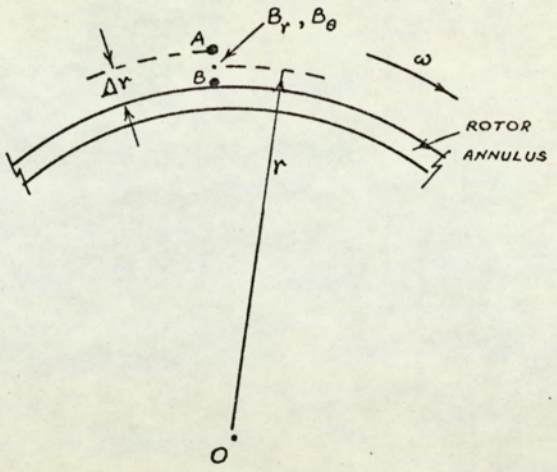

Fig. 3.3

ΔB_r, then the e.m.f.s induced in the coil sides will be

$$e_A = \omega\, l \left(r + \frac{\Delta r}{2}\right)\left(B_r + \frac{\Delta B_r}{2}\right) \qquad 3.1a$$

$$e_B = \omega\, l \left(r - \frac{\Delta r}{2}\right)\left(B_r - \frac{\Delta B_r}{2}\right) \qquad 3.1b$$

where l is the axial length of the coil and ω the angular speed of rotation relative to the field.

The output from the integrator will be

$$o/p = \int \left(e_A - e_B\right) dt$$

and the (apparent) peripheral flux density, B'_θ, related to the output

$$B'_\theta = -\frac{1}{a}\int \left(e_A - e_B\right) dt \ , \qquad a = \text{area of the coil } (l\,\Delta r).$$

Substitution for e_A and e_B followed by some simplification gives,

$$B'_\theta = -\int \left(r\,\frac{\Delta B_r}{\Delta r} + B_r\right)\omega\, dt \qquad 3.2$$

or

$$B'_\theta = -\int \left(r\,\frac{\Delta B_r}{\Delta r} + B_r\right) d\theta \qquad 3.3$$

Now at the mean radius

$$\nabla \cdot \bar{B} = \frac{1}{r}\frac{\partial B_\theta}{\partial \theta} + \frac{\partial B_r}{\partial r} + \frac{B_r}{r} = 0 \quad .$$

or $$-\left(r\frac{\partial B_r}{\partial r} + B_r\right) = \frac{\partial B_\theta}{\partial \theta} \qquad 3.4$$

If therefore the width of the coil is 'sufficiently small', the partial derivatives of equation 3.4 can be replaced by the incremental values ΔB_r, ΔB_θ, Δr and

$$B'_\theta = B_\theta \quad . \qquad 3.5$$

3.3.2.3 Problems encountered in 'time integration'

The limitations imposed by the theoretical considerations on the width of the coil result in low values of induced e.m.f. and the terminal voltage of interest may be as small as 10 - 15 μV. When fed to an electronic integrator, the output is affected seriously by the d.c. drift invariably present in the circuit as a whole, resulting from imperfections. The recording of the integrator output, B_θ, and the subsequent allowance for drift in the analysis of the waveforms, thus becomes extremely difficult.

Two methods sometimes used in practice to attenuate the drift are shown in Fig. 3.4, and consist of either a resistor in parallel with the feedback capacitor C_o or a capacitor C_c in series with the output. Both methods were tried, but were found unsatisfactory in

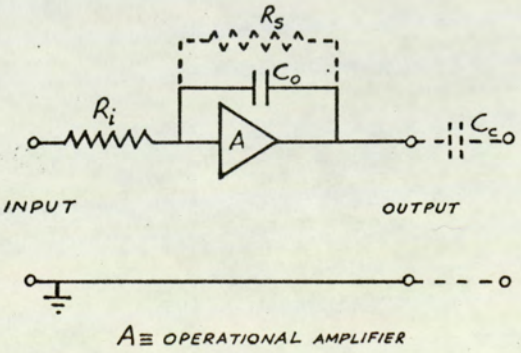

Fig. 3.4

the present context because of the very low frequencies being recorded. Consequently the integration was performed with standard integrator circuits.

3.3.2.4 'Errors' involved and further limitations

Notwithstanding the problem of drift, a drawback with the calculated value of B_θ from the integrated search coil output is that it is essentially a mean value making any analysis involving B_θ on the rotor surface erroneous.

In addition, it can be shown that the coefficients of sine and cosine terms of the high order harmonics, in the time - integrated B_θ waveforms, may differ appreciably from the correct values.

Consider a scalar magnetic potential distribution in the air region

$$\phi = A_n r^n \sin n\theta \qquad 3.6$$

where n is the order of harmonic and A_n the coefficient of n^{th} term.

The correct expressions for the B_r and B_θ components are derived from equation 3.6 (using $\overline{H} = -\overline{\nabla}\phi$) as

$$B_r = \mu_o H_r = -\mu_o \frac{\partial \phi}{\partial r} = - A_n \mu_o n r^{n-1} \sin n\theta \qquad 3.7a$$

$$B_\theta = \mu_o H_\theta = -\mu_o \frac{1}{r} \frac{\partial \phi}{\partial \theta} = - A_n \mu_o n r^{n-1} \cos n\theta \qquad 3.7b$$

If the coil sides (A, B) of the 'B_θ search coil' (Fig. 3.3) are located at radii a and b , then B_θ at a mean radius $r = (a+b)/2$ will be

$$B_\theta = - A_n \mu_o n \left[\left(\frac{a+b}{2} \right)^{n-1} \right] \cos n\theta \qquad 3.8$$

and the radial flux densities at a and b

$$B_{r_a} = - A_n \mu_o n a^{n-1} \sin n\theta \qquad 3.9a$$

$$B_{r_b} = - A_n \mu_o n b^{n-1} \sin n\theta \qquad 3.9b$$

For B_θ obtained from the time - integration of the difference of the induced e.m.f.s proportional to B_{r_a} and B_{r_b}, it can be shown, using equation 3.3, that the apparent peripheral flux density at $r = (a+b)/2$ is given by

$$B'_\theta = - A_n \mu_o n \left[\left(\frac{1}{n} \frac{a^n - b^n}{a-b} \right) \right] \cos n\theta \qquad 3.10$$

Comparison of equation 3.8 and 3.10 shows that the coefficients of cos nθ terms are different for the two cases and depend on the order of harmonic n. To give an idea of the extent of error involved, the expressions within the brackets were evaluated for various values of n and are reproduced in Table 3.1 below. The error becomes progressively worse as the harmonic order increases. It can be seen that the error for the same order of harmonic will be worse still for the larger values of $|a-b|$.

Table 3.1 $a = 1.0$, $b = 0.99$

Order of Harmonic, n / Terms in [ ] brackets	1	3	5	7	9	19	49	99	199	499	999
$\left(\frac{a+b}{2}\right)^{n-1}$	1.0	0.9900	0.9801	0.9704	0.9607	0.9138	0.7861	0.6119	0.3707	0.0824	0.0067
$\frac{a^n - b^n}{n(a-b)}$	1.0	0.9900	0.9802	0.9705	0.9609	0.9149	0.7936	0.6366	0.4345	0.1991	0.1001

3.3.2.5 'Field theory' integration

Because of these limitations, it was clear that an alternative approach was required to obtain the peripheral flux density waveforms in the non-magnetic regions of the machine. The basis for this was provided by the methods of mathematical physics - field theory. If the radial flux density waveforms could be determined accurately at two different radii in the region, and expanded into Fourier series, then the B_θ waveforms could be derived using the coefficients of the harmonic terms in these series (for details of the derivation and 'computerisation' of the expressions, see Appendix V). Since the radial flux density waveforms on the external and internal rotor surfaces were to be obtained using two full pitch search coils (see Section 3.3.1), similar waveforms at another point on the same radius vector could be derived from two other coils. The constructional details of these coils have been described in Chapter II (Section 2.5). To achieve better accuracy, the two coils on each side of the rotor annulus were connected electrically to provide the e.m.f. from the inner coil and an e.m.f. proportional to the difference of radial flux densities, ΔB_r. The two e.m.f.s were added to give the e.m.f. in the outer coil. A schematic diagram of the connections is given in Fig. 3.5 (next page).

Using the field theory approach enabled the inaccuracies due to drift from the integrator to be eliminated. It was also possible to calculate B_θ at any point within the appropriate region and, in particular, on the rotor surfaces.

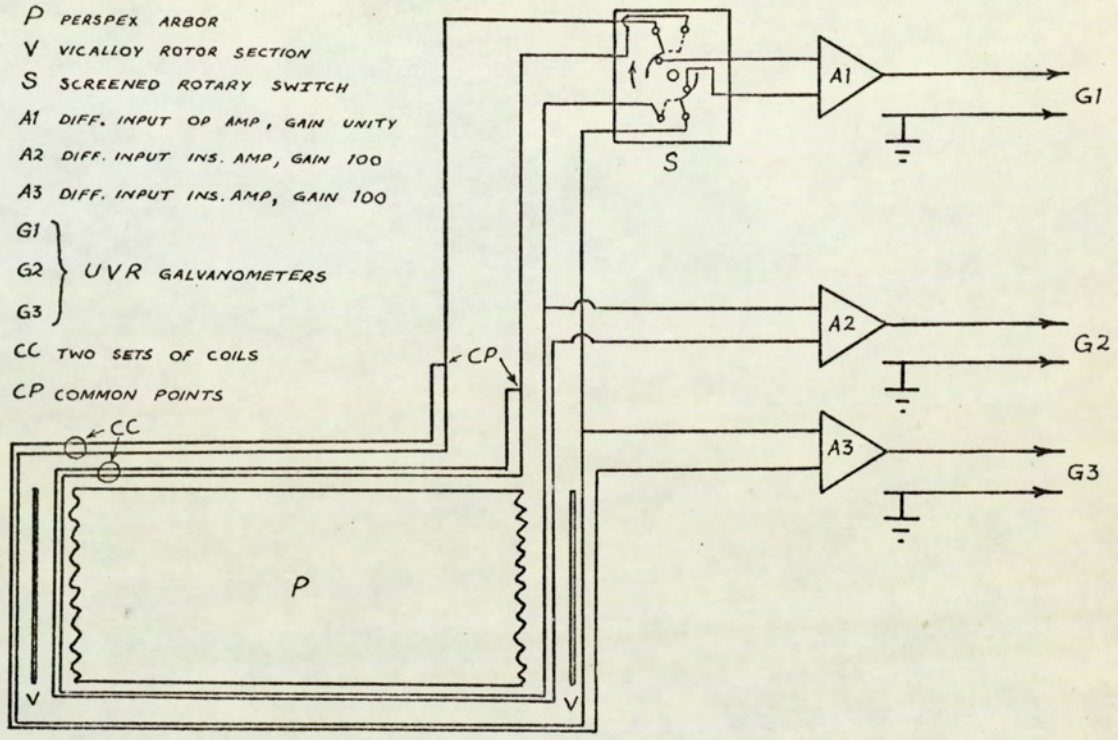

Fig. 3.5

3.4 Magnetic Flux Density Measurements

3.4.1 B_r and ΔB_r with the air-rotor

The experiments with a non-magnetic, non-metallic rotor were suggested by early tests in which the machine was treated as a stationary, non-linear magnetic circuit (see Appendices III and IV). Such a rotor would cause a similar flux distribution to the low-permeability Vicalloy rotor, but without the complication of spatial hysteresis. Teledeltos paper plots and analytical calculations using conformal transformation, discussed in Appendix III, revealed that some of the characteristic features, observed during the operation of the machine, were due to its

geometry. Although the analogue models were intended as a guide, the actual measurements of flux density with the air-rotor showed good correlation.

It was mentioned in Section 2.5.4 that a set of search coils were wound on the air-rotor corresponding to those on the external surface of the Vicalloy rotor. The B_r and ΔB_r waveforms obtained from these coils are shown in oscillograms 1 to 4 of Fig. 3.6 at two different excitations, 0.1 A and 0.3 A*. In shape the B_r waveforms closely resemble the theoretical waveforms given in Appendix III, and show sharp peaks at the pole tips. These peaks, which also occur in the B_θ waveforms, are caused by the sudden change in the geometry at the pole tips and are significant to the whole machine operation. The low permeability of the rotor results in a low radial flux density under the pole-centre which is observed also in the waveforms using the Vicalloy rotor, reported in the next section. The low flux density is not due solely to low rotor permeability, but is also a function of the radial thickness of the rotor annulus and so may be present even with high permeability material if the annulus is very thin.

3.4.2 B_r and ΔB_r with the Vicalloy rotor

These are reported separately for the airgap and the arbor region.

---

*These excitation currents are representative of non-hysteretic and pronounced hysteretic conditions in the rotor and have been chosen to typify the various measured waveforms and to make comparisons possible. See Appendix VII for waveforms at other excitations.

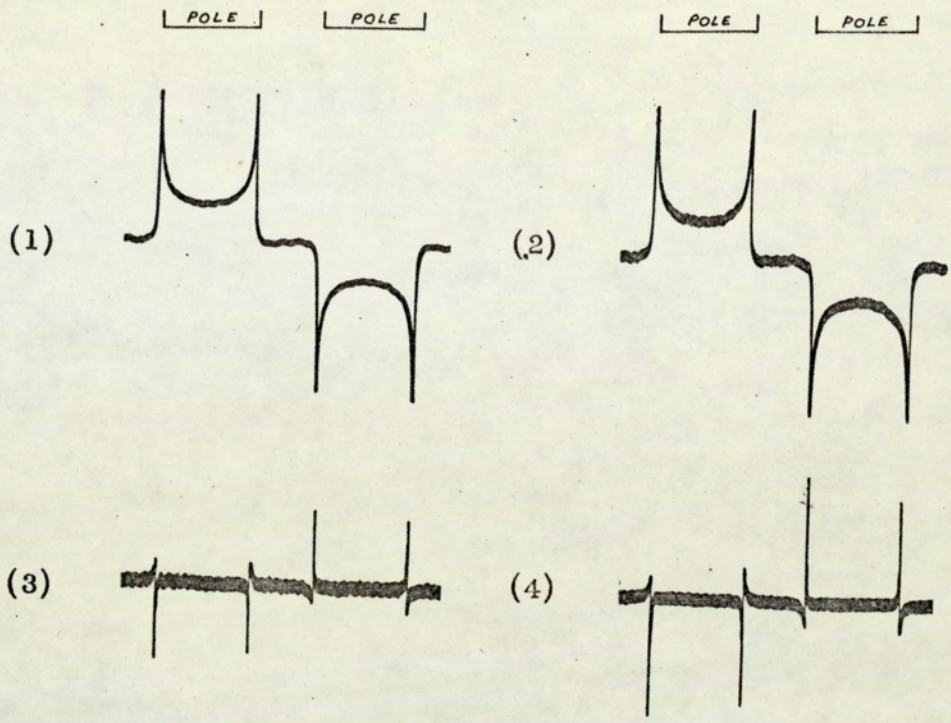

B_r and ΔB_r with the air - rotor

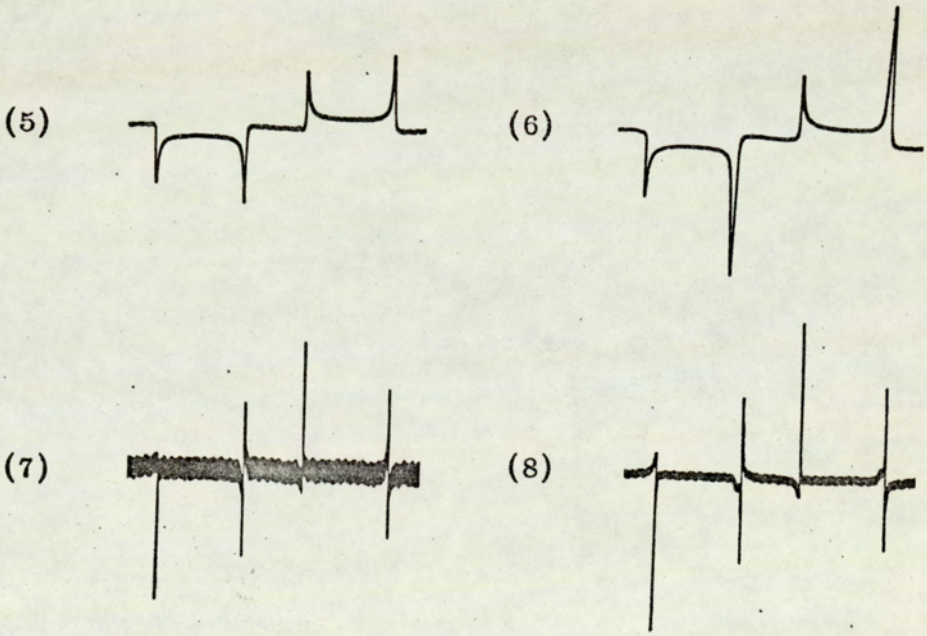

B_r and ΔB_r in the airgap - Vicalloy rotor

Fig. 3.6

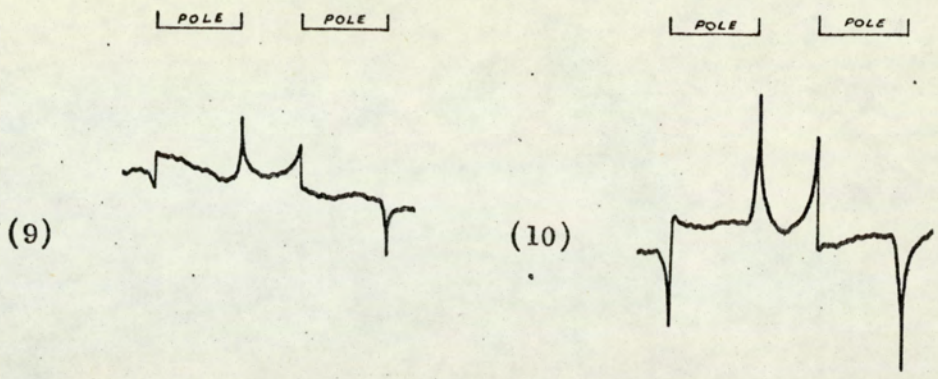

Time - integrated B_θ in the airgap - Vicalloy rotor

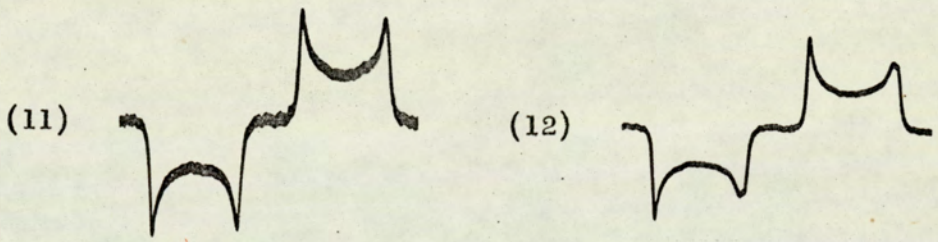

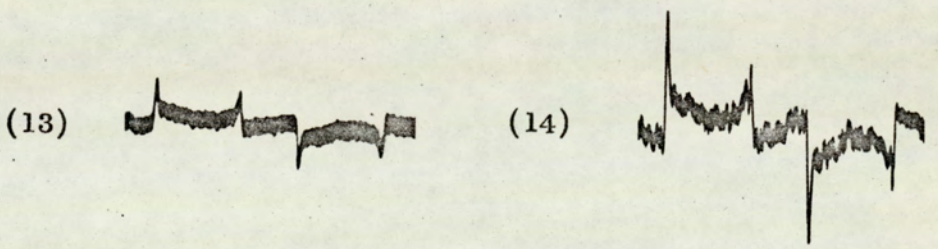

B_r and ΔB_r in the arbor region - Vicalloy rotor

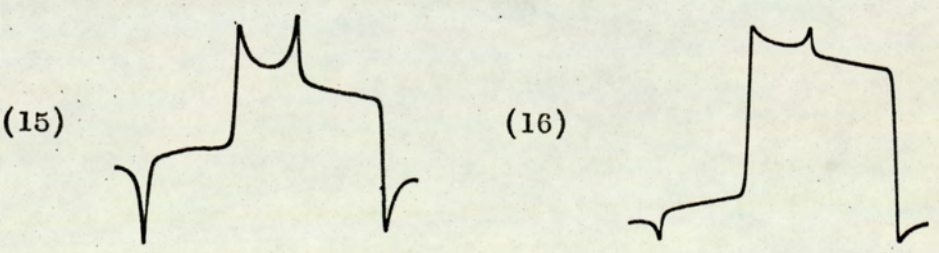

Time - integrated (or average) B_θ in the Vicalloy annulus

Fig. 3.6 (Contd.)

3.4.2.1 B_r and ΔB_r measurements in the airgap

The waveforms of B_r and ΔB_r in the airgap are shown in oscillograms 5 to 8 of Fig. 3.6. A comparison of the waveforms, with those obtained using the air-rotor, brings out the role played by the rotor hysteresis effect in space. As shown in Fig. 3.7, the flux is strengthened at one pole tip and weakened at the other, and this uneven distribution of the flux

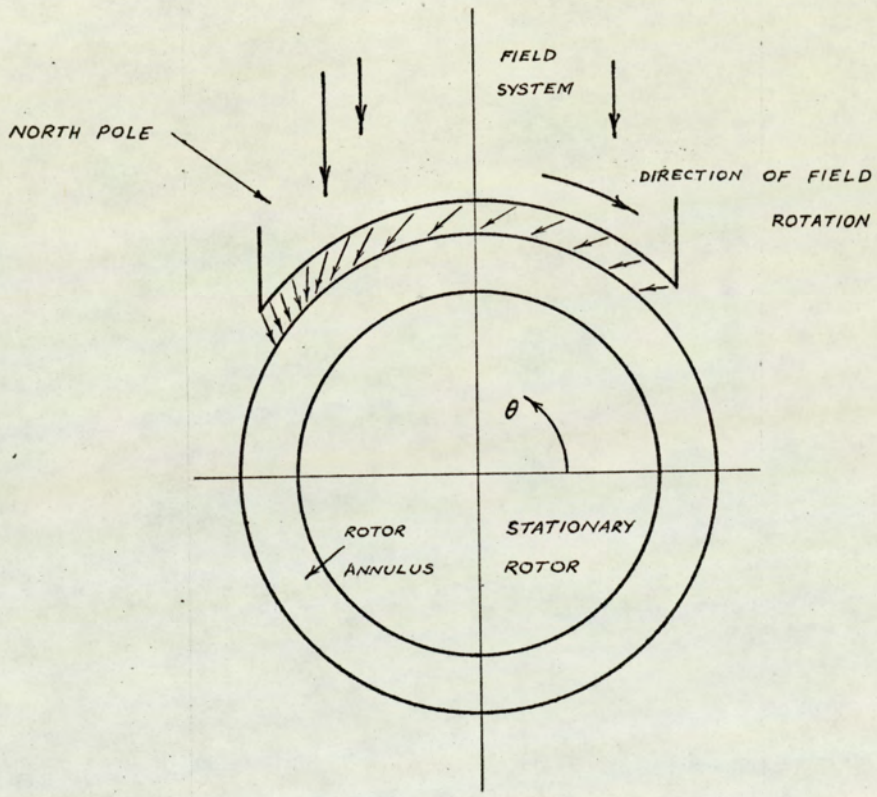

Fig. 3.7

in the two half-portions results in peaks of unequal heights in the measured waveforms. The hysteresis effect is seen to be more intense at the higher excitation (0.3 A) and the difference in the two peaks is very much increased (Fig. 3.6). Further discussion of flux distribution in the machine will

follow in Chapter IV.

The ΔB_r waveforms, shown in oscillograms 7 and 8, also highlight the effect of spatial hysteresis on the radial flux density distribution. Since the B_r values at the two radii are almost equal under the pole-centre and also in the interpolar region, ΔB_r is small and any space variation is obscured by the noise from amplifiers and 50 Hz pick-up from mains supply sources.

It should be noted that the sharp peaks in these waveforms do not occur necessarily opposite the pole tips, because the B_r waveforms, although very much similar in shape, differ appreciably at certain positions in space. This makes it essential to record B_r AND ΔB_r, instead of the two B_r waveforms.

3.4.2.2 Time - integrated B_θ waveforms in the airgap

These waveforms were recorded to give an idea of the general shape of the peripheral flux density variation under the effect of rotor hysteresis and are shown in oscillograms 9 and 10 of Fig. 3.6. It can be seen that the waveforms are influenced greatly by drift present in the circuit* and, except for the existence of peaks near pole tips, they do not convey much information. However, at higher excitations (>0.4 A) where the drift is much smaller than the signal (see oscillograms 5 and 6 of Fig. 3.8, Appendix VII) the effect of hysteresis

---

*A pre-amplifier with gain 100 connected to an integrator: overall gain = 10^4.

results in a non-zero peripheral flux density opposite the pole surfaces with reversal at the pole tip. This supports the computed B_θ waveforms of Chapter IV.

3.4.2.3 B_r and ΔB_r measurements in the arbor region

These are illustrated in oscillograms 11 to 14 of Fig. 3.6. The shape of the B_r waveforms indicates that the spatial hysteresis effect, shown by the difference in the heights of the peaks at the pole tips, is not present to the same degree as in the airgap. The waveforms therefore approach closely the B_r distribution of the air-rotor, having symmetrical peaks. Nevertheless, an appreciable flux crosses the arbor region, for the amplitudes of the waveforms are comparable to those in the airgap. The peaks, though still occurring near pole tips, are attenuated both in the B_r as well as in the ΔB_r waveforms which means that the rotor shields the arbor region to some extent from higher order harmonics, in spite of its poor relative permeability.

It is observed that the ΔB_r waveforms, in addition to being affected by noise, are distorted in shape due to slight inaccuracies in the winding of the coils and the dressing of inactive portions, resulting in some pick-up of stray magnetic fields.

Unlike the distribution in the airgap, the radial flux densities differ considerably at two points on the same radius vector in the arbor, and a measurable output is obtained both opposite the pole-centre and in the interpolar space.

Time integrated B_θ waveforms were obtained for arbor

region for similar reasons as in the airgap. These are shown in oscillograms 5 and 6 of Fig. 3.9, Appendix VII. Again, even though the shape is affected greatly by drift, the waveforms give support to the computed B_θ waveforms (Chapter IV).

3.4.2.4 Peripheral flux density waveforms for Vicalloy annulus

A single turn search coil, surrounding the annulus section, was used to obtain these waveforms. The output from the coil was amplified and then integrated. Since the drift was small and the harmonic content low, the errors due to time integration could be assumed negligible. These waveforms are illustrated in oscillograms 15 and 16 of Fig. 3.6 and were used to derive a torque-excitation curve based on pure alternating-hysteresis loss. The peaks occur almost opposite the pole tips at low values of excitation because the flux distribution within the rotor is governed by low permeability and negligible hysteresis. At an excitation of 0.3 A, spatial hysteresis is more pronounced and the flux distribution is nearly constant as shown by the 'square - shape' waveform of oscillogram 16*. At higher excitations, Fig. 3.10, Appendix VII, the peaks re-appear opposite the pole tips pointing to a modified flux distribution in the

---

*The slight slope that is observed is partly due to the recording being obtained on the oscilloscope where capacitance-coupled amplifiers are involved, affecting the low-frequency response, and partly to the finite thickness of the rotor.

annulus. The reversal of the peripheral flux densities in the airgap and Vicalloy occur opposite different tips of the same pole. This phenomenon is discussed in the following chapters.

3.5 Concluding Remarks

The tests described in the present chapter elucidate characteristic features of the experimental machine. The torque-excitation curve has a particular shape depending on the magnetic states of the rotor. In the range of excitation currents 0.15 A to 0.25 A the curve is nearly a straight line and this is a desirable feature for the application of the machine in some control systems. The torque has a maximum value very nearly equal to the theoretical maximum torque available on the basis of pure alternating-hysteresis loss. There is a reduction in torque at higher excitations ($>$ 0.3 A) which can be attributed to alteration of the magnetisation cycle in the rotor, as well as to a general modification of the flux distribution in the machine. These points will be discussed further in Chapters IV and V.

It may seem that undue prominence was given to the measurement and recording of induced e.m.f.s from which the flux density waveforms were deduced. This was not so, because an accurate knowledge of these waveforms is vital to the qualitative theory of operation and to the quantitative analysis of power flow developed later in the thesis. Using search coils, it was possible to determine the radial flux density waveforms at four different radii. Unfortunately because of drift and other limitations, peripheral flux density waveforms could not be determined from the experimental results.

The effect that a rotor having poor permeability but no spatial hysteresis, can have on the flux distribution has been shown by measuring B_r waveforms with an air-rotor. Subsequently the space hysteresis effect has been illustrated by comparing the waveforms with those obtained using a Vicalloy rotor. The shape of these waveforms is typical of the experimental machine. The field system geometry gives rise to sharp peaks in B_r and ΔB_r waveforms at all excitations and, as discussed in Appendix II, an elaborate method to expand the waveforms into Fourier series becomes indispensable, in preparation for the analysis discussed in the following chapters.

To eliminate errors arising from excitation current variation and changes in speed, the B_r and ΔB_r waveforms for the external and internal rotor surface were recorded simultaneously on the UVR. This was particularly important from the point of the power flow calculations dealt with in Chapter VI.

CHAPTER IV

COMPUTED MAGNETIC FLUX DENSITY VARIATION

CHAPTER IV

COMPUTED MAGNETIC FLUX DENSITY VARIATION

4.1 Chapter Outline

A comprehensive study of the flux density variation in the machine follows in the present chapter. No attempt is made to deduce this from first principles because of the non-linear B/H relations for the steel and Vicalloy, and the complex machine geometry. Instead the measured radial flux density waveforms form the starting point and are used with the Maxwell's equations to derive other waveforms in the air spaces. In particular, the peripheral flux density waveforms are obtained for both the Vicalloy and air-rotors. A characteristic feature of these waveforms is the existence of a unidirectional flux density under the poles. This indicates clearly a shift in the 'pole-axis', during operation, in the direction of rotation of the field system.

The resultant flux density variation in the airgap and the arbor regions (on the rotor surfaces) is presented in the form of polar plots. These show how the hysteresis effect, due to rotor, modifies the flux distribution in the two regions.

It should be noted that the term 'hysteresis' implies spatial hysteresis in discussions in this as well as following chapters. Extensive use was made of the digital computer and the term 'computation' will mean generally the computer

calculations (and results).

4.2 Computation of Waveforms : General Considerations

The details of proceeding from the recorded B_r and ΔB_r waveforms to expressions for the peripheral flux density variations, and the scalar magnetic potentials, are given in Appendix V. The digital computer* programme, incorporating a refined harmonic analysis procedure is given in Appendix II. In addition to the necessary mathematical statements for the derivation of various flux density waveforms, the programme includes the calculation of the power flow based on Poynting's theorem - this part of the programme is cosidered in detail in Chapter VI. The results described in this and subsequent chapters are obtained as a single print-out (specimen records of these are shown in Appendix VIII).

The first important step in computation was to decide on the highest order of harmonic where the Fourier series of B_r and ΔB_r waveforms could be truncated, since all the calculations were dependent basically on the harmonic analysis of these waveforms. To do this, various orders in ascending value were assumed and a set of calculations was performed for each, and it was found that the changes in the results (for the peak values of either the radial or peripheral flux density, or for the power flow) was less than 0.1% for harmonic orders over 199 (i.e. 100 harmonic terms as only odd harmonics are present).

---

* ICL 1905. Language used for programming: ALGOL 1960.

All subsequent computation was therefore carried out for 100 harmonics*.

The peak value of radial flux density was computed as a check on the input data and was very nearly equal to the peak value in the measured waveforms. The accuracy of the method does not depend simply on the use of a 'sufficient' number of ordinates and careful measurements, but is noticeably affected by the choice of points, which determines the 'fit' of the computed curves through the sets of three consecutive points. As shown by the oscillograms 7 and 8 of Fig. 3.6, page 67, this is more critical in the case of ΔB_r waveforms for the airgap, because of the sharp peaks.

4.3 Computed Radial Flux Density Waveforms

Although waveforms of radial flux density, B_r, were available from the outputs of the full pitch search coils, both in the airgap as well as in the arbor region, new waveforms were calculated for two main reasons. Firstly, the new waveforms were calculated at the same values of angular position as all other

---

*That a reasonable 'accuracy' could be achieved by considering only 100 harmonics in the results computed here need not undermine the theoretical importance of high order harmonics in building-up the peaks and hence the seriousness of the errors of time - integration (see Chapter III, page 62). The limitations in practice are due to several reasons; e.g., those in the measurement, recording and reading the data from the waveforms, or the self - cancelling effects of the terms in the series.

waveforms, which made comparison much easier. In general it was impossible to measure the ordinates at the required positions, because these would not give the best computer fit, and because allowance had to be made for the variation of paper speed in the UVR recordings, and in the speed of rotation of the field system, occurring during complete range of tests. Secondly, it was essential to have the variation known on the internal and external rotor surfaces rather than at any other radii. While the measured waveforms in the airgap approximately met this requirement, the recordings in the arbor region were for B_r determined from the output of the inner search coil, i.e., away from the rotor surface*.

4.3.1 B_r on the external rotor surface

The general shape of the radial flux density waveforms was interpreted in Chapter III where the increase in height of the peak on one side of the pole-axis, and corresponding reduction on the other, was attributed to spatial hysteresis. With the field system rotating in a clockwise direction and measurements made on search coils placed on the stationary rotor, the peak with smaller height will occur when pole tip A moves

---

*This scheme of measuring B_r and ΔB_r in a similar manner on either side of the annulus allowed the same computer programme to be used in all cases.

past the ~~the~~ coil (see Fig. 4.1). This will be referred to as the 'leading' pole tip (θ measured antiçlockwise in the rotor reference frame) and the other, B, as 'lagging' pole tip in all subsequent discussions.

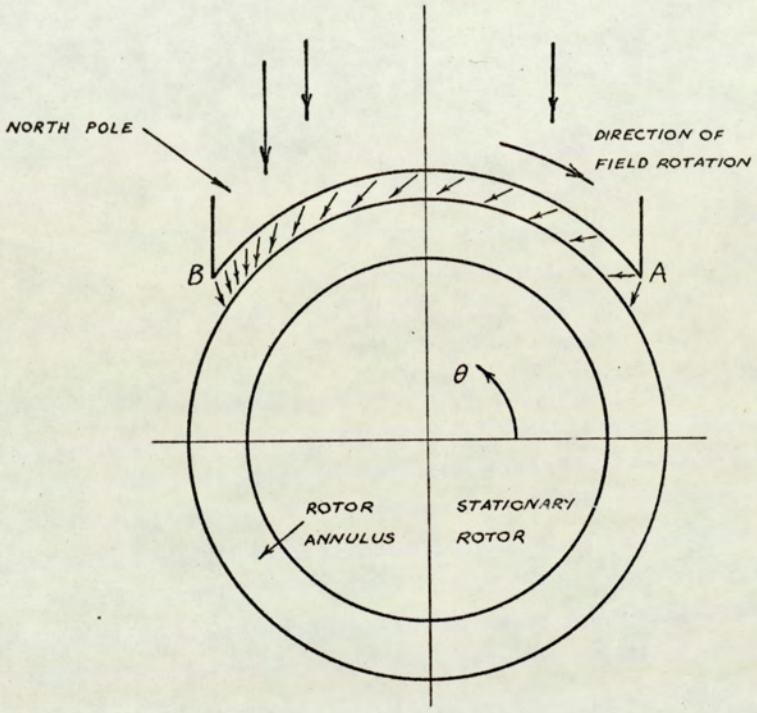

Fig. 4.1

The computed B_r waveforms on the external rotor surface for excitation currents in the range 0.1 A to 1.0 A are shown in Fig. 4.2 (next page) and are seen to be similar in shape to the oscillograms 5 and 6 of Fig. 3.6, page 67. The general comments made in Section 3.4.2.1 apply and the waveforms are representative of hysteretic conditions in the machine. The shape under the poles and the relative heights of the peaks at the pole tips undergo distinct changes at increasing excitations. The waveforms under the poles are almost 'flat' upto an excitation of 0.3 A, but become smoothly curved at higher

currents accompanied by changes in the relative heights under the pole-centre. This means that a greater proportion of flux reaches the rotor from the central part of the pole at higher excitations (> 0.3 A) than from the pole tips; the reverse being true at low excitation currents (0.2 A, 0.3 A). Considering the flux entering the rotor from the pole, there is a noticeable tendency for some of this flux to leave the external rotor surface in the interpolar region at excitations 0.6 A and 1.0 A as shown by a reversal in sign of the flux density at the interpolar axis. This is due mainly to the intense saturation and resulting low permeability of the surface in this region.

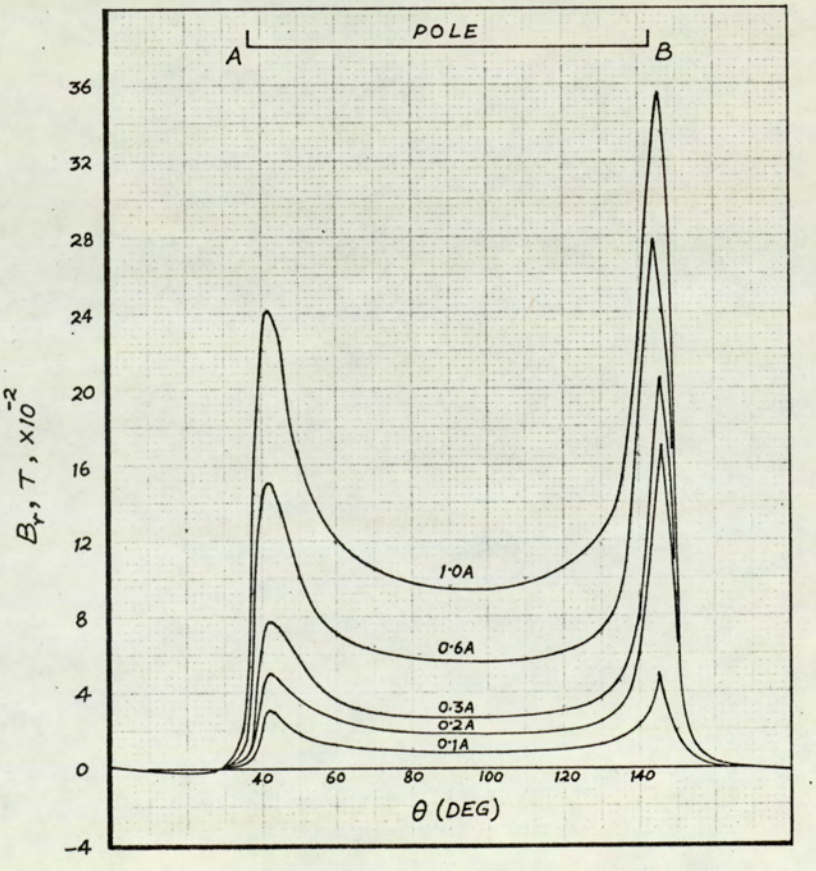

Fig. 4.2

A trend clearly observed in the waveforms is the rapid growth of the peak at pole tip B, relative to that at A, in the current range 0.1 A - 0.3 A. At higher currents, 0.3 A - 1.0 A, the increases become comparable. To some extent, this is due to the pole tips becoming highly saturated at higher currents, and because the flux within the pole is much greater, and therefore the distribution is less affected by the spatial hysteresis of the rotor.

The role of the radial flux density variation, with excitation, in the airgap is almost as significant as that of the peripheral flux density within the rotor in producing torque, and some of the points made above can be related to the machine performance on a qualitative basis. This is enlarged upon in Chapter V when dealing with the physical aspects of torque production in the machine.

4.3.2 B_r on the internal rotor surface

The waveforms showing the radial flux density variation for the Vicalloy rotor are given in Fig. 4.3 (next page) together with the waveforms for the air-rotor, since these are similar in shape and can be compared.

At 0.1 A excitation both waveforms appear symmetrical regarding the location and height of peaks, thus indicating negligible spatial hysteresis. Whereas there is a marked difference at 0.3 A excitation: the variation for the air-rotor is still symmetrical; that for the Vicalloy rotor has peaks with slightly different heights. This apparent space hysteresis effect with the Vicalloy rotor is due to rotor magnetisation (see

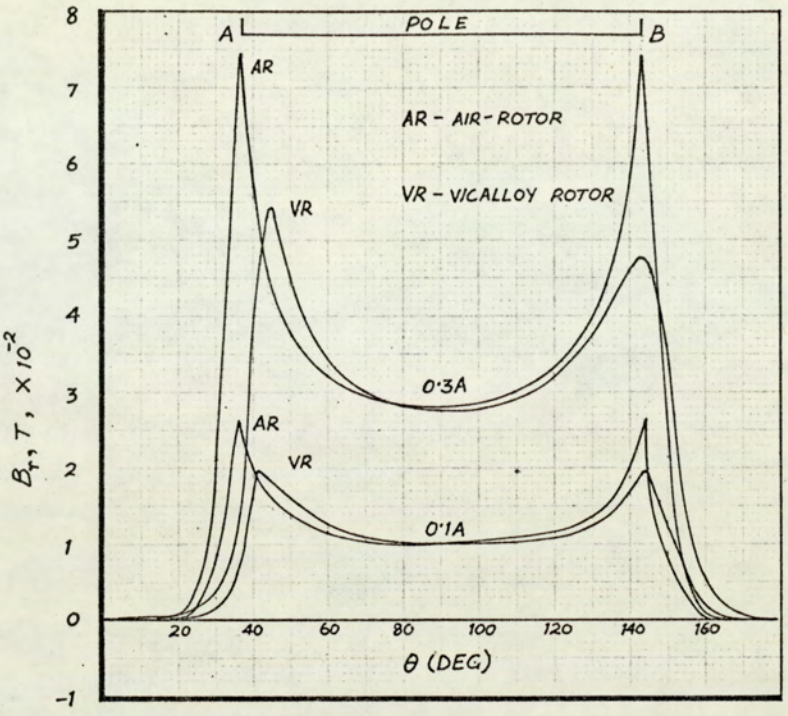

Fig. 4.3

Section 5.3), and results in a power flow through the inner surface (see Chapter VI). It is to be noted that the larger peak now occurs opposite the leading pole tip (A), instead of opposite the lagging tip as in the airgap.

4.4 Computed Peripheral Flux Density Waveforms

4.4.1 External rotor surface

The B_θ waveforms for both the air- and Vicalloy rotors are illustrated in Figs. 4.4 and 4.5, pages 84 and 85, respectively, together with the computed B_r waveforms. With the air-rotor the B_θ and B_r waveforms are symmetrical and displaced in space by $\pi/2$. This depicts the non-hysteretic situation and results in zero power flow over a closed cylindrical surface. Apart from an increase in height, there is little change in the

general shape from 0.1 A to 1.0 A excitation.

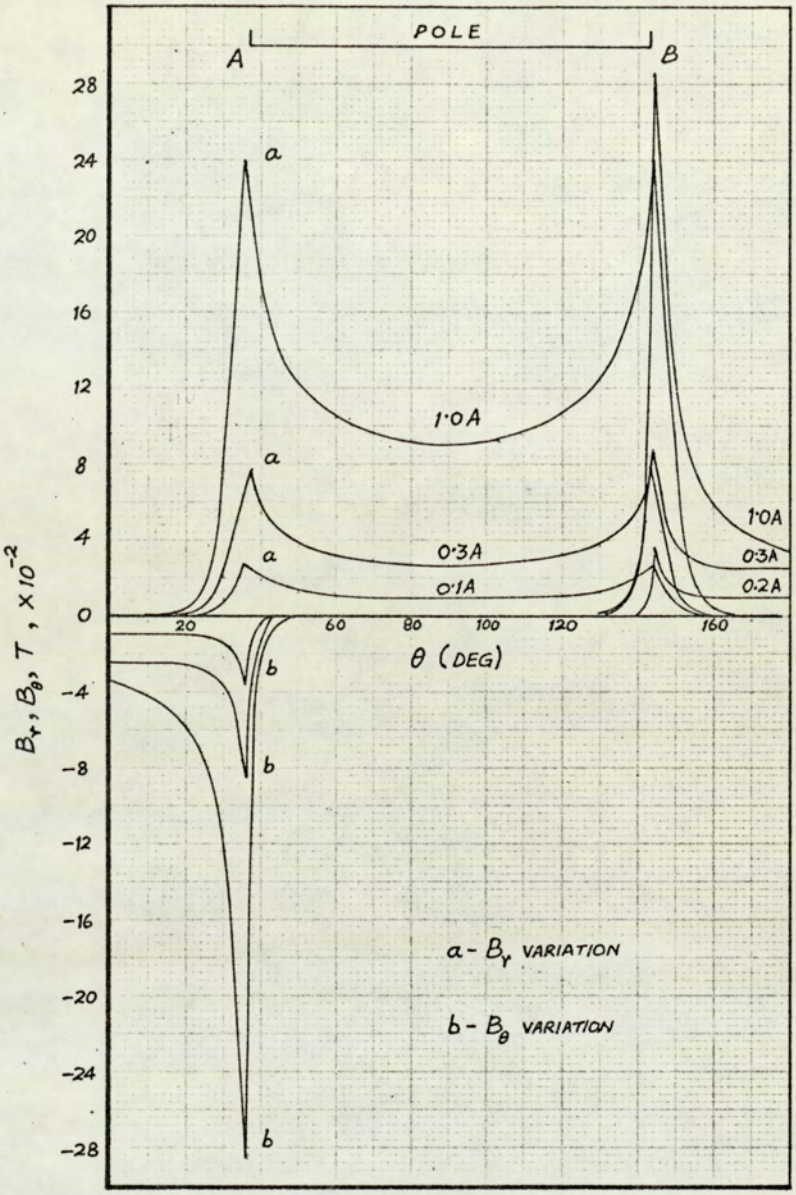

Fig. 4.4

A very important feature of the B_θ waveforms at all excitations for the Vicalloy rotor (Fig. 4.5) is the non-zero value under the poles which is practically constant over the pole arc. The existence of a non-zero, unidirectional B_θ under the pole is a sufficient but not a necessary mathematical condition for nett power flow and hence the production of torque. That it is a necessary magnetic condition in the experimental machine

is established in Chapters V and VI.

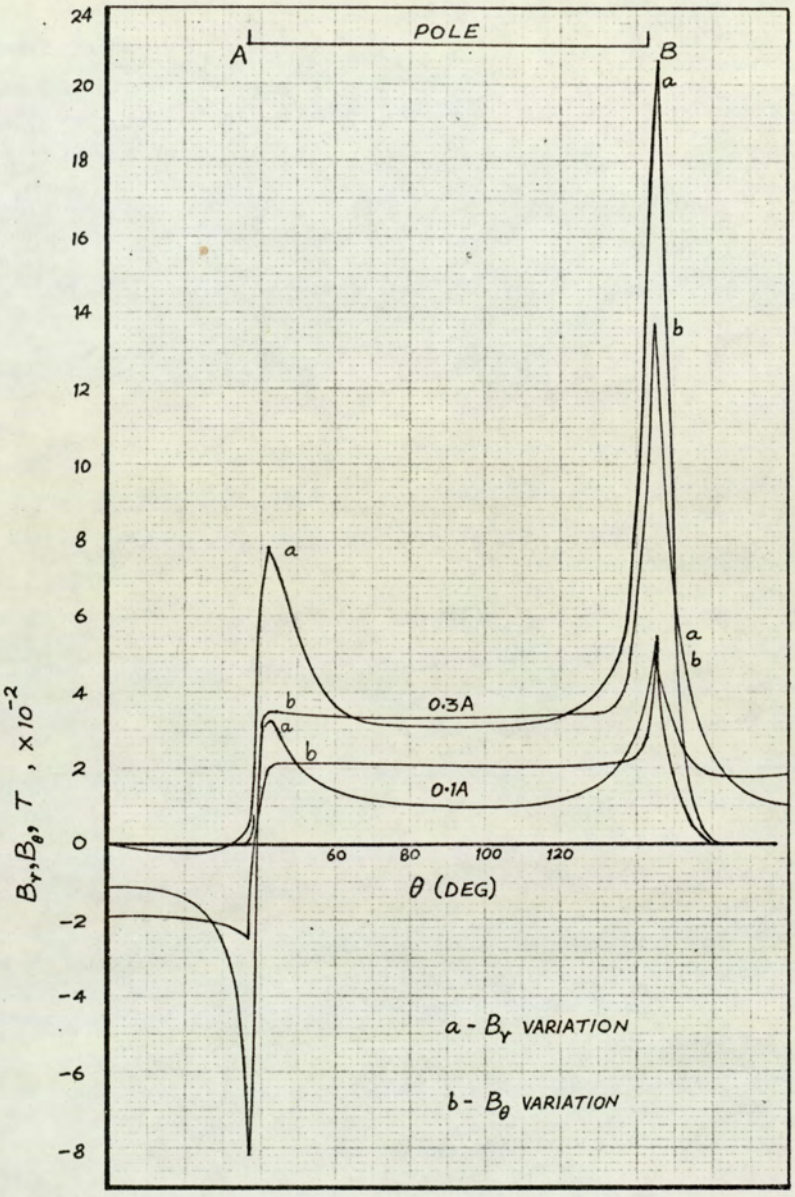

Fig. 4.5

Another important feature is that reversals in the waveforms occur nearly opposite the leading pole tips. This is confirmed by the oscillograms 9 and 10 of Fig. 3.6, page 68. With reference to the flux leaving the pole, this means that the pole-axis has shifted in space in the direction of the field system rotation and the flux now bifurcates near the leading

pole tips instead of at the centre. This effect is a special feature of the experimental machine since the location of flux division, even at a very low excitation current, is dictated by the sharp edge of the pole. The flux at the pole tip can flow either to the opposite pole or to the yoke, but with the poor permeability of the rotor, reduced further by the intense magnetic saturation, tends to leak away into the interpolar region towards the yoke. The approximate conditions pertaining to other common electric machines are compared with the experimental machine in Fig. 4.6. The inclined flux lines in the airgap of the latter (Fig. 4.6 b) were deduced from the waveforms of Fig. 4.5 and are further discussed in Section 4.5.

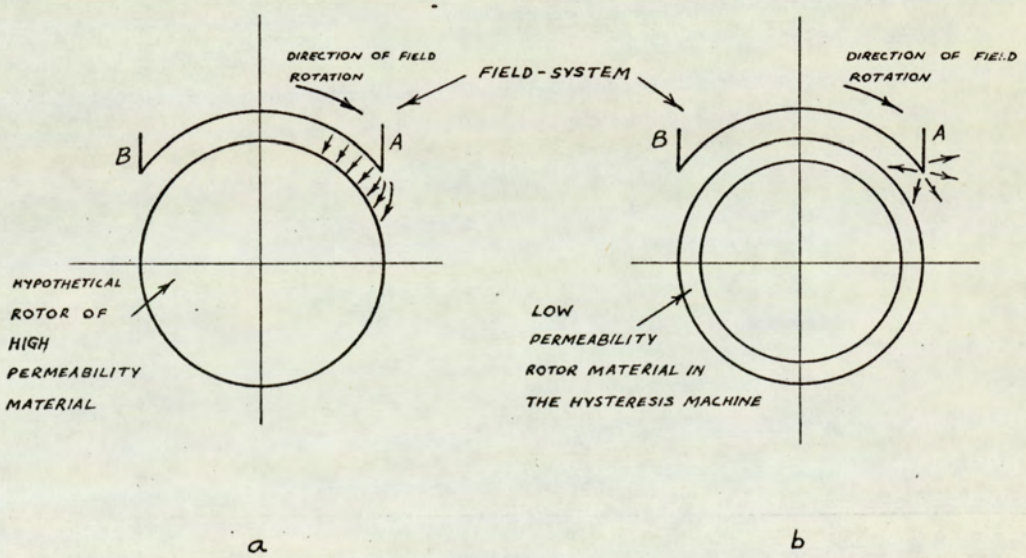

Fig. 4.6

4.4.2 Internal rotor surface

The waveforms on the internal surface, given in Fig. 4.7 (next page), differ in two main respects from those on the

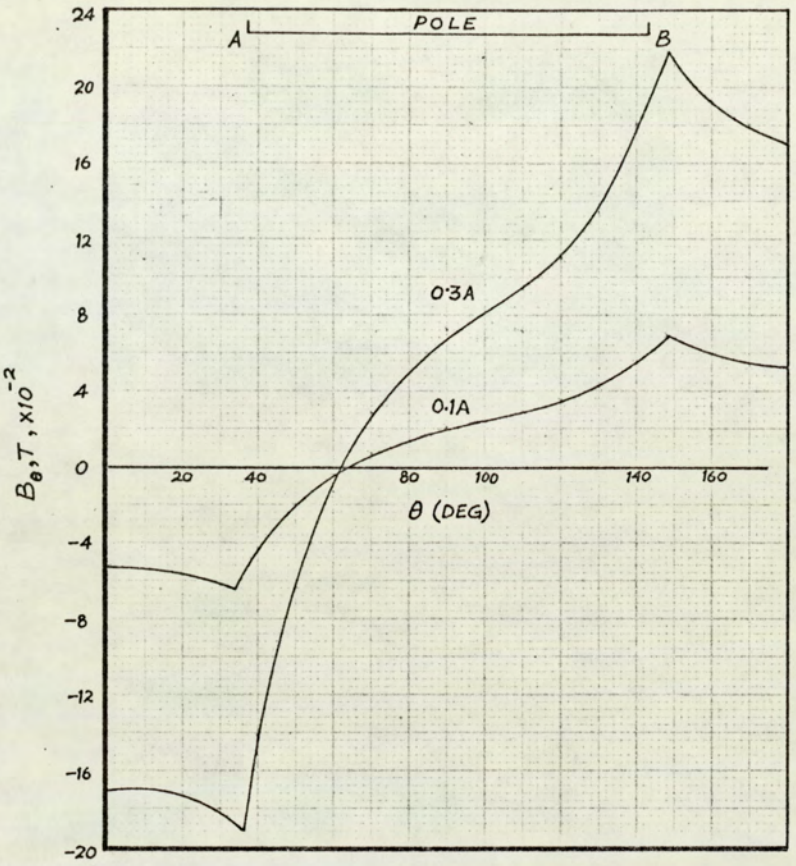

Fig. 4.7

external surface. Firstly, the values of B_θ on the interpolar axis are much higher than the corresponding values on the outer surface. Although this may appear an improbable phenomenon at first sight, a qualitative explanation can be extended as follows.

Consider the field system of the machine without the Vicalloy rotor (or with an air-rotor). At low excitation currents the flux distribution in the region between the pole surfaces takes the form shown in Fig. 4.8, page 88 (this corresponds to Fig. A4.1, Appendix IV, obtained as iron filing pattern, and later verified by the field plot calculations of Appendix III, Fig. A3.7).

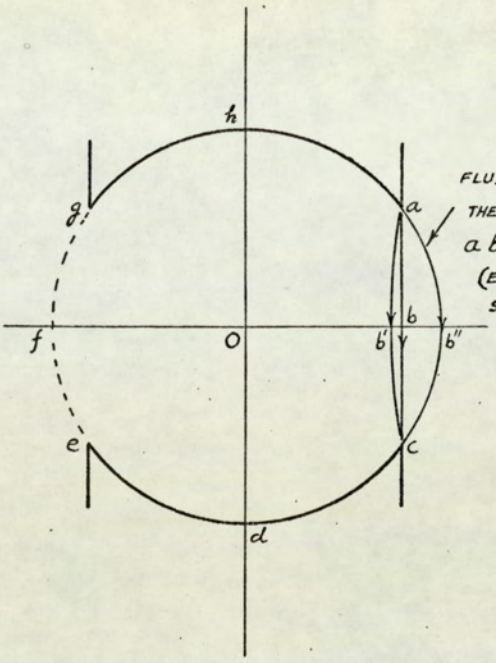

Fig. 4.8

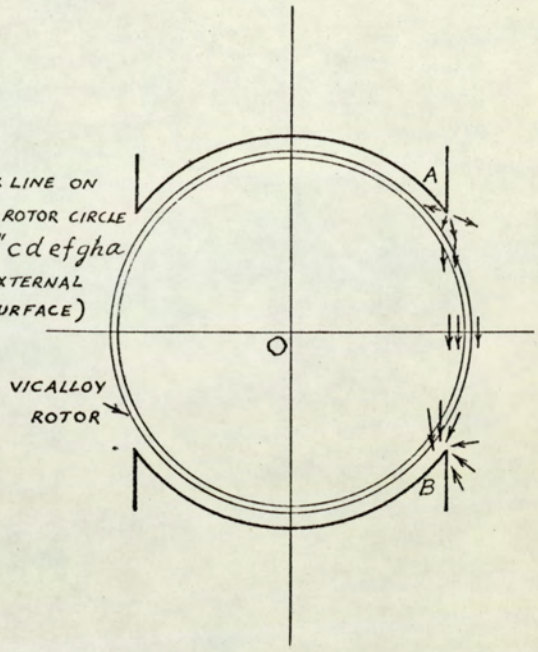

Fig. 4.9

With the concentration of flux at the pole tips, it is obvious that the flux between the tips will take a path such as a b c or a b' c rather than a b'' c which corresponds to the external surface of the air-rotor. This will result in a higher flux density in the inner region (point b or b'), compared to that at b'' .

A similar situation occurs with the Vicalloy rotor in the machine because the concentration of flux at the pole tips is very great. In particular, referring to Fig. 4.9, the flux density at the lagging pole tip B is always much higher than at A during operation. The direction of the flux lines at key positions will be as indicated by small arrows in the figure. The presence of a thin rotor forces most of flux leaving A in the direction of B to pass through the Vicalloy and the inner region

rather than take the path along the external rotor surface. A large proportion of the flux on the external pole surface in the interpolar region leaks away towards the yoke, particularly from the lagging pole tip B (confirmed by the iron filing patterns of Appendix IV), instead of crossing the interpolar region to the opposite pole tip, again reducing the flux density on the external surface of the rotor.

The other difference between the waveforms on the two rotor surfaces is the point at which the peripheral flux density reverses. On the internal surface this lies between the leading pole tip and the pole-axis. Further consideration to this aspect is given in Section 5.3.4, Chapter V.

4.5 Resultant Flux Density Distribution

The resultant flux density variation was obtained by vectorially combining the B_r and B_θ values at any point in space. This was used to study the direction of the flux lines entering different points on the rotor surface. Displayed as polar plots, these provide a clear picture of the flux distribution in the regions of interest both in magnitude and direction, and are given in Figs. 4.10 and 4.11 (pages 90, 91) for the representative currents of 0.1 A and 0.3 A.

4.5.1 Plots for the air-rotor

The variation for the air-rotor is depicted in Figs. 4.10 a and 4.11 a. It is seen that the flux in the airgap under the pole surface is radial but at the pole tips changes

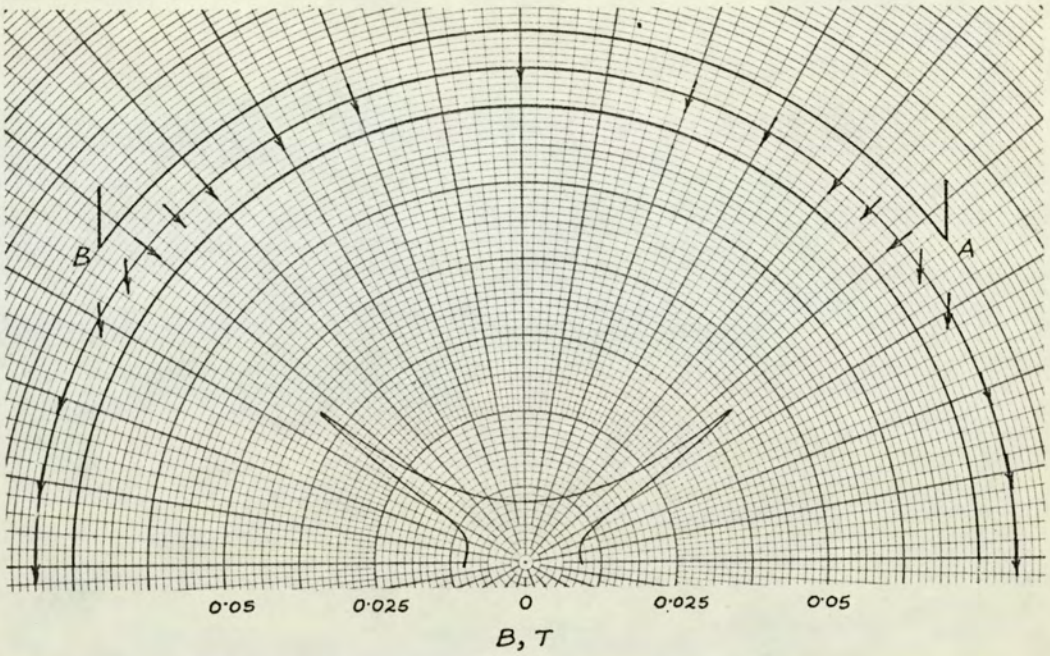

Fig. 4.10 a

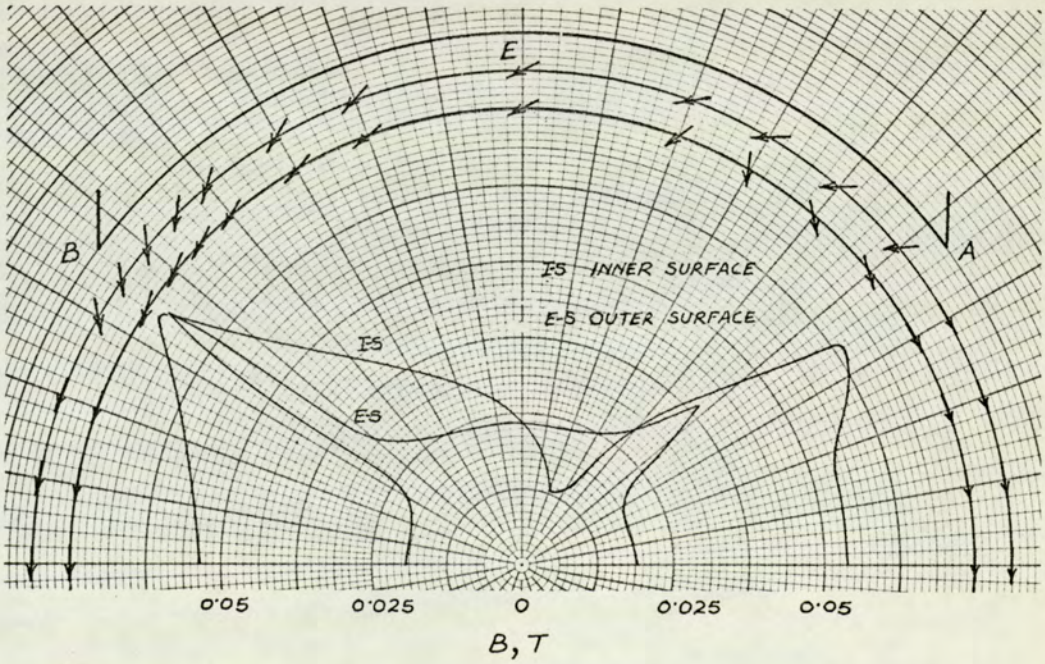

Fig. 4.10 b

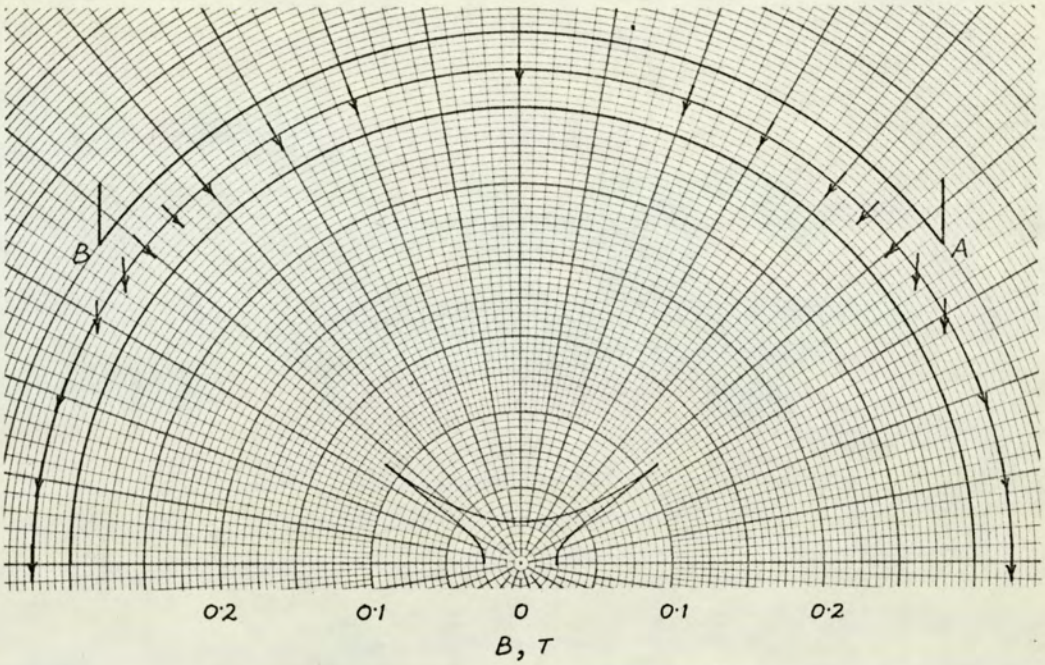

Fig. 4.11 a

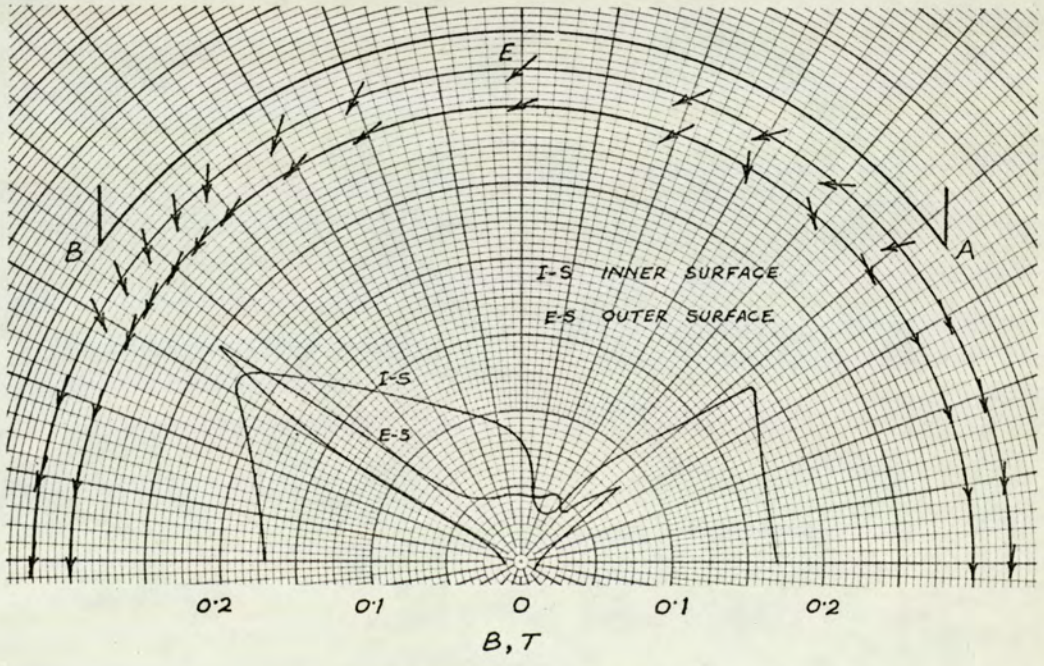

Fig. 4.11 b

direction to take a short path to the opposite pole, supporting the arguments given in Section 4.4.2. The resultant flux density is a maximum and has the same value opposite the two pole tips. There is little alteration in the trend of the variation at the two excitations. These plots match the flux distributions arrived at analytically (Appendix LII), and by the iron filing analogue (Fig. A4.1, Appendix IV).

4.5.2 Plots with the Vicalloy rotor

These plots, shown in Figs. 4.10 b and 4.11 b, are very different from those for the air-rotor. The flux lines are no longer radial in the airgap but inclined in a special manner, characteristic of this machine, because of the non-zero peripheral flux density under the pole surface. The angle of inclination at different points on the external rotor surface under the poles is in the range 20° to 50° to the radial direction. Without the Vicalloy rotor this angle would approach zero. A qualitative explanation for why this angle lies in the above range is given below.

4.5.2.1 Angle of inclination of the flux density

The angle of entry (α) of the flux density on the pole-axis, point E in Figs. 4.10 b and 4.11 b, will be considered. A current of 0.3 A will be taken as representative and the demagnetisation portion of the B - H curve for Vicalloy is shown in Fig. 4.12 (next page). It is shown in Section 5.3.2.1 (Chapter V) that for this part of the rotor

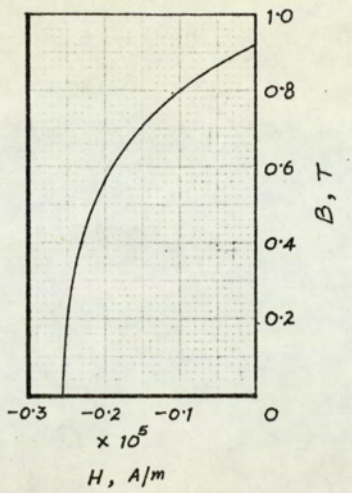

Fig. 4.12

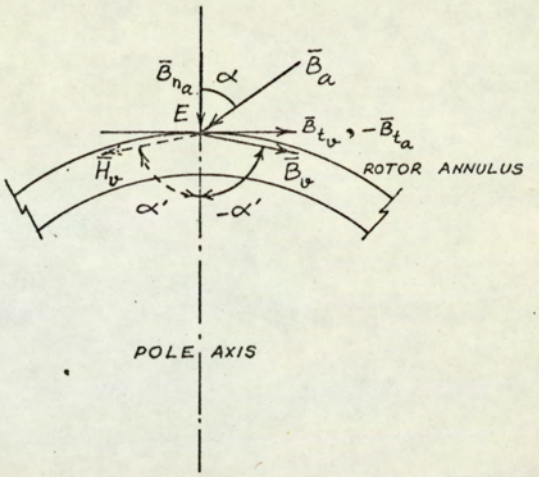

Fig. 4.13

B_θ and H_θ are oppositely directed, so that the vectors are disposed as shown in Fig. 4.13. Since the flux density in the airgap is small compared with that in the Vicalloy, it is assumed that the magnitude of the average B_θ in the Vicalloy is obtained from the B - H curve using the peripheral component of the airgap magnetising force H_θ, and that the angle α' is deduced from B_θ and the normal component of the airgap flux density. Hence

in Vicalloy $\quad \tan(-\alpha') = -\dfrac{B_{t_v}}{B_{n_a}}$

in airgap $\quad \tan(\alpha) = \dfrac{B_{t_a}}{B_{n_a}}$

or $\quad \dfrac{\tan(\alpha)}{\tan(-\alpha')} = \dfrac{B_{t_a}}{B_{t_v}}$ (for the same values of H_t)

Therefore $\quad \alpha = \arctan\left[\dfrac{B_{t_a}}{B_{t_v}} \tan(-\alpha')\right]$ 4.1

If H_t is taken as 10^{-4} A/m then $B_{t_a} = 1.257 \times 10^{-2}$ T and $B_{t_v} \doteq -0.8$ T.

Substituting in equation 4.1,

$$\alpha = \arctan \left[\frac{\tan (-\alpha')}{63.7} \right]$$

The basic assumption throughout has been that the flux density in the Vicalloy is predominantly peripheral, and therefore a value of α' of about 89^{o} is to be expected. In this particular case α would then be 45^{o} or slightly less. A similar situation obtains for other values of current because of the similarity of the demagnetisation curves.

This explanation is possible because the value of H_t in the airgap is approximately the same as the average value of H_t in the Vicalloy under the pole. It cannot be extended to the inner surface because the approximation is not valid.

4.5.2.2 Hysteresis effect

Plots of the magnitude of the flux density in the airgap show that the resultant flux density is much higher at the lagging pole tip (B), and that the relative difference between the peak values at the two pole tips is considerably more at 0.3 A excitation. As expected, the hysteresis effect is not so pronounced on the inner surface. The large peripheral component of flux density results in the 'butterfly' shaped patterns in the figures.

An advantage of the polar plots is in indicating the physical location of the 'equivalent' poles in the airgap and the arbor region. In terms of the direction of the flux density, it would appear that the equivalent pole-axes have shifted towards

the leading pole tips during the operation, as pointed out by the B_θ waveforms.

4.6 Comments

Comparing the measured and computed waveforms for the air-rotor with those for the Vicalloy rotor, the most significant changes in the flux density variation, when the machine is in operation, are the concentration of flux in the airgap near the lagging pole tips, and the existence of a noticeable peripheral component of flux density under the pole surface. Since the material outcome of these changes is observed in the form of developed torque at the shaft, this suggests a relationship between the two effects.

This, however, is not easy to establish and a first step in this direction is to evolve a qualitative theory relating the magnetic conditions in the rotor to the phenomenon of torque production. This approach, followed in the next chapter, has in addition the distinct advantage of presenting simultaneously a physical picture of the operation at different stages, and leads to a more realistic treatment of the problem.

CHAPTER V

QUALITATIVE THEORY OF OPERATION

CHAPTER V

QUALITATIVE THEORY OF OPERATION

5.1 Chapter Outline

A general discussion of the torque - excitation curve for the experimental machine was given in Chapter III where the developed torque was related to the stages of magnetisation of the rotor in the light of the alternating-hysteresis loss curve. One object of this chapter is to develop that discussion by considering in detail the phenomenon of torque production, particular attention being paid to the reduction of torque at higher excitation currents.

The possibility of obtaining the torque analytically, in different ranges of excitation, is explored and approximate formulae, relating torque to excitation, are derived. A point to note in this connection is the assumption that the developed torque is numerically equal to the hysteresis loss/revolution. This relationship is established in the next chapter.

Following the detailed study of flux density variation in Chapter IV, a qualitative theory is now developed to explain the operation of the machine. This takes into account the various factors responsible for the observed performance, including leakage flux and the redistribution of the magnetic field in different regions. The phenomenon of rotor magnetisation is considered in detail and its importance in

relation to the theory demonstrated. It is shown that the physical principle of machine operation cannot be comprehended without treating the rotor magnetisation as an independent entity.

Graphs of scalar magnetic potential on the external rotor surface, derived from the measured flux density waveforms, are given and a possible analytical treatment of the machine performance is postulated on the basis of the potential distribution in the airgap.

5.2 The Torque - Excitation Curve

The measured torque curve of Fig. 3.1, page 55 is reproduced in Fig. 5.1 below. It can be divided in three distinct

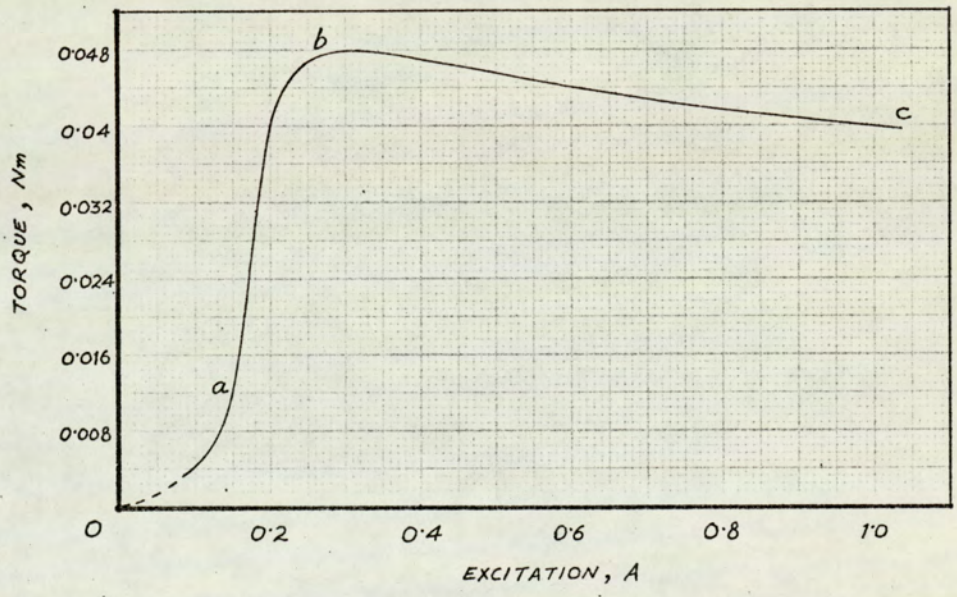

Fig. 5.1

regions or parts according to shape : a lower bend, 0 a, over which the torque rises slowly; a steeply rising portion a b where the torque is almost proportional to the excitation; and a second nearly linear portion b c. In the present arrangement, a

'maximum' torque is reached at b and b c shows the torque decreasing with increasing excitations.

For future reference, the three regions are defined as I, II, and III, corresponding to the excitation current ranges 0 - 0.15 A, 0.15 - 0.25 (or 0.3 A), 0.4 - 1.0 A respectively for the experimental machine. These current ranges will also be identified as 'low excitation currents', 'normal excitation currents' and 'higher excitation currents'.

The following sections discuss in detail the relation between the torque in the three regions and the magnetic conditions of the rotor and the machine in general.

5.2.1 Torque at low excitation currents (Region I)

The torque equivalent to the alternating-hysteresis loss in this region corresponds to the initial part of the magnetisation loss/excitation curve; it can be expressed analytically and related to the magnetising force in the rotor. This is because the hysteresis loops can be represented in 'parabolic' form[54] to a good approximation and their area calculated mathematically. Referring to Fig. 5.2 (next page), the B - H curve for Vicalloy (reproduced from Appendix I) can be approximated upto a certain point P by the relationship

$$B = \mu_i H + \nu H^2 \qquad 5.1$$

where μ_i and ν are constants. When evaluated for the present curve, these are found to be

$$\mu_i = -0{\cdot}02 \times 10^{-4} \ H/m$$

and $$\nu = 1{\cdot}24 \times 10^{-9} \ H/A$$

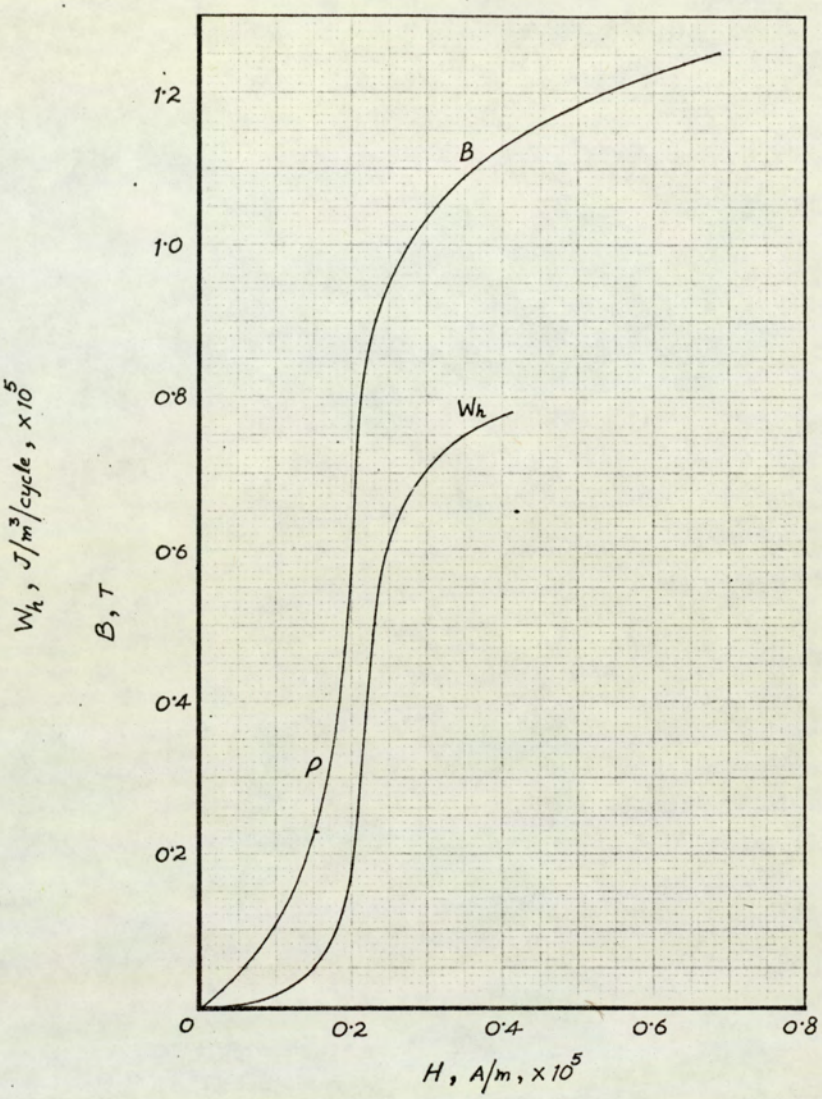

Fig. 5.2

for an upper limit of $H = 0.15 \times 10^5$ A/m.

The equation of the total loop a b c d a, Fig. 5.3 (next page), is given by[37]

$$B = (\mu_i + \nu \hat{H})\, H \pm \frac{\nu}{2} (\hat{H}^2 - H^2) \qquad 5.2$$

and the area of the closed loop, representing alternating hysteresis loss/m^3/cycle is

$$W_h = \oint B\, dH = 2 \int_{-\hat{H}}^{+\hat{H}} B\, dH \qquad 5.3$$

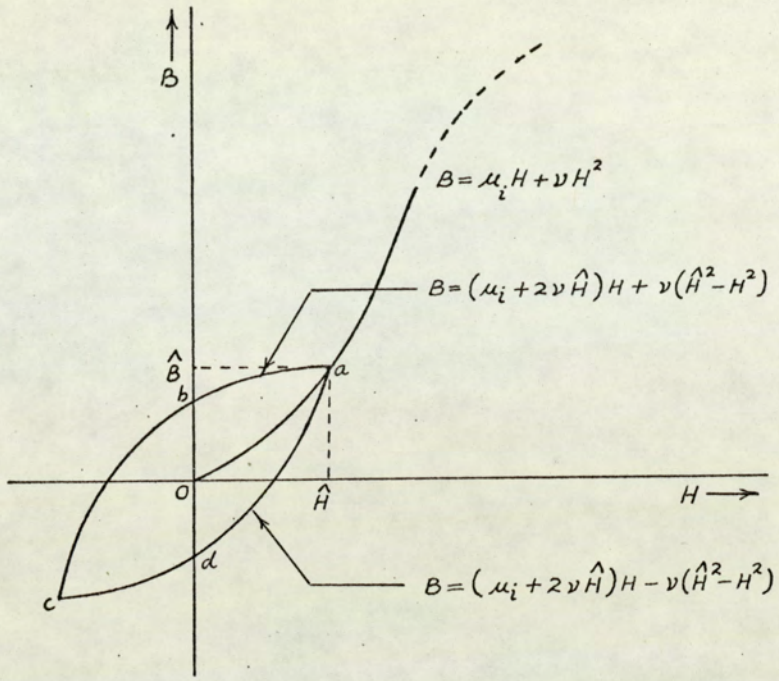

Fig. 5.3

Substituting for B from equation 5.2 and simplifying,

$$W_h = 4/3 \ \nu \ \hat{H}^3 \qquad 5.4$$

This shows that the curve of alternating hysteresis loss follows a 'cubic law' with regard to the applied magnetising force. For the constant ν evaluated above, W_h is expressed in Joule/m^3/cycle when $\hat{H}$ is in A/m. Thus

$$W_h = (4/3) \times 1.24 \times 10^{-9} \ \hat{H}^3$$

or

$$W_h = 1.66 \times 10^{-9} \ \hat{H}^3 \qquad 5.5$$

The following table compares the values of loss calculated from equation 5.5 with those obtained by measuring the areas of B - H loops (see Fig. 5.2) for different values of $\hat{H}$.

Table 5.1

$\hat{H}$ A/m x 10^5	0.1	0.15	0.2
W_h calculated using equation 5.5 $J/m^3/cycle \times 10^5$	0.0166	0.056	0.133
W_h noted from Fig. 5.2 $J/m^3/cycle \times 10^5$	0.015	0.05	0.3

The expression for the loss W_h can be converted easily into that for the developed torque (see Section 6.5.1, Chapter VI). Thus, if v is the volume of the rotor annulus and p the number of pairs of poles, the torque in Nm is given by

$$T = \frac{p\, v\, W_h}{2\pi} \quad Nm \qquad 5.6$$

In the experimental machine, $p = 1$ and $v = 2.67 \times 10^{-6}\ m^3$. Hence

$$T = \frac{1 \times 2.67 \times 10^{-6} \times 1.66 \times 10^{-9}}{2\pi} \times \hat{H}^3 \quad Nm$$

$$= 0.71 \times 10^{-15} \times \hat{H}^3 \quad Nm \qquad 5.7$$

Values of $\hat{H}$ in the Vicalloy are not directly available and calculations of torque cannot be made with equation 5.7. However, an approximate form of equation 5.7, relating the torque to the excitation current, can be worked out on the following

basis : For a given current, the maximum value of the average flux density, B_θ, in Vicalloy rotor is known, and the corresponding values of $\hat{H}$ can be obtained from the B - H curve (Fig. 5.2). Using this approach, the relation between $\hat{H}$ and I, the excitation current, is determined to be

$$\hat{H} = 2.24 \times I^{1.14}$$

and this, when substituted in equation 5.7, results in

$$T = 8.1 \times I^{3.42} \quad \text{Nm} \qquad 5.8$$

For excitation currents upto 0.15 A, the calculated values are compared with the measured torque values in Table 5.2 below. It is noticed that while the two values are within 4.0% at 0.15 A excitation, the calculated value is 22.5% lower than the measured value at 0.1 A. Although this discrepancy may be due to experimental errors to some extent, since accurate measurement of torque in the range 0 - 0.005 Nm is not possible

Table 5.2

Excitation current, I A	0.05	0.1	0.15
Torque calculated using equation 5.8, Nm	0.000275	0.0031	0.0124
Measured torque, Nm	-	0.004	0.012
% error based on the measured torque	-	-22.5%	3.67%

with the present assembly, there are other factors as well to account for it (see Section 5.5.2).

5.2.2 Torque in the normal excitation range (Region II)

Contrary to region I, the torque in this range increases rapidly in accordance with the steeply rising

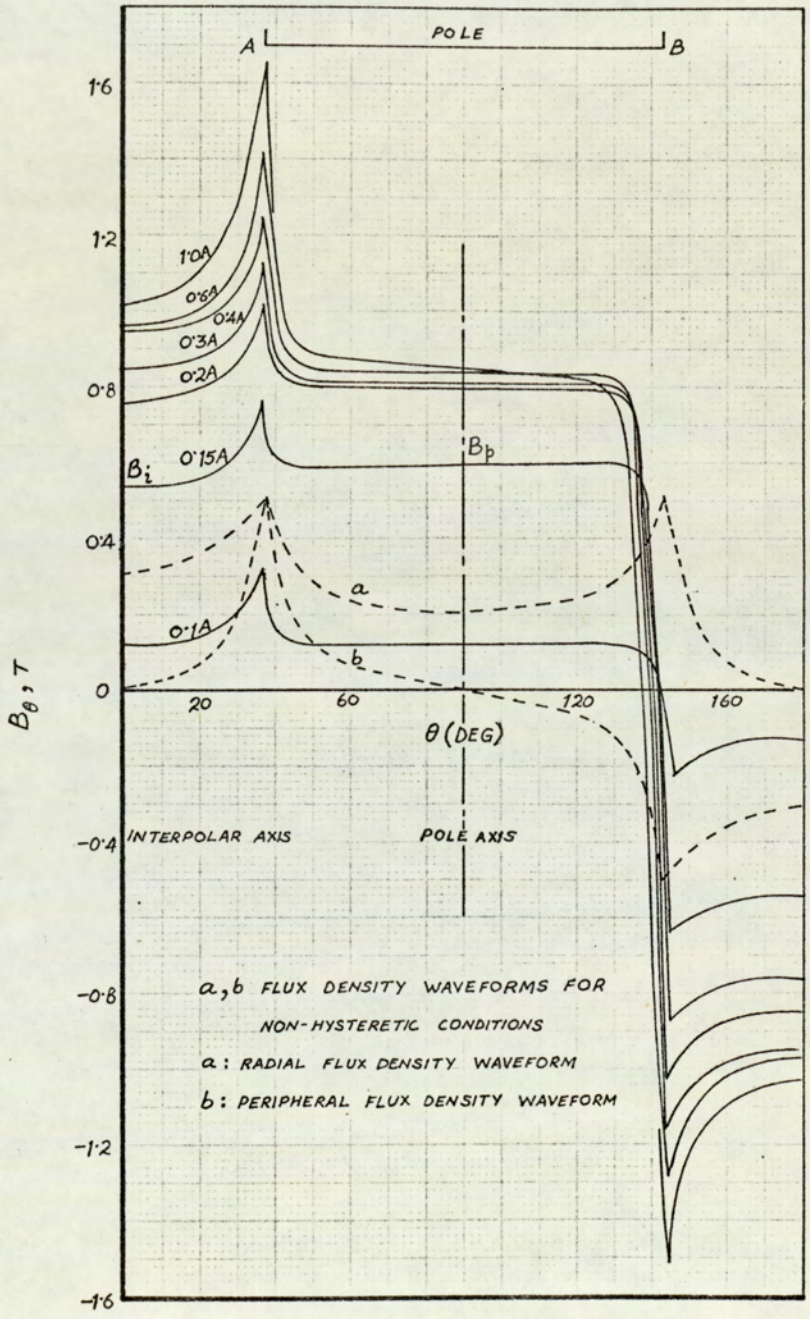

Fig. 5.4

alternating-hysteresis loss curve, and the peripheral flux density variation in the rotor annulus changes more noticeably with excitation current (see Fig. 5.4, page 104). A relationship between the torque and current, on the similar lines as above, cannot be derived since the hysteresis loops are indescribable by a single mathematical expression. A torque equation can nevertheless be obtained from the torque-excitation characteristic.

The average B_θ waveforms for various excitation currents are given in Fig. 5.4. Under the pole surface and in the interpolar region the variation of B_θ is seen to be uniform, increasing rapidly in magnitude for excitations from 0.1 A to 0.3 A. This 'growth' of B_θ apparently follows the same trend as the developed torque. Fig. 5.5 shows the plots of B_i and B_p, the values of B_θ on the interpolar and the pole axis respectively, against excitation while a plot of B_p against developed torque is given in Fig. 5.6 (next page). The latter shows that for the current range 0.15 A - 0.25 A (region II), the torque is proportional to B_p.

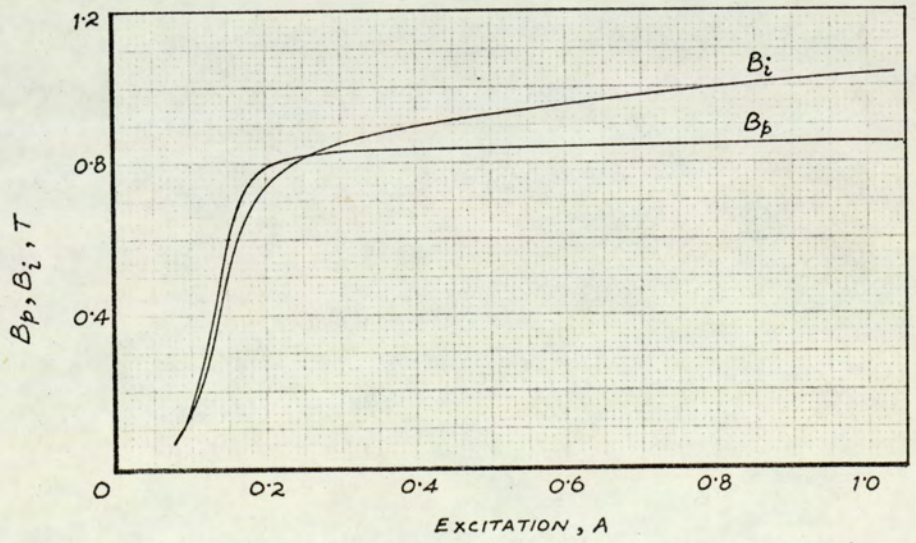

Fig. 5.5

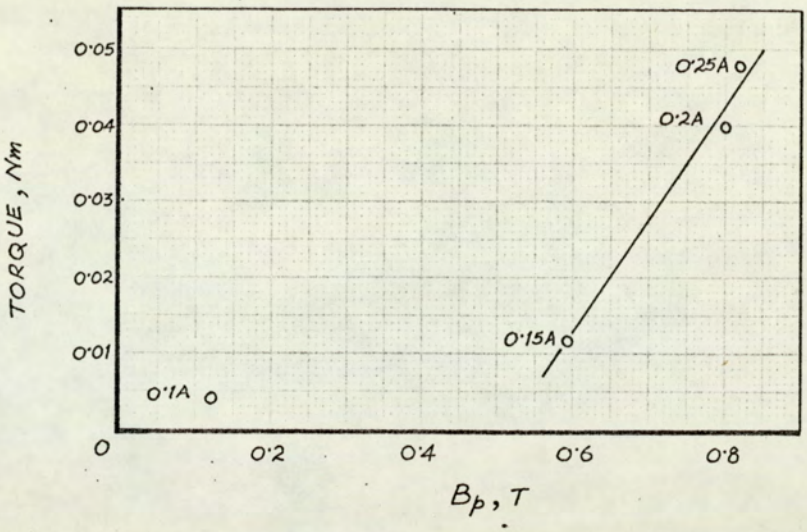

Fig. 5.6

Thus, assuming that the developed torque is dependent on the 'average' flux density under the pole surface, B_p, the form of the mathematical relationship between B_p and the excitation, I, will also govern the developed torque in region II. The torque expression so obtained is

$$T = 0.29 \times I^{0.62} - 0.077 \quad \text{Nm} \qquad 5.9$$

in the current range $0.15\ A < I < 0.25\ A$. The 'calculated' torque curve using equation 5.9, the calculated curve for region I, and the measured characteristic upto 0.3 A excitation are shown in Fig. 5.7 (next page). It is seen that at the common excitation of 0.15 A, the torque given by expressions 5.8 and 5.9 is the same and within 4% of the measured value. The former relationship, however, is simpler to apply, and related to the alternating loss more realistically.

The assumed dependence of torque on B_p reflects an important feature of machine operation. As discussed in Section 5.3.2, the flux density in that part of the annulus

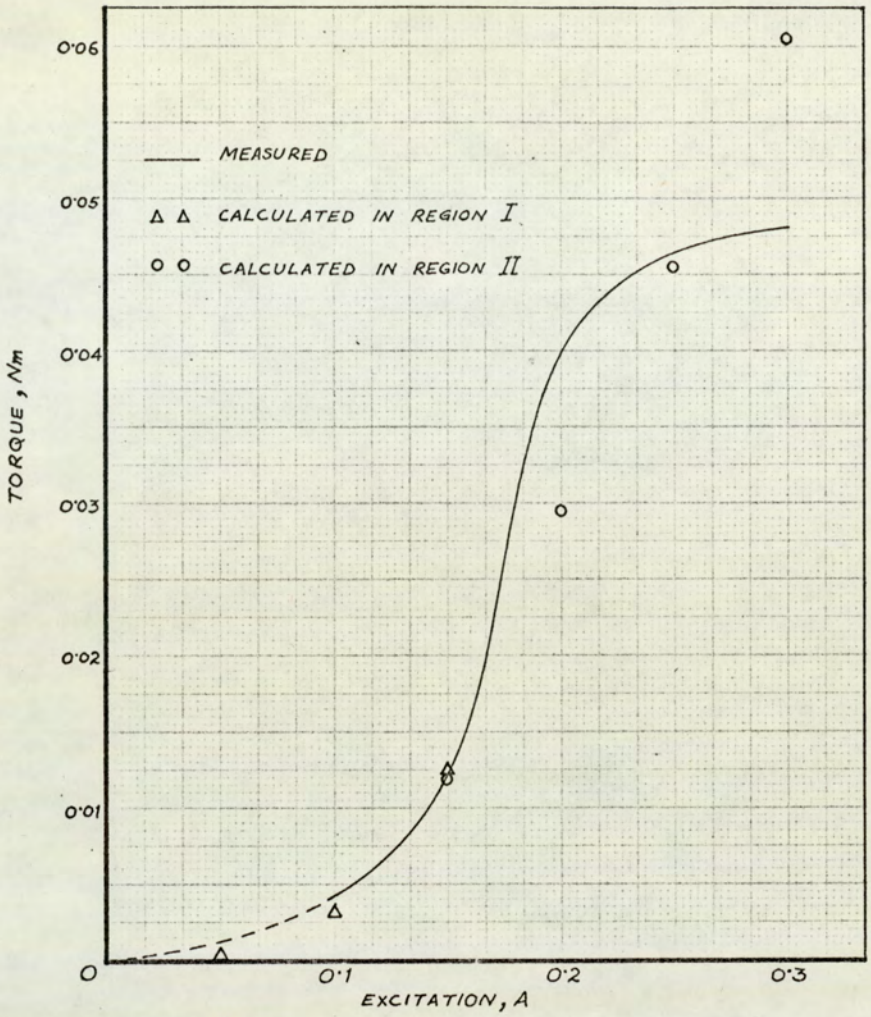

Fig. 5.7

opposite the poles is predominantly due to the 'rotor magnetisation', and the magnetic saturation shown by the distinct upper bend in the plot of B_p in Fig. 5.5 corresponds to the upper bend in the torque-excitation curve (see Fig. 5.7). The plot of B_i against excitation, on the other hand, shows a continuous increase, although at a reduced rate for excitations above 0.3 A.

5.2.2.1 A general empirical torque expression

The torque-excitation curve in regions I and II is a smooth curve, and a general torque expression in a purely empirical form can be derived for the complete range 0 to 0.25 A. Assume

that the torque-excitation curve follows the law,

$$T = k\, I^{n} \qquad 5.10$$

where k is a constant and n a positive number.

A plot of T and I on log - log paper is shown in Fig. 5.8 and the values of k and n are found to be

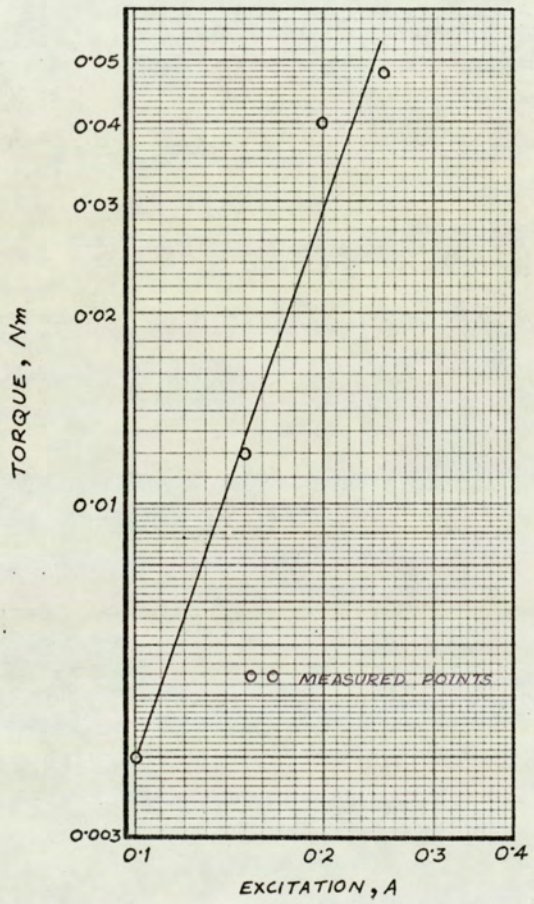

Fig. 5.8

$$k = 8.0$$

$$n = 3.3$$

Therefore, the general torque expression is

$$T = 8.0 \times I^{3.3} \quad \text{Nm}$$

This may be compared with equation 5.8 for region I showing a close resemblance.

5.2.3 Torque at higher excitations (Region III)

The developed torque in region III shows a steady decrease above an excitation of 0.3 A, the torque at 1.0 A being 16.7% less than at 0.3 A. This makes the torque at 0.3 A a maximum and results in a hump between 0.25 A and 0.4 A.

Undue prominence should not be given to the existence of a maximum torque. It is not a feature of every hysteresis motor design, although there is always a noticeable change of slope corresponding to the change of slope in the alternating-hysteresis loss curve. The reduction in torque at higher currents is a special characteristic of the experimental machine. Theoretically, the variation of developed torque at increasing magnetising force or excitation currents should be governed by the trend of the alternating hysteresis loss with m.m.f.[55]. This is depicted by the graph of Fig. 5.9 which shows that the loss goes on increasing beyond the initial bend a , though at a slower rate, until a point b after which it tends to level-off.

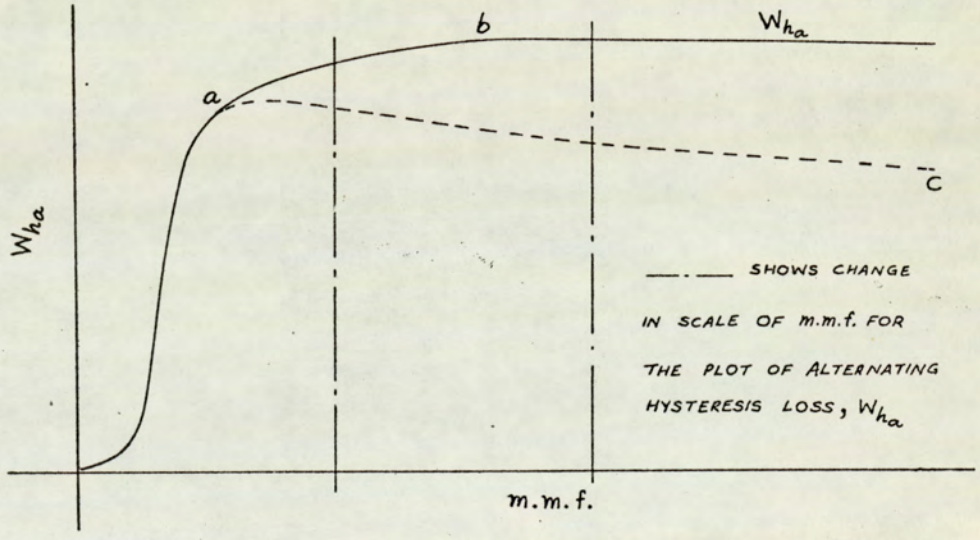

Fig. 5.9

That the developed torque follows an opposite trend (dotted line a c) is due to changes occurring in the flux distribution within the machine. This aspect of the operation will be considered fully in Section 5.5.

5.3 Rotor Magnetisation

It was demonstrated in the preceding section that the developed torque is related to excitation currents and to different stages of magnetic conditions of the rotor. To explain the basic physical principles involved in the production of torque, it is necessary to consider in detail the phenomenon of rotor magnetisation, during the machine operation, because the rotor annulus consists of a hard magnetic material. This treatment of rotor magnetisation is then linked to the experimental study of field distribution in preceding chapters.

5.3.1 Peripheral flux density waveforms in Vicalloy rotor

An important feature of the magnetism in the rotor is its effect on the point of reversal in the waveforms of average peripheral flux density in the Vicalloy. These waveforms have been shown in Fig. 5.4 for different excitations, and one of them (at 0.3 A) is reproduced in Fig. 5.10 (next page), together with that computed for the external rotor surface (in the airgap). Note that while the reversal in the B_{θ} waveform on the surface occurs near the leading pole tip A, that in the waveform for the annulus takes place opposite the lagging pole tip B. This means that the flux within the rotor annulus, predominantly peripheral on account of its thinness, divides at a point opposite the lagging pole tip. In the non-hysteretic condition the flux divides equally opposite the pole-centre, as shown by the dotted waveform of B_{θ} in Fig. 5.10, and also in Fig. 5.4. Reference to the latter shows that the point of reversal is shifted from the

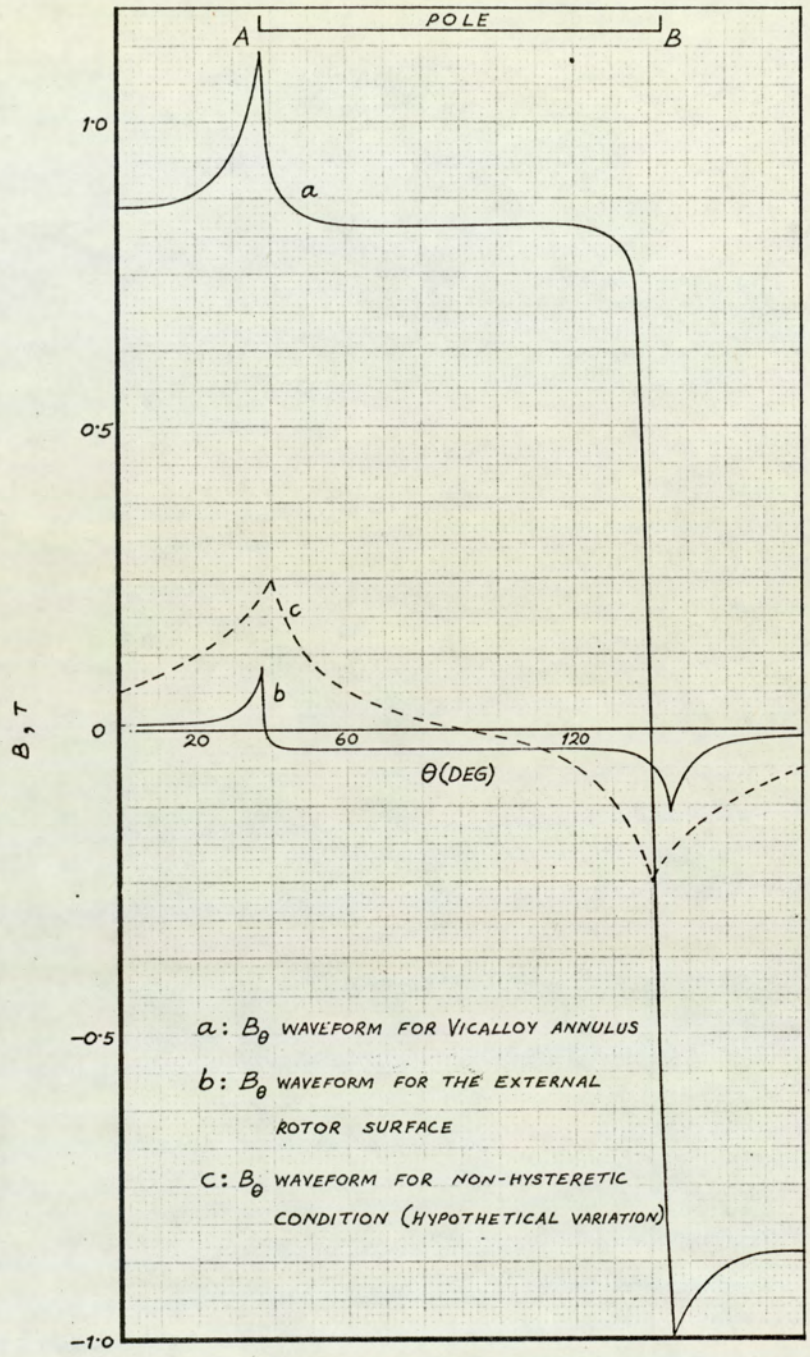

Fig. 5.10

pole-centre to the pole tip apparently for even the smallest excitation current. There is no evidence, from the waveforms, to show that the geometrical pole-centre has any effect on the flux distribution or that more than two reversals occur in the flux direction within the rotor per cycle. Therefore it is

reasonable to conclude that the flux leaving the lagging pole tip, which is larger than that from the leading pole tip (see Fig. 4.10 b and 4.11 b), dominates the flux pattern in the rotor, and hence the division of this flux naturally takes place opposite the lagging pole tip in the annulus.

The above experimental evidence together with the waveforms of Fig. 5.10 are presented qualitatively in Fig. 5.11. It is evident that the rotor behaves as if it comprised two permanently magnetised semi-annular cylinders butted together at the interfaces X, X′. The two cylinders exhibit the same polarities at the interfaces shown as NN and SS in the figure.

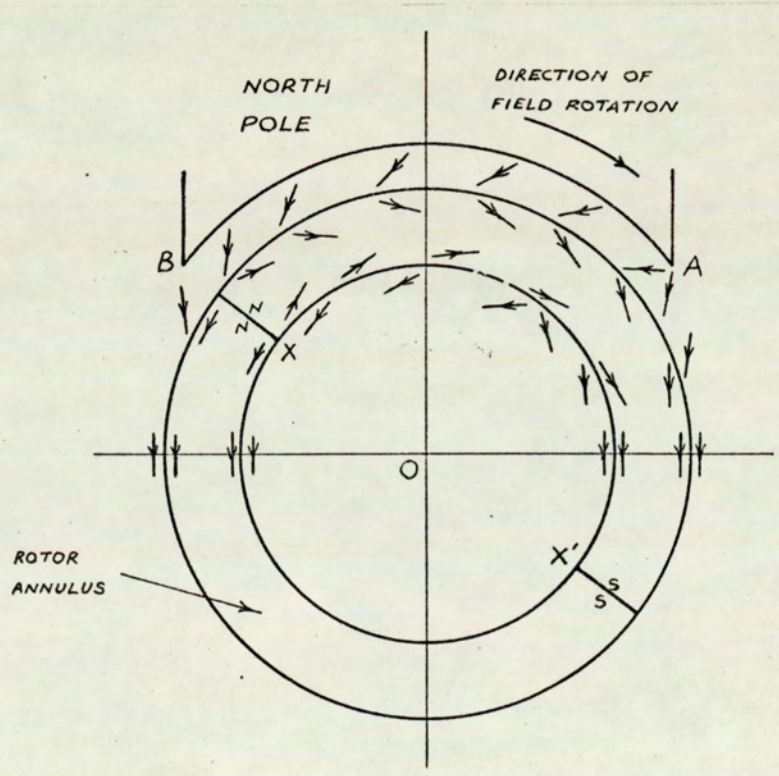

Fig. 5.11

Obviously, the existence of these 'poles' opposite the pole tips during machine operation is the 'effect of rotor hysteresis in

space' since, in the absence of such effect, the 'poles' will occur under the field pole-centres. This quality of the rotor is further elaborated in the following sections, in terms of characteristic aspects of permanent magnetism.

5.3.2 Equivalent vacuo model for the rotor

To apply the concepts of permanent magnetism, a magnetisation vector $\overline{M}$ is introduced to represent the rotor magnetisation and an analogy in terms of fictitious magnetic surface charges (on interfaces of Fig. 5.11) for an equivalent vacuo model is proposed. Consider Fig. 5.12 which shows the magnetic conditions for the rotor in space at any instant. The surface charges are distributed as shown in the two cases*

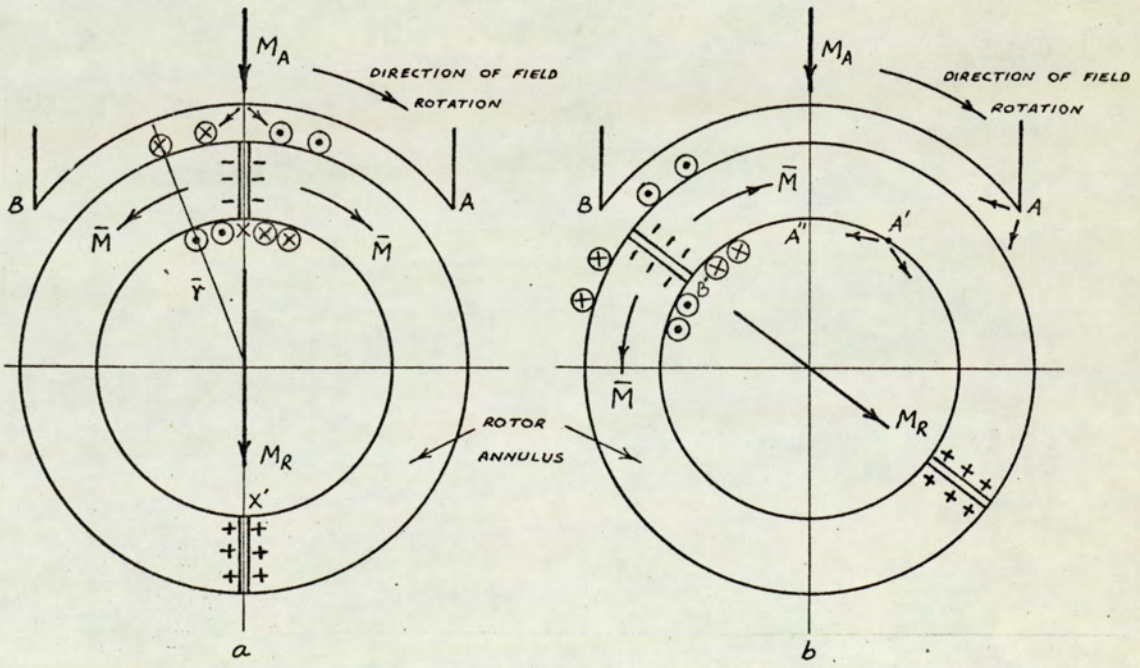

Fig. 5.12

---

*Ideal conditions are assumed in this discussion, i.e., uniform magnetisation of the annulus which gives $\overline{\nabla} \cdot \overline{M} = 0$.

(for the moment, ignore the current elements shown as ⊗ ⊙), and the direction of 'rotor magnetisation' vector is indicated by the arrows within the rotor annulus.

Fig. 5.12 a illustrates the non-hysteretic condition when the flux from the pole (assumed a north pole in the diagram) divides at the centre both in the airgap as well as the annulus. Treating the rotor as a single magnetised body, this is equivalent to a 'resultant rotor m.m.f.', M_R , in space phase with the applied m.m.f., M_A , since $\overline{M}$ is equal but oppositely directed at X . This condition also exists when the field system is held stationary, as with some of the earlier tests on the machine, and the rotor magnetised by the m.m.f. M_A.

Fig. 5.12 b shows the situation when the rotor m.m.f. lags the applied m.m.f., and the division of flux within the rotor annulus occurs opposite the lagging pole tip. This is identified as 'the hysteresis effect'. The distribution of $\overline{M}$, as seen from the field system, is modified accordingly. Within region A B of the airgap, and A′ B′ on the inside of the rotor, the tangential component of $\overline{H}$ is <u>oppositely directed</u> to $\overline{B}$ within Vicalloy annulus.

This magnetic condition is analogous to the conditions prevailing in a bar magnet where the lines of $\overline{B}$ coincide with $\overline{H}$ outside the magnet but are oppositely directed inside (see Fig. 5.13 a , page 115). The diagram of Fig. 5.13 b represents a section of the rotor annulus in the common region A′ B′ and shows the field components for the airgap, the Vicalloy rotor and the arbor region. It is observed that in spite of the peripheral flux density, $\overline{B}_v$, in Vicalloy being directed opposite

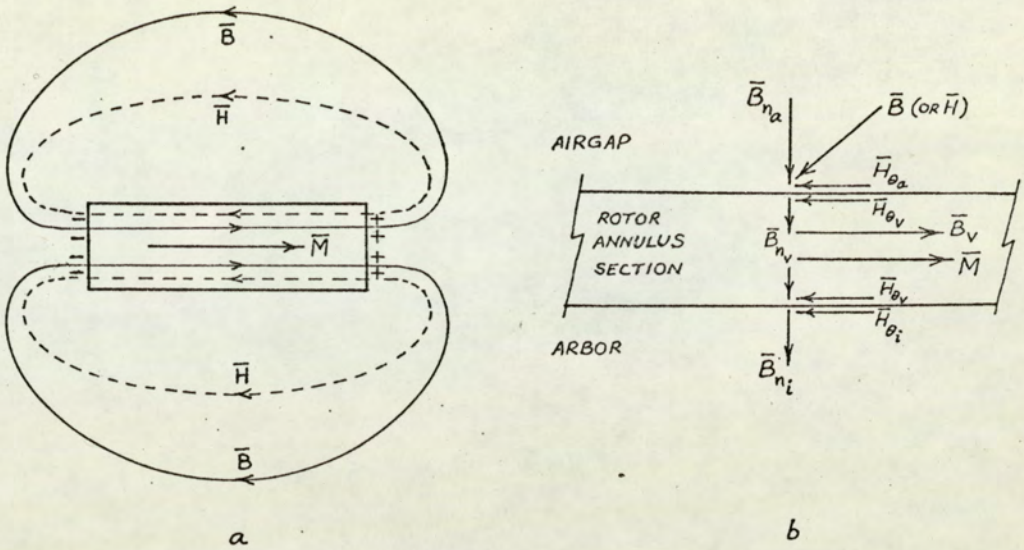

Fig. 5.13

to $\overline{H}$ on either side, the boundary conditions are satisfied, i.e., the normal components of $\overline{B}$ and tangential components of $\overline{H}$ are continuous. It follows therefore, that under the influence of strong rotor magnetisation, the peripheral flux density in the annulus is largely due to $\overline{M}$, being governed by the relation

$$\overline{B} = \mu_o (\overline{M} + \overline{H}) \quad , \quad \overline{M} >> \overline{H} \text{ in the present case.}$$

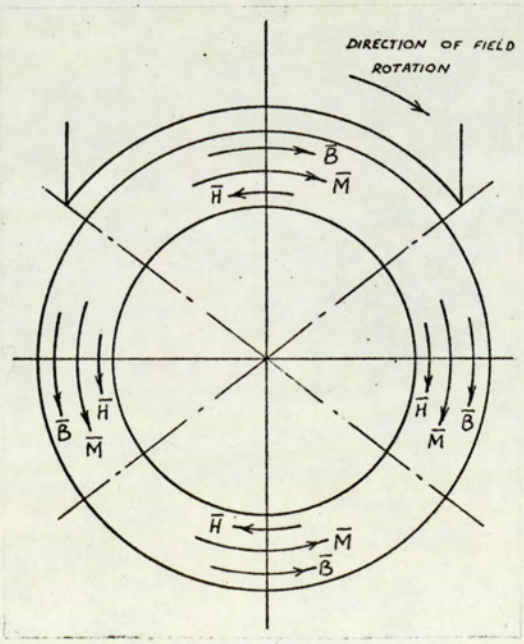

Fig. 5.13c

In the interpolar region however, the original field due to the field system is intensely peripheral. This means that $\overline{H}$ in the air-region as well as $\overline{M}$ and the tangential component of $\overline{H}$ in the Vicalloy annulus have the same direction. Fig. 5.13 c summarises the directions of the field vectors for the different regions of

the rotor.

The foregoing considerations point to an important aspect of the flux density distribution around the whole periphery of the rotor annulus. Since the flux density in the section under the poles is predominantly due to $\bar{M}$, it is representative of the intensity of magnetisation, M_o, for Vicalloy; while that in the interpolar region is the 'true' flux density value according to the relation

$$\bar{B} = \mu \bar{H}$$

where $\mu = \mu_o \mu_r$. This interpretation is in close agreement with the measured waveforms of average flux density in the annulus at increasing excitation as revealed by the graphs of Fig. 5.5. The graph of B_p, equivalent to M_o according to the present interpretation, indicates intense saturation at higher excitation currents which is not observed in the plot of B_i.

In the discussion below, further corroboration of the magnetic phenomenon in the rotor is provided by the traversal of the magnetisation cycle in space.

5.3.2.1 Rotor field distribution and cycle of magnetisation

The $\bar{B}/\bar{H}$ relationship for any magnetic material is characterized by four trends.

Let the cyclic variation be represented by Fig. 5.14 (next page). The four 'changeover' points marked in the figure have a particular meaning*:

---

*The shape of the loop may be disregarded at this stage.

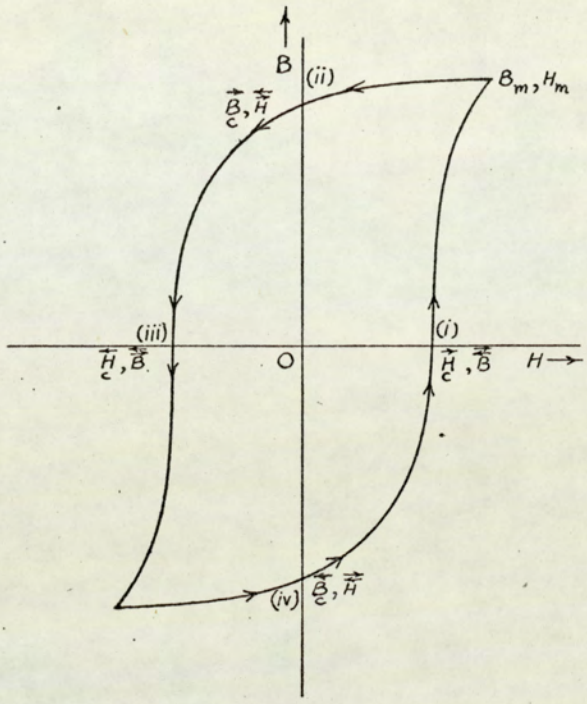

Fig. 5.14

(i) $\vec{H}_c, \vec{B}$ - Near constant H in a '+ve' direction, reversal of B from '-ve' to '+ve' direction

(ii) $\vec{B}_c, \vec{H}$ - Near constant B in a '+ve' direction, reversal of H from '+ve' to '-ve' direction

(iii) $\vec{H}_c, \vec{B}$ - Near constant H in a '-ve' direction, reversal of B from '+ve' to '-ve' direction

(iv) $\vec{B}_c, \vec{H}$ - Near constant B in a '-ve' direction, reversal of H from '-ve' to '+ve' direction.

As is well known, the four key points (together with the B - H curve) define completely the B - H loop and must occur in the same cyclic order.

The excursion of the hysteresis loop can be observed in a similar manner with the rotor annulus for all points around the

periphery at any instant, or for a single point in space with varying time. The magnetic conditions in the rotor are shown in Fig. 5.15 a and $\overline{B}$,$\overline{H}$ are assumed to have constant magnitudes. The magnetisation loop is shown in Fig. 5.15 b (solid line) and is rectangular because of the constant values of B and H. The 'operating points' are the 4 corner points, and the loop is traversed as a series of 'jumps' between these. Even in a physical model B and H cannot be constant and the rectangular hysteresis loop is replaced by the usual form (shown dotted). This loop is traversed in a non-uniform manner, although not in steps, and points on the loop correspond to points on the rotor.

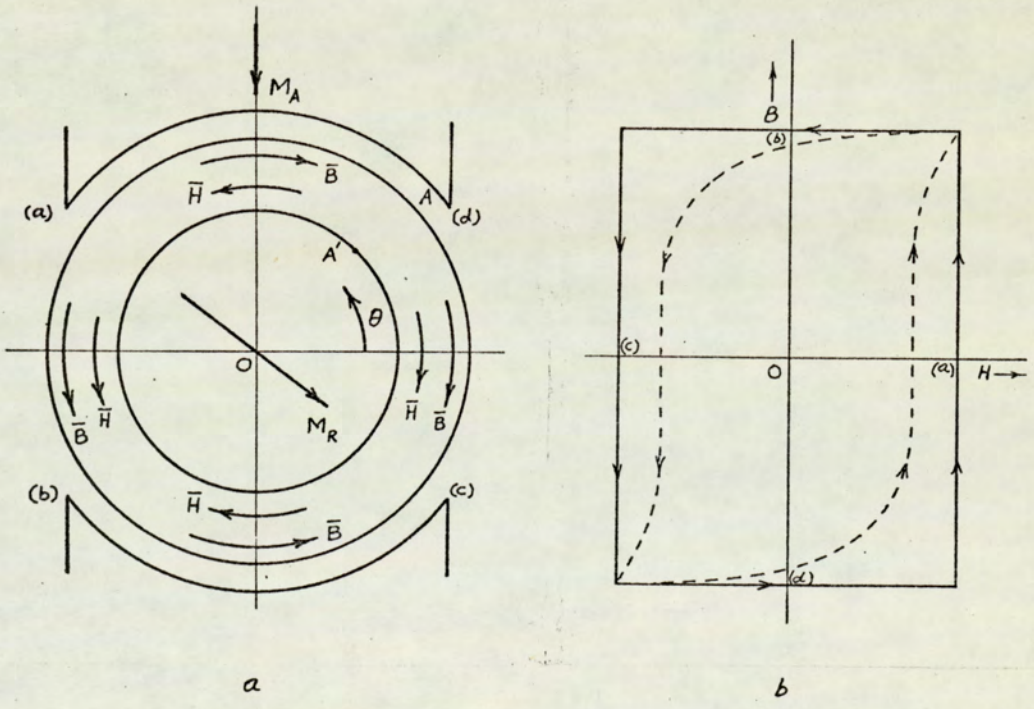

Fig. 5.15

In the actual operation of the machine, though the sequence represented by Fig. 5.15 still applies, the hysteresis loop will be modified and must include recoil loops because of the shape of the flux density waveforms. No experimental

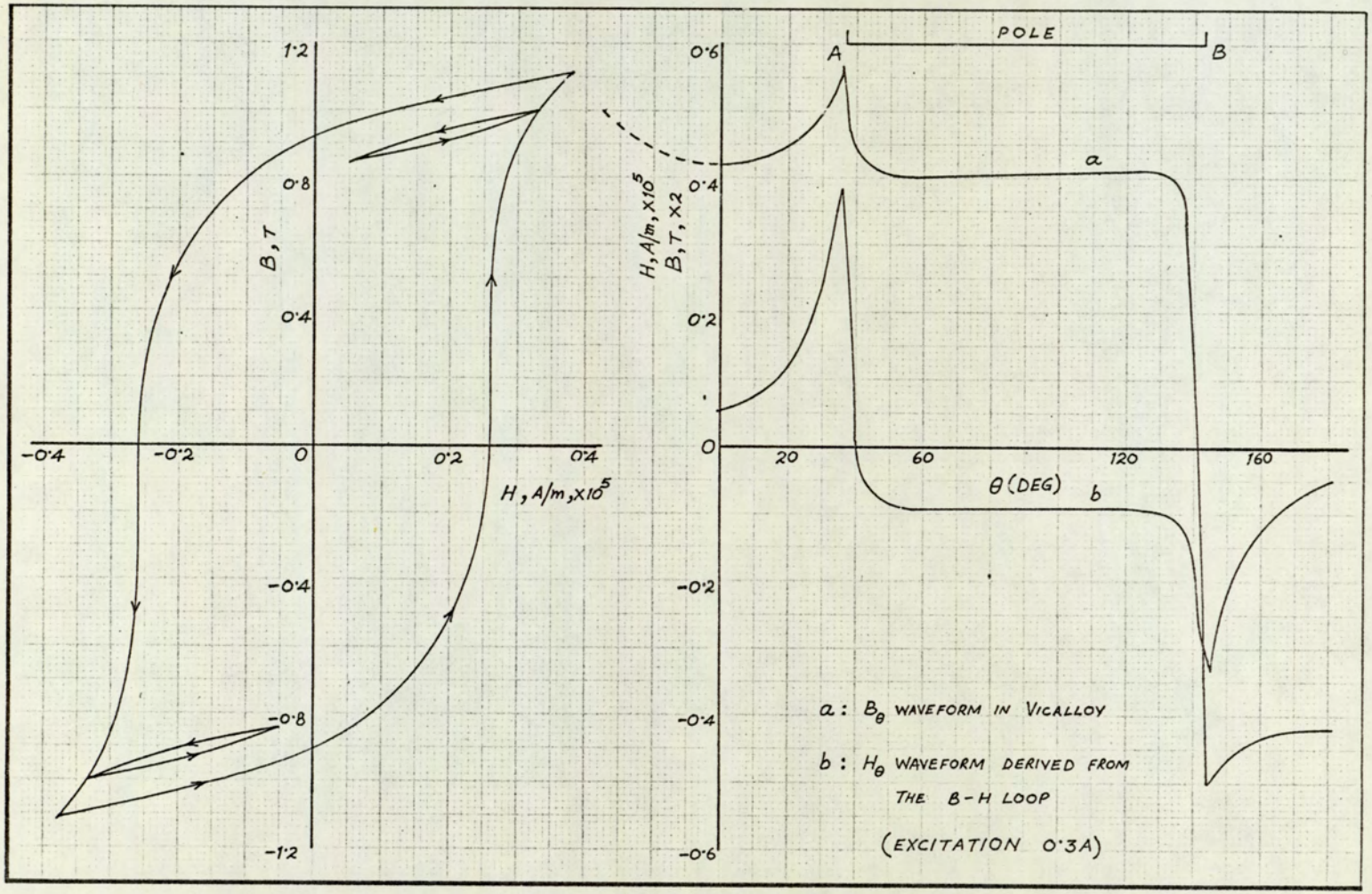
1·2
0·8
0·4
B, T
-0·4
-0·8
-1·2
-0·4
-0·2
0
0·2
0·4
H, A/m, x10^5
POLE
A
B
0·6
0·4
0·2
0
-0·2
-0·4
-0·6
H, A/m, x10^5
B, T, x2
a
20
60
120
160
θ (DEG)
b
a : Bθ WAVEFORM IN VICALLOY
b : Hθ WAVEFORM DERIVED FROM THE B-H LOOP
(EXCITATION 0·3A)

verification of this point is possible since the magnetic excitation waveform for the Vicalloy cannot be obtained. Nevertheless it is a reasonable assumption and can be used to deduce the average magnetising force variation, if approximate recoil loops are sketched in. Assuming that the B_θ variation in Vicalloy represents the resultant flux density at any point (negligible radial component), then the H_θ variation is shown in Fig. 5.16, page 119, for 0.3 A excitation. Note that the H_θ waveform contains appreciable peaks. The values of H_θ so obtained are plotted in Fig. 5.17, together with corresponding B_θ in Vicalloy and H_θ on the external rotor surface (available from the B_θ waveforms, Fig. 4.5). A close agreement is noticed

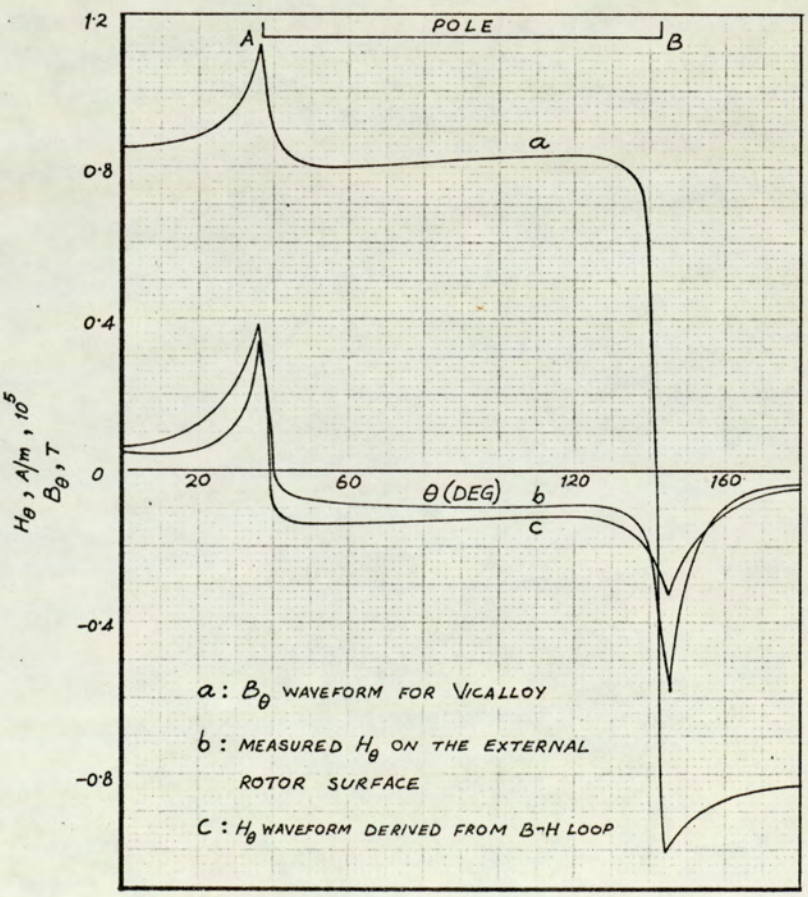

Fig. 5.17

between the two H_θ waveforms and this in association with the B_θ waveform tends to confirm the general relationships between $\bar{B}$ and $\bar{H}$ illustrated in Fig. 5.16.

The recoil loops, occurring in the magnetisation cycle of the rotor during operation, may contribute to the developed torque. As shown in Fig. 5.16, their area is small compared to the main loop and hence their torque contribution is probably negligible. Further work on the effect of recoil loops could not be undertaken with the present equipment.

5.3.3 Minimum - energy - conditions in the rotor

When discussing the hysteretic condition of the rotor in Section 5.3.2, the 'effective' rotor m.m.f., M_R, was taken to be in the direction BB on the basis of the flux dividing in the annulus opposite B, and under the assumption of uniform rotor magnetisation (Fig. 5.12). It may be argued that this effective m.m.f. could instead lie in the direction AA, as shown in Fig. 5.18 (next page), since the flux in the airgap divides at A, not B, during the machine operation (cf. Fig. 5.12 a). However, reference to the polar plots for the airgap (Figs. 4.10 b and 4.11 b, pages 90,91) shows that the resultant flux density at B, BR2, is far greater than that at A, BR1. Since the whole rotor is being treated as a single magnetised body, its effective m.m.f. is directed so that the total energy of the system (i.e. the rotor and the field system) is always a minimum. Compliance with this condition is dictated physically by BR2 being greater than BR1, and hence M_R is in the direction BB. Accordingly, if the field system were stationary and the

rotor free to rotate, the minimum-energy requirement would cause the rotor to revert to the conditions of Fig. 5.12 a, when M_R would be directed along CC (Fig. 5.18). This is the condition analogous to the synchronous operation of a conventional hysteresis motor and is represented on the torque-slip curve of Fig. 3.2 (page 57) by the line PQ.

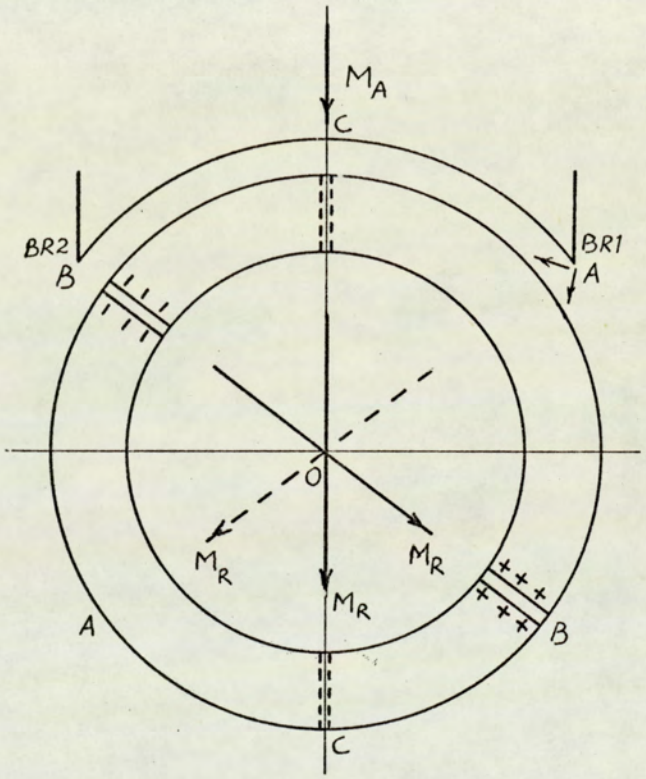

Fig. 5.18

The only limitation of the discussion in practice can be that the rotor magnetisation is not uniform along the entire periphery of the rotor (i.e. $\overline{\nabla}\cdot\overline{M} \neq 0$), especially at excitations outside the range 0.15 A to 0.4 A , as indicated by appreciable peaks occurring in the B_θ waveforms for Vicalloy near the pole tips. Nevertheless, the general conditions illustrated in Fig. 5.12 will hold since the behaviour of various waveforms

in general is observed to be consistent in the whole range of excitation currents.

5.3.4 Magnetic flux density patterns on the internal rotor surface

In the light of the discussion of rotor magnetisation, it is possible to extend further the explanation given to the pattern of flux distribution on the internal rotor surface in Section 4.4.2. As seen from the B_θ waveforms of Fig. 4.7, and the resultant flux density plots of Figs. 4.10 b and 4.11 b, the flux on the inner surface divides at a point such as A', Fig. 5.12 b, under a combined effect of the flux leaving the inner rotor surface and that crossing the annulus from the pole tip A (see also the diagram of Fig. 5.11). A definite trend to the flow of magnetic flux, on the basis of available waveforms in the airgap and arbor region, is not possible on account of the role played by rotor magnetisation. From A' to B', Fig. 5.12 b, H_θ and B_θ in Vicalloy are oppositely directed, the boundary conditions being satisfied as indicated in Fig. 5.13. The tendency for the flux to bifurcate at A' also accounts for an increase in radial flux density near the leading pole tip rather than the lagging pole tip (see Fig. 4.3, page 83). If no hysteresis effect were present, the point of flux division must occur at A'' (Fig. 5.12 b). However, as the flux in the airgap divides at pole tip A under hysteretic conditions, the corresponding point on the inner surface is shifted from the pole-centre to A', a point intermediate between the two extreme positions. This represents weak hysteresis effect prevailing on the inner rotor surface.

5.4 Production of Torque

The concept of rotor magnetisation in the form established in the preceding section is an integral feature of the phenomenon of torque production in the machine. Before connecting the two ideas, it is useful to consider the principles of torque production.

5.4.1 Basic requirements

The simplest physical explanation for the production of driving torque in an electric machine is normally couched in terms of magnetic lines of force in strain in the airgap. In many cases this situation is arrived at by the action of the field due to current carrying conductors on the rotatable member, on the field originally existing in the airgap.

A similar explanation applies to the experimental machine from the study of flux distribution reported in Chapter IV. The angles at which the flux enters at different points on the rotor surface (computed from the airgap flux density distribution, Figs. 4.10 b and 4.11 b, pages 90,91) are represented diagrammatically in Fig. 5.19 (next page). This shows how the lines of force (direction indicated by small, solid arrows) are strained due to 'rotor hysteresis' and the applied magnetic field. Had there been no spatial hysteresis effect due to the rotor, as for example at very low excitation currents or with the air-rotor, the magnetic field in the airgap would be directed as shown by the dotted arrows. Effectively, this means that rotor hysteresis, taken alone, provides the secondary magnetic flux which 'reacts'

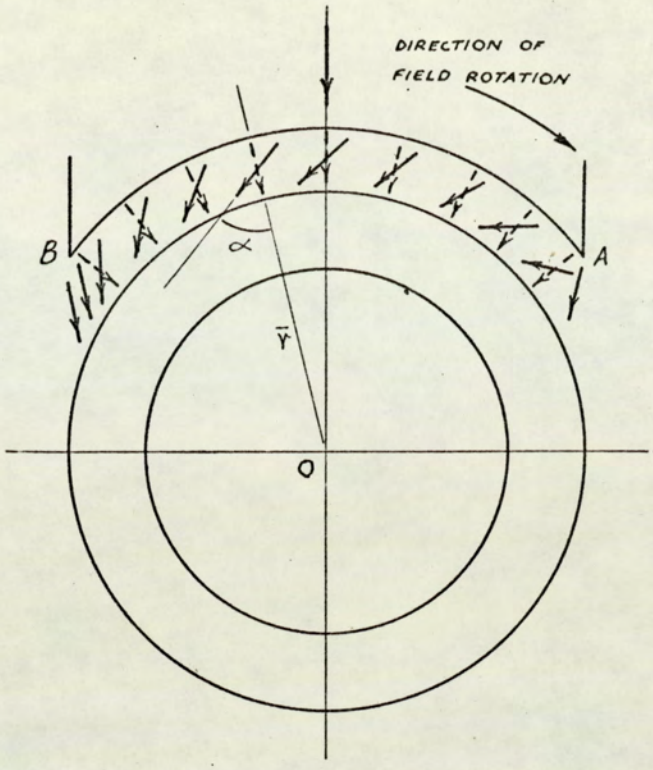

Fig. 5.19

with the primary magnetic field (dotted arrows) and gives rise to torque, according to the 'BℓI' concept.

The inclined field in the airgap therefore emerges with a particular meaning. According to the Maxwell's stress considerations, the angle at which the resultant flux enters the rotor surface is a significant factor in deciding the magnitude of the developed torque. For maximum tangential force acting on the rotor surface, this angle should be 45° at any point with respect to the radius vector, i.e., $\alpha = 45^{\circ}$, Fig. 5.19. On the external rotor surface and under the pole-centre, this value of α is met very nearly; the angle lies in the range $45^{\circ} - 40^{\circ}$ for excitations in the range 0.3 A - 1.0 A and the Maxwell stress concept is shown in Fig. 5.20 a, page 126. Other values of α

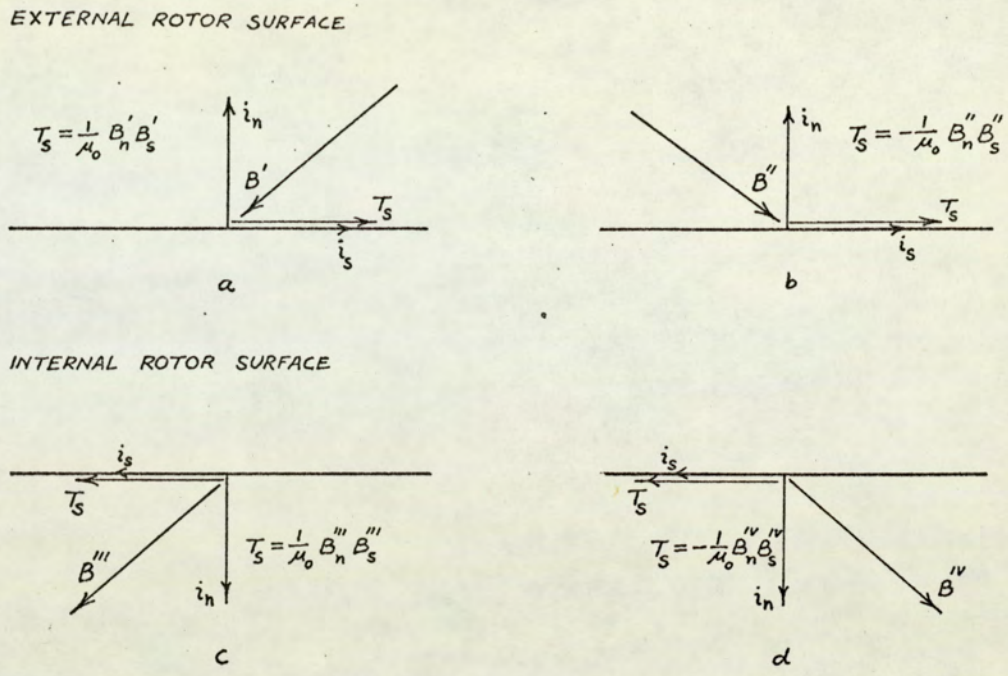

Fig. 5.20

are to be found, particularly in the interpolar region where the angle and the corresponding stress are negative and the conditions are as shown in Fig. 5.20 b. Therefore the nett force is a combination of both positive and negative peripheral surface stresses. On the internal surface similar angles are to be found although these tend to have a higher value, typically 60° to 70° in the range 0.1 A to 1.0 A. This means that the magnitude of the force, applying Maxwell's stress criterion, is smaller. Again both positive and negative values of α and of surface stress are present and the conditions are illustrated in Fig. 5.20 c and d.

The nett force on the external surface is in the direction of the rotating field, while that on the internal surface is oppositely directed and smaller in magnitude. Hence the nett torque on the annulus is also in the direction of the rotating field.

Clearly, the existence of an inclined magnetic field, as a necessary condition for the production of torque, requires that a peripheral component of $\bar{B}$, B_θ (or H_θ), must exist in the airgap under the pole surface, and this should be unidirectional if the maximum possible torque is to be realised at a given excitation. The lagging rotor m.m.f., resulting from the hysteresis effect, fulfils this requirement.

5.4.2 Rotor magnetisation and production of torque

5.4.2.1 Inclined magnetic field in the airgap

The physical picture of radial lines of force in the airgap (shown dotted in Fig. 5.19) becoming inclined under the action of a lagging rotor m.m.f. emerges from the consideration of 'independent' rotor magnetisation. This property of the rotor annulus was first referred to in Section 5.3.1, where each interface of the semi-annular cylinder was treated as a fictitious 'pole' (see Fig. 5.11). In the simplest sense, these poles can be imagined to 'pull' the lines of force in the airgap from their normal direction, and to result in a flux concentration towards the lagging pole tip B. This resultant effect is in line with the minimum-energy-requirement condition discussed in Section 5.3.3.

An alternative and more convincing explanation for the inclined field can be developed by replacing the rotor magnetisation by surface currents. The behaviour then has many parallels with armature reaction in a d.c. generator.

5.4.2.2 Alternative vacuo model for rotor magnetisation

To explain the production of torque in terms of rotor magnetisation $\bar{M}$, the concept of equivalent fictitious 'magnetic' surface currents can be introduced; in the sense that the fictitious currents give rise to $\bar{B}$ which when combined with $\bar{M}$ gives $\bar{H}$. Under this assumption the rotor annulus can be replaced by current elements distributed on the surface according to the relation

$$\bar{J}_s = \bar{M} \times \bar{i}_n \qquad 5.11$$

where $\bar{J}_s$ is the surface 'magnetic' current density and $\bar{i}_n$ is a unit vector directed normal to the surface*. These current elements are shown as ⊗ ⊙ in Fig. 5.12.

The current elements on the same radius vector such as $\alpha'\alpha''$ in Fig. 5.21 (next page) can be regarded as closed loops/ dipoles, each having a dipole moment $\bar{\mathcal{M}}$. The complete rotor annulus thus consists of a very large number of identical dipoles situated along the rotor periphery. Under the action of an applied $\bar{B}$ field, each dipole experiences a torque governed by the expression

$$\bar{T} = \bar{\mathcal{M}} \times \bar{B} \qquad 5.12$$

which will be maximum when $\bar{\mathcal{M}}$ and $\bar{B}$ are orthogonal.

---

*Again uniform magnetisation is assumed such that the volume current density $\bar{J}_v = \bar{\nabla} \times \bar{M}$ is zero.

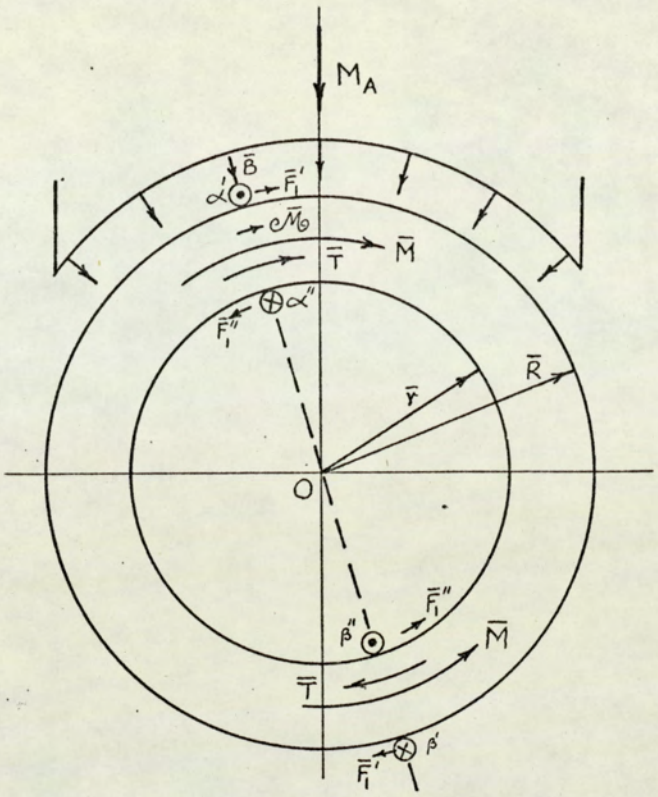

Fig. 5.21

As shown in Fig. 5.21, the torque $\bar{T}$ is directed to rotate the dipole in a clockwise direction so as to make its plane at right angles to $\bar{B}$. Taking into account the location of the current elements constituting the dipole the above tendency is equivalent to a couple acting on the dipole with the forces $\bar{F}_1'$ and $\bar{F}_1''$ in the directions shown. In terms of the annulus radii $\bar{r}$ and $\bar{R}$, $\bar{F}_1'$ and $\bar{F}_1''$ result in torques on the rotor of the values given by

$$\bar{T}_1 = \bar{F}_1' \times \bar{R} \qquad \text{and} \qquad \bar{T}_2 = \bar{F}_1'' \times \bar{r}$$

with $\bar{T}_1$ opposing $\bar{T}_2$. However, since $\bar{R} > \bar{r}$, the resultant torque on the rotor is seen to be in clockwise direction under the assumed field distribution of Fig. 5.21, and this is added to

the torque arising from the current elements $\beta'\beta''$ at the opposite side of the rotor.

* * * *

It follows that for equal surface currents (or uniform magnetisation of the rotor), the torque developed as a result of dipole moments is a function of rotor radii. In a qualitative theory, with torque proportional to total hysteresis loss in the rotor active material, the above conclusion points to the obvious requirement of thick rotor to give rise to more developed torque. This can be shown mathematically as follows:

Let N = number of dipoles/unit angle

Therefore in an angle $d\theta$, number of dipoles = $N\, d\theta$

For constant current in the elements, the magnitude of a dipole moment is

$$\mathcal{M} \propto l(R-r) \qquad \text{on any radius vector.}$$

The torque at the shaft due to dipoles in angle $d\theta$ is

$$T' \propto l(R-r)\,d\theta$$

and the total torque

$$T \propto \int_0^{2\pi} l(R-r)\,d\theta$$

or proportional to the volume of the rotor annulus.

In practice this is not realised because the rotor magnetisation is not uniform, and the change-over between the two directions of rotor magnetisation no longer takes place along a radial plane.

* * * *

Referring back to Fig. 5.12 a, it can be noticed that for the non-hysteretic condition when the magnetisation and hence the dipole moments are oppositely directed in the two halves of the rotor, symmetrically positioned with respect to the applied field, the torque developed according to equation 5.12 will be equal but in opposite direction and the nett torque will be zero. However, when the rotor magnetisation takes the form shown in Fig. 5.12 b, a nett torque is produced which causes the rotor to rotate in the clockwise direction.

Because of the cross product in equation 5.12, the torque is developed chiefly in the rotor material under the poles. This suggests the use of a pole-arc almost equal to the pole-pitch, to obtain maximum utilization of the rotor material. Subsequent research along these lines has shown that there is a considerable increase in torque in regions I and II of the torque-excitation curve (Fig. 5.1, page 98) but there is little or no change in region III. This would be expected because the peripheral flux density variation for saturated conditions in the Vicalloy rotor is not affected by a change in pole arc.

5.4.3 Resumé

The discussion of Sections 5.3 and 5.4 explains qualitatively the mechanism of torque production in the experimental machine. To put the phenomena in proper perspective, the salient features of the discussion can be summarised as follows.

The production of torque basically derives from the spatial hysteretic property of the rotor. After a minimum of one

complete revolution of the field system, in the ideal circumstances, the rotor annulus is in a cyclically magnetised state and can be treated as an independent secondary member of the machine. At any instant, the rotor magnetisation in space has an effective, 'resultant' m.m.f. which lags behind the applied m.m.f. In this condition, the usual hysteresis loop is a natural, equivalent representation for the B - H relationships within the rotor, and the size of this loop is dictated by the originally applied m.m.f. due to the field system, responsible for the 'magnetisation of the rotor'.

The lagging rotor m.m.f. is then visulized as an equivalent vacuo model which replaces the rotor annulus by an array of fictitious magnetic surface current elements forming magnetic dipoles, distributed around the rotor. These dipoles, under the action of the applied field, experience a torque which is 'transferred' to the rotor appearing as developed torque at the shaft.

The interpretation automatically underlines the two normally accepted requirements for torque production : hysteretic material on the rotor and a rotating magnetic field on the stator. The theory developed in the preceding sections establishes the rotor magnetisation as the connecting link.

5.5 Developed Torque in the Higher Excitation Range

It was pointed out in Section 5.2.3 that for this machine the developed torque at higher excitation currents (Region III) is less than the maximum value. The graph of Fig. 5.1 shows that the reduction is almost linearly proportional

to the excitation current. The aim of this section is to discuss the reasons for this reduction, by relating it to the modification in the flux distribution in the machine.

5.5.1 Effect of flux distribution

The physical principles of machine operation established in the previous two sections demonstrate that a concentration of flux at the lagging pole tip in the airgap is a key factor associated with developed torque. The extent to which this phenomenon explains the value of the measured torque depends on two criteria :

(i) the proportion of flux reaching the rotor from the lagging side of the pole compared to the leading side, and

(ii) the point of flux division in the uniformly magnetised annulus, which determines the angle between the resultant, effective rotor m.m.f. and the applied m.m.f.

5.5.1.1 Relative flux distribution in the pole sides

The B_r waveforms in the airgap, which are a measure of the total 'useful' flux supplied by each pole, give a good indication of the 'concentration' of flux on the two sides of the pole. Since the salient pole construction automatically results in the point of maximum flux concentration being the pole tip, the effect of hysteresis and its intensity is exhibited by larger peaks occurring in the waveforms at the lagging pole tip B and smaller peaks at the leading pole tip A. This happens regardless of the value of excitation current as discussed in Chapter IV.

Qualitatively, therefore, the greater the difference in the heights of two peaks, the more pronounced is the hysteresis effect. In other words, it is only the 'difference' portion in the B_r waveform under the pole which is responsible for producing torque (see Fig. 5.22). The remaining portion, which is symmetrical about the pole-axis, contributes nothing to the developed torque. The difference Δh in the peak heights would thus appear to be directly related to the torque.

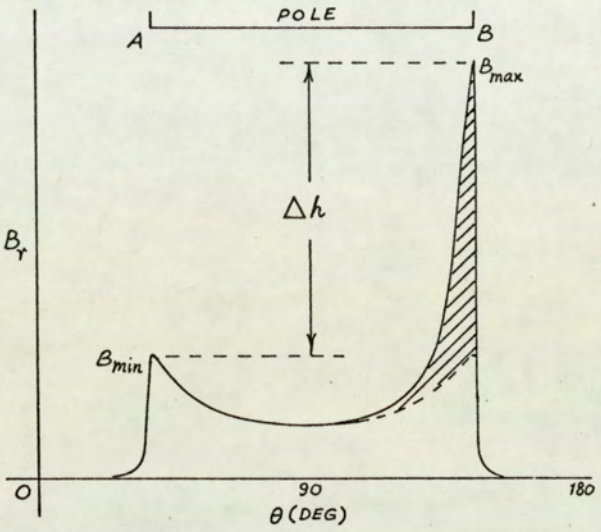

Fig. 5.22

A plot of Δh, together with the developed torque, corresponding to various excitations is given in Fig. 5.23 and the similarity of the two curves is remarkable. It is noticed that Δh is maximum at 0.35 A which is nearly equal to the excitation current for maximum developed torque (0.3 A). While beyond this

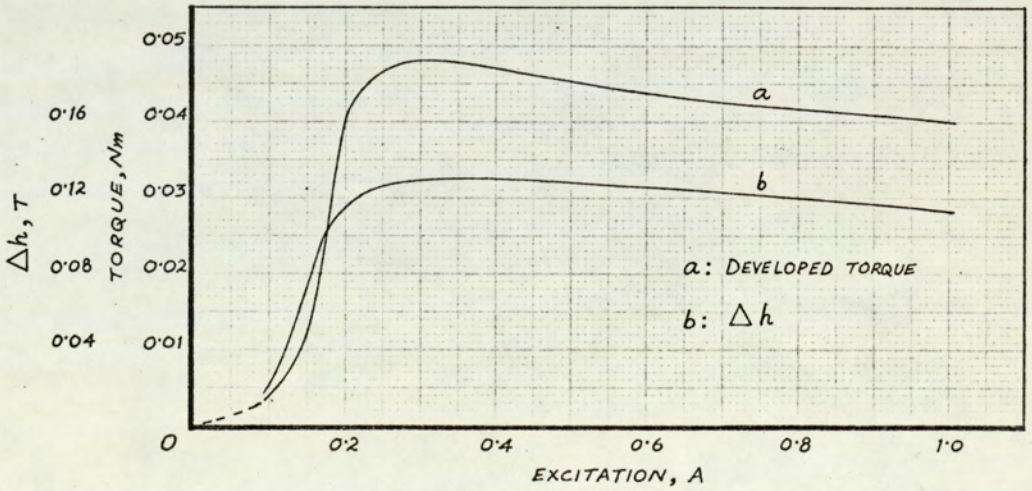

Fig. 5.23

excitation, Δh is seen to decrease and the trend coincides with that observed in the torque-excitation curve. A direct, linear dependence of the torque on Δh is also apparent from the graph of Fig. 5.24.

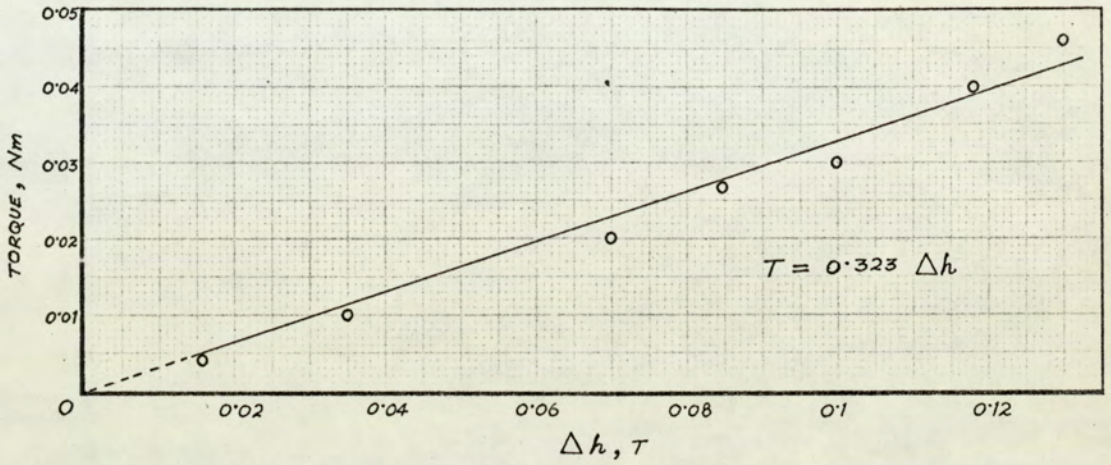

Fig. 5.24

Considering then that a reduction in Δh is equivalent to a greater proportion of flux leaving the pole tip A compared with B (Fig. 5.22), the variation of Fig. 5.23 points to a "shift" in flux distribution in the pole. This concept originated in the first series of tests, using iron filings, to study leakage flux distribution in the interpolar region (see Fig. A4.4, Appendix IV). That the reduction in torque cannot be due to a reduction in the total flux leaving the pole is demonstrated by the graph a of Fig. 5.25 (next page) which shows a plot of flux/pole, represented by the area of the B_r waveforms (for a unit axial length and fixed pole arc) against excitation current. The lagging pole tip is heavily saturated at higher excitations and the shift of the flux away from it is to be expected. As shown by graph b in Fig. 5.25, the flux density on the external rotor surface on the interpolar axis, B_{i_p} , exhibits a peak value

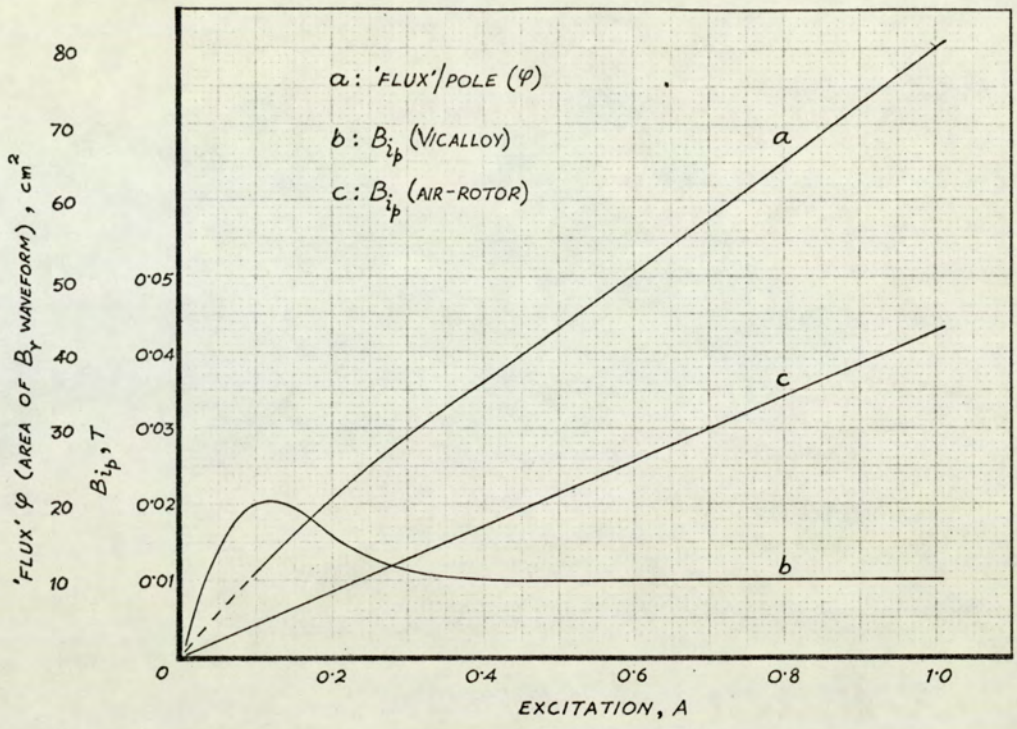

Fig. 5.25

thereby suggesting alternative paths for the flux. Below 0.3 A excitation, this variation of B_{i_p} (Vicalloy), and also a slight curvature in the plot of flux/pole, φ, are indicative of relatively more flux entering the rotor corresponding to increased permeability of Vicalloy. The flux paths in the interpolar region tend to be more 'conventional' in this range of current, resulting in less leakage towards the yoke and higher flux density on the external rotor surface. Graph c shows the variation of B_{i_p} at the same point on the interpolar axis with the air-rotor.

5.5.1.2 Change in direction of the rotor m.m.f.

The significance of the second criterion, mentioned in Section 5.5.1, derives directly from the mechanism of torque production explained in terms of the rotor magnetisation $\bar{M}$. It has been stated that the point of flux division within the annulus,

and hence the direction of resultant rotor m.m.f., shifts to the lagging pole tip in space with respect to the applied m.m.f. even at the smallest excitation, and remains fixed in that position. Assuming a direct proportionality of $\bar{M}$ (B_θ under the pole surface) to developed torque, the torque-excitation curve should be similar to a plot of $\bar{M}$ with excitation, in other words, to the graph of B_p against I (Fig. 5.5), which points to a constant torque at excitations greater than 0.3 A. Therefore reduction of torque should be equivalent to either a reduced value of $\bar{M}$ at higher excitation (which is not possible) or a shift of the rotor m.m.f., M_R, in the direction of the applied m.m.f., M_A. The second possibility would mean an increased torque in a 'negative' sense with a consequent reduction in the nett torque (see Fig. 5.26). In this context, the role of the angle δ, which M_R makes with M_A, is that of a 'load angle'. The value of this angle affects the

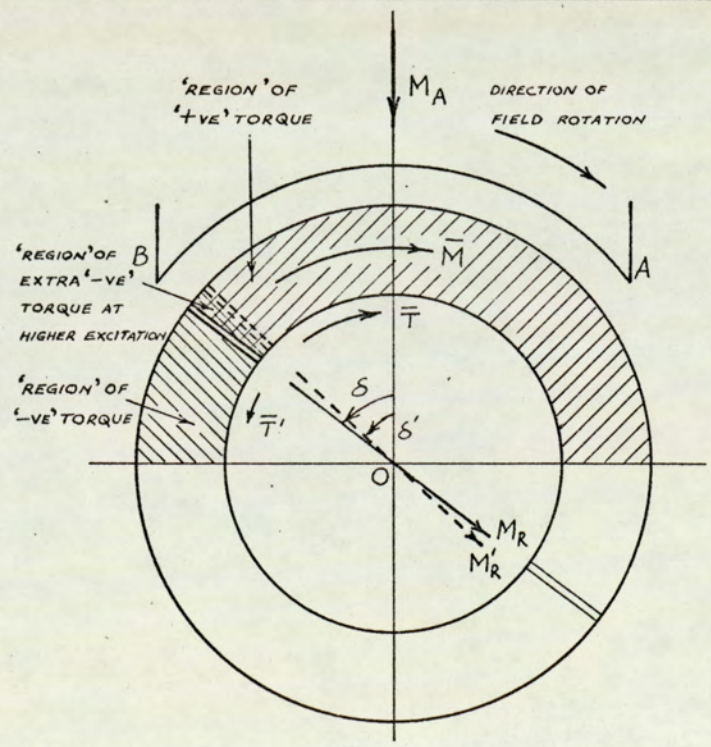

Fig. 5.26

torque observed at the shaft. Any reduction in it is tantamount to a reduction in the developed torque. Although δ is almost constant in the experimental machine, because of the pole tip, a close examination of Fig. 5.4 reveals that the point of flux density reversal moves to the left, although only slightly, at increasing excitation currents, i.e., from the lagging to the leading side of the pole.

Clearly, these considerations are in accordance with the discussion of Section 5.5.1.1 and it is concluded that the shift of flux from the lagging to leading side of the pole which occurs for excitation currents in excess of 0.4 A is equivalent to diminishing the "rotor hysteresis effect", and therefore the developed torque.

The above two reasons for the reduction of torque point to possible means for preventing it. The shifting of flux in the pole towards the leading side can be checked by 'controlling' the total m.m.f. within the pole body; an obvious method being to have a 'suitably designed' slot in the pole providing a high reluctance path for the flux. The dependence of the rotor m.m.f. direction on the location of pole tips can be minimised by bridging the interpolar region using thin bridge pieces. Neither of these suggestions has been investigated in the present research.

5.5.2 Effect of rotational hysteresis

A topic that is sometimes associated with the developed torque in hysteresis machines is the contribution from rotational hysteresis loss. This loss increases rapidly at low values of flux density (theoretically being twice as much as the alternating

hysteresis loss[56]), reaches a maximum near the knee of the saturation curve, and then decreases to become zero at intense saturation. A typical variation is illustrated by Fig. 5.27, together with the alternating loss.

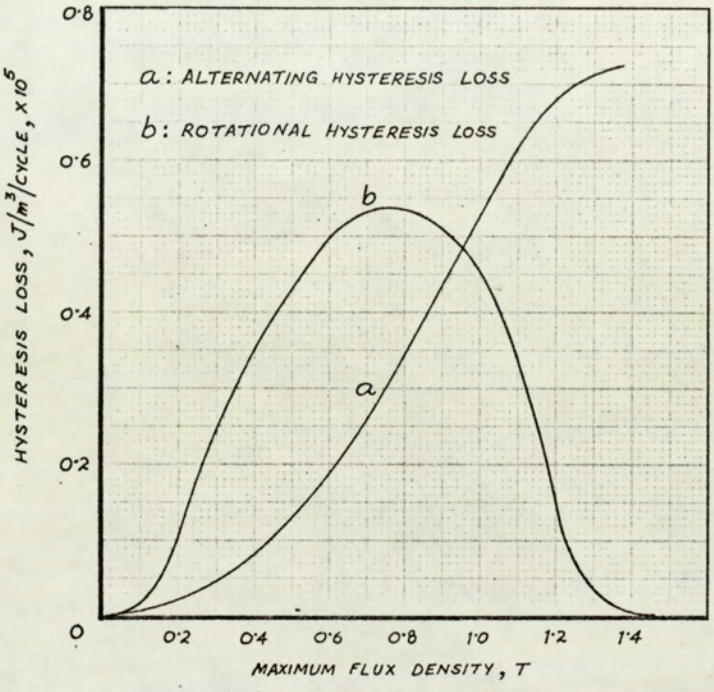

Fig. 5.27

Generally it is assumed that both losses may contribute to torque. As the loss due to rotational hysteresis is the result of directional changes[57,58], it is not inappropriate to assume that it is a consequence of radial flux density in the rotor annulus. However, it is more realistic to contemplate the effect as a result of directional changes in the small elements which comprise the annulus, on the basis of the single particle theory of magnetism[59]. This approach is consistent with that of earlier sections to explain the production of torque, by replacing the rotor magnetisation by magnetic dipoles.

In the experimental machine, changes in the directions of any particle of the rotor occur principally under the pole tips

taking it through one revolution for every complete revolution of the rotor. This is evident from the B_θ. waveforms for Vicalloy shown in Fig. 5.4. Under the leading pole tip the changes will be merely oscillatory about a mean position, the angle of swing not reaching even 90^o. Under the lagging pole tip the flux density in the Vicalloy reverses and it is here that the particle rotates through 180^o. Rotation through another 180^o takes place opposite the other lagging pole tip to complete the cycle. Although these conditions can give rise to rotational hysteresis loss, the flux density 'level' of the particle is in the intense saturation region for excitation currents greater than 0.15 A (suggested by appreciable peaks in B_θ waveforms), and therefore the rotational hysteresis loss and the contribution to torque would be insignificant. It is shown in Appendix I that the maximum developed torque in the experimental machine is very nearly equal to the theoretically calculated value due to pure alternating loss. Hence it is reasonable to conclude that rotational loss does not contribute to the torque in the working range of excitation, and therefore it cannot be a contributory factor responsible for the overall reduction of torque in region III. The latter conclusion specifically applies to the experimental machine; for it is a reasonable conjecture that in some hysteresis motor designs rotational loss is the more important, and therefore is one reason for the decrease in torque at high excitation.

The only stage of torque production where the rotational loss can contribute to the developed torque is in the very low/low excitation current range, i.e., 0 - 0.1 or 0.15 A. It was noted in Section 5.2.1, when applying the Rayleigh loop approximation to

calculate torque, that the values obtained from pure alternating loss were less than those measured. Since the peak flux densities in Vicalloy may lie in the range of rising portion of the rotational loss curve, this could account for the excess measured torque.

5.6 Scalar Magnetic Potential Distribution in the Airgap

5.6.1 Resultant computed waveforms

The significance of rotor magnetisation on the machine performance is also reflected in the form of the scalar magnetic potential distribution on the external surface of the rotor. Its derivation from the measured radial flux density waveforms in the airgap is described in Appendix V and the computed results are illustrated by the waveforms of Figs. 5.28 and 5.29, pages 142 and 143. The distribution shown in Fig. 5.28 corresponds to an excitation of 0.3 A and can be compared with that obtained with the air-rotor at the same excitation (also shown in the figure). The latter has the same shape as that for the Vicalloy rotor under non-hysteretic conditions, since the relative permeabilities in the two cases are insignificant when compared with the high permeability of the poles and yoke.

It can be noticed from the two graphs that the simple, almost trapezoidal, distribution of potential without spatial hysteresis (the waveform for the air-rotor) is modified to a characteristic triangular shape, with slight curvature in the interpolar region, by the rotor magnetisation. The striking feature of the Vicalloy waveform is the straight-line portion stretching from the leading to the lagging pole tip.

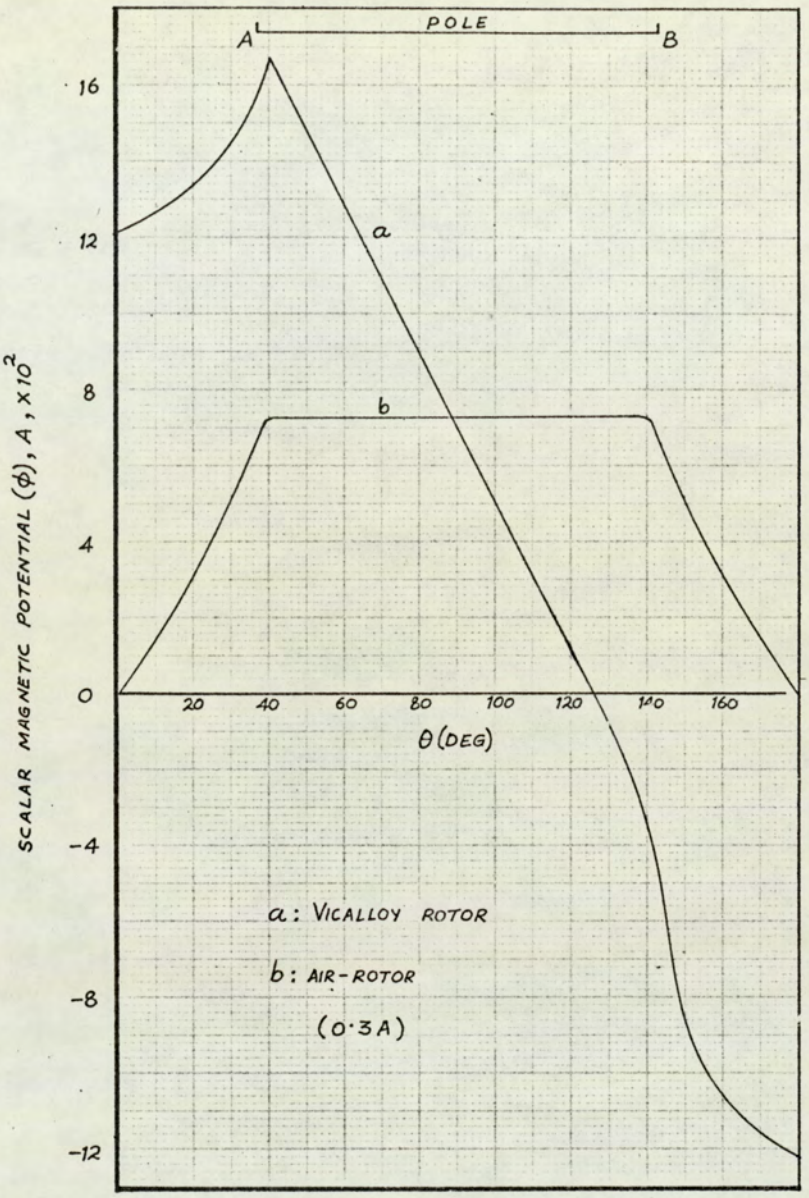

Fig. 5.28

Mathematically, this derives directly from the B_θ waveforms on the external rotor surface, which have a constant (and non-zero) value under the poles (see Fig. 4.5, page 85). The plots of Fig. 5.29 confirm that this is a common feature for all excitations, with the slope of the straight portion becoming steeper at increasing excitation currents. Physically, it would appear that the magnetic conditions in the rotor result in the type of

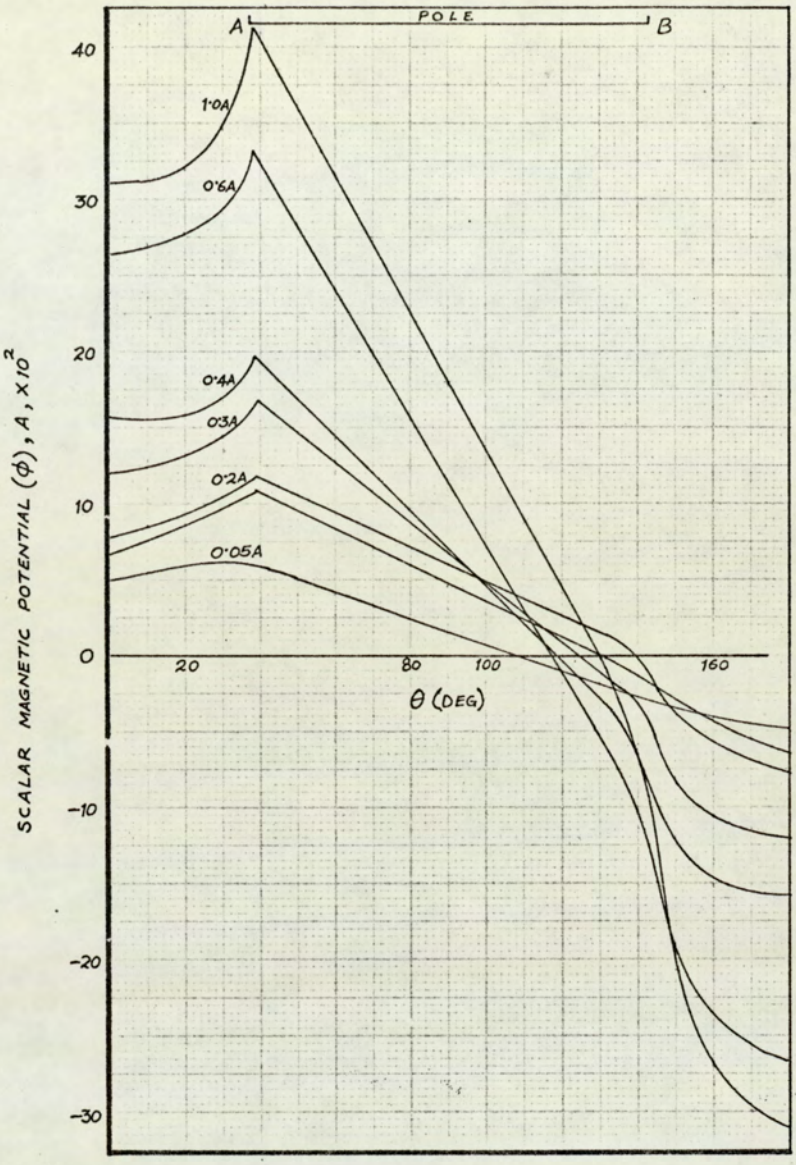

Fig. 5.29

potential distribution shown. A point to note, however, is that this is the 'equivalent' effect of rotor magnetisation, since the resultant potential variation is derived from the flux density distribution in the airgap.

5.6.2 Potential distribution in the airgap 'due to rotor magnetisation'

If the waveforms of the potential distribution with the

air-rotor are assumed to be representative, to some extent, of those obtained with the Vicalloy rotor under non-hysteretic situation, then an idea of the rotor magnetisation effect can be formed by studying the waveforms of Fig. 5.30. These show the difference of potential between the air- and Vicalloy rotors, for the same radius and excitation currents. The two main features of these waveforms are discussed below.

(i) As pointed out earlier, at a very low excitation current, 0.05 A, when the spatial hysteresis effect is negligible, the

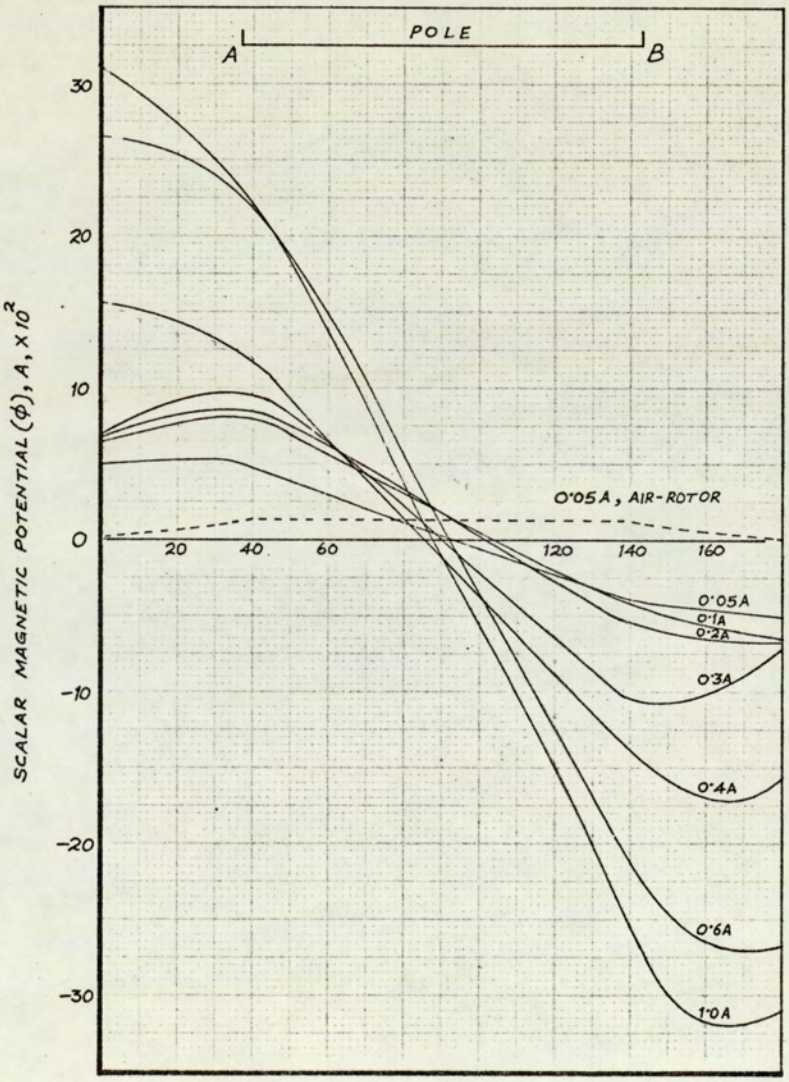

Fig. 5.30

shape of the waveform approaches a trapezoid, but is displaced in space by approximately 90^{o}(E) from the corresponding one for the air-rotor (shown dotted in the figure). This emphasises the independent nature of the rotor magnetism once it has been magnetised. Experimental evidence of this effect can be seen from the iron filing pattern of Fig. A4.3, Appendix IV. This shows the residual magnetism of the rotor immediately after switching off the excitation.

(ii) For an increasing excitation current, the 'rotor potential' is gradually modified in shape in the interpolar region, approaching a near-triangular variation, similar in shape to the armature reaction m.m.f. waveforms in an ordinary d.c. machine. It can be seen that the waveforms go through zero at approximately the 90^{o} position, for all currents greater than 0.2 A . Apart from the changing shape, this again supports the arguments extended in (i) above.

In conclusion therefore it may be stated that the equivalent potential distribution in the airgap due to rotor magnetisation taken alone, is approximately trapezoidal or triangular in the current ranges 0 - 0.2 A and 0.2 A - 1.0 A respectively . This characteristic rotor quality could be particularly useful in developing an approximate linear analysis of the machine performance, with simplifying assumptions, for example with regard to the permeability of the rotor material and a quantitative link between the rotor and field system potentials.

5.7 Comments

The qualitative theory developed in this chapter emphasises the significance of the rotor magnetisation. However, its role in the production of torque in the experimental machine cannot be realized until the effect is considered independently. Normally, the rotor active material is assumed to be one of the hard magnetic materials having special ferromagnetic qualities and its function in hysteresis motors is treated electromagnetically in terms of simple physical properties such as low relative permeability, 'fat' hysteresis loop resulting in high hysteresis loss/unit volume, and saturation flux density. This is because an analytical treatment is given primary importance and the physical aspects of torque production are not properly explained.

In developing the theory the magnetisation in the rotor annulus is assumed uniform to make the explanations simple. This assumption is justified in the present machine since the radial thickness of the rotor is very small. Nevertheless, the assumption is not a limitation of the theory and it will apply to a rotor having any thickness, although the flux distribution in the latter case will be more complicated.

The theory also is unaffected by the limitations arising from the short axial length of the machine, which have been excluded from the discussion at all stages. The 'end effects' caused by the short length will change the field distribution slightly by introducing variations in the axial direction.

CHAPTER VI

TORQUE CALCULATION USING POYNTING'S THEOREM

CHAPTER VI

TORQUE CALCULATION USING POYNTING'S THEOREM

6.1 Chapter Outline

The accurate calculation of torque from values of $\bar{B}$ and $\bar{H}$ within the Vicalloy rotor would require a precise knowledge of the field distribution and this is not possible. Now the natural laws ensure that the magnetic conditions of the rotor are distinctly reflected in the adjacent non-magnetic regions, and this provides an alternative method for computing the power flow into the rotor and hence the torque at the shaft. The method uses Poynting's theorem. An introduction of the theorem and a discussion of its application to the experimental machine is the subject of the present chapter.

The appropriate form of the Poynting vector is derived and its salient features discussed. A 'surface' for the integration of the vector is defined, showing that it is necessary to account for the power flow on both the internal and external rotor surfaces to arrive at the nett power responsible for torque. This is computed from the measured field waveforms and discussed in the light of the m.m.f. harmonics.

The mechanism of converting nett power flow into torque at the shaft is discussed, and a torque-excitation curve obtained which is compared with the measured curve.

6.2 The Poynting's Theorem

According to the Poynting's theorem[60] the vector

$$\bar{S} = \bar{E} \times \bar{H} \qquad 6.1$$

defines the instantaneous rate of flow of energy through unit surface area. Since the units of $\bar{E}$ and $\bar{H}$ are V/m and A/m respectively, the unit of $\bar{S}$ is W/m^2 and total power flow across a given surface is obtained by integrating the normal component of $\bar{S}$ over the appropriate closed surface. That is

$$\text{Total power} = \oiint_{\Sigma} \bar{S} \cdot \bar{i}_n \, ds = \oiint_{\Sigma} (\bar{E} \times \bar{H}) \cdot \bar{i}_n \, ds \qquad 6.2$$

where ds is an elemental area of the surface on which $\bar{S}$ is defined and $\bar{i}_n$ is the unit normal.

When evaluating power flow with the theorem, two points to consider are :

(a) according to expression 6.2, it is only the total surface integral of $\bar{S}$ which gives the nett power flow across a closed surface, although ordinarily a useful interpretation of $\bar{E} \times \bar{H}$ is the power density at a point on the surface

(b) the postulate (a) implies that $\bar{S}$ is not a uniquely defined vector. Any other vector whose integral over the closed surface vanishes, can be added to $\bar{S}$ without altering the total power given by expression 6.2. A common example is curl of a vector; in some cases this permits a more convincing interpretation of the power crossing the closed surface[61]. However, there is little to be gained by these additions when only the total power flow is of interest.

6.3 Applicability of the Theorem to the Experimental Machine

6.3.1 Regions of power flow

A reference to the constructional features and mode of operation of the experimental machine reveals that the 'power' crossing the airgap does not come essentially from the field system, as in a conventional hysteresis motor, because it is driven mechanically and d.c. excitation is provided separately. It is the combination of these two, with the latter playing the role of an additional but essential element, which causes the hysteresis loss and the production of torque. In this context, the machine can be recognized more easily as a hysteresis coupling than a motor.

To illustrate the above concepts further, a simple block diagram of the machine is given in Fig. 6.1, showing the main regions where flow of energy exists. The driving motor supplies mechanical power to the rotating field system through the belt (see also Plate 2.1). In a simple device this power would

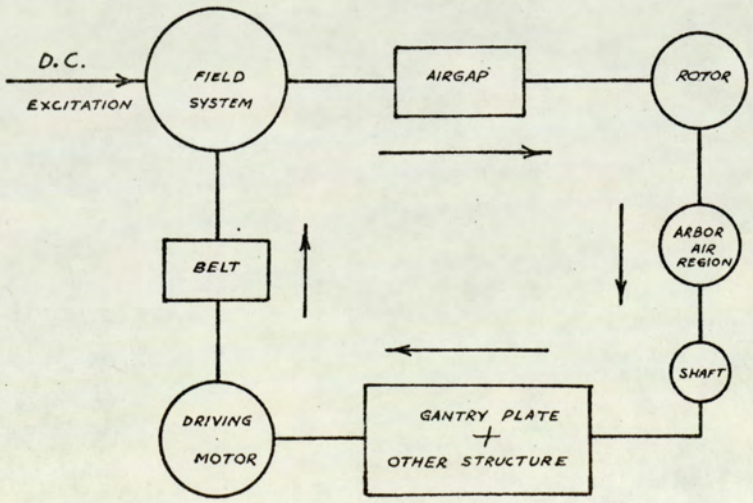

Fig. 6.1

equal the mechanical losses. However, when electrical power is supplied to the field system as well, energy crosses the airgap towards the rotor and 'returns' to the motor via the arbor region, the rotor shaft, the gantry plate and other mechanical structure of the assembly. Some of this energy is used to supply the rotor hysteresis loss.

Fig. 6.1 gives only a general sense of energy flow with disregard to the sinks and sources of power at different stages of the route. However, referring to the air spaces adjacent to the rotor, the nett power loss across them corresponds to the power dissipated in heat as hysteresis loss.

If a suitable Poynting vector can be formulated for the air regions, the integral over a closed surface enclosing the rotor is the nett power referred to above. This applies to a general, three-dimensional picture, and any arbitrarily chosen surface containing the rotor, on each element of which the vectors $\bar{E}$ and $\bar{H}$ are known, can be considered. In the present case this surface is chosen to coincide with that comprising the rotor cylinder, and measurements of $\bar{E}$ and $\bar{H}$ are made accordingly. The total power entering the rotor is then given by equation 6.2 while the form of the vector adopted is defined by 6.1.

6.3.2 The two rotor surfaces

From the aspect of measurement of the component vectors $\bar{E}$ and $\bar{H}$, the simplest method to obtain the nett power flow into the rotor active material (since no nett power flow can take place in the adjacent air spaces) is to integrate the Poynting vectors independently on all the surfaces of the annulus. With a proper

sign convention, this automatically accounts for the nett power entering the rotor from the airgap and leaving it through the arbor region, in accordance with the diagram of Fig. 6.1. As shown in Fig. 6.2, the total surface for integration will comprise the two cylindrical surfaces 1 and 2, and the annular discs 3 at each end. The first two are referred in this thesis as external and internal surfaces, and if the corresponding radii are R and r respectively, the values of their areas for an axial length ℓ will be

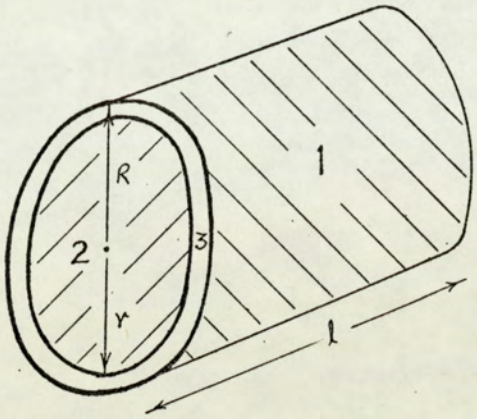

Fig. 6.2

$$S_1 = 2\pi R\ell \quad \text{and} \quad S_2 = 2\pi r\ell \qquad 6.3$$

The areas of the two annular discs (3) can be calculated similarly. However, since these will be very small when compared to either S_1 or S_2, the contribution of the energy flow through them to the integral 6.2 is ignored. This is in line with the assumption that the field distribution in the experimental machine is two-dimensional, and 'end effects' are neglected.

Hence, the two rotor surface areas over which the distribution of $\bar{E}$ and $\bar{H}$ is required to be known are S_1 and S_2.

6.3.3 Distribution of $\bar{E}$ and $\bar{H}$ on the rotor surfaces

The basic measured quantities in the tests performed on the machine, given in Chapter III, were induced e.m.f.s proportional to the radial components of flux density in the airgap and the arbor regions. Thus, with a relative speed of

rotation of the field system ω rad/s, the induced e.m.f. will be

$$e = B_r \, l \, \omega \, r \qquad 6.4$$

where B_r is the radial flux density component, l is the total axial length of the search coil and r the radius.

The expression 6.4 therefore allows the distribution of the electric field intensity to be deduced. As a cylindrical co-ordinate system is used, the only component of $\overline{E}$ is in the axial direction for a constant peripheral velocity ($v = \omega r$) at a given radius r . Hence,

$$\overline{E} = E_z \cdot \overline{i}_z \qquad 6.5$$

where $\overline{i}_z$ is the unit vector in the axial or z-direction and E_z is obtained from 6.4 as e/l .

The distribution of $\overline{H}$ on the corresponding surface is easily available from the knowledge of $\overline{B}$ at different points (since the measurements are made in the non-magnetic regions, $\overline{B} = \mu_o \overline{H}$). More specifically, the tangential component of $\overline{H}$ is required in association with $\overline{E}$ above to give power flow in the radial direction (see Fig. 6.3). This component is obtained from the B_θ variation on the surface, described in Chapter IV, as

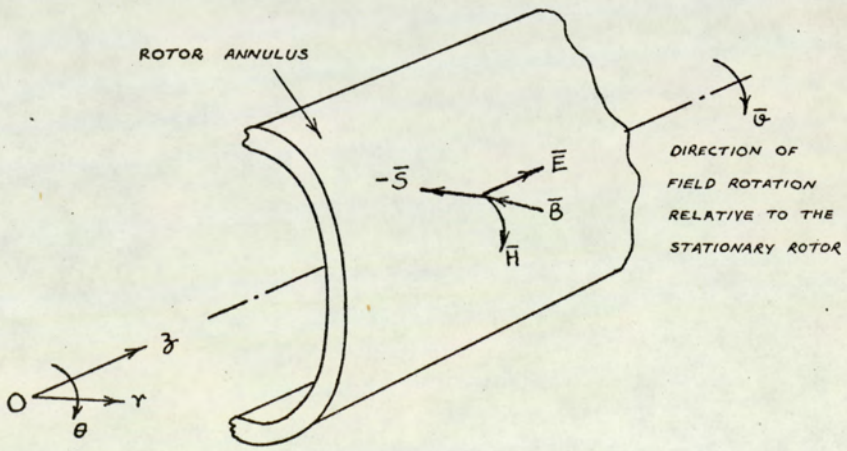

Fig. 6.3

$$H_\theta = B_\theta / \mu_o \qquad 6.6$$

With these components known, the appropriate Poynting vector is given by

$$S_r \bar{i}_r = - E_z H_\theta \bar{i}_r \qquad \text{(i.e. into the rotor)} \qquad 6.7$$

Since in the experimental machine B_r is measurably non-zero only under the poles, being negligible in the interpolar region, a necessary condition for radial power flow is a non-zero average value of H_θ under the poles. This stresses the importance attached to B_θ in the preceding chapters.

Clearly, if B_r were symmetrical about the pole axis, and H_θ was symmetrical about the interpolar axis, no nett power flow would be possible. This can be proved easily :

Let B_r be expandable in Fourier series of the form

$$B_r = k' \sum_{n=1,3,..}^{\infty} B_{m_n} \sin n\theta \qquad 6.8$$

giving E_z as

$$E_z = k \sum_{n=1,3,..}^{\infty} B_{m_n} \sin n\theta \qquad 6.9$$

and H_θ as

$$H_\theta = k'' \sum_{n=1,3,..}^{\infty} H_{m_n} \cos n\theta \qquad 6.10$$

Then the radial Poynting vector will be

$$S_r = -E_z H_\theta = -kk'' \sum_{n=1,3,..}^{\infty} \sum_{n=1,3,..}^{\infty} B_{m_n} H_{m_n} \sin n\theta \cos n\theta \qquad 6.11$$

and its integrated value over a closed surface of radius r will be zero. The analysis shows that no nett power transfer can be

obtained for the rotor under non-hysteretic conditions or with the air-rotor, and leads to simple mathematical conclusion: for nett power flow to be obtainable a necessary, but not sufficient, condition is the existence of both sine and cosine terms in the expressions of B_r and H_θ. This point is taken up again in the sub-section below.

6.3.3.1 Non-dependence of nett power flow on radius

A particularly important property of S_r defined in equation 6.7 is that the calculation of the total power, i.e., the integral of S_r over the closed rotor surface, is independent of radius. This can be proved in terms of general expressions for B_r and H_θ derived from a scalar magnetic potential function ϕ, and speed of rotation of the field system ω.

In the airgap region considered (Fig. 6.4), ϕ is governed by Laplace's equation and its variation expressed as a

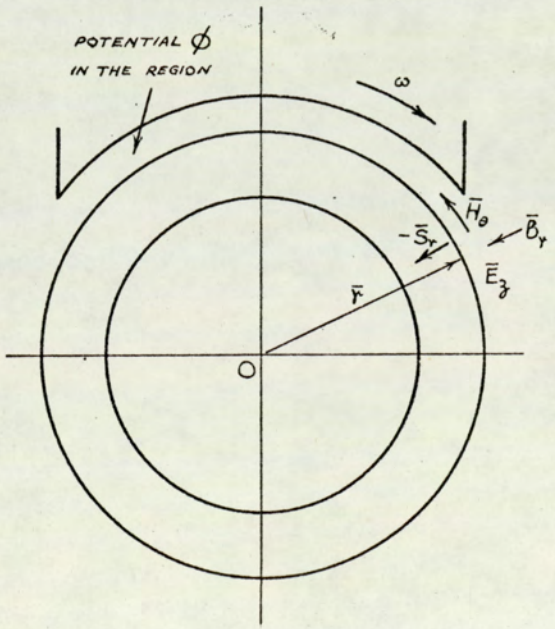

Fig. 6.4

series of harmonically varying terms. Hence,

$$\phi = (A_n r^n + B_n r^{-n}) \sin n\theta + (C_n r^n + D_n r^{-n}) \cos n\theta \qquad 6.12$$

The radial flux density B_r is given as

$$B_r = \mu_o H_r = -\mu_o \frac{\partial \phi}{\partial r} \qquad (\text{from } \bar{H} = -\bar{\nabla}\phi)$$

or
$$B_r = -\mu_o n \left[(A_n r^{n-1} - B_n r^{-n-1}) \sin n\theta + (C_n r^{n-1} - D_n r^{-n-1}) \cos n\theta \right] \qquad 6.13$$

and the induced e.m.f. in the axial direction

$$e_z = B_r \omega l r \qquad \text{giving} \qquad E_z = B_r \omega r$$

or
$$E_z = -\mu_o n \omega r \left[(A_n r^{n-1} - B_n r^{-n-1}) \sin n\theta + (C_n r^{n-1} - D_n r^{-n-1}) \cos n\theta \right] \qquad 6.14$$

Similarly H_θ is obtained from equation 6.12 as

$$H_\theta = -\frac{1}{r} \frac{\partial \phi}{\partial \theta}$$

$$= -n \left[(A_n r^{n-1} + B_n r^{-n-1}) \cos n\theta - (C_n r^{n-1} + D_n r^{-n-1}) \sin n\theta \right] \qquad 6.15$$

Hence from equations 6.14 and 6.15,

$$S_r = -E_z H_\theta$$

$$= -K_1 r \left\{ A1 \sin^2 n\theta + A2 \cos^2 n\theta + A12 \sin n\theta \cos n\theta \right\} \qquad 6.16$$

where $K_1 = \mu_o n^2 \omega$

$$A1 = -\left[A_n C_n r^{2n-2} - B_n C_n r^{-2} + A_n D_n r^{-2} - B_n D_n r^{-2n-2} \right]$$

$$A2 = \left[A_n C_n r^{2n-2} + B_n C_n r^{-2} - A_n D_n r^{-2} - B_n D_n r^{-2n-2} \right]$$

$$A12 = \left[A_n^2 r^{2n-2} - B_n^2 r^{2n-2} - C_n^2 r^{2n-2} + D_n^2 r^{-2n-2} \right]$$

When integrated over the cylindrical rotor surface, the last term on the right hand side of equation 6.16 will vanish and the total power is given by

$$P = -K_1 K_2 r \int_0^{2\pi} (A1 \sin^2 n\theta + A2 \cos^2 n\theta) r \, d\theta$$

or $$P = -K' r^2 (A1 + A2) \qquad 6.17$$

where K_1, K_2 and K' are constants.

Substituting for $A1$ and $A2$ in equation 6.17,

$$P = K \left[B_n C_n + A_n D_n \right] \qquad K = \text{constant.} \qquad 6.18$$

This shows that the total power is only a function of the coefficients $A_n, \ldots . D_n$, and not of the radius r. This is to be expected since no nett power is absorbed in the air spaces. It is also clear that the expressions for E_z and H_θ must be representable in the form given by equations 6.14 and 6.15 in order to provide a nett power flow; in other words the coefficients of sin nθ and cos nθ terms should be independent of each other and functions of r.

The non-dependence of total power on the radius of calculation has a useful bearing on the principle behind the measurement of power flow using search coils in a particular region : so long as the radii of the two coils are accurately known, apparently to calculate B_r values, their actual position is not critical.

6.3.3.2 Poynting vector in the peripheral direction

The existence of a component of $\bar{\Pi}$ in the radial direction indicates a second Poynting vector in the peripheral direction on the rotor surfaces, given by

$$S_\theta \bar{i}_\theta = E_z H_r \bar{i}_\theta \qquad 6.19$$

This has a mathematical, non-zero value on each elemental area of either surface, but does not contribute to the power flow in a radial direction.

6.4 Computation of Power Flow

Following the procedural steps of Section 6.3.3.1, if the measured waveform of E_z and computed waveform of B_θ (or H_θ) at any excitation are expressed as

$$E_z = K_1' \sum E_{1_n} \sin n\theta + E_{2_n} \cos n\theta$$

and $$H_\theta = K_2' \sum H_{1_n} \sin n\theta + H_{2_n} \cos n\theta$$

then the radial Poynting vector for the computation of power flow will be

$$S_r = -E_z H_\theta$$

$$= -K_1' K_2' \left\{ \sum E_{1_n} \sin n\theta + E_{2_n} \cos n\theta \right\} \times \left\{ \sum H_{1_n} \sin n\theta + H_{2_n} \cos n\theta \right\}$$

and the total power flow on either rotor surface (for which $E_{1_n} \ldots H_{2_n}$ stand) is

$$P = K'' \sum E_{1_n} H_{1_n} + E_{2_n} H_{2_n} \qquad 6.20$$

The computer programme of Appendix V incorporates the necessary steps to obtain S_r and hence P (PVI in the programme), while the constant K'', to give the power flow in synchronous watts, is evaluated in Appendix VI.

6.4.1 The nett power absorbed in the rotor

The results of power flow calculations from the measured waveforms for both the external and internal rotor surfaces are plotted against excitation in Fig. 6.5 (next page, graphs I and II respectively).

It is observed that the value of power flow on either

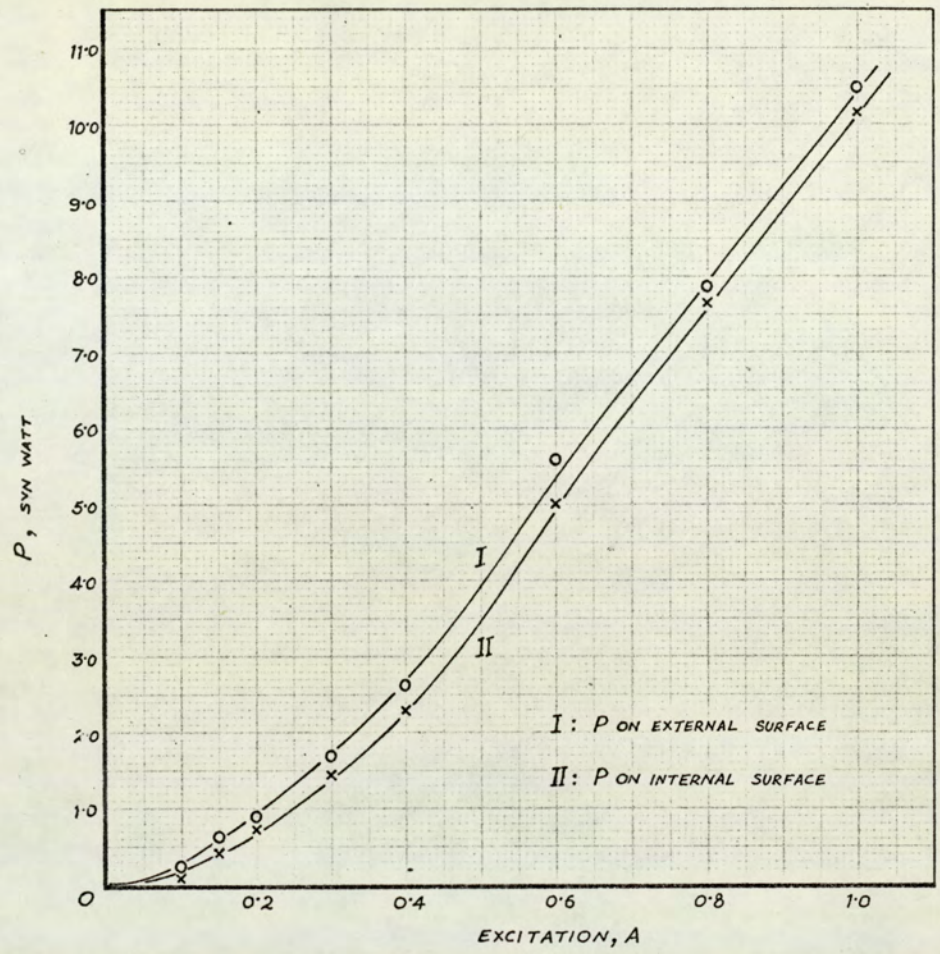

Fig. 6.5

surface increases sharply with excitation, being almost directly proportional to it beyond 0.6 A. This trend is understandable as mathematically the integrated Poynting vector is the summation of the product of B_r- and B_θ-series coefficients. As shown by the waveforms of Figs. 4.2 and 4.5, pages 81 and 85 respectively, the magnitude of these flux density components under the poles increases steadily with increasing excitation currents. Although the radial component is smaller on the inner surface, the peripheral component is relatively large compared to that on the external surface and therefore the product, in the form of power flow given by graph II (Fig. 6.5), closely follows the variation on the outer surface of the rotor.

The nett power flow, equal both to hysteresis loss and torque, is the difference of the power flow computed for the two surfaces. This is because during computation the components of the Poynting vector, and hence the vector itself, are considered identically directed on either side of the annulus such that the power represented by curve I enters the rotor from the airgap and leaves the rotor through the arbor. It is apparent from the two curves of Fig. 6.5 that only a small percentage of the total power entering the rotor is 'utilized', the rest returning to the shaft.

6.4.2 'Shape' of the Poynting vector

It was noted in Section 6.2 that the magnitude of the Poynting vector at a particular point on the rotor surface has no meaning since it is an integrand and any other vector having zero divergence over the whole surface can be added to it. Mathematically, therefore, any point-to-point interpretation of the Poynting vector evaluated during calculations is not necessarily valid. Nevertheless, a qualitative picture of the power flow at different points on the surface can still be conceived from the plot of this vector around the rotor periphery.

As an illustration, plots for the external surface at excitation currents of 0.1 A, 0.3 A, and 1.0 A are given in Fig. 6.6 a (page 161). Since the direction of both E_z and H_θ reverses under each pole, the plots in the figure apply over either pole pitch and the power flow under the pole arc is always positive as shown. It is seen that in spite of the magnitude of the vector changing considerably at increasing excitations, the shape does not change much. The magnitude, at any excitation,

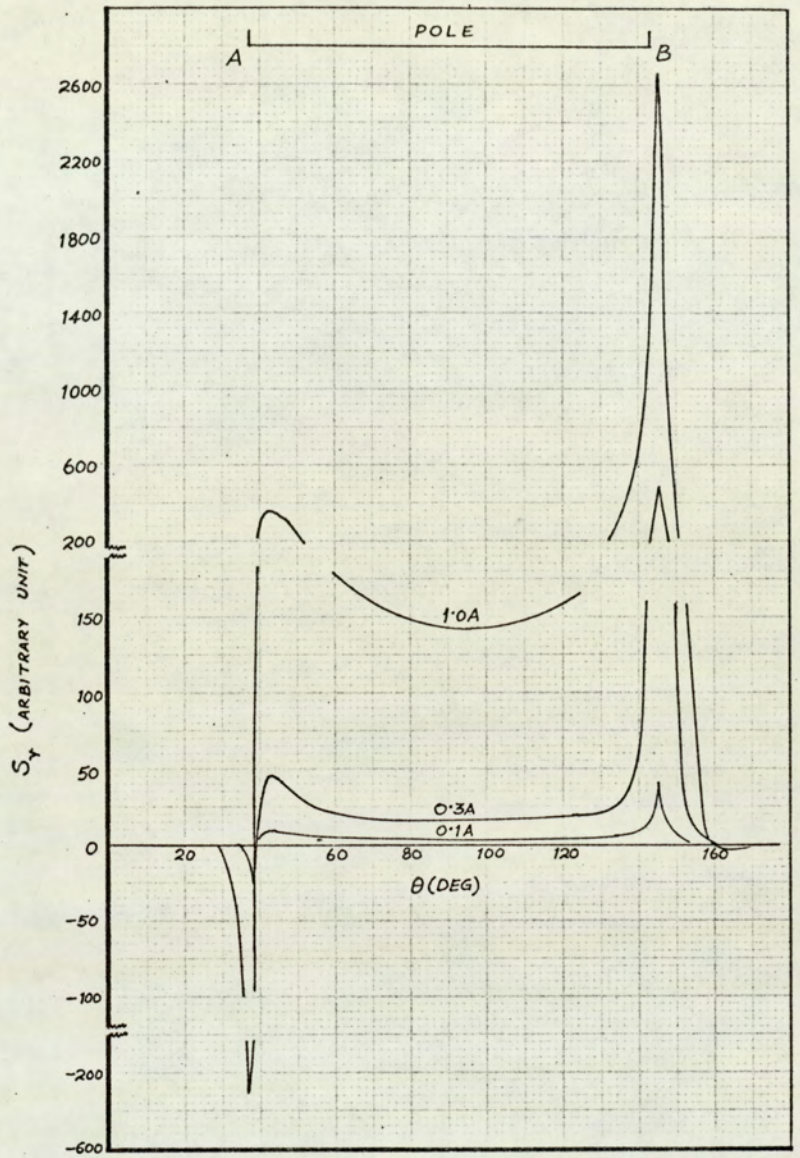

Fig. 6.6 a

is greatest at the lagging pole tip suggesting that a large proportion of the power flow takes place from these pole tips. Again this emphasises the significance of these pole tips, in keeping with the influence on the general field distribution discussed in Chapters IV and V. Irrespective of the condition that no specific meaning can be attached to the Poynting vector at a point, the above description is reasonable since both E_z (Cf. B_r waveforms) and H_θ are a maximum at the lagging pole tips.

The plots have negative values opposite the leading pole tip and if the previous interpretation is preserved, this means that energy leaves the external rotor surface to return to the field system. This reversal of power flow is indicated also by the graphs for the internal surface at similar currents, shown in Fig. 6.6 b, where the relative height of the peak in the negative direction is much larger. This phenomenon, too, supports the explanation for the reduction of torque at higher currents due to the modification of flux distribution.

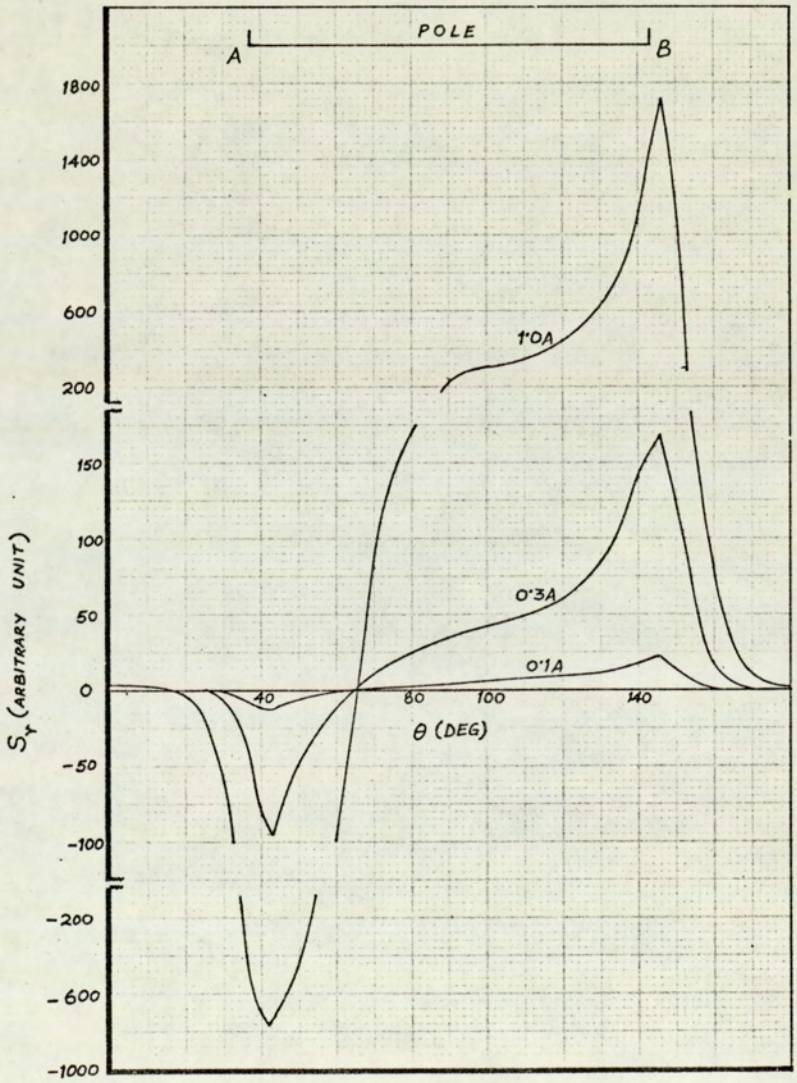

Fig. 6.6 b

6.4.3 Effect of m.m.f. harmonics

The consideration of space harmonics in practical hysteresis motors involves complications introduced by their relative speeds of rotation. In the present study the harmonic effects are realizable from the simple principle of superposition as in Section 6.3.3.1. As a typical example, the power flow on the external rotor surface was computed at 0.3 A excitation for a number of harmonics in the range 1 to 100. The extent to which these contribute to the total power is recorded in Table 6.1.

Table 6.1

Order of harmonic	Range of the order	Contribution as percentage of the fundamental, %	Total nett contribution in terms of the fundamental, %
1		100.0	
3		0.92	
5		14.92	
7		9.57	
9		2.31	
11		9.42	
13		0.71	
15		4.2	
17		2.8	
19		0.506	
21		3.06	
23		- 0.04	
	3 - 23		48.4
	25 23 - 29		2.5
	31 29 - 39		1.26
	41 39 - 49		0.35
	51 49 - 99		0.78
	101 99 - 199		0.0175
	3 - 199		53.0

General conclusions that can be drawn from the table are:

(i) The harmonics contribute as much as 50% of the total power. Of this, a large proportion is due to harmonics in the range 3 - 21, the higher harmonics are not so effective in this respect.

(ii) The effect of all harmonics which contribute appreciably is additive to the power resulting from the fundamental alone. Since all of the harmonic m.m.f.s are stationary with respect to fundamental, it is reasonable to conclude that all of them should contribute to the power. Where this is apparently invalid, the magnitudes are relatively small and liable to experimental error.

A point to note is that the relative contribution of the 5th harmonic is about 15 times that of the 3rd harmonic. This is due primarily to the pole arc of 106°, or almost 2/3 of the pole pitch, and the characteristic shapes of the B_r and B_θ waveforms. The waveforms at 0.3 A excitation are reproduced in Figs. 6.7 a and b , pages 165 and 166 respectively, together with the harmonic terms 1st, 3rd and 5th. The contribution of any harmonic to the total power is expressed by equation 6.20, and involves the sum of the product of the harmonic coefficients. It is observed that for the 3rd harmonic, the cosine waves are in an opposite sense, while the sine waves have the same sense (in addition to the amplitudes of both the waves being very small), and hence the nett power contribution tends to be small. However, with the 5th harmonic the contributions add directly, thus giving a much larger total.

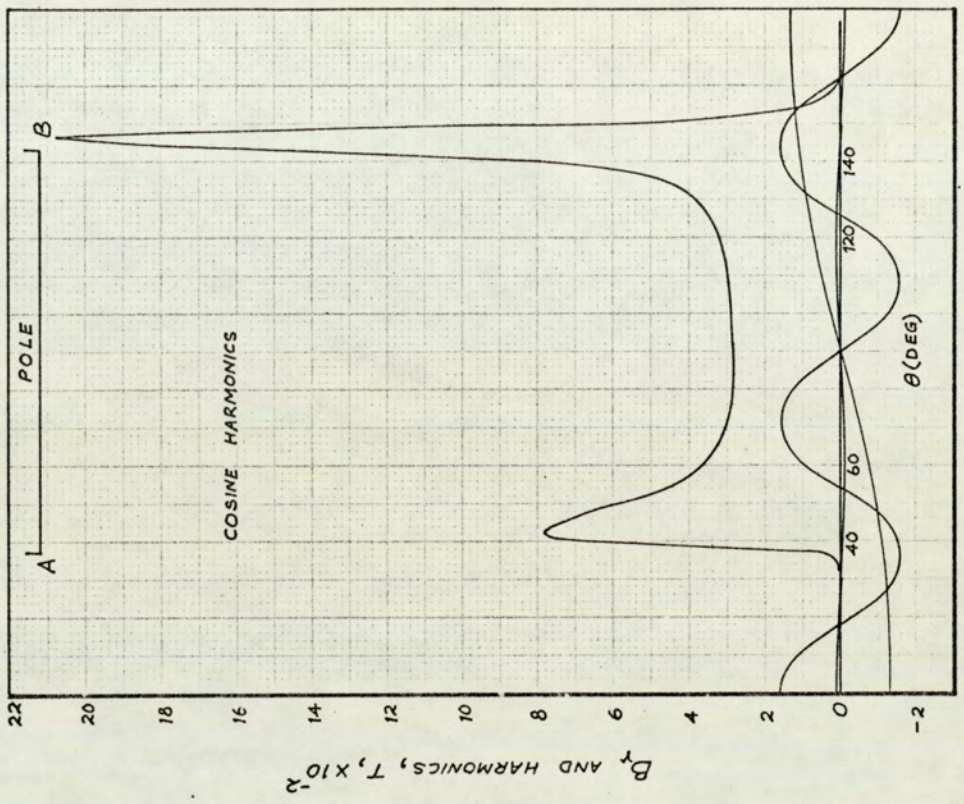
B_r AND HARMONICS, T, x 10^{-2}
22
20
18
16
14
12
10
8
6
4
2
0
-2
A
B
POLE
COSINE HARMONICS
40
60
120
140
θ(DEG)

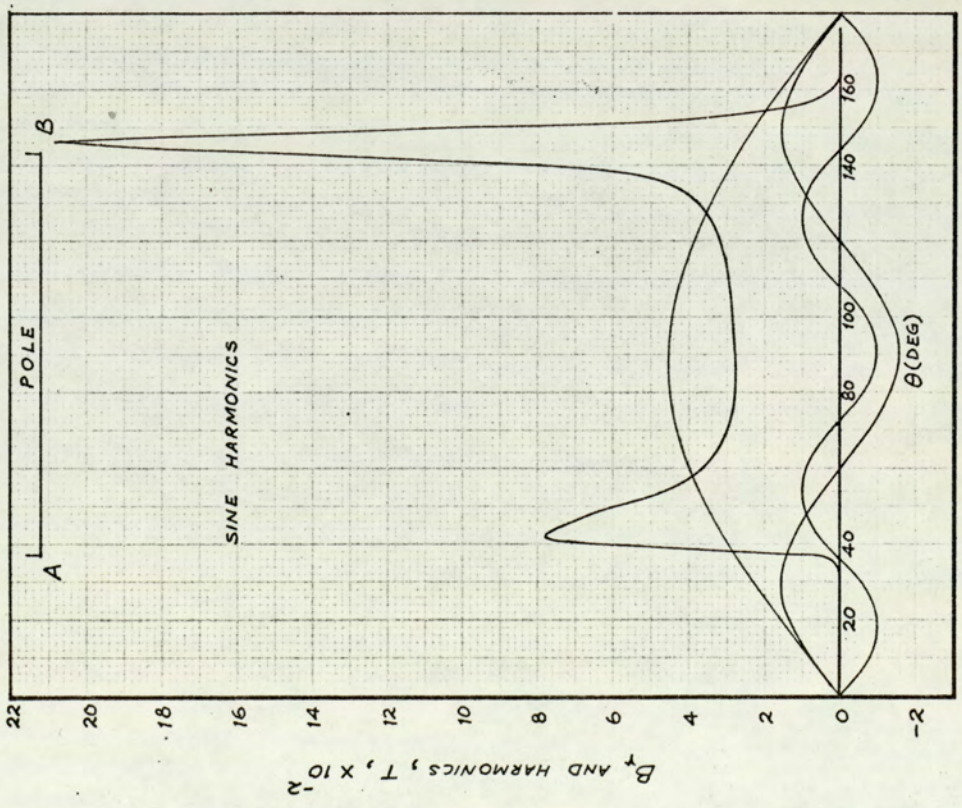
B_r AND HARMONICS, T, x 10^{-2}
22
20
18
16
14
12
10
8
6
4
2
0
-2
A
B
POLE
SINE HARMONICS
20
40
80
100
140
160
θ(DEG)

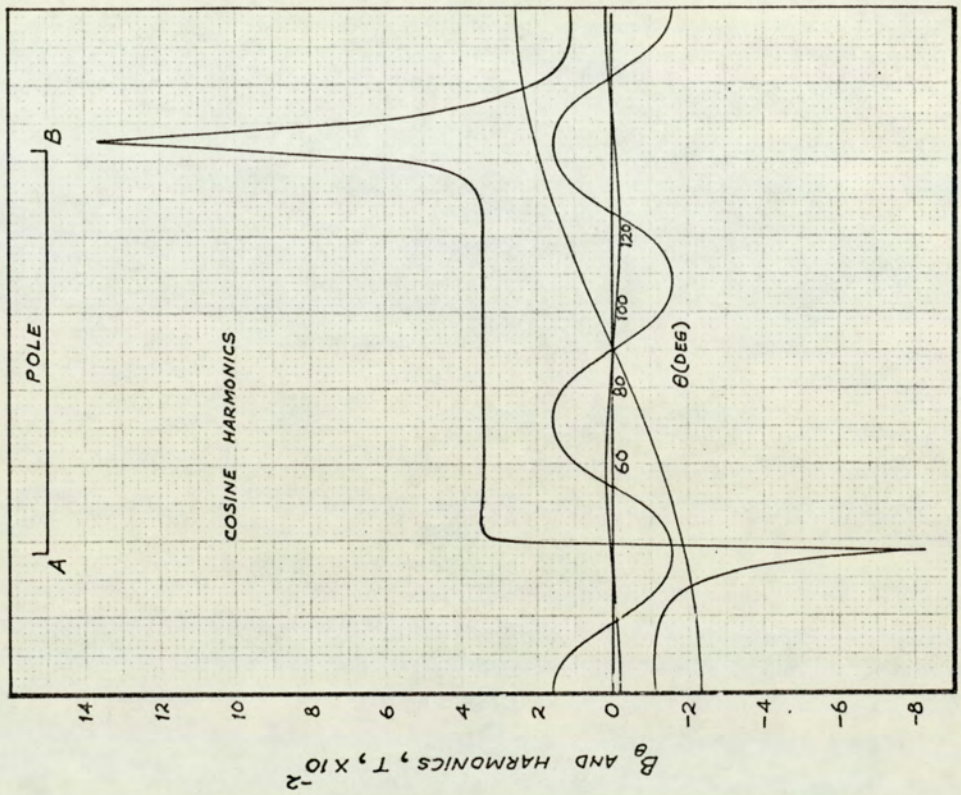
POLE
A
B
COSINE HARMONICS
θ(DEG)
60
80
100
120
14
12
10
8
6
4
2
0
-2
-4
-6
-8
B_θ AND HARMONICS, T, X 10^{-2}

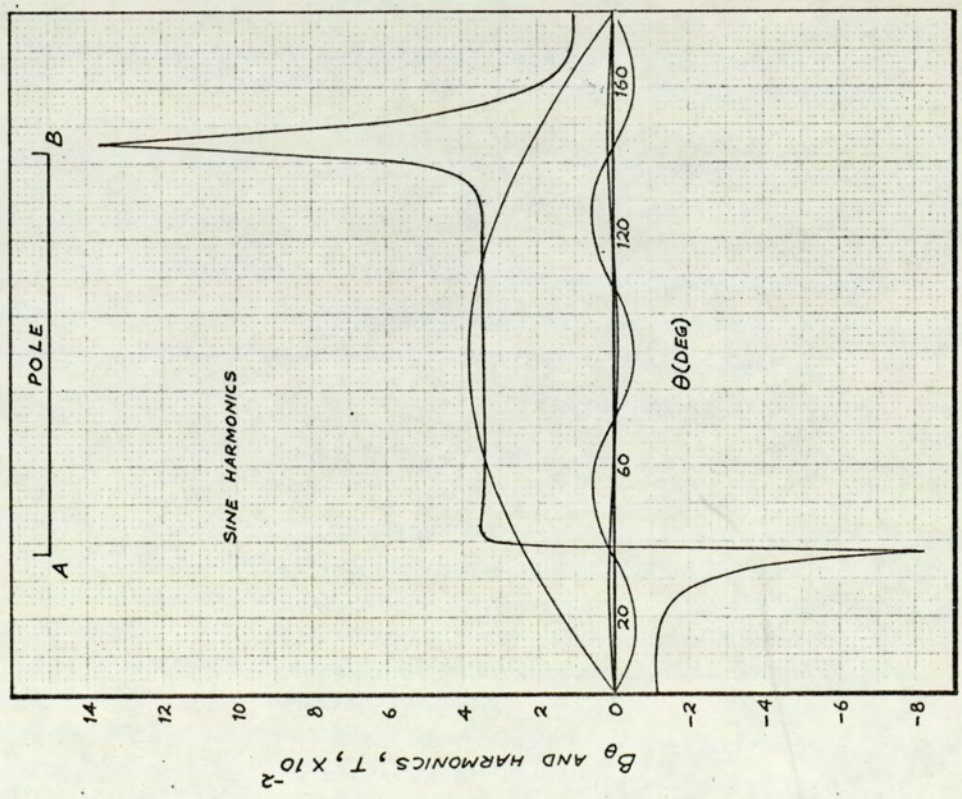
POLE
A
B
SINE HARMONICS
θ(DEG)
20
60
120
160
14
12
10
8
6
4
2
0
-2
-4
-6
-8
B_θ AND HARMONICS, T, X 10^{-2}

6.5 Calculation of Torque from the Nett Power Flow

The nett power flow in the airgap of a conventional machine consists chiefly of the power equivalent to torque at the shaft and the hysteresis loss in the annulus. This section establishes the corresponding relationship for the experimental machine.

6.5.1 Transference of power in the machine

Fig. 6.8 gives the schematic details of the machine and the driving motor. The power from the motor, P_B, is transmitted

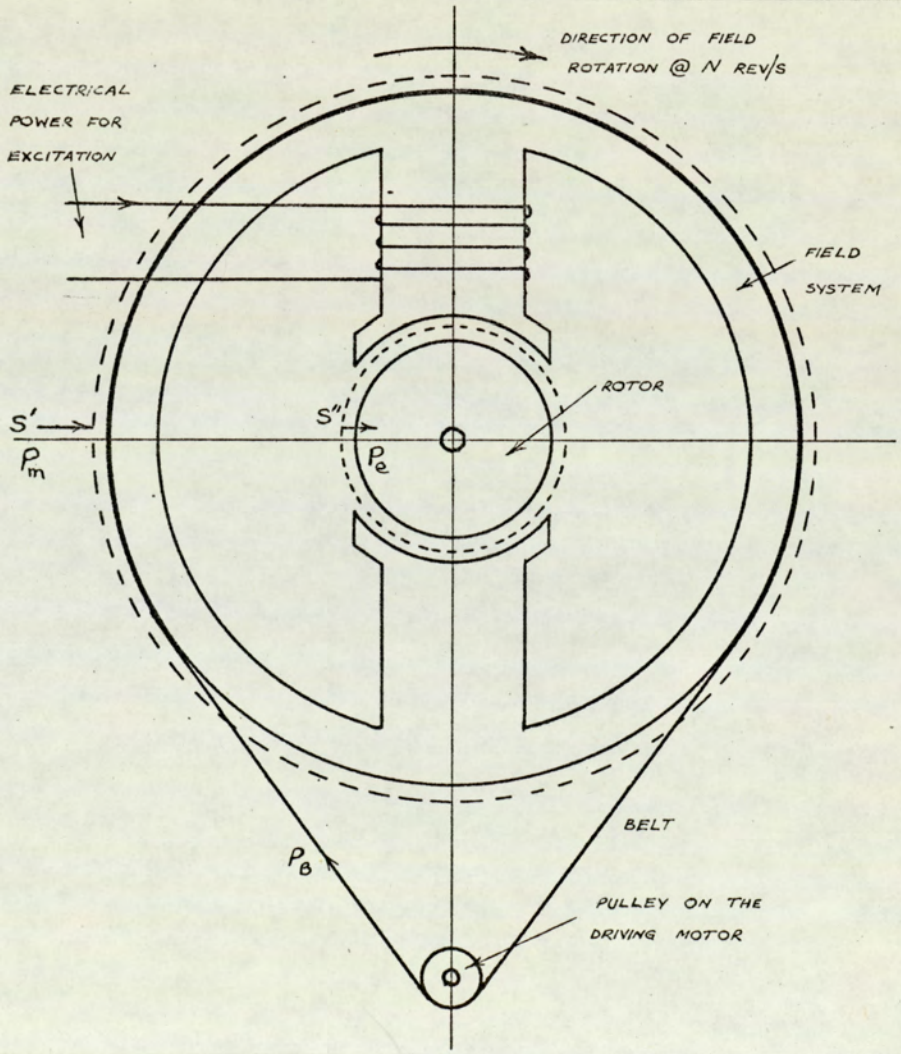

Fig. 6.8

through the belt and drives the field system at N rev/s. Applying Poynting's theorem to two stationary annular surfaces S' and S'', surrounding the field system and the rotor respectively, a nett energy flows into S' and emerges from S''. Hence if P_m is the nett mechanical power flow from the motor through S' and P_e that through S'' then, neglecting any friction and windage losses,

$$P_e = P_m \qquad 6.21$$

The electrical power through S' is not included as this only supplies the copper loss of the excitation winding.

Since the rotor and the two surfaces S' and S'' are stationary with respect to the same reference frame, P_e must equal the power dissipated as heat in the rotor hysteresis loss.

Let the hysteresis loss/rev be W_h W. Then the total loss/s will be $N W_h$ W and

$$P_e = N W_h \qquad 6.22$$

The hysteresis loss, or P_e, is equal to P_m and is observed as a torque, T, exerted on the rotating field system because of the relative motion.

Hence, if angular speed of rotation is ω rad/s,

$$P_m = \omega T$$

so that $$T = \frac{P_m}{\omega} = \frac{P_e}{\omega} = \frac{N W_h}{\omega} \quad \text{Nm} \qquad 6.23$$

or putting $N = \frac{\omega}{2\pi}$

$$T = \frac{W_h}{2\pi} \quad \text{Nm} \quad \text{or} \quad W_h \ \text{W(syn)} \qquad 6.24$$

Equation 6.24 shows that the developed torque is numerically equal to the hysteresis loss in the rotor material/rev and is independent of speed, provided that the standstill condition is excluded.

6.5.2 Calculated and measured torque-excitation curves

The torque-excitation curve derived from the calculated power is shown in Fig. 6.9 together with the measured curve. Although the shape of the two curves is similar, the calculated torque is in excess of the measured torque. The error is a maximum in the lower excitation range (0.1 A - 0.15 A) and is then almost constant at 20 - 25% in the range 0.3 A - 1.0 A excitation. A satisfactory correlation is observed in the linear or normal range of excitation current.

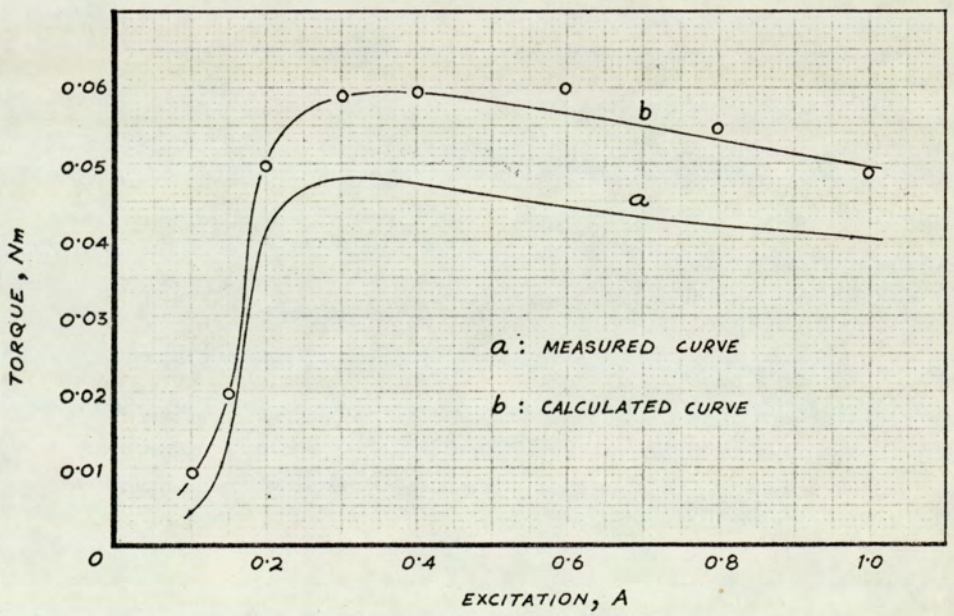

Fig. 6.9

It must be realized that these are apparent errors. The calculated torque is obtained from the difference of the total power flows on the external and internal surfaces. These are

almost equal quantities, especially in the higher excitation range (see Fig. 6.5), and the apparent error of 25% at (say) 1.0 A excitation is really equivalent to 2.5% based on the power flow curve (graph I of Fig. 6.5). Notwithstanding this, the three regions of the torque curve are clearly in evidence. This reflects on the overall accuracy of the semi-theoretical approach for calculation of torque.

The discrepancy in the two torque curves is attributable to many factors. These are discussed in the sub-sections below.

6.5.2.1 Experimental errors

These constitute the main source of inaccuracy because the computed power flow depends directly on measured quantities. The flux density waveforms were recorded on a UVR to reduce the noise from the instrumentation circuit, but measurement of the ordinates was impaired by the thickness of the galvanometer traces (0.4 to 0.6 mm), being comparable with the signal magnitude at some points. This was especially true for the ΔB_r waveforms. Although maximum precautions were taken, it was found impossible to eliminate the problem of noise, pick-up and drift from the amplifiers, and the recordings had to be 'smoothed' to read the data. The drift from the integrator made it necessary to obtain the B_θ waveforms in the non-magnetic regions by an indirect method (the field theory approach) which required the measurement and analysis of ΔB_r waveforms containing very sharp peaks.

The large error in the low-excitation range results mainly from the inaccuracy in the measurement of torque on the

transducer meter. As seen from the calibration curve (Fig. 2.5, page 44) the minimum torque value for which the instrument could be calibrated satisfactorily was about 0.02 Nm and it is reasonable to assume that for very low values of torque the output from the strain gauges was too small to give a reliable deflection.

Another major uncertainty was the location of the "effective" contour of the active sides of the full pitch coils when measuring the difference output ($\triangle B_r$ waveforms). The effective distance between the two coil-sides (of two search coils on the same side of the annulus) is not necessarily the mechanical mean distance between the axes of the conductors, but may vary considerably as the width becomes comparable with the conductor diameter. This feature is illustrated in Fig. 6.10 where a graph of the ratio of effective to physical area of a narrow search coil is plotted against the ratio of mechanical distance between the conductor axes to its diameter. The graph was obtained experimentally. Although a suitable multiplying factor was considered, using the curve, to arrive at the effective width of

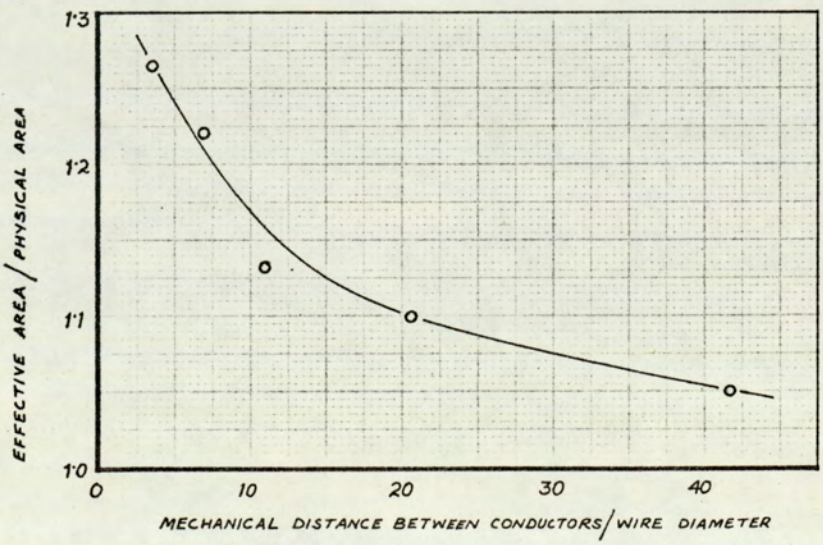

Fig. 6.10

search coils on the rotor, an error in the value of this factor because of uncertainty in the mechanical dimensions, could result in serious error in the calculations. Hence physical dimensions were used throughout.

6.5.2.2 Theoretical limitations

The basic theoretical limitation of the method is the two-dimensional treatment of the problem for a machine having a short axial length compared to the diameter. Thus, the two end surfaces of the rotor annulus have not been considered in obtaining the nett power flow in the rotor. While this may be justified to some extent by the thinness of the rotor so that the total end surface area is only 5% of either of the side surfaces, there might still be some flow of power taking place through these surfaces and might affect the results. This appears all the more possible at higher excitations when experimental evidence suggests changes in flux distribution in the axial directions (Fig. A3.8, Appendix III). Although the 'end effects' tend to minimise the errors of an assumed two-dimensional analysis, the relative effect in the sense of power flow from the end surfaces may be predominant.

The nett power flow is obtained by measuring total power flow separately on the two surfaces and then taking the difference of the two values. Theoretically, a more accurate method would be to apply direct subtraction during the measurement of flux density components using search coils. However, this is not possible in practice as the low signal strengths are seriously affected by noise and drift from the amplifiers. Also,

measurements at two radii are necessary to obtain B_θ in either region and require the schemes discussed.in Chapter III.

An alternative theoretical approach to overcome the drawbacks of two-dimensional analysis is to use a single surface in either region, extending sufficiently beyond the axial length. This would require dubious assumptions about the fall-off of the magnetic field in the axial direction, away from the rotor edges. With a rotor of poor permeability this fall-off is not sharp enough to justify the approach in the present case.

APPENDICES

APPENDIX I

VICALLOY AND ITS USE IN THE EXPERIMENTAL MACHINE

Vicalloy is a permanent magnet material comprised chiefly of Cobalt, Iron and Vanadium. Its development in commercially usable form is due to Nesbitt[62] who had the original patent in 1946. Although much research work has been carried out since then[63,64,65], the metallurgy of Vicalloy is still not fully understood.

This alloy was found to be particularly suitable for use in the experimental machine owing to advantages such as availability in strip form, ease of machining and drilling prior to heat treatment, and high resistivity.

A1.1 Heat Treatment of the Rotor Annulus

The magnetic and electrical properties of Vicalloy are dependent on the heat treatment it finally undergoes[66]. Both time and temperature are critical factors.

To heat-treat the rotor annulus an electric furnace, soaked for several hours at $600^{\circ}C \pm 2^{\circ}C$ (ambient temperature $17^{\circ}C$), was used. The ageing time was about $2\frac{1}{2}$ hours and the annulus, held in a clamp, was then allowed to cool down to room temperature in air. Quenching at high temperature (as recommended in the literature[67]) was found to be un-necessary and the above treatment resulted in good magnetic properties.

A1.2 Magnetic Measurements

Magnetic measurements on the rotor annulus were essential to ascertain that the heat treatment carried out was satisfactory. However, such measurements are usually difficult to make on permanent magnet materials because of the requirement of high magnetising field, and low relative permeability of the material. Moreover, in the present case, it was desired to relate measured magnetic properties to the excitation obtainable in the machine during operation. The results in terms of the machine excitation current could then be used to make an assessment of torque equivalent to pure alternating hysteresis loss.

These requirements called for a rather unusual scheme of magnetic measurements, to be made with the finished rotor aligned in the machine. While there was no difficulty in measuring peripheral flux density in the rotor, it was necessary to be able to measure the magnetising force to obtain the B-H curve. This was achieved by using a special technique.

A1.2.1 Scheme for the measurement of B - H curve

It was mentioned in Chapter II that an axial slot, measuring 10 mm x 5 mm, was cut in the rotor arbor, the width of the slot being symmetrical about a centre line for two small holes (dia 0.25 mm) in the rotor. These holes were used to wind a five - turn search coil using No. 49 SWG (O D: 0.0375 mm) enamelled copper wire.

As shown in Fig. A1.1 (next page), the diametrical plane of the rotor, on which the above coil lies, was aligned with the interpolar axis of the field system, the latter being secured

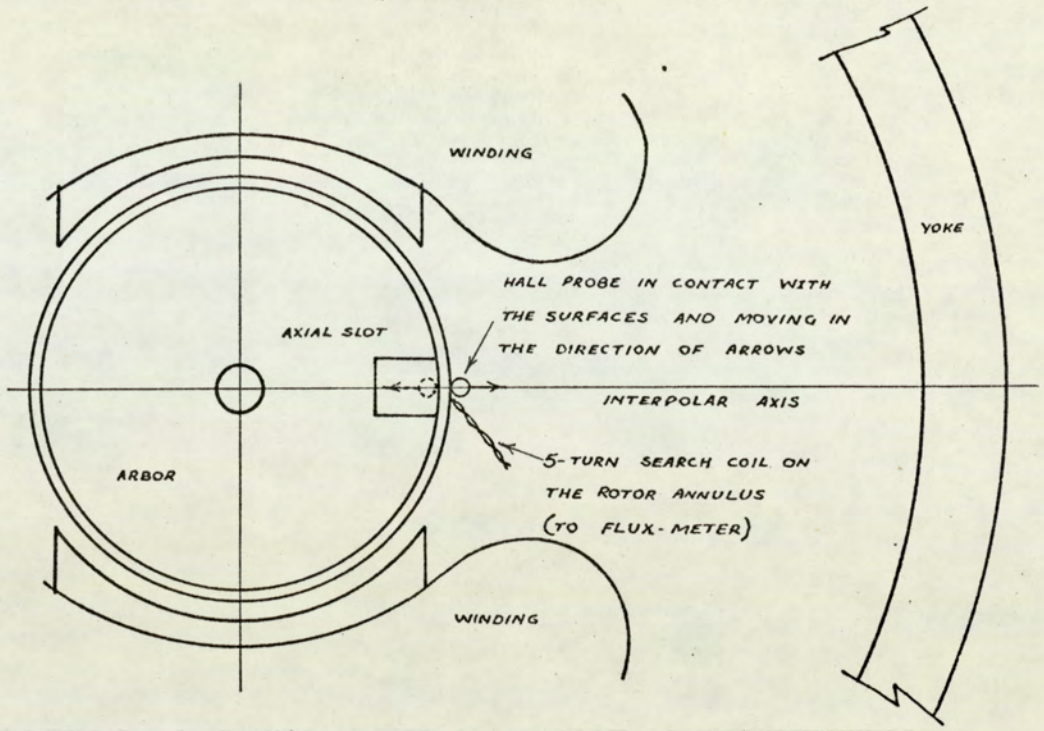

Fig. A1.1

in this position. The output from the search coil, connected to a flux meter, measured flux density in the rotor corresponding to any excitation.

The measurement of magnetising field IN the rotor was based on the assumption that the peripheral component of this field in the vicinity of the rotor surface, both internal and external, was measurable and could be extrapolated to give the value in the rotor. This assumption was suggested by the fact that the rotor was sufficiently thin compared to other dimensions of the machine. There was no spatial hysteresis effect due to rotor as both the field system as well as the rotor were held stationary during the tests.

A suitably prepared Hall-probe assembly, placed parallel to the axis of the machine and capable of adjustment, was used and measurement of the peripheral magnetising field was made at a

series of points on both sides of the rotor from as ~~far~~ near to the surface as possible to a distant point (see Fig. A1.1).

Measurements were made at different excitation currents which therefore was the common parameter. The variations of the fields on the inside and outside of the rotor are shown in Fig. A1.2 and it is clear that extrapolation for the magnetising field within the rotor is justifiable. The experimentally derived relation between the excitation current, I, and the magnetising force, H, in the Vicalloy was noted to be $H = 3.5 \times 10^4 I$ A/m.

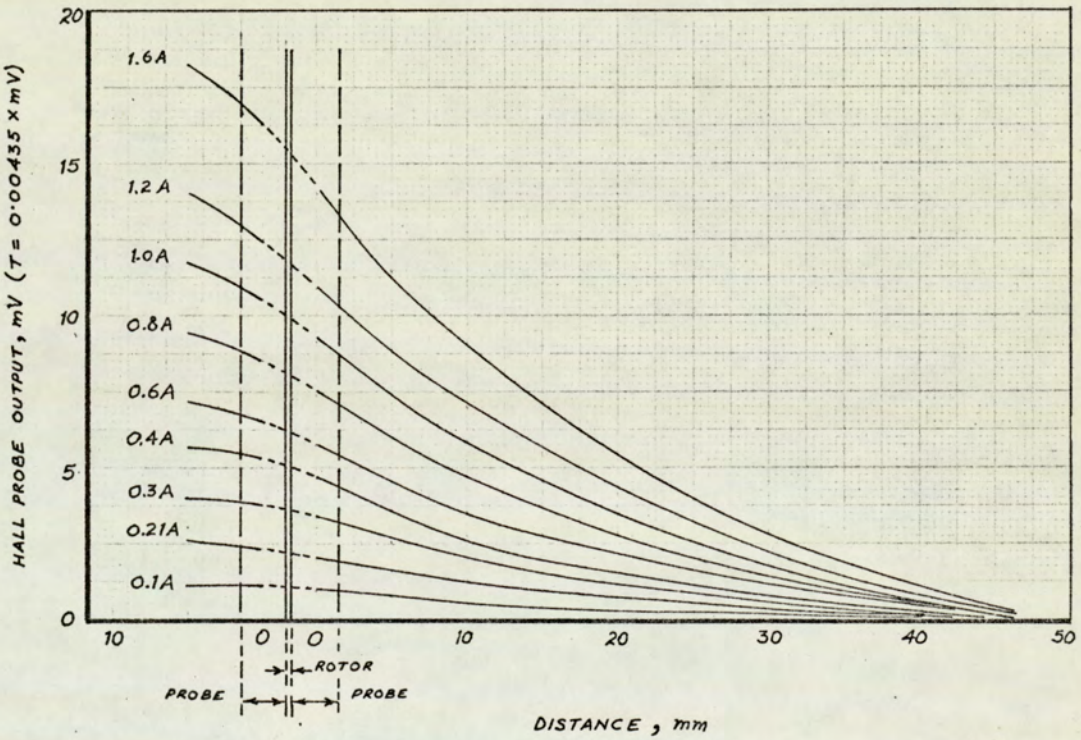

Fig. A1.2

The B - H curve derived from the above sets of measurements is shown in Fig. A1.3 (next page) which is compared with the curve supplied by the manufacturer and one available from previous tests (using a toroid) on a different sample of the alloy. The data is presented in tabular form in Table A1.1.

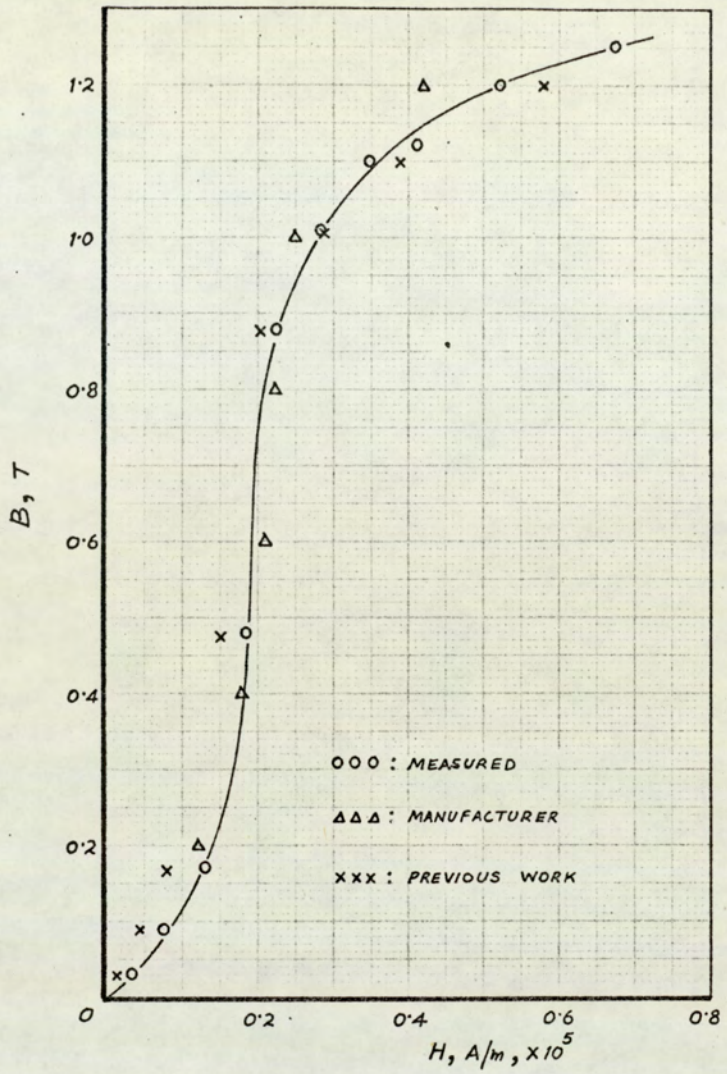

Fig. A1.3

Table A1.1

Excitation A	Extrapolated values of H for the rotor mV	Calculated values of H in the rotor A/m x 10^5	Measured flux in the rotor μWb	Flux density value in the rotor Tesla	Remarks
0.1	1.0	0.0346	0.75	0.03	B - H curve from the manufacturer and previous work : as available. Manufacturer: M/s Telcon Metals Ltd. U K
0.21	2.22	0.0758	2.25	0.09	
0.3	3.78	0.131	4.25	0.17	
0.44	5.38	0.186	12.0	0.48	
0.6	6.5	0.224	22.0	0.88	
0.8	8.18	0.283	25.25	1.01	
1.0	10.05	0.348	27.5	1.1	
1.2	11.9	0.412	28.0	1.12	
1.6	15.15	0.523	30.0	1.2	
2.0	19.5	0.675	31.25	1.25	

A1.3 Measurements for B - H Loops

The technique described above was extended to obtain B - H loops for Vicalloy at various excitations. Like any other permanent magnet material, the B - H curve for Vicalloy has a typical shape and this proved an asset in plotting the loops. Eight experimental points were determined for the different maximum values of the excitation and the B - H loops are shown in Fig. A1.4. The details are tabulated in Table A1.2.

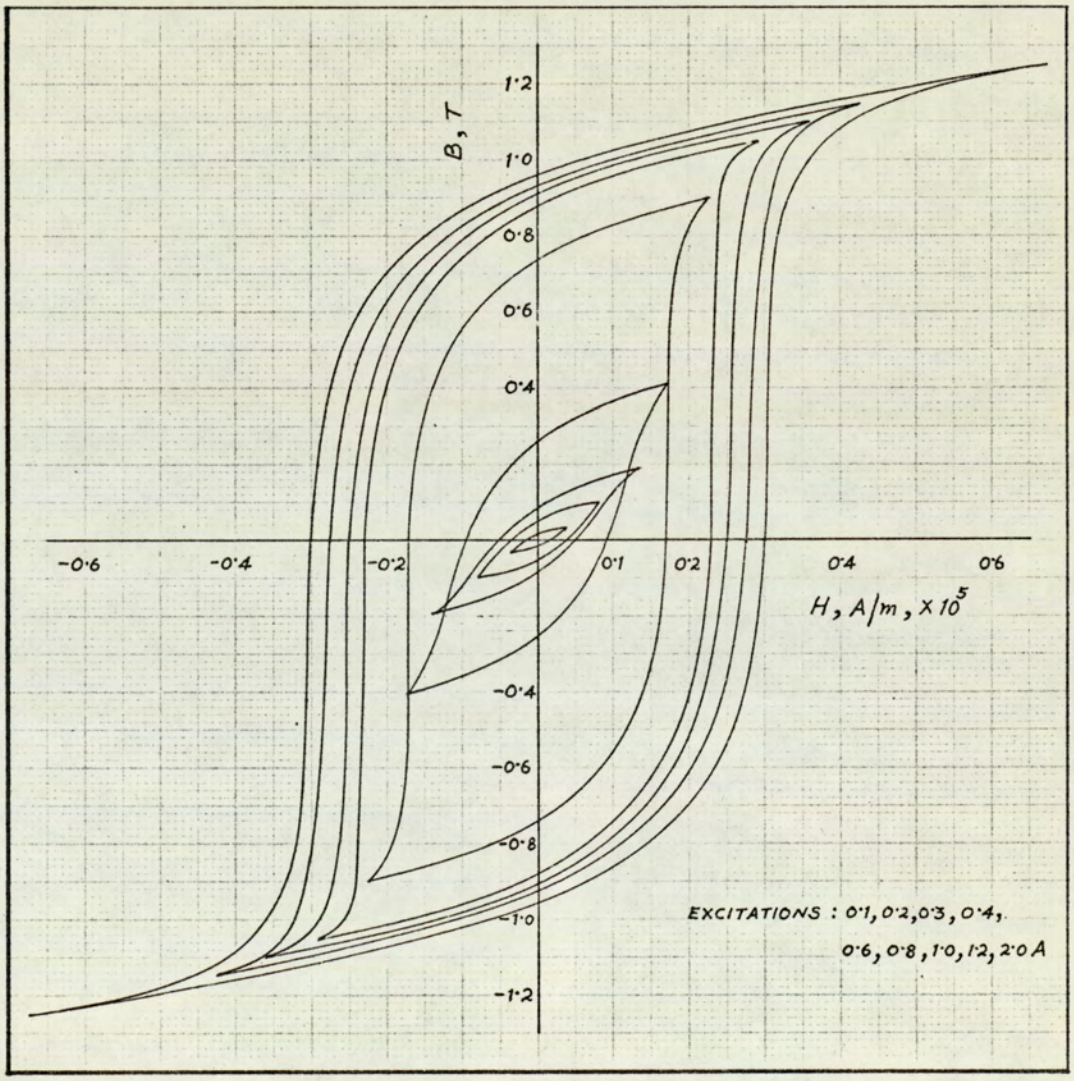

Fig. A1.4

Table A1.2

Fig. A1.4 a

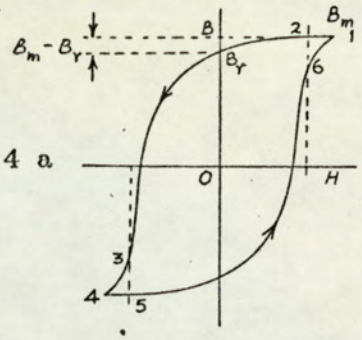

Excitation A	Details of the 'Steps', (Ref: Fig. A1.4a)												Maximum - residual flux density, $B_m - B_{res.}$ (obtained separately) Tesla
	Point 1		Step 1 - 2		Step 2 - 3		Step 3 - 4		Step 4 - 5		Step 5 - 6		
	H_m A/m x 10^5	B_m Tesla	ΔH_1 A/m x 10^5	ΔB_1 Tesla	ΔH_2 A/m x 10^5	ΔB_2 Tesla	ΔH_3 A/m x 10^5	ΔB_3 Tesla	ΔH_4 A/m x 10^5	ΔB_4 Tesla	ΔH_5 A/m x 10^5	ΔB_5 Tesla	
0.1	0.035	0.03	0.01	0.0	0.05	0.04	0.01	0.0	0.01	0.0	0.05	0.06	
0.2	0.079	0.1	0.022	0.0	0.114	0.12	0.022	0.02	0.022	0.0	0.114	0.12	0.05
0.3	0.134	0.19	0.037	0.02	0.194	0.22	0.037	0.06	0.037	0.02	0.194	0.22	0.1
0.4	0.176	0.41	0.039	0.02	0.274	0.5	0.039	0.3	0.039	0.02	0.274	0.44	0.14
0.6	0.226	0.9	0.043	0.02	0.366	1.5	0.043	0.26	0.043	0.0	0.366	1.5	0.14
0.8	0.288	1.05	0.06	0.02	0.456	1.9	0.06	0.14	0.06	0.02	0.456	1.9	0.16
1.0	0.352	1.1	0.075	0.04	0.554	2.1	0.075	0.1	0.075	0.0	0.554	2.1	0.18
1.2	0.425	1.15	0.094	0.04	0.662	2.2	0.094	0.04	0.094	0.04	0.662	2.2	0.2
1.6	0.545	1.2	0.11	0.06	0.87	2.3	0.11	0.06	0.11	0.02	0.87	2.3	0.26
2.0	0.675	1.25	0.15	0.06	1.05	2.4	0.15	0.04	0.15	0.0	1.05	2.4	0.28

An alternating hysteresis loss curve was derived from the hysteresis loops by measuring the area of each curve. This is shown in Fig. A1.5 (next page) plotted against the maximum flux density in the rotor. The upper portion of the curve, shown dotted, is the approximation for the loss reaching a final steady value corresponding to intense saturation in Vicalloy : as the m.m.f. is increased, the maximum flux density still increases[66], but there is little increase in hysteresis loss.

A1.4 Torque - Excitation Curve

As discussed in Chapter II, a thin rotor was used to ensure a uniform peripheral flux density distribution. Reference

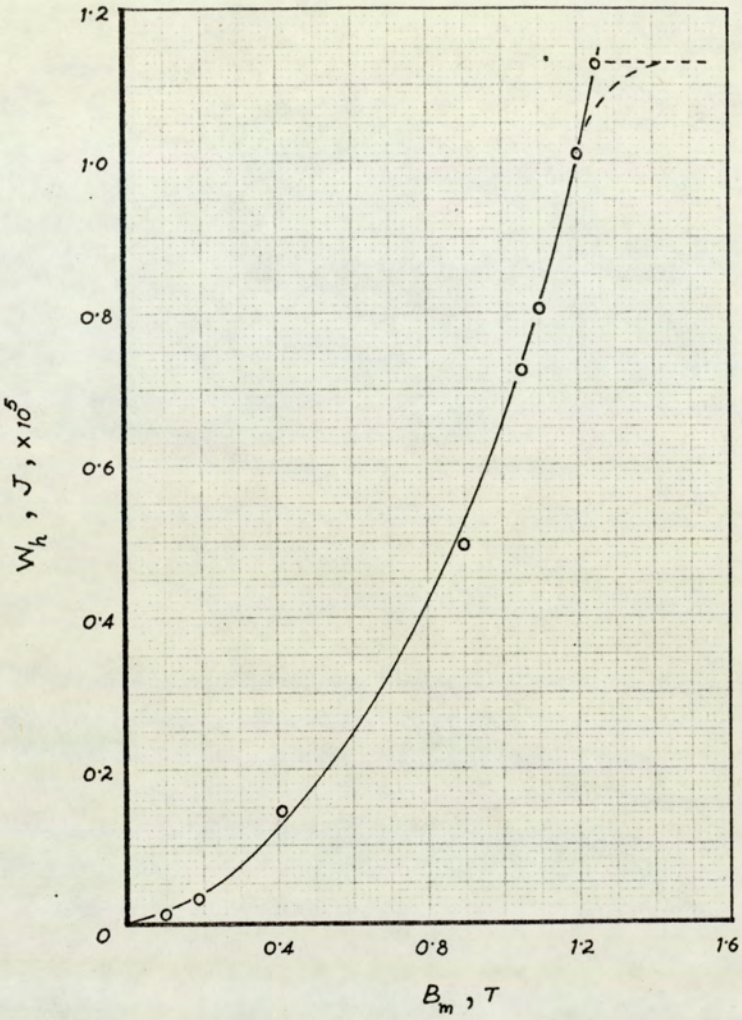

Fig. A1.5

to oscillograms 15 and 16, Chapter III, shows that such a distribution could be assumed upto an excitation of 0.4 A (or more specifically in the range 0.15 A - 0.4 A), but beyond this there are irregularities near the pole tips (oscillograms of Fig. 3.10, Appendix VII).

The ordinates of these waveforms in the interpolar region were a measure of the mean flux density in Vicalloy at a given excitation and, under an assumption of a square-wave variation, the corresponding value of maximum flux density could be calculated.

The torque-excitation curve based on the alternating hysteresis loss at maximum flux density values calculated as described above is given in Fig. A1.6, together with the measured curve (data listed in Table A1.3).

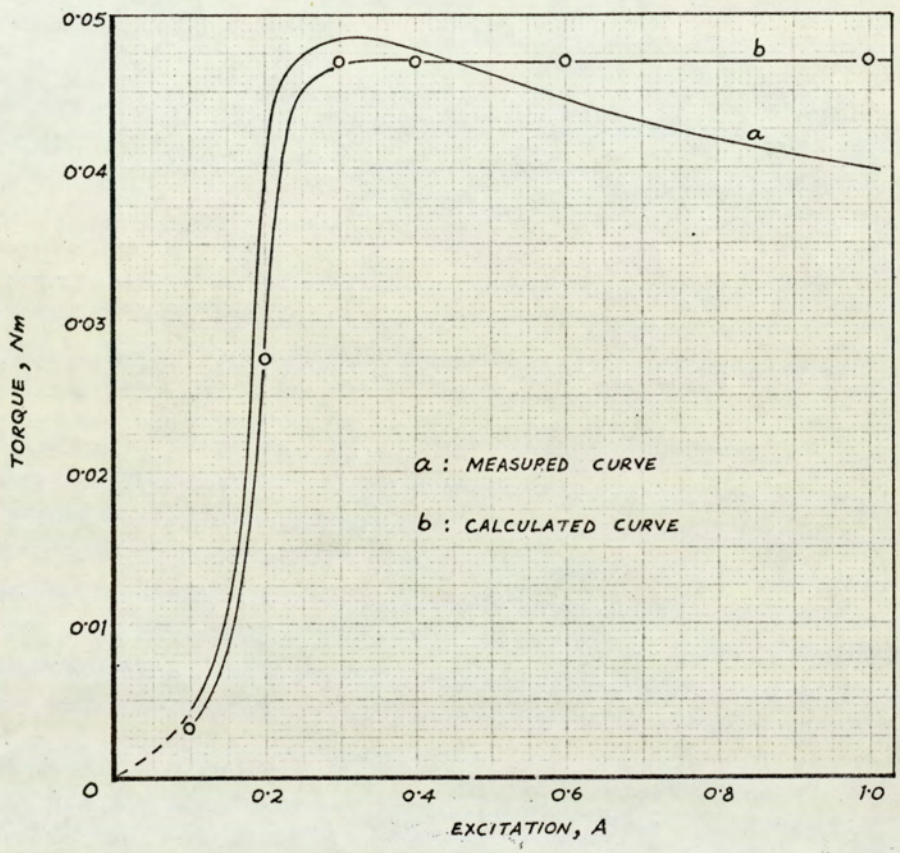

Fig. A1.6

Table A1.3

Excitation A	Time integrated mean B in the rotor on interpolar axis Tesla	Maximum flux density value, B_m Tesla	Alternating hysteresis loss corresponding to B_m $J/m^3/cycle \times 10^5$	Torque equivalent to alternating hysteresis loss Nm	Measured developed torque in the machine Nm
0.1	0.055	0.07	0.075	0.0031	0.004
0.15					0.012
0.2	0.79	1.01	0.67	0.0275	0.04
0.25					0.048
0.3	1.02	1.3	1.137	0.047	0.048
0.4	1.09	1.39	1.137	0.047	0.048
0.6	1.12	1.43	1.137	0.047	0.044
1.0	1.14	1.45	1.137	0.047	0.04

Although the measured torque is seen to be greater than the calculated values, the two curves follow the same pattern and are very similar upto an excitation of 0.4 A. The maximum torque values at 0.3 A agree within 2%. While the calculated torque is constant beyond this excitation, the measured curve shows reduction in torque. It can be concluded that :

(a) in the idealized machine a uniform peripheral flux density distribution for low excitations (< 0.4 A) supports Steinmetz's theory,

(b) the upper bend in the torque-excitation curve, occurring at 0.3 A, corresponds with the sudden change in shape of the alternating-hysteresis loss curve and the intense saturation in the B-H curve. These need not occur at the same values of excitation current.

APPENDIX II

DIGITAL COMPUTER PROGRAMME FOR THE CALCULATION OF FLUX DENSITY AND POWER FLOW

A2.1 Characteristic Features

The programme can be divided into two main parts. The first part, written in the form of a PROCEDURE deals with the harmonic analysis of the measured waveforms; the second part is the main programme for the calculation of flux density and power flow.

The object of using an elaborate method for harmonic analysis of peaky waveforms has been discussed in Chapter III. With the usual methods, based for example on calculus of variation, the resolution of such waveforms into higher order harmonics would require a large number of equally spaced ordinates and even then the results may be erroneous. Moreover, the waveforms are relatively 'flat' and smoothly varying under the poles and in the interpolar region, and the measurement of a large number of ordinates is time consuming.

A2.1.1 The 'procedure'

These drawbacks are avoided in the present method by 'integrating by parts' portions of the waveform to evaluate Fourier coefficients for each harmonic. Commencing at the

beginning of the waveforms under the pole-centre (or the interpolar axis), each portion could be described by three successive points, joined to provide either a 'linear' or 'quadratic' variation or 'fit', the latter being more elaborate to make up for smooth variation of the waveform. Either fit would depend on the relative location of the three points. The mathematical checks for these are included in 'Programme' POLYFIT (see Flow diagram on page 188), to 'decide' the type of the fit. These three-point fits could cover the whole waveform and when analysed give the necessary coefficients for the sine and cosine terms.

Advantages which distinguish this procedure from other methods of harmonic analysis are :

(a) Discrete, unequal intervals can be chosen depending on the variation in the waveforms; closer intervals near the peaks and wider ones elsewhere.

(b) Coefficients for any particular order harmonic can be obtained.

(c) The accuracy of the analysis can be improved by a sufficient number of ordinates and also by making any particular portion follow an appropriate fit.

A2.2 The Complete Programme

The complete programme is given on pages 191 to 194, with the key flow diagrams on pages 187 to 190 (see also the 'Computerisation' details in Section A5.1.1, Appendix V).

PROCEDURE POLYFIT

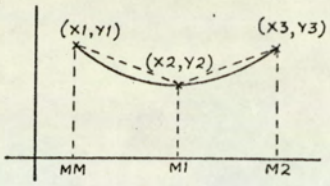

A SECTION OF THE CURVE DESCRIBED BY THREE POINTS

PROCEDURE FIT 1

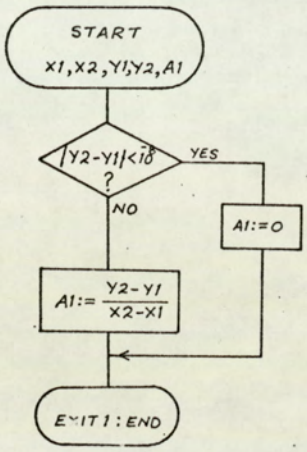

PROCEDURE FIT 2

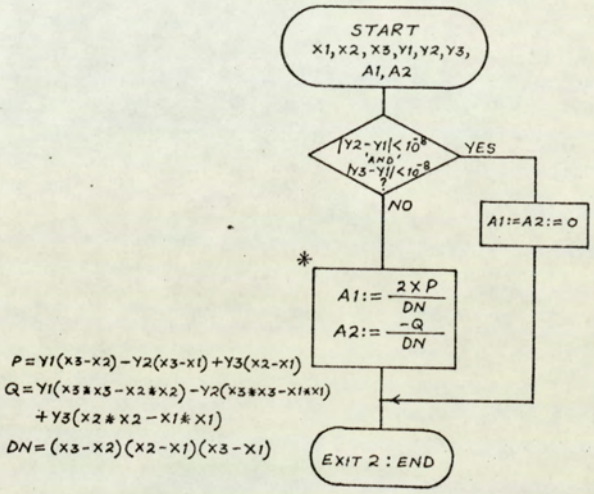

PROCEDURE WRITE

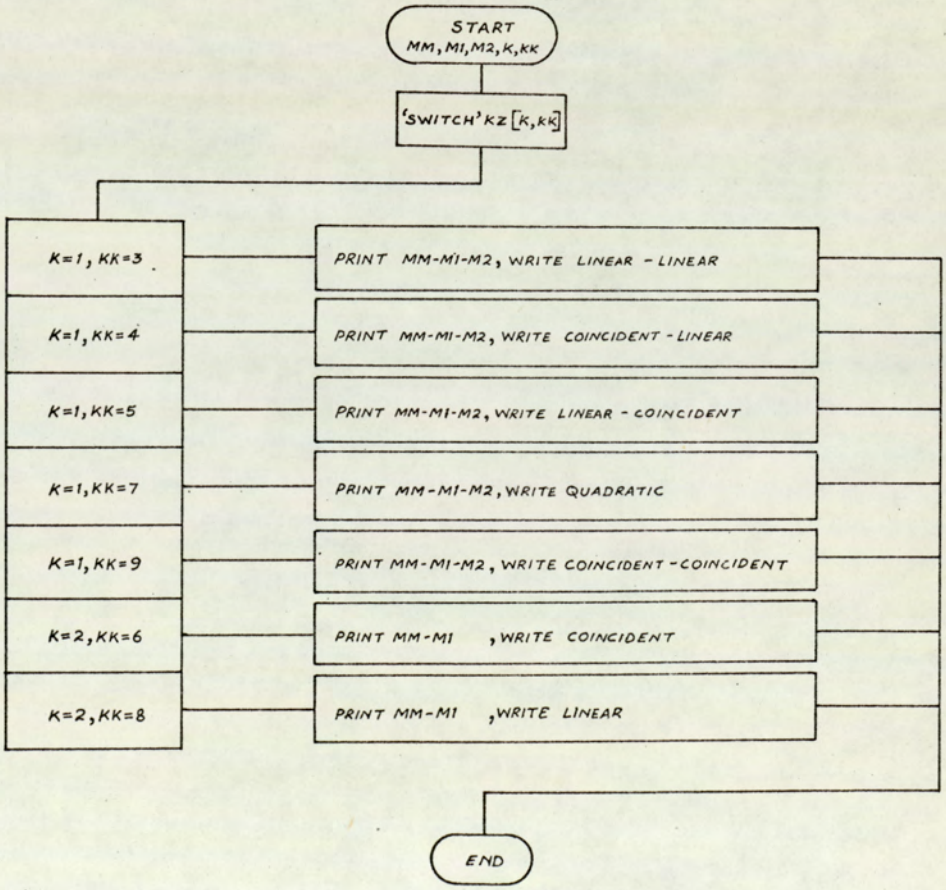

'PROGRAMME' POLYFIT

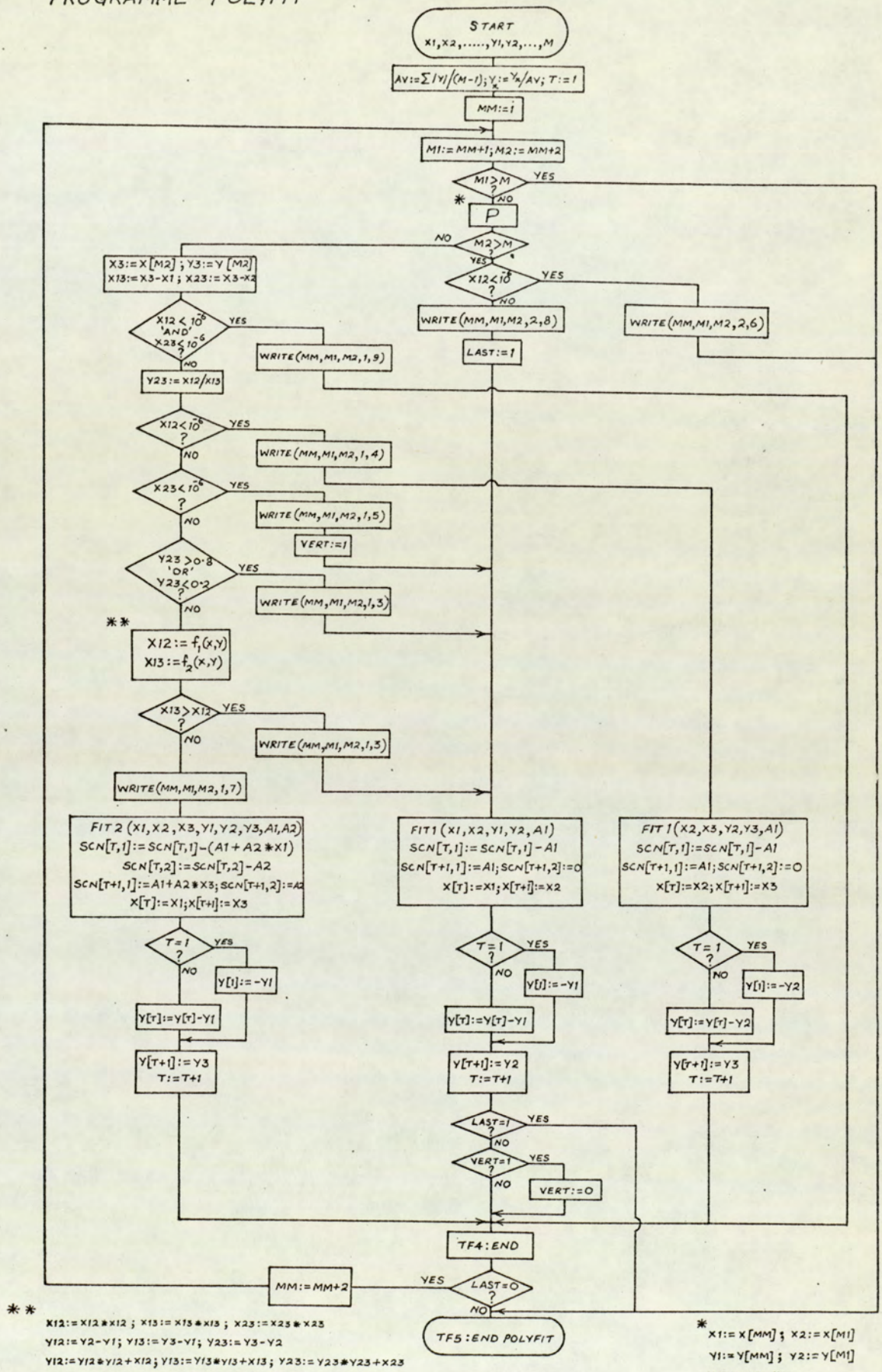

** X12:=X12*X12 ; X13:=X13*X13 ; X23:=X23*X23
Y12:=Y2-Y1; Y13:=Y3-Y1; Y23:=Y3-Y2
Y12:=Y12*Y12+X12; Y13:=Y13*Y13+X13; Y23:=Y23*Y23+X23
X12:=Y13-Y12-Y23; X12:=X12*X12; X13:=2·25*Y12*Y23

* X1:=X[MM]; X2:=X[M1]
Y1:=Y[MM]; Y2:=Y[M1]
X12:=X2-X1

PROCEDURE COEFSUM

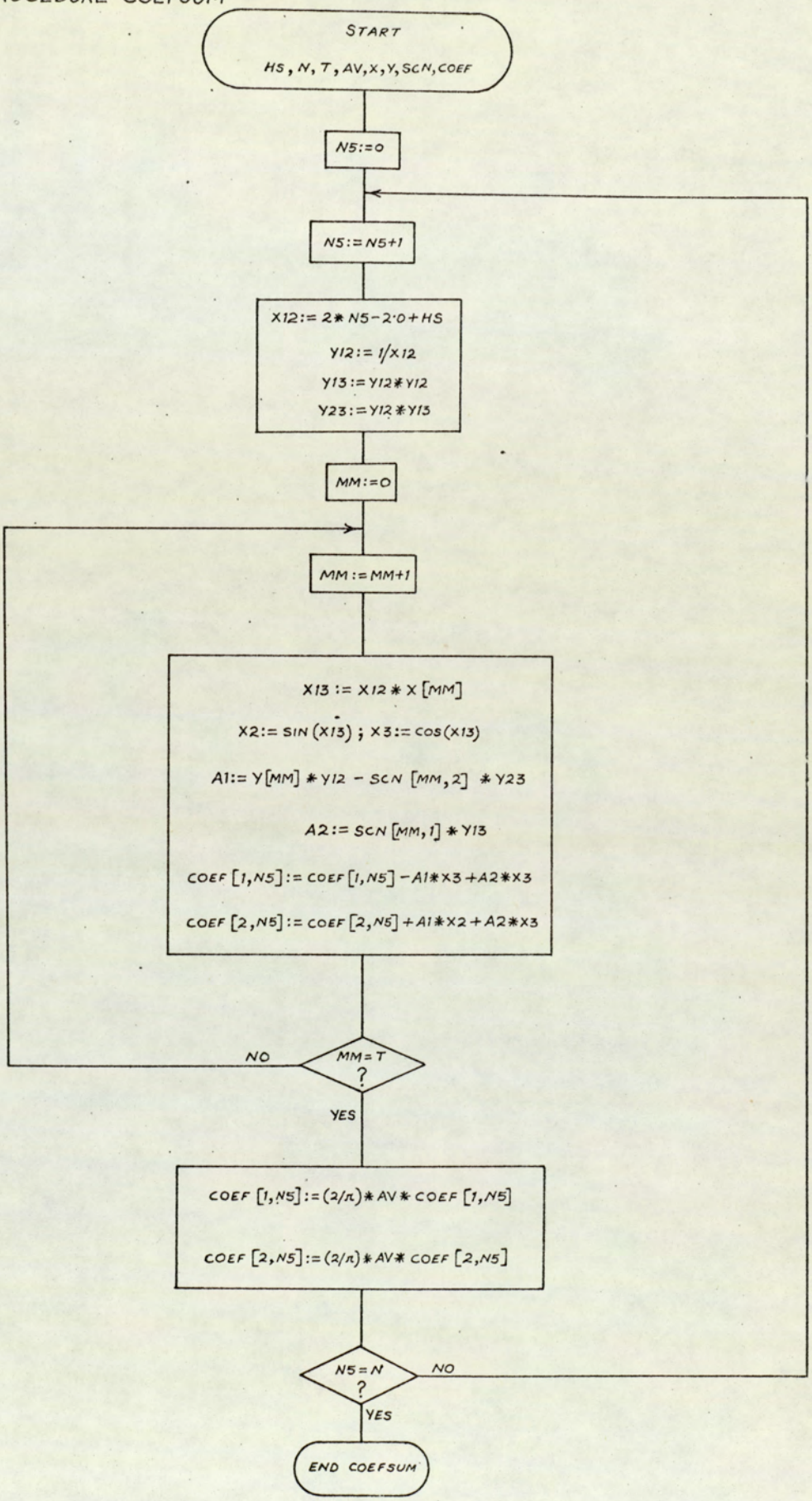

MAIN PROGRAMME

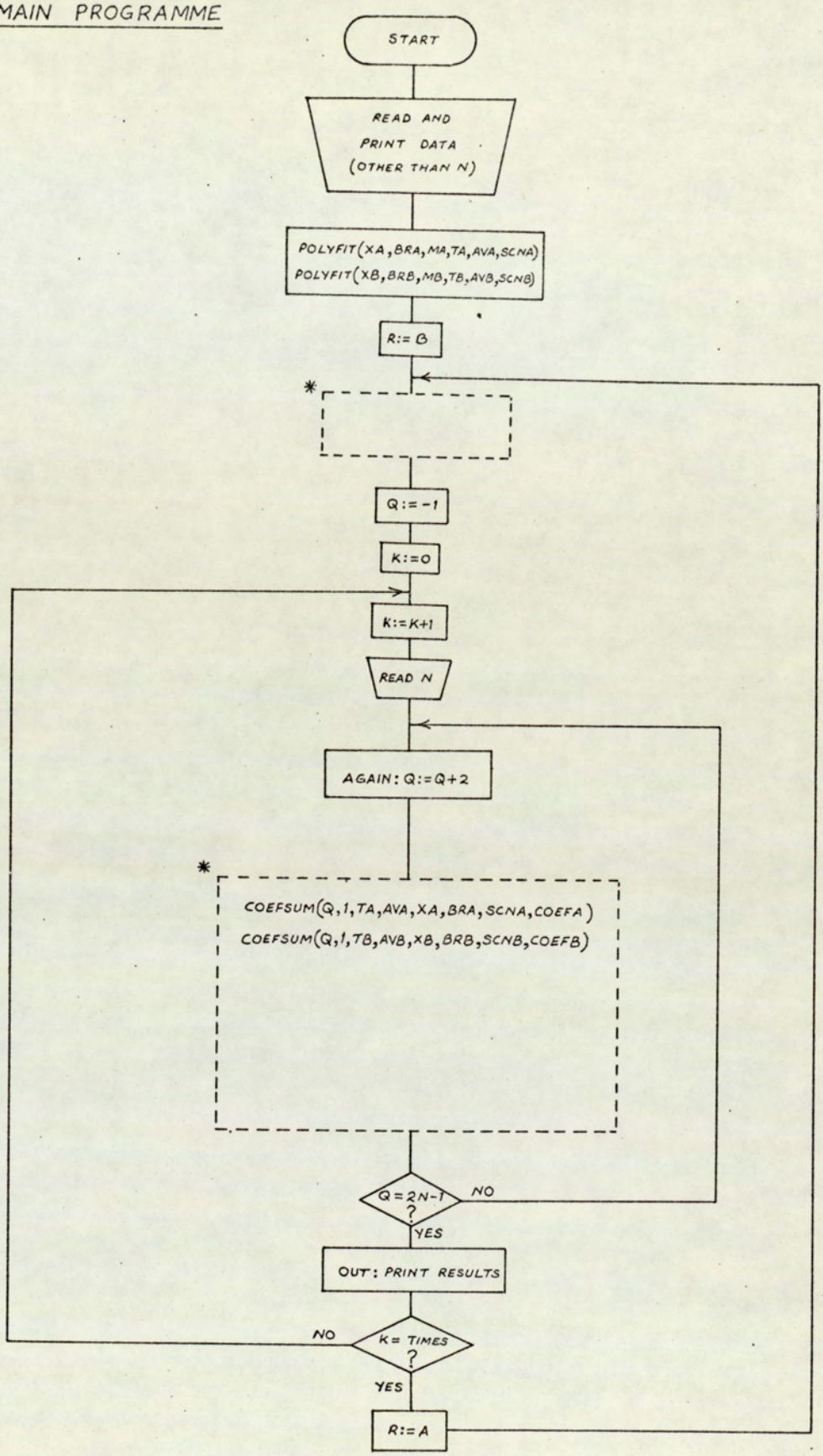

* DOTTED RECTANGULAR BLOCKS CONTAIN STEPS FOR THE CALCULATION OF FLUX DENSITY AND POWER FLOW IN ACCORDANCE WITH THE ANALYSIS IN APPENDIX V

```
'BEGIN' 'COMMENT' BHARGAVA EEPSF088 TRIGFIT HARMONIC ANALYSIS (ODD HARMONICS ONLY);    HAR 0000
'PROCEDURE' POLAR(X,Y,R,PHI);                                                         POL  100
'VALUE' X,Y; 'REAL' X,Y,R,PHI;                                                        POL  200
'BEGIN' R:= SQRT(X*X + Y*Y);                                                          POL  300
        PHI:='IF' X=0 'THEN' 90*SIGN(Y) 'ELSE' 57.295779513*ARCTAN(Y/X) +             POL  400
        ('IF' X 'GE' 0 'THEN' 0 'ELSE' 'IF' Y 'GE' 0 'THEN' 180 'ELSE' -180);         POL  500
  'END' POLAR ;                                                                       POL  600
'PROCEDURE' POLYFIT(X,Y,M,T,AV,SCN);                                                  PFT  100
'VALUE' M; 'REAL' AV; 'INTEGER' M,T;  'ARRAY' X,Y,SCN;                                PFT  200
'BEGIN' 'REAL' A1,A2,X1,X2,X3,X12,X13,X23,Y1,Y2,Y3,Y12,Y13,Y23;                       PFT  300
        'INTEGER' M1,M2,MM,N5,N6,NN,P,LAST,VERT;                                      PFT  400
        'PROCEDURE' FIT1(X1,X2,Y1,Y2,A1);                                             PFT  500
        'VALUE' X1,X2,Y1,Y2;  'REAL' X1,X2,Y1,Y2,A1;                                  PFT  600
        'BEGIN' 'IF' ABS(Y2-Y1)< 1.0 & -8 'THEN'                                      PFT  700
                'BEGIN' A1:=0; 'GOTO' EXIT1; 'END';                                   PFT  800
                A1:= (Y2-Y1)/(X2-X1);                                                 PFT  900
          EXIT1 : 'END';                                                              PFT 1000
        'PROCEDURE' FIT2(X1,X2,X3,Y1,Y2,Y3,A1,A2);                                    PFT 1100
        'VALUE' X1,X2,X3,Y1,Y2,Y3;  'REAL' X1,X2,X3,Y1,Y2,Y3,A1,A2;                   PFT 1200
        'BEGIN' 'REAL' N1,N2,N3,DN,Z1,Z2,Z3;                                          PFT 1300
                'IF' ABS(Y2-Y1)< 1.0 & -8 'AND' ABS(Y3-Y1)< 1.0 & -8 'THEN'           PFT 1400
                'BEGIN' A1:=A2:=0; 'GOTO' EXIT2; 'END';                               PFT 1500
                N1:=X1+X2; N2:=X1+X3; N3:=X2+X3; Z2:=X2-X1; Z3:=X3-X1;                PFT 1600
                Z1:=X3-X2; DN:=1/(Z1*Z2*Z3); Z1:=Z1*Y1; A2:=Z3*Y2;                    PFT 1700
                Z3:=Z2*Y3; Z2:=A2; A2:=2*(Z1-Z2+Z3)*DN;                               PFT 1800
                Z1:=Z1*N3; Z2:=Z2*N2; Z3:=Z3*N1; A1:=-(Z1-Z2+Z3)*DN;                  PFT 1900
          EXIT2 : 'END';                                                              PFT 2000
        'PROCEDURE' WRITE(MM,M1,M2,K,KK);                                             PFT 2100
        'VALUE' MM,M1,M2,K,KK;  'INTEGER' MM,M1,M2,K,KK;                              PFT 2200
        'BEGIN' 'SWITCH' KZ:= K1,K2,K3,K4,K5,K6,K7,K8,K9,K10;                         PFT 2300
                NEWLINE(1); 'GOTO' KZ[K];                                             PFT 2400
           K1 : PRINT(MM,3,0); WRITETEXT('(' - ')'); PRINT(M1,3,0);                   PFT 2500
                WRITETEXT('(' -')'); PRINT(M2,3,0); 'GOTO' KZ[KK];                    PFT 2600
           K2 : SPACE(4); PRINT(MM,3,0);WRITETEXT('(' -')');                          PFT 2700
                PRINT(M1,3,0); SPACE(3); 'GOTO' KZ[KK];                               PFT 2800
           K3 : WRITETEXT('(''('14S')'LINEAR'('S')'-'('S')'LINEAR')');                PFT 2900
                'GOTO' K10;                                                           PFT 3000
           K4 : WRITETEXT('(''('10S')'COINCIDENT'('S')'-'('S')'                       PFT 3100
                LINEAR')'); 'GOTO' K10;                                               PFT 3200
           K5 : WRITETEXT('(''('14S')'LINEAR'('S')'-'('S')'                           PFT 3300
                COINCIDENT')'); 'GOTO' K10;                                           PFT 3400
           K6 : WRITETEXT('(''('16S')'COINCIDENT')'); 'GOTO' K10;                     PFT 3500
           K7 : WRITETEXT('(''('17S')'QUADRATIC')'); 'GOTO' K10;                      PFT 3600
           K8 : WRITETEXT('(''('18S')'LINEAR')'); 'GOTO' K10;                         PFT 3700
           K9 : WRITETEXT('(''('10S')'COINCIDENT'('S')'-'('S')'                       PFT 3800
                COINCIDENT')');                                                       PFT 3900
          K10 : 'END';                                                                PFT 4000
        AV:=0; 'FOR' MM:= 1 'STEP' 1 'UNTIL' M 'DO' AV:=AV+ABS(Y[MM]);                PFT 4100
        AV:=AV/(M-1); 'FOR' MM:= 1 'STEP' 1 'UNTIL' M 'DO'                            PFT 4200
        Y[MM]:=Y[MM]/AV; T:=1;  SCN[1,1]:=SCN[1,2]:=0;                                PFT 4300
        WRITETEXT('(''('3C15S')'CURVE'('S')'FITTING'('S')'ANALYSIS                    PFT 4400
        '('2C7S')'POINTS'('26S')'TYPE'('1C')'')'); LAST:=VERT:=0;                      PFT 4500
        'FOR' MM:= 1,MM+2 'WHILE' LAST=0 'DO'                                         PFT 4600
```

```
'BEGIN' M1:=MM+1;  M2:=MM+2;  'IF' M1>M 'THEN' 'GOTO' TF5;                                  PFT 4700
        X1:=X[MM]; X2:=X[M1] ; Y1:=Y[MM]; Y2:=Y[M1] ; X12:=X2-X1;                          PFT 4800
        'IF' M2>M 'THEN' 'BEGIN' 'IF' X12<1.0 &-6 'THEN' 'BEGIN'                           PFT 4900
        WRITE(MM,M1,M2,2,6); 'GOTO' TF5; 'END'; WRITE(MM,M1,M2,2,8);                       PFT 5000
        LAST:=1; 'GOTO' TF1; 'END'; X3:=X[M2]; Y3:= Y[M2]; X13:=X3-X1;                     PFT 5100
        X23:=X3-X2; 'IF' X12<1.0 &-6 'AND' X23<1.0 &-6 'THEN'                              PFT 5200
        'BEGIN' WRITE(MM,M1,M2,1,9); 'GOTO' TF4; 'END';                                    PFT 5300
        Y23:=X12/X13; 'IF' X12<1.0 &-6 'THEN' 'BEGIN' WRITE(MM,M1,M2,1,4);                 PFT 5400
        'GOTO' TF2; 'END'; 'IF' X23<1.0 &-6 'THEN' 'BEGIN' WRITE(MM,M1,M2,1,5)             PFT 5500
        ; VERT:=1; 'GOTO' TF1; 'END'; 'IF' Y23>0.8 'OR' Y23<0.2 'THEN'                      PFT 5600
        'BEGIN' WRITE(MM,M1,M2,1,3);  'GOTO' TF1; 'END'; X12:=X12*X12;                     PFT 5700
        X13:=X13*X13; X23:=X23*X23; Y12:=Y2-Y1; Y13:=Y3-Y1; Y23:=Y3-Y2;                    PFT 5800
        Y12:=Y12*Y12+X12; Y13:=Y13*Y13+X13; Y23:=Y23*Y23+X23;                              PFT 5900
        X12:=Y13-Y12-Y23; X12:=X12*X12; X13:=2.25*Y12*Y23;                                 PFT 6000
        'IF' X13>X12 'THEN' 'BEGIN' WRITE(MM,M1,M2,1,3); 'GOTO' TF1; 'END'                 PFT 6100
        'ELSE' 'BEGIN' WRITE(MM,M1,M2,1,7); 'GOTO' TF3; 'END';                             PFT 6200
  TF1 : FIT1(X1,X2,Y1,Y2,A1); SCN[T,1]:=SCN[T,1]-A1;                                       PFT 6300
        SCN[T+1,2]:=0; SCN[T+1,1]:=A1; X[T]:=X1; X[T+1]:=X2;                               PFT 6400
        'IF' T=1 'THEN' Y[1]:= -Y1; 'ELSE' Y[T]:=Y[T]-Y1; Y[T+1]:=Y2; T:=T+1;             PFT 6500
        'IF' LAST = 1 'THEN' 'GOTO' TF5; 'IF' VERT = 1 'THEN' 'BEGIN'                      PFT 6600
        VERT:=0; 'GOTO' TF4; 'END';                                                        PFT 6700
  TF2 : FIT1(X2,X3,Y2,Y3,A1); SCN[T,1]:=SCN[T,1]-A1;                                       PFT 6800
        SCN[T+1,2]:=0; SCN[T+1,1]:=A1; X[T]:=X2; X[T+1]:=X3;                               PFT 6900
        'IF' T=1; 'THEN' Y[1]:= -Y2; 'ELSE' Y[T]:=Y[T]-Y2; Y[T+1]:=Y3;                    PFT 7000
        T:=T+1;  'GOTO' TF4;                                                               PFT 7100
  TF3 : FIT2(X1,X2,X3,Y1,Y2,Y3,A1,A2); SCN[T,1]:=SCN[T,1]-(A1+A2*X1);                      PFT 7200
        SCN[T+1,1]:=A1+A2*X3; SCN[T,2]:=SCN[T,2]- A2; SCN[T+1,2]:=A2;                      PFT 7300
        X[T]:=X1; X[T+1]:=X3; 'IF' T=1 'THEN' Y[1]:= -Y1 'ELSE' Y[T]:=Y[T]-Y1;             PFT 7400
        Y[T+1]:=Y3; T:=T+1;                                                                PFT 7500
  TF4 : 'END';                                                                             PFT 7600
TF5 : 'END' POLYFIT ;                                                                      PFT 7700
'PROCEDURE' COEFSUM(HS,N,T,AV,X,Y,SCN,COEF);                                               CFS  100
'VALUE' HS,N,T,AV; 'REAL' AV; 'INTEGER' HS,N,T; 'ARRAY' X,Y,SCN,COEF;                      CFS  200
'BEGIN' 'REAL' A1,A2,X2,X3,X12,X13,Y12,Y13,Y23;  'INTEGER' MM,N5;                          CFS  300
        'FOR' N5:= 1 'STEP' 1 'UNTIL' N 'DO'                                               CFS  400
        'BEGIN' X12:=2*N5-2.0+HS; Y12:=1/X12; Y13:=Y12*Y12; Y23:=Y12*Y13;                  CFS  500
        COEF[1,N5]:=COEF[2,N5]:=0;                                                         CFS  600
        'FOR' MM:= 1 'STEP' 1 'UNTIL' T 'DO' 'BEGIN'  X13:=X12*X[MM];                      CFS  700
        X2:=SIN(X13); X3:=COS(X13); A1:=Y[MM]*Y12 - SCN[MM,2]*Y23;                         CFS  800
        A2:=SCN[MM,1]*Y13; COEF[1,N5]:=COEF[1,N5]- A1*X3+A2*X2;                            CFS  900
        COEF[2,N5]:=COEF[2,N5] + A1*X2+A2*X3;  'END';                                      CFS 1000
              COEF[1,N5]:= 0.6366199724*AV*COEF[1,N5];                                     CFS 1100
              COEF[2,N5]:= 0.6366199724*AV*COEF[2,N5];                                     CFS 1200
        'END' ;                                                                            CFS 1300
'END' COEFSUM ;                                                                            CFS 1400
```

```
'COMMENT' PROPER PROGRAMME STARTS HERE ;                                                    HAR 100
'INTEGER' N,P,Q,MA,MB,NA,TA,TB,K, TIMES ;                                                   HAR 200
'REAL' AVA,AVB,A,B,R,B3,B4,B5,B6,RA,RA1,RB,RB1,ML,AC,RI,PN1,PN2,QN1,QN2,PN,QN,             HAR 300
       LMA,LMB,B7,RN,SN,PVI,PI,OM,PHI1,PHI2,MU,MUI,BA,Y,Z,C,PHIP1,PHIP2,T,NR,              HAR 400
       GX1,GX2 ;                                                                            HAR 500
       TIMES:= READ; NA:=READ; NR:=READ; GX1:=READ; GX2:=READ; T:=READ;                     HAR 600
       MA:=READ; MB:=READ; LMA:=READ; LMB:=READ;                                            HAR 700
'COMMENT' T IS TIME IN SECONDS FOR NR REVOLUTIONS OF THE FIELD SYSTEM MEASURED BY           HAR 800
       THE ELECTRONIC TIMER. GX1 AND GX2 ARE GALVANOMETER CONSTANTS (MV/MM) ;               HAR 900
       PI:= 3.14159265359;  LMA:= PI/LMA;  LMB:= PI/LMB;                                    HAR 1000
       OM:= 2.0*PI*(NR/T);  MU:= 4.0*PI*10 ↑(-7);  MUI:= 1/MU;  Y:= 1/(25.4*OM);           HAR 1100
'BEGIN' 'ARRAY' XA,BRA[1:MA], XB,BRB[1:MB], COEFA,COEFB[1:2,1:1],                           HAR 1200
       SCNA[1:MA,1:2], SCNB[1:MB,1:2], AM,AN,BT,CC,CS,BR,BX,PA,PHI,PHIP[1:NA];              HAR 1300
       WRITETEXT('('('2C')' DATA%FROM%RADIAL%FLUX%DENSITY%WAVEFORM%-%THE%FULL%             HAR 1400
       PITCH%COIL'('30S')' GX1%(MV/MM)%= ')'); PRINT(GX1,2,8);                              HAR 1500
            WRITETEXT('('('2C2S')'MA'('16S')'XA'('17S')'BRA'('13S')'                        HAR 1600
            BRA%IN%MV '('2C')'')') ;                                                        HAR 1700
            'FOR' P:= 1 'STEP' 1 'UNTIL' MA 'DO'                                            HAR 1800
            'BEGIN' NEWLINE(1); PRINT(P,3,0); SPACE(10);  XA[P]:=READ;                      HAR 1900
                 PRINT(XA[P],3,2); SPACE(10); BRA[P]:=READ; PRINT(BRA[P],3,2);              HAR 2000
                 SPACE(9); BRA[P]:= BRA[P]* GX1; PRINT(BRA[P],3,4);                         HAR 2100
                 XA[P]:= XA[P]* LMA;                                          'END';        HAR 2200
  PAPERTHROW;                                                                               HAR 2300
       WRITETEXT('('('2C')' DATA%FROM%THE%'DIFFERENCE'%WAVEFORM '('30S')'                   HAR 2400
       GX2%(MV/MM)%= ')') ;  PRINT(GX2,2,8);                                                HAR 2500
            WRITETEXT('('('2C2S')'MB'('16S')'XB'('17S')'BRB'('13S')'                        HAR 2600
            BRB%IN%MV '('2C')'')') ;                                                        HAR 2700
            'FOR' P:= 1 'STEP' 1 'UNTIL' MB 'DO'                                            HAR 2800
            'BEGIN' NEWLINE(1); PRINT(P,3,0); SPACE(10); XB[P]:=READ;                       HAR 2900
                 PRINT(XB[P],3,2); SPACE(10); BRB[P]:=READ; PRINT(BRB[P],3,2);              HAR 3000
                 SPACE(9); BRB[P]:= BRB[P]* GX2; PRINT(BRB[P],3,4);                         HAR 3100
                 XB[P]:= XB[P]* LMB;                                          'END';        HAR 3200
  PAPERTHROW;                                                                               HAR 3300
       POLYFIT(XA,BRA,MA,TA,AVA,SCNA) ;    POLYFIT(XB,BRB,MB,TB,AVB,SCNB) ;                HAR 3400
       A:=READ;  B:=READ;  A:=A*0.0254;  B:=B*0.0254;                                       HAR 3500
       'COMMENT' B IS OUTER ROTOR SURFACE RADIUS . ALL RADII IN INCHES ;                     HAR 3600
       AC:= 0.01745329252 ;                                                                 HAR 3700
       'FOR' P:= 1 'STEP' 1 'UNTIL'  NA 'DO'                                                HAR 3800
       'BEGIN' AM[P]:=READ;  AN[P]:= AC*AM[P];                                  'END';      HAR 3900
 'FOR' R:= B,A 'DO'                                                                         HAR 4000
 'BEGIN'   'FOR' P:= 1 'STEP' 1 'UNTIL' NA 'DO'                                             HAR 4100
       BT[P]:= BR[P]:= BX[P]:= PHI[P]:= PHIP[P]:=0.0;                                       HAR 4200
       B3:= B/A; B4:=B5:=B7:= B3*B3; B6:=B4*B4; BA:= B/A;                                   HAR 4300
       RA:= R/A; RA1:= RA*RA; RB:= B/R; RB1:= RB*RB;                                        HAR 4400
       Q:= -1 ;        PVI:= 0.0 ;                                                          HAR 4500
  'FOR' K:= 1 'STEP' 1 'UNTIL' TIMES 'DO'                                                   HAR 4600
  'BEGIN'  'INTEGER' N ;   N:=READ ;                                                        HAR 4700
    AGAIN : Q:= Q+2 ;                                                                       HAR 4800
       COEFSUM(Q,1,TA,AVA,XA,BRA,SCNA,COEFA) ;                                              HAR 4900
       COEFSUM(Q,1,TB,AVB,XB,BRB,SCNB,COEFB) ;                                              HAR 5000
       COEFB[1,1]:=COEFA[1,1] + COEFB[1,1] ; COEFB[2,1]:=COEFA[2,1] + COEFB[2,1] ;          HAR 5100
       COEFA[1,1]:=COEFA[1,1]/B;    COEFA[2,1]:=COEFA[2,1]/B;                               HAR 5200
       COEFB[1,1]:=COEFB[1,1]/A;    COEFB[2,1]:=COEFB[2,1]/A;                               HAR 5300
```

```
            ML:= 1.0/(B4 - 1);   B4:= B6*B4;   ML:= (A/B) * ML;                    HAR 5400
            PN1:= COEFB[2,1] - B7 * COEFA[2,1] ;                                   HAR 5500
            QN1:= COEFB[1,1] - B7 * COEFA[1,1] ;                                   HAR 5600
            B7:= B5 * B7 ;                                                         HAR 5700
            PN2:= B3 * COEFB[2,1] - BA * COEFA[2,1] ;                              HAR 5800
            QN2:= B3 * COEFB[1,1] - BA * COEFA[1,1] ;                              HAR 5900
            B3:= B5 * B3 ;                                                         HAR 6000
            PN1:= RA * PN1 ; QN1:= RA * QN1 ;    RA:= RA1 * RA ;                   HAR 6100
            PN2:= RB * PN2 ; QN2:= RB * QN2 ;    RB:= RB1 * RB ;                   HAR 6200
            PN:= ML * (PN1 + PN2) ;     QN:= -ML * (QN1 + QN2) ;                   HAR 6300
            RN:=-ML * (PN1 - PN2) ;     SN:= -ML * (QN1 - QN2) ;                   HAR 6400
            PHI1:= PN * (R/Q) ;         PHI2:= QN * (-R/Q) ;                       HAR 6500
            'FOR' P:= 1 'STEP' 1 'UNTIL' NA 'DO'                                   HAR 6600
            'BEGIN'  RI:= Q * AN[P];    CC[P]:= COS(RI) ;   CS[P]:= SIN(RI) ;      HAR 6700
            BT[P]:= BT[P] + PN * CS[P] + QN * CC[P] ;                              HAR 6800
            BR[P]:= BR[P] + RN * CC[P] + SN * CS[P] ;                              HAR 6900
            PHI[P]:= PHI[P] + PHI1 * CC[P] + PHI2 * CS[P] ;                        HAR 7000
            POLAR (BT[P],BR[P],BX[P],PA[P] );                                      HAR 7100
            'END' ;                                                                HAR 7200
            PVI:= PVI + PN * SN + QN * RN ;                                        HAR 7300
            'IF' Q = 2*N - 1 'THEN' 'GOTO' OUT 'ELSE' 'GOTO' AGAIN ;               HAR 7400
        OUT:PAPERTHROW ;                                                           HAR 7500
            WRITETEXT('('''('1C')' RESULTS%FROM%CALCULATION%OF%FLUX%DENSITY%AND%POWER%  HAR 7600
            FLOW%-%FIELD%THEORY%APPROACH '('2C')' THIN%ROTOR '('25S')' SURFACE     HAR 7700
            '('30S')' EXCITATION%=%'('2C')' RADIUS%FOR%CALCULATIONS,R%(M)%= ')') ; HAR 7800
            PRINT(R,2,7); WRITETEXT('('''('2C')'%ANGLE'('6S')' RAD.FLUX%DENSITY    HAR 7900
            '('4S')' TAN.FLUX%DENSITY'('8S')' RESULTANT'('8S')' PHASE%ANGLE '('3S')'  HAR 8000
            MAG.POTENTIAL- '('3S')' POYNTING%VECTOR '('1C')'% (DEG) '('10S')' (TESLA)  HAR 8100
            '('13S')' (TESLA) '('14S')' (TESLA) '('10S')' (DEGREES) '('4S')' AT%RAD.R%  HAR 8200
            (AMP) '('6S')' -SHAPE%OF '('2C')''')') ;                               HAR 8300
            'FOR' P:= 1 'STEP' 1 'UNTIL' NA 'DO'                                   HAR 8400
            'BEGIN' NEWLINE(1); PRINT(AM[P],3,1); SPACE(7); PRINT(BR[P]*Y,0,4);    HAR 8500
            SPACE(7); PRINT(BT[P]*Y,0,4); SPACE(7); PRINT(BX[P]*Y,0,4); SPACE(7);  HAR 8600
            PRINT(PA[P],3,2); SPACE(5); PRINT(PHI[P]*MUI*Y,0,4); SPACE(4);         HAR 8700
            PRINT(BR[P] *BT[P],0,4);                                               HAR 8800
            'END' ;                                                                HAR 8900
            WRITETEXT('('''('2C')'POWER%FLOW(IN%SYN.%WATTS) = '('2S')''')');       HAR 9000
            Z:= PVI * R * R * (250.0/(2.54*0M)); PRINT(Z,0,6);                     HAR 9100
            WRITETEXT('('''('2C')' TORQUE%EQUIVALENT%TO%POWER%FLOW%(N-M)%=%')');  HAR 9200
            PRINT(( Z/0M ),4,7);                                                   HAR 9300
            WRITETEXT('('''('2C')'ORDER%OF%HARMONIC%='('1S')''')'); PRINT(Q,3,0);  HAR 9400
            WRITETEXT('('''('10S')'NUMBER%OF%HARMONICS%='('1S')''')'); PRINT(N,3,0); HAR 9500
          'END' ;                                                                  HAR 9600
        'END' ;                                                                    HAR 9700
      'END' ;                                                                      HAR 9800
'END' ;                                                                            HAR 9900
```

APPENDIX III

ANALOGUE AND MATHEMATICAL MODELS

A3.1 Teledeltos Plots

These plots were obtained to study the effect of pole shape on the flux distribution in the machine, with special regard to the leakage and fringing at the pole tips.

A3.1.1 Plots without a rotor

The air region enclosed by the magnetic circuit of the machine without a rotor was considered. Symmetry was assumed and plots were obtained for one-quarter of the field system only, Fig. A3.1. The conjugate system of field plotting was employed,

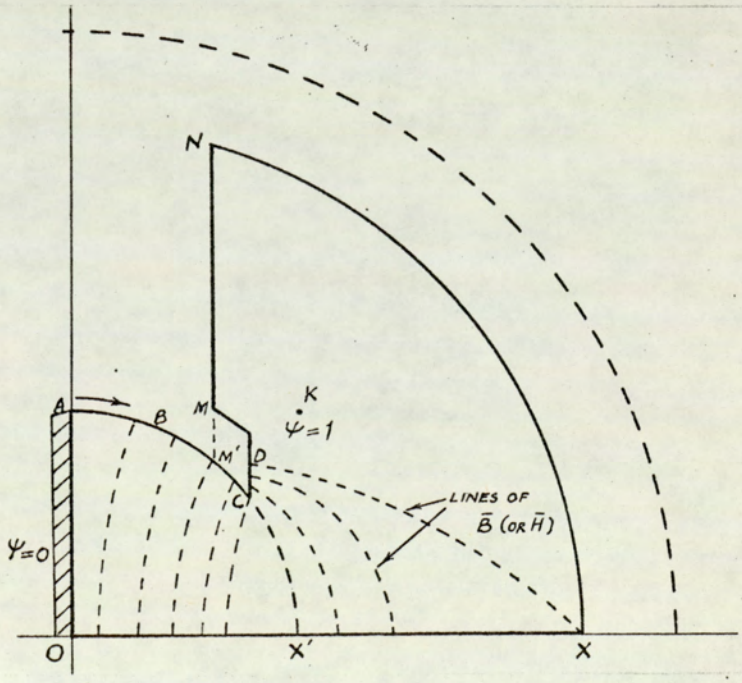

Fig. A3.1

in which the iron surfaces were treated as flow line boundaries and the field winding was replaced by a current kernel, so that equipotential lines correspond to lines of $\overline{B}$ (or $\overline{H}$). The position of the kernel (point K in the figure) was determined by the extrapolation of the iron filing plots in the interpolar region into the winding space, shown dotted* (see Fig. A4.1 b, Appendix IV).

The values of the conjugate potential ψ_θ, along the pole surface A,B,C, and a point D on the side as shown (where the potential at D is the same as at X; the contour of the pole providing flux/pole that crosses the interpolar axis therefore consists of the portion A B C D), were measured at regular intervals.

A graph of ψ_θ along A B C D, together with $\partial\psi_\theta/\partial\theta$, are drawn in Fig. A3.2 (next page). This shows that the B_r distribution (which is equivalent in magnitude to $\partial\psi_\theta/\partial\theta$ in the present case) under the pole surface (i.e. in the airgap of the machine) invariably contains a peak at the pole tip C where the boundary profile changes suddenly (this corresponds nearly to the point of inflation in the plot of ψ_θ).

With the knowledge of the potential at X (Fig. A3.1 or inset in Fig. A3.2), the B_r distribution was computed for an m.m.f. of 2200 A/pole (corresponding to an excitation of 1.0 A in the experimental machine). The ratio of peak value to that under

---

*The plots were repeated with a graded potential distribution along M N and gave similar results as with $\psi = 1$ at K.

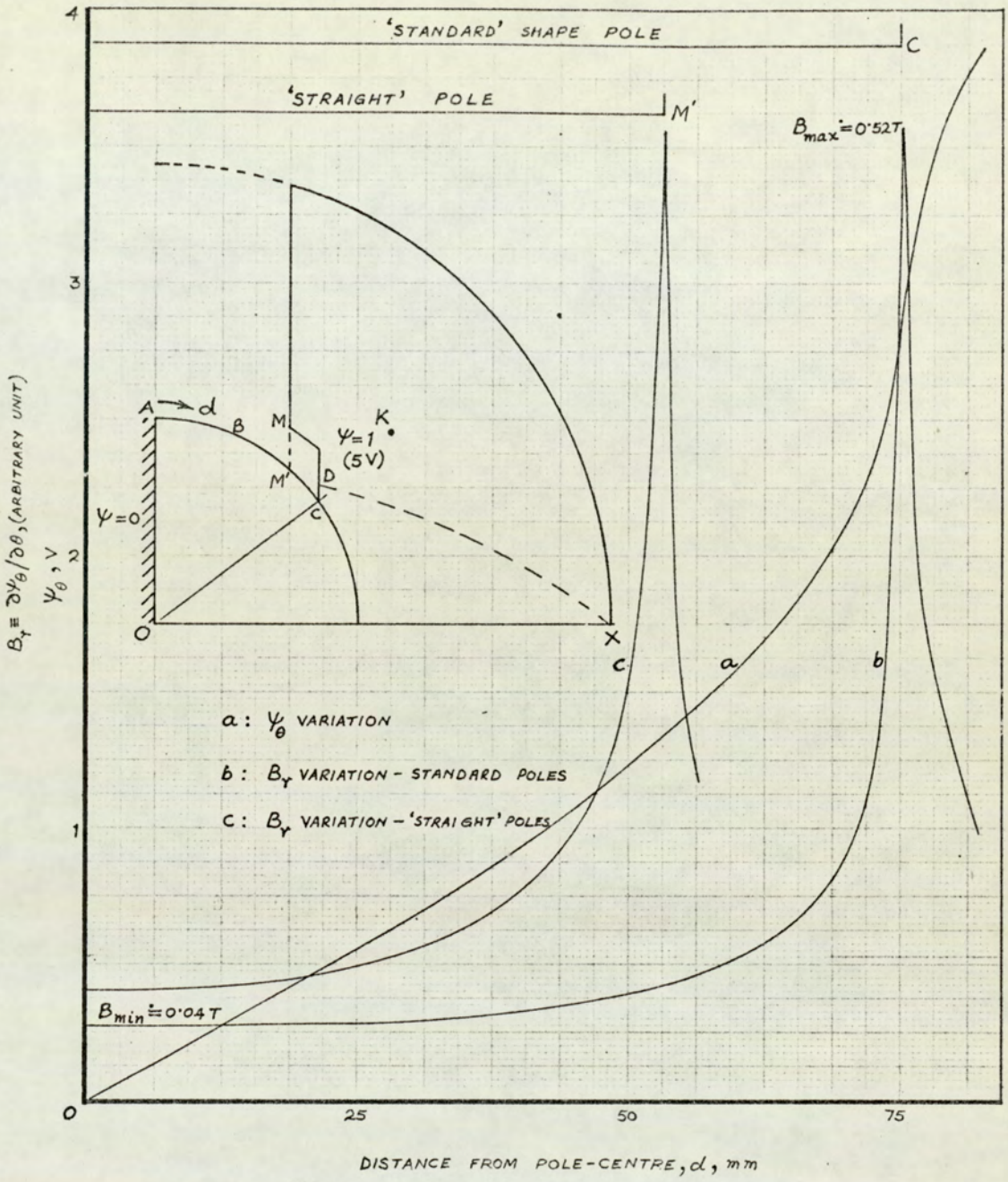

Fig. A3.2

the pole-centre compares favourably with the ratio of previously measured values in the machine using a Hall probe.

The calculations showed that, in addition to the peak in the B_r waveform at the pole tip, the pole/yoke geometry results in about one-third flux leaking away, owing to the low permeability of the region.

Plots on the same scale were also obtained for 'straight' poles (contour A B M′ M N in Fig. A3.1) and the B_r variation is given in Fig. A3.2. It can be seen that peak still occurs at the pole tip, M′, but the ratio of maximum to minimum flux density is reduced to 8.7 as against 13.0 with the 'standard' shape poles.

A3.2 Analytical Field Plots

The above tests were supplemented by analysing a purely theoretical model of the region within the poles to determine the field distribution more accurately, and to some extent, overcome the errors and limitations of analogue plots[68,69]. The analytical field plots, in addition, served the important requirement of checking the accuracy of the computer programme used for the calculation of B_θ from the B_r waveforms.

Both the iron filing and Teledeltos plots reveal that the arc formed by extending the circle containing the pole surfaces into the interpolar region, is a flow line boundary for all practical purposes in the absence of the rotor. This concept forms the basis of the analytic model which comprises a circular region.

A3.2.1 Conformal transformation

The field within a circle of radius R_o in ζ - plane, in which the pole arcs are represented by two electrodes on the perimeter (Fig. A3.3 a, page 199), is transformed to a uniform field in the χ - plane (Fig. A3.3 c) by the transformation

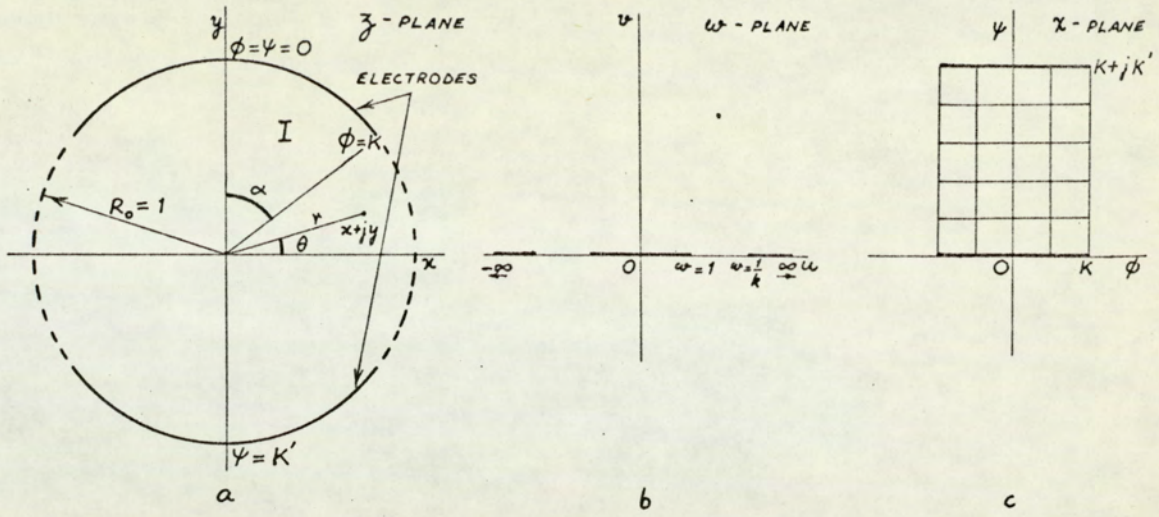

Fig. A3.3

$$z^* = \frac{R_o}{j}\left(\frac{1+jJk\ sn\chi}{1-jJk\ sn\chi}\right)^{\dagger} \qquad \text{A3.1}$$

where z is any point within the field of z - plane, $z = r e^{j\theta}$

2α is the arc of each electrode

$sn\chi$ is a Jacobian elliptic function to modulus k ($=\tan^2\alpha/2$).

A3.2.2 Calculation of field components

The magnetic excitation $\bar{H}$ in the region is given by $\bar{H} = -$ grad ψ , i.e.,

$$H_r = -\frac{\partial\psi}{\partial r} \quad \text{and} \quad H_\theta = -\frac{1}{r}\frac{\partial\psi}{\partial\theta} = -\frac{\partial\phi}{\partial r} \qquad \text{(applying}$$

Cauchy - Riemann conditions).

---

†The usual transformation from the z - plane through w - plane to the χ - plane, using elliptic functions, gives electrodes parallel to the ψ - axis. In the present case, the anti-clockwise rotation by $\pi/2$ is obtained by using z^* (conjugate function of z) in equation A3.1.

Hence for a two-dimensional $\bar{H}$ field, using complex variable notation,

$$\bar{H} = H_r + jH_\theta = -\frac{\partial}{\partial r}(\psi + j\phi) = j\frac{\partial}{\partial r}(\phi + j\psi)$$

or $$\bar{H} = j\frac{\partial \chi}{\partial r} \qquad \text{A3.2}$$

Now for any point $z = re^{j\theta}$, equation A3.1 can be written

$$jre^{-j\theta} = R_o\left\{\frac{1 + j\sqrt{k}\, sn\chi}{1 - j\sqrt{k}\, sn\chi}\right\} \qquad \text{A3.3}$$

Differentiating with respect to r

$$je^{-j\theta} = \frac{j2R_o\sqrt{k}\, sn'\chi}{(1 - j\sqrt{k}\, sn\chi)^2}\frac{\partial \chi}{\partial r} \qquad \text{A3.4}$$

or $$e^{-j\theta} = \frac{2R_o\sqrt{k}\, sn'\chi}{(1 - j\sqrt{k}\, sn\chi)^2}\left(\frac{\partial \phi}{\partial r} + j\frac{\partial \psi}{\partial r}\right) \qquad \text{A3.5}$$

since $$\frac{\partial}{\partial r} = \frac{\partial}{\partial \chi}\frac{\partial \chi}{\partial r} = \frac{\partial}{\partial \chi}\left(\frac{\partial \phi}{\partial r} + j\frac{\partial \psi}{\partial r}\right)$$

The solution of equation A3.5, giving values of $\frac{\partial \phi}{\partial r}$ and $\frac{\partial \psi}{\partial r}$, therefore provides the required field components in accordance with the relationships derived in equation A3.2, in terms of the known quantities R_o, r, θ. This is done as follows:

Let $$\frac{2R_o\sqrt{k}\, sn'\chi}{(1 - j\sqrt{k}\, sn\chi)^2} = C + jD \quad \text{and} \quad \frac{\partial \phi}{\partial r} + j\frac{\partial \psi}{\partial r} = A + jB$$

Then, from equation A3.5,

$$\cos\theta - j\sin\theta = (C + jD)(A + jB) = CA + jBC + jDA - DB$$

or in matrix form, equating real and imaginary parts,

$$\begin{bmatrix} \cos\theta \\ -\sin\theta \end{bmatrix} = \begin{bmatrix} C & -D \\ D & C \end{bmatrix}\begin{bmatrix} A \\ B \end{bmatrix}$$

Now let $\Delta = C^2 + D^2$ which gives

$$A = (C \cos\theta - D \sin\theta)/\Delta$$

$$B = (-C \sin\theta - D \cos\theta)/\Delta$$

or $$H_r = -\frac{\partial \psi}{\partial r} = -B$$

and $$H_\theta = -\frac{\partial \phi}{\partial r} = -A$$

The value of $sn\chi$ is obtained using equation A3.3 and $sn'\chi$ calculated from

$$sn'\chi = cn\chi \; dn\chi \quad \text{where} \quad cn\chi = \sqrt{1-sn^2\chi} \quad \text{and} \quad dn\chi = \sqrt{1-k^2 sn^2\chi}$$

The computer programmes, given in Appendix IX*, were used to compute the values of H_r, H_θ and H , for different angles and radii and the variation of the field components for $r = 0.25$ to $r = 0.99$ is shown in Figs. A3.4, A3.5 and A3.6, pages 202 and 203, which clearly demonstrate the effect of pole tip for differing values of r. A field plot giving the pattern of flow lines in one-quarter region (z - plane) is shown in Fig. A3.7 (page 203).

Calculations were also made for the variation of H_r along the pole axis, from the centre of the machine to the pole surface, corresponding to an excitation of 1.0 A and the results

---

*The procedures to calculate the values of $sn\chi$ and K and K', the complete integral values to modulus k and k' respectively, in the programmes are based on the information available in References 70 and 71.

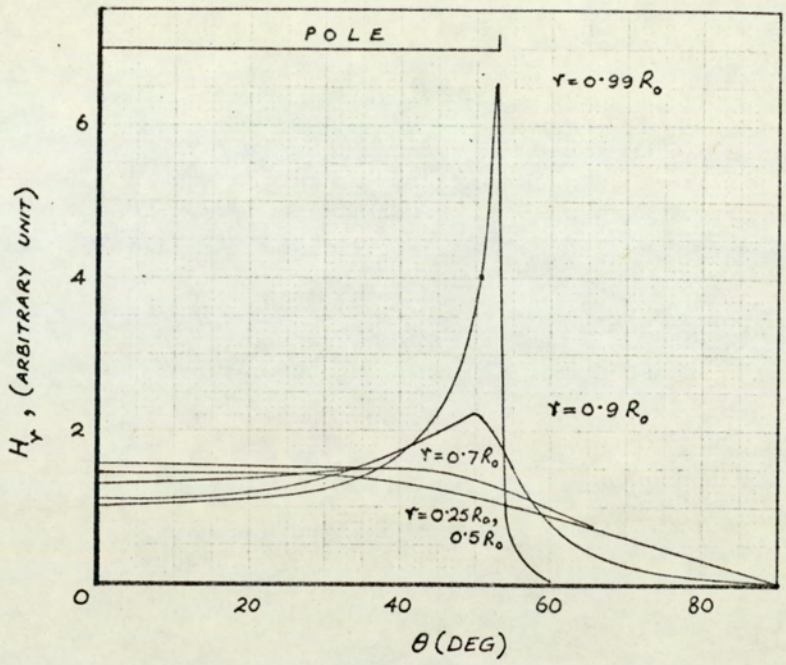

Fig. A3.4

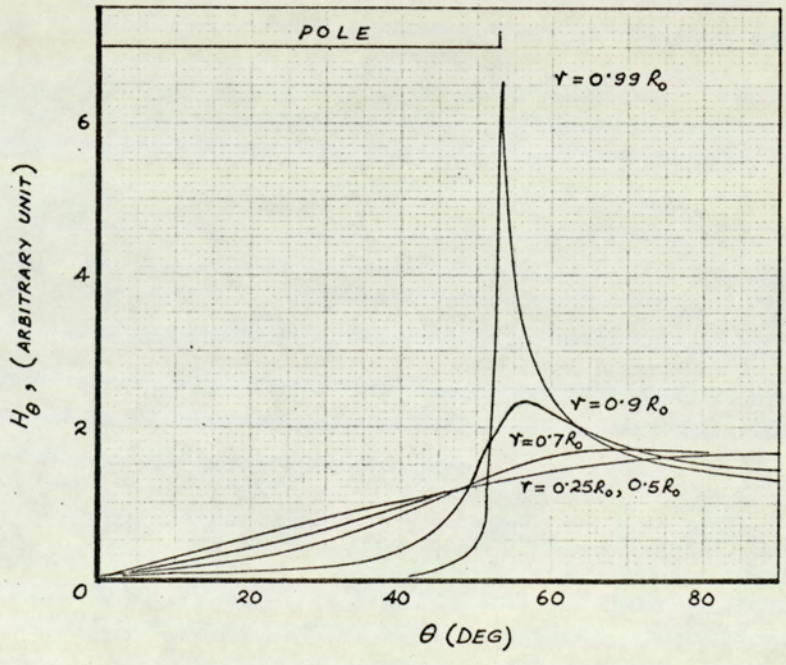

Fig. A3.5

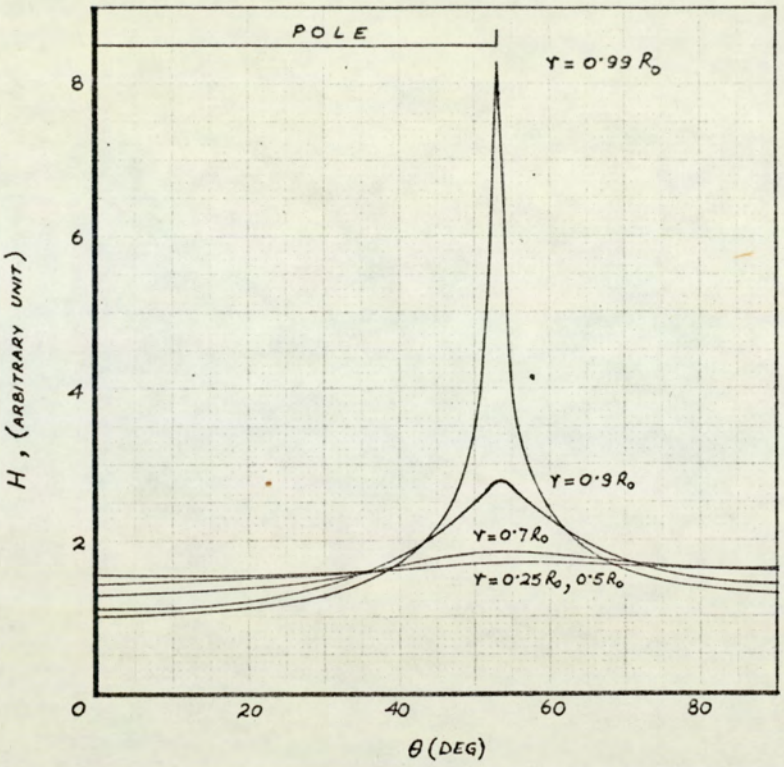

Fig. A3.6

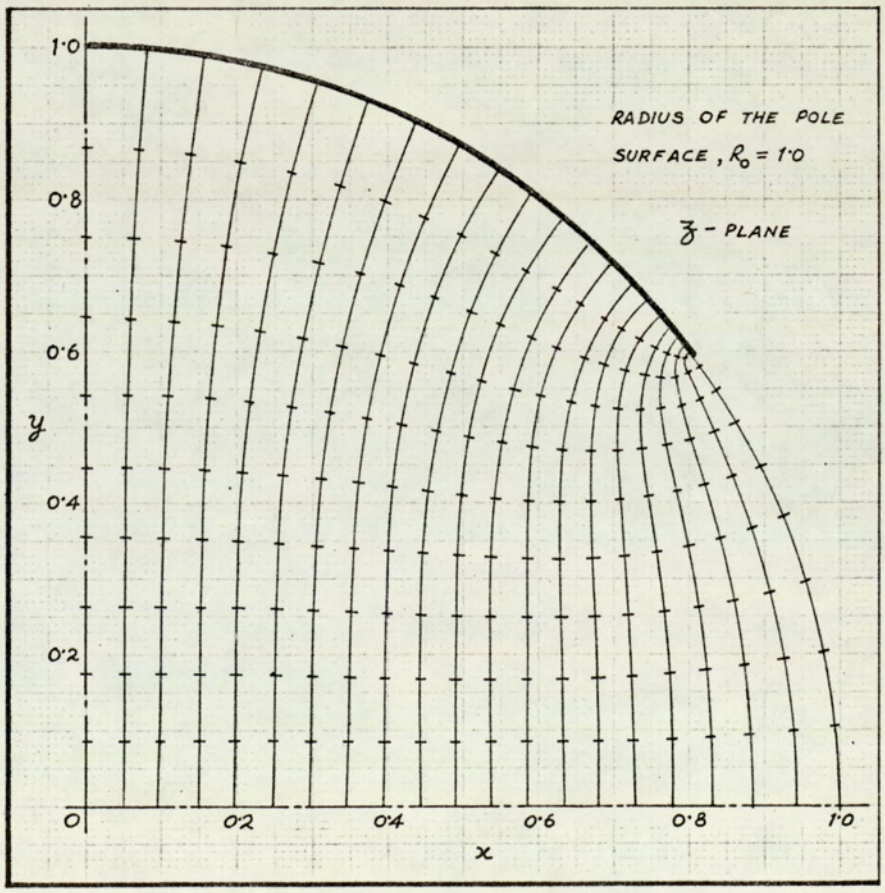

Fig. A3.7

are plotted in Fig. A3.8, which also shows the measured variation using a calibrated Hall probe. Whereas the theoretical H_r is minimum near the pole surface and rises to a maximum at the centre, the measured field shows a maximum at a point about 6 mm away from the pole surface. This feature is due to the short axial

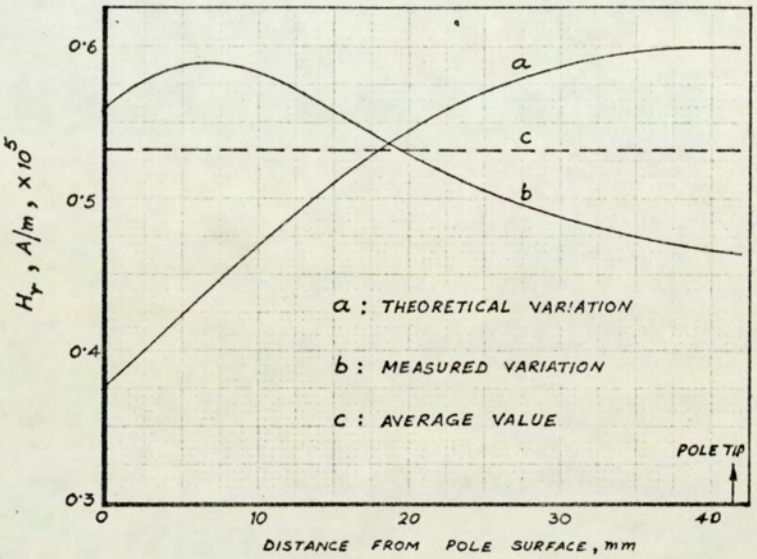

Fig. A3.8

length of the rotor annulus which when saturated exhibits 'end effects' in the sense of flux leaving the edges* axially and then bending over. Reference to the construction of the machine (see Plate 2.1) also shows that the appreciable overhang of the field winding, protruding in the axial direction, can contribute to the flux in the vicinity of the internal rotor surface, i.e., the flux bending over the edge of the rotor and reaching inside it. This again is due to the edges of the annulus becoming highly saturated.

---

*This is because the annulus is basically a permanent magnet material and once magnetised behaves accordingly.

APPENDIX IV

IRON FILING PATTERNS

The simple technique of using iron filings was employed during preliminary experimental work on the machine to observe the leakage flux distribution in the interpolar and arbor regions. The patterns were obtained by sprinkling iron filings on a piece of DUOSTAT paper, cut to the shape of the region of interest and positioned in the machine, and carrying out the whole process in a suitable dark-room. A good, direct record of the patterns was thus available, with the experiments performed with and without a Vicalloy rotor, and at varying excitations. For convenience of handling, a rotor having a radial thickness of 0.6 inch (15.2 mm) was used.

The patterns, for various test conditions, are illustrated in Figs. A4.1 to A4.4, pages 207 to 209 .

The patterns of Fig. A4.3 give a clear indication of 'independent' rotor magnetisation in the form of residual magnetism when the excitation is switched off. When compared with the patterns of Fig. A4.1 showing the flux due to field system alone, the rotor magnetisation effect is observed to be in 'space quadrature'.

The hysteresis effect, exhibited in Fig. A4.4, was produced by rotating the rotor annulus by hand 4-5 times in a clockwise direction, and holding it stationary without slipping

back. It is noted that the flux has shifted towards the lagging pole tip and the leakage in the direction of the yoke is increased. This spatial shift was observed to be most pronounced at an excitation of 0.3 A and to diminish to the case of non-hysteretic patterns at about 1.0 A.

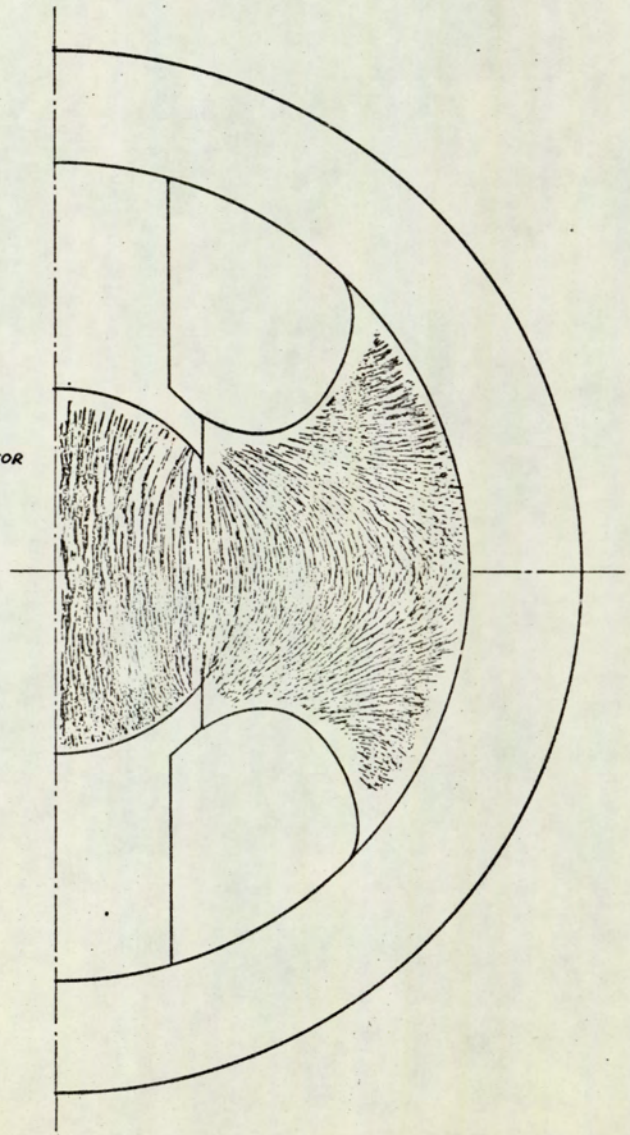

FIG. A4.1 a

FIELD SYSTEM FLUX DISTRIBUTION : NO ROTOR EXCITATION 0·05 A

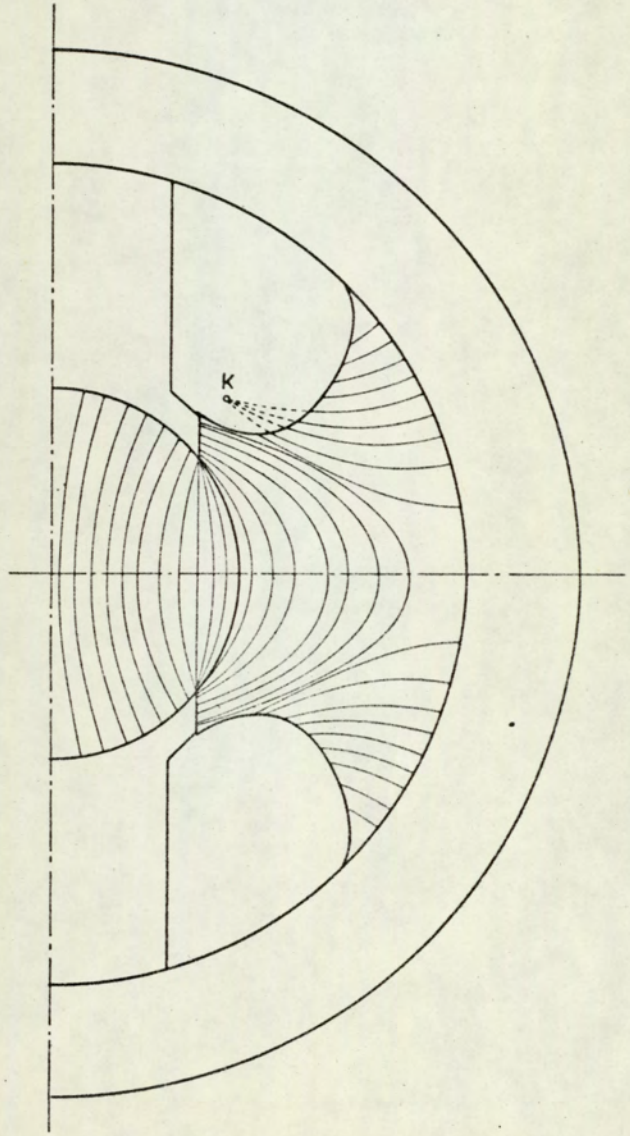

FIG. A4.1 b

DIAGRAMMATIC REPRESENTATION OF FIG. A4.1 a

FIG. A3.2

LEAKAGE FLUX

NO SPATIAL HYSTERESIS

EXCITATION 0·3A

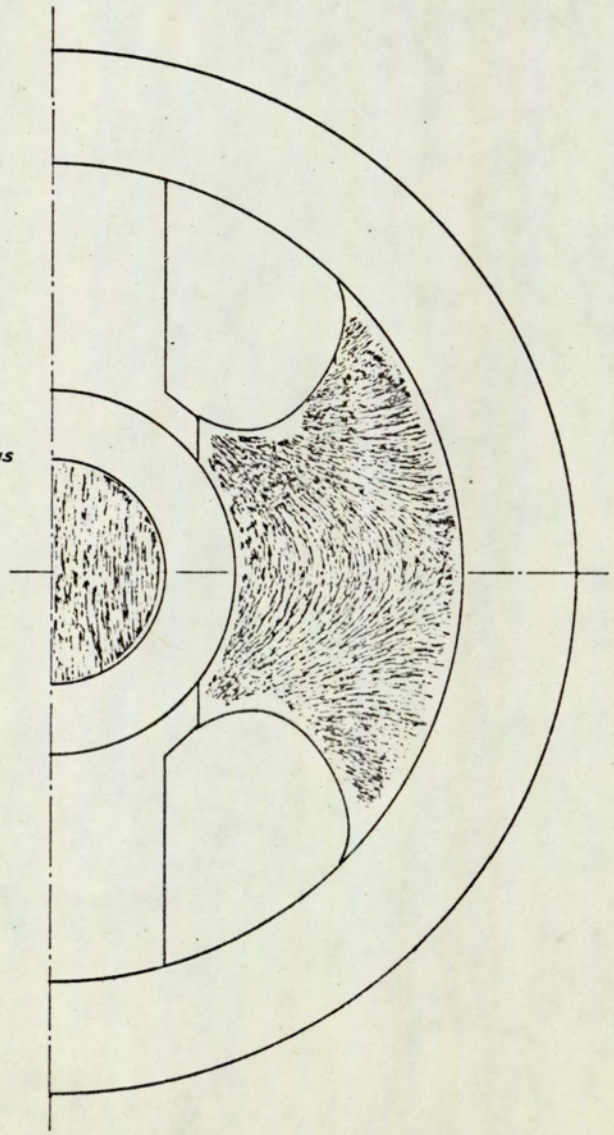

FIG. A3.3

ROTOR MAGNETISATION

EFFECT : RESIDUAL

MAGNETISM

EXCITATION 0·3A

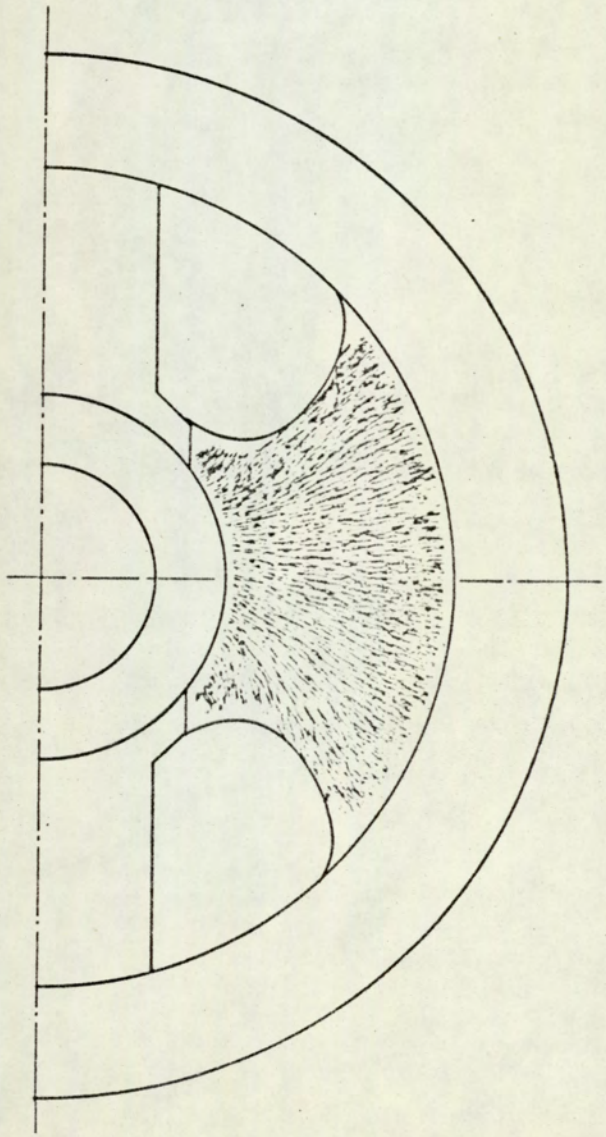

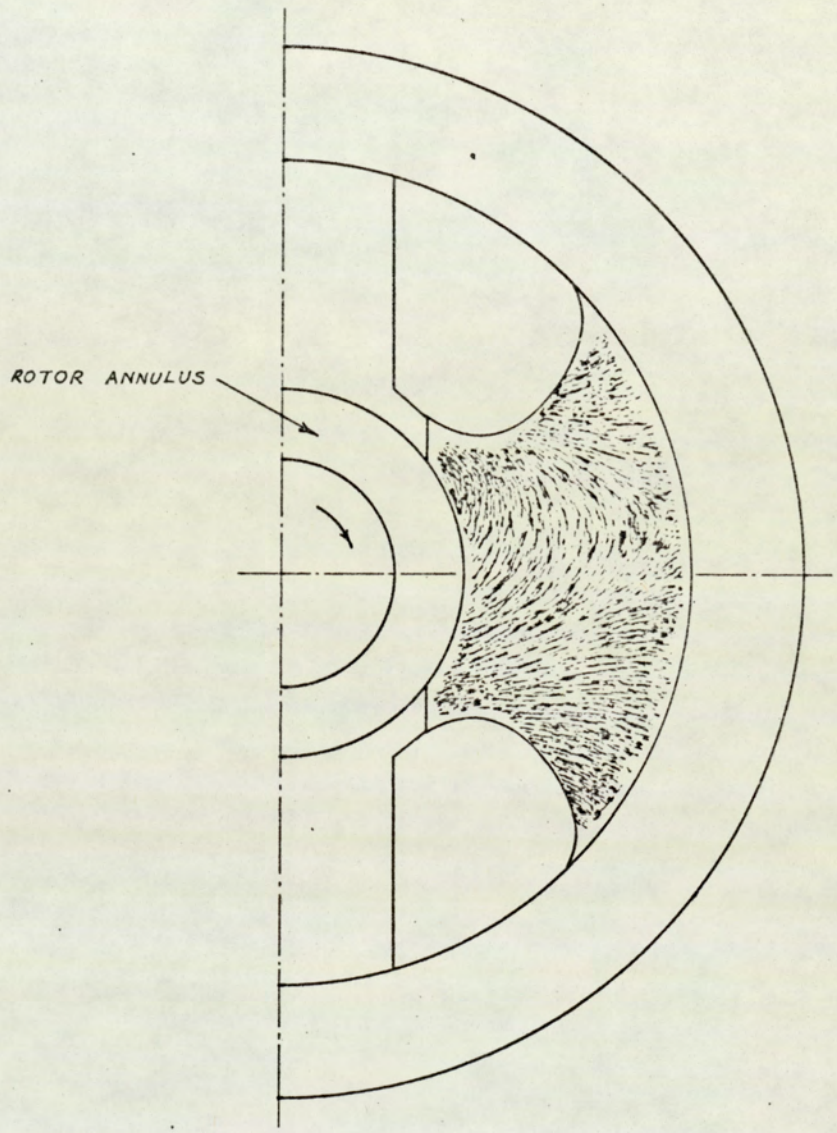

Fig. A4.4

APPENDIX V

FIELD THEORY CALCULATIONS

A5.1 Evaluation of Coefficients for B_θ Waveforms Derived from B_r Waveforms Using Field Theory

In the airgap or arbor region of the machine, $\bar{H}$ is irrotational (assuming a non-time dependent field) and can be expressed as the negative gradient of a scalar magnetic potential, which is governed by the Laplace's equation.

Let the general solution of the Laplace's equation in the region, based on separation of variables, be

$$\phi = (A_n r^n + B_n r^{-n}) \cos n\theta + (D_n r^n + E_n r^{-n}) \sin n\theta \qquad A5.1$$

Then
$$H_r = -\frac{\partial \phi}{\partial r}$$
$$= -n(A_n r^{n-1} - B_n r^{-n-1}) \cos n\theta - n(D_n r^{n-1} - E_n r^{-n-1}) \sin n\theta$$

$$B_r = \mu_o H_r \qquad A5.2$$

and
$$H_\theta = -\frac{1}{r}\frac{\partial \phi}{\partial \theta}$$
$$= n(A_n r^{n-1} + B_n r^{-n-1}) \sin n\theta - n(D_n r^{n-1} + E_n r^{-n-1}) \cos n\theta$$

$$B_\theta = \mu_o H_\theta \qquad A5.3$$

From the harmonic analysis of measured B_r waveforms, using the PROCEDURE described in Appendix II, at $r = a$

$$B_{r_a} = A_n' \sin n\theta + B_n' \cos n\theta \qquad A5.4a$$

and at $r = b$

$$B_{r_b} = A_n'' \sin n\theta + B_n'' \cos n\theta \qquad \text{A5.4 b}$$

where, if $a > b$, B_{r_a} is obtained by adding to expansion of B_{r_b} the expansion of ΔB_r waveforms.

The coefficients $A_n' \ldots . B_n''$ are therefore known.

From the field theory above (equation A5.2, at $r = a$ and b),

$$B_{r_a} = -\mu_o n (A_n a^{n-1} - B_n a^{-n-1}) \cos n\theta - \mu_o n (D_n a^{n-1} - E_n a^{-n-1}) \sin n\theta \qquad \text{A5.5 a}$$

$$B_{r_b} = -\mu_o n (A_n b^{n-1} - B_n b^{-n-1}) \cos n\theta - \mu_o n (D_n b^{n-1} - E_n b^{-n-1}) \sin n\theta \qquad \text{A5.5 b}$$

Equating the expressions on the right hand side of equations A5.4 a and A5.4 b to A5.5 a and A5.5 b respectively, and solving for $A_n , B_n , D_n , E_n ,$

$$A_n = \frac{a^{-n+1}}{n\mu_o \left[(b/a)^{2n} - 1 \right]} \left[B_n' - (b/a)^{n+1} B_n'' \right] \qquad \text{A5.6 a}$$

$$B_n = \frac{a^{n+1}}{n\mu_o \left[(b/a)^{2n} - 1 \right]} \left[(b/a)^{2n} B_n' - (b/a)^{n+1} B_n'' \right] \qquad \text{A5.6 b}$$

$$D_n = \frac{a^{-n+1}}{n\mu_o \left[(b/a)^{2n} - 1 \right]} \left[A_n' - (b/a)^{n+1} A_n'' \right] \qquad \text{A5.6 c}$$

$$E_n = \frac{a^{n+1}}{n\mu_o \left[(b/a)^{2n} - 1 \right]} \left[(b/a)^{2n} A_n' - (b/a)^{n+1} A_n'' \right] \qquad \text{A5.6 d}$$

At any radius $r = R$ in the region, B_θ from equation A5.3 is given by,

$$B_\theta = \mu_o n (A_n R^{n-1} + B_n R^{-n-1}) \sin n\theta - \mu_o n (D_n R^{n-1} + E_n R^{-n-1}) \cos n\theta \qquad \text{A5.7}$$

where $A_n \ldots . E_n$ have the values given in A5.6.

Let $$B_\theta = P_n \sin n\theta + Q_n \cos n\theta \qquad \text{A5.7 a}$$

where $$P_n = \mu_o n \left(A_n R^{n-1} + B_n R^{-n-1}\right) \qquad \text{A5.8 a}$$

and $$Q_n = -\mu_o n \left(D_n R^{n-1} + E_n R^{-n-1}\right) \qquad \text{A5.8 b}$$

Then substituting for $A_n \ldots . E_n$, in expressions for P_n and Q_n

$$P_n = \frac{1}{\left[(b/a)^{2n} - 1\right]} \left\{ (R/a)^{n-1} \left[B_n' - (b/a)^{n+1} B_n'' \right] + (a/R)^{n+1} \left[(b/a)^{2n} B_n' - (b/a)^{n+1} B_n'' \right] \right\} \qquad \text{A5.9 a}$$

$$Q_n = \frac{-1}{\left[(b/a)^{2n} - 1\right]} \left\{ (R/a)^{n-1} \left[A_n' - (b/a)^{n+1} A_n'' \right] + (a/R)^{n+1} \left[(b/a)^{2n} A_n' - (b/a)^{n+1} A_n'' \right] \right\} \qquad \text{A5.9 b}$$

P_n and Q_n may be further written

$$P_n = ML \left\{ P_{n_1} + P_{n_2} \right\} \qquad \text{A5.9 c}$$

$$Q_n = -ML \left\{ Q_{n_1} + Q_{n_2} \right\} \qquad \text{A5.9 d}$$

where $$ML = \frac{1}{\left[(b/a)^{2n} - 1\right]} \qquad \text{A5.10 a}$$

$$P_{n_1} = (R/a)^{n-1} \left[B_n' - (b/a)^{n+1} B_n'' \right] \qquad \text{A5.10 b}$$

$$P_{n_2} = (a/R)^{n+1} \left[(b/a)^{2n} B_n' - (b/a)^{n+1} B_n'' \right] \qquad \text{A5.10 c}$$

$$Q_{n_1} = (R/a)^{n-1} \left[A_n' - (b/a)^{n+1} A_n'' \right] \qquad \text{A5.10 d}$$

$$Q_{n_2} = (a/R)^{n+1} \left[(b/a)^{2n} A_n' - (b/a)^{n+1} A_n'' \right] \qquad \text{A5.10 e}$$

Equation A5.7 a thus becomes

$$B_\theta = ML \left\{ \left[P_{n_1} + P_{n_2} \right] \sin n\theta - \left[Q_{n_1} + Q_{n_2} \right] \cos n\theta \right\} \qquad \text{A5.11}$$

A5.1.1 'Computerisation' of P_n and Q_n

In accordance with the requirements for ALGOL, ICL 1900 Language, used for present computation work, lower case letters used in equations A5.1 to A5.11, are replaced by upper case and hence $P_{n_1} \ldots . Q_{n_2}$ written

$$P_{n_1} \equiv PN1[Q] = (R/A)^{Q} \left(B1[M] - (B/A)^{Q+1} B2[M] \right) \qquad \text{A5.12 a}$$

$$P_{n_2} \equiv PN2[Q] = (B/R)^{Q} \left((B/A)^{Q} B1[M] - (B/A)\, B2[M] \right) \qquad \text{A5.12 b}$$

$$Q_{n_1} \equiv QN1[Q] = (R/A)^{Q} \left(A1[M] - (B/A)^{Q+1} A2[M] \right) \qquad \text{A5.12 c}$$

$$Q_{n_2} \equiv QN2[Q] = (B/R)^{Q} \left((B/A)^{Q} A1[M] - (B/A)\, A2[M] \right) \qquad \text{A5.12 d}$$

where $A1[M]$, $A2[M]$, $B1[M]$ and $B2[M]$ are the coefficients of $\sin n\theta$ and $\cos n\theta$ terms respectively in the Fourier analysis of measured waveforms and Q the order of harmonic. Similarly,

$$ML = 1/((B/A)^{2Q} - 1)$$

A5.1.2 Calculation of magnetic scalar potential

The assumed expression for the scalar potential in the region is

$$\phi = (A_n r^{n} + B_n r^{-n}) \cos n\theta + (D_n r^{n} + E_n r^{-n}) \sin n\theta \qquad \text{A5.1}$$

$A_n \ldots . E_n$ have been derived previously in terms of $A'_n \ldots . B''_n$; coefficients from harmonic analysis for B_r waveforms at two radii, a and b .

Now PN and QN (corresponding to P_n and Q_n of equation A5.9) used to obtain B_θ in the computer are related to $A_n \ldots . E_n$:

$$\mu_o n (A_n r^{n-1} + B_n r^{-n-1}) = PN \qquad \text{A5.8 a}$$

$$-\mu_o n (D_n r^{n-1} + E_n r^{-n-1}) = QN \qquad \text{A5.8 b}$$

Therefore, replacing A_n by A_n/μ_o etc. and multiplying by r/n and $-r/n$ respectively,

$$A_n r^n + B_n r^{-n} = PN\,(r/n) \qquad \text{A5.13 a}$$

$$D_n r^n + E_n r^{-n} = QN\,(-r/n) \qquad \text{A5.13 b}$$

The expressions on the left hand side in equation A5.13 are the coefficients of cos nθ and sin nθ respectively in the equation for ϕ , A5.1.

In the computer, therefore,

$$\phi \equiv PHI = PHI1 \cos n\theta + PHI2 \sin n\theta \qquad \text{A5.14}$$

where $PHI1 = PN\,(R/Q)$ A5.15 a

and $PHI2 = QN\,(-R/Q)$ A5.15 b

APPENDIX VI

MULTIPLYING FACTORS IN COMPUTER CALCULATIONS OF FLUX DENSITY AND TORQUE (SI UNITS)

The two inputs in the form of data from the measured waveforms are identified as BRA and DBR in the computer programme. The unit for BRA and DBR is mV.

BRA then becomes:

$$BRA = \frac{\text{input in mV} \times 10^{-3}}{l\ \omega\ R\ (=A)}\ T\ ,$$ giving the radial flux density at the radius, R = A.

The units for l , ω and R are m , 1/s , and m respectively.

The radial flux density at the other radius (R + ΔR) is given by,

$$BRB = \frac{(\text{ input in mV for BRA + input in mV for DBR }) \times 10^{-3}}{l\ \omega\ (R+\Delta R)\ (=B)}\ T$$

Since the coefficients are divided by A and B respectively soon after the harmonic analysis, the multiplying factor to obtain the radial and peripheral flux densities in the last stage of computation is

$$M1 = \frac{10^{-3}}{l\omega} = \frac{10^{-3}}{25{\cdot}4 \times \omega \times 10^{-3}}\ , \qquad \text{for } l = 25{\cdot}4 \text{ mm}$$

Using BRA and BRB in T , B_θ is also obtained in T for further calculations.

Now for calculations on the external rotor surface, R = A ,

$$H_\theta = \frac{B_\theta}{\mu_o} \quad A/m$$

and $$E_z = \frac{\text{input in mV for BRA (R = A)} \times 10^{-3}}{l} \quad V/m$$

$$H_\theta \text{ in computer} = \frac{10^{-3}}{4\pi \times 10^{-7} \times l \times \omega} \sum_{n=1}^{199} \left[PN \sin n\theta + QN \cos n\theta \right] \quad A/m$$

$$E_z \text{ in computer} = \frac{10^{-3}}{l} \sum_{n=1}^{199} \left[RN \cos n\theta + SN \sin n\theta \right] \times A \quad V/m$$

(to be multiplied by A because RN and SN have previously been divided by A, B).

Power flow into the rotor on the outer surface

$$P = 2 \int_0^l \int_0^\pi (E_z \times H_\theta)\, A \, d\theta \, dz$$

$$= \frac{2 \times l \times \pi \times A \times 10^{-3} \times 10^{-3} \times A}{l \times 4\pi \times 10^{-7} \times l \times \omega \times 2} \sum_{n=1}^{199} \left[PN \times SN + QN \times RN \right] \quad W \text{ (SYN)}$$

$$= \left(\frac{A^2}{\omega l} \right) \times 2.5 \sum_{n=1}^{199} \left[PN \times SN + QN \times RN \right] \quad W \text{ (SYN)}$$

Torque equivalent to power flow, $T = \frac{P}{\omega}$ Nm.

The calculations for the internal surface are on similar lines.

APPENDIX VII

OSCILLOGRAMS OF RADIAL AND PERIPHERAL FLUX DENSITY AT MISCELLANEOUS EXCITATIONS

The B_r and B_θ waveforms for the airgap and arbor region, and B_θ waveforms for the Vicalloy are given on pages 218 to 220.

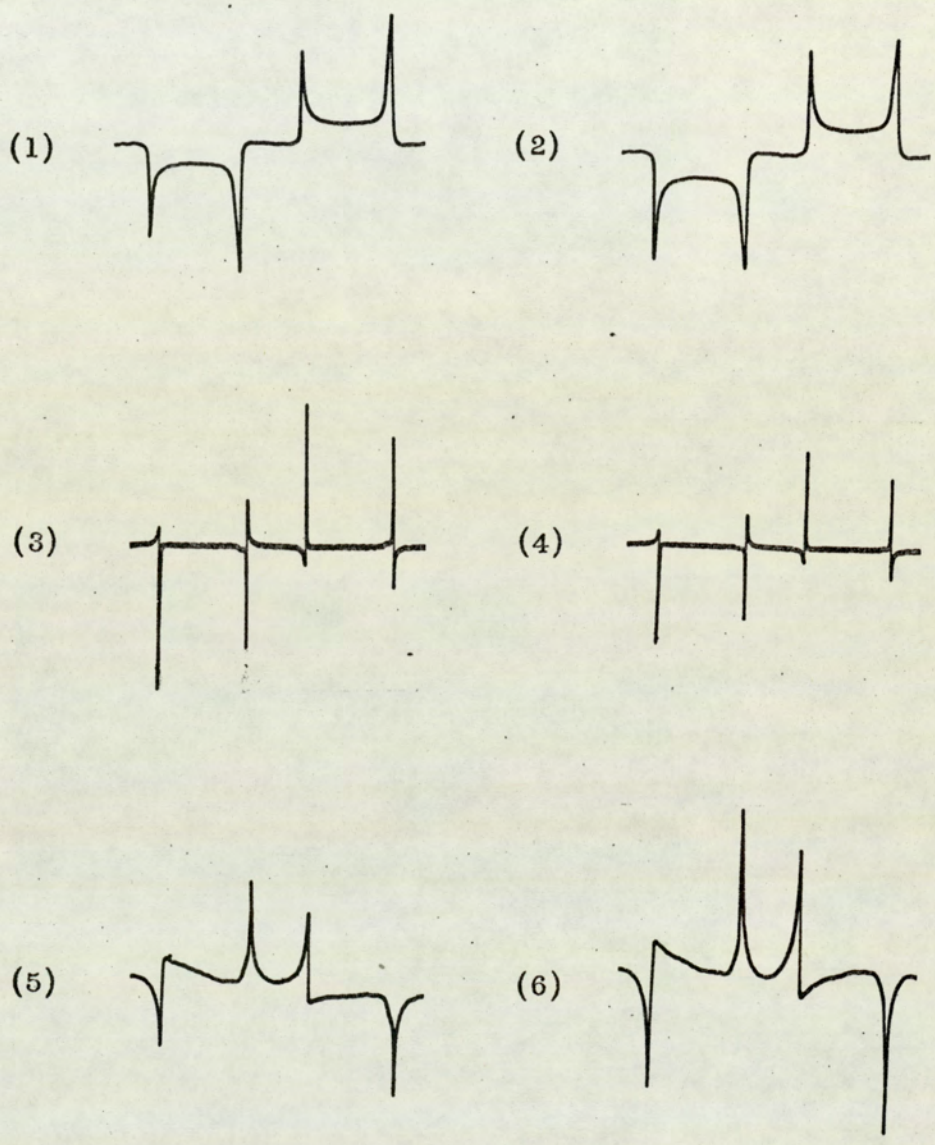

B_r, ΔB_r and time - integrated B_θ in the airgap
- Vicalloy rotor

Fig. 3.8

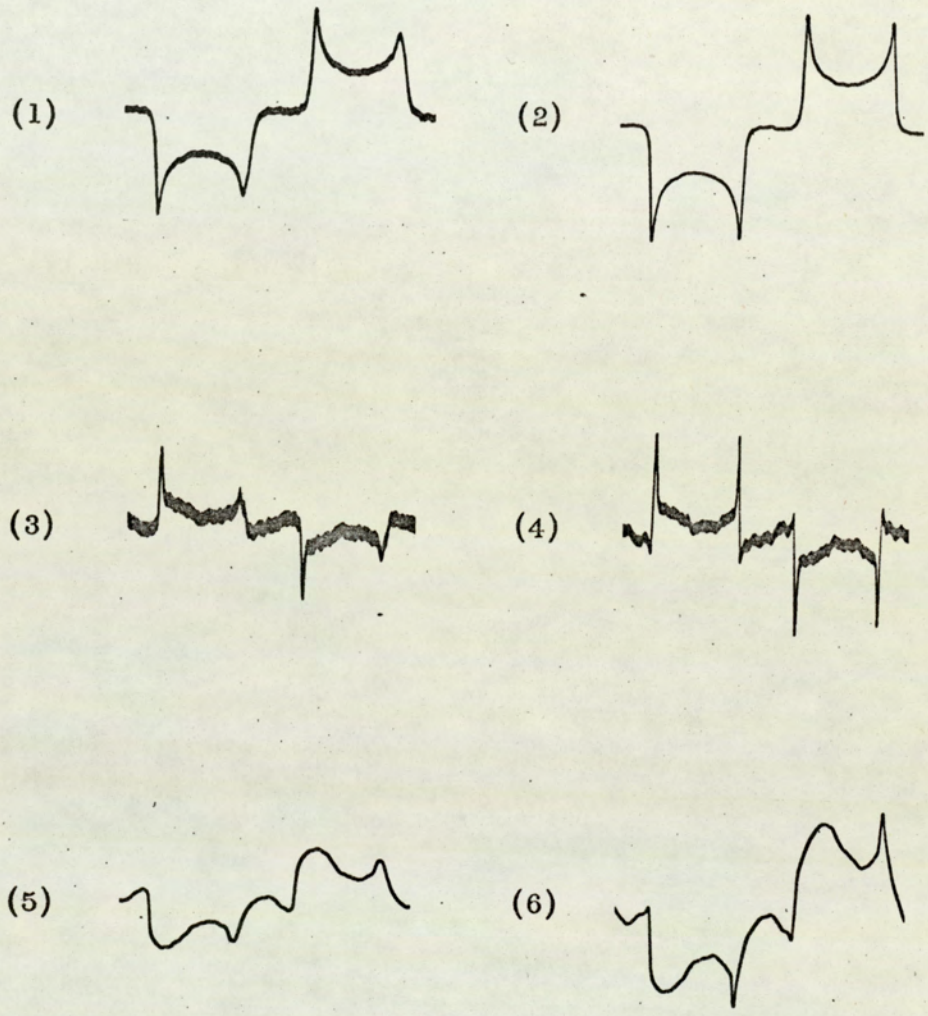

B_r, ΔB_r and time - integrated B_θ in the arbor region
- Vicalloy rotor

Fig. 3.9

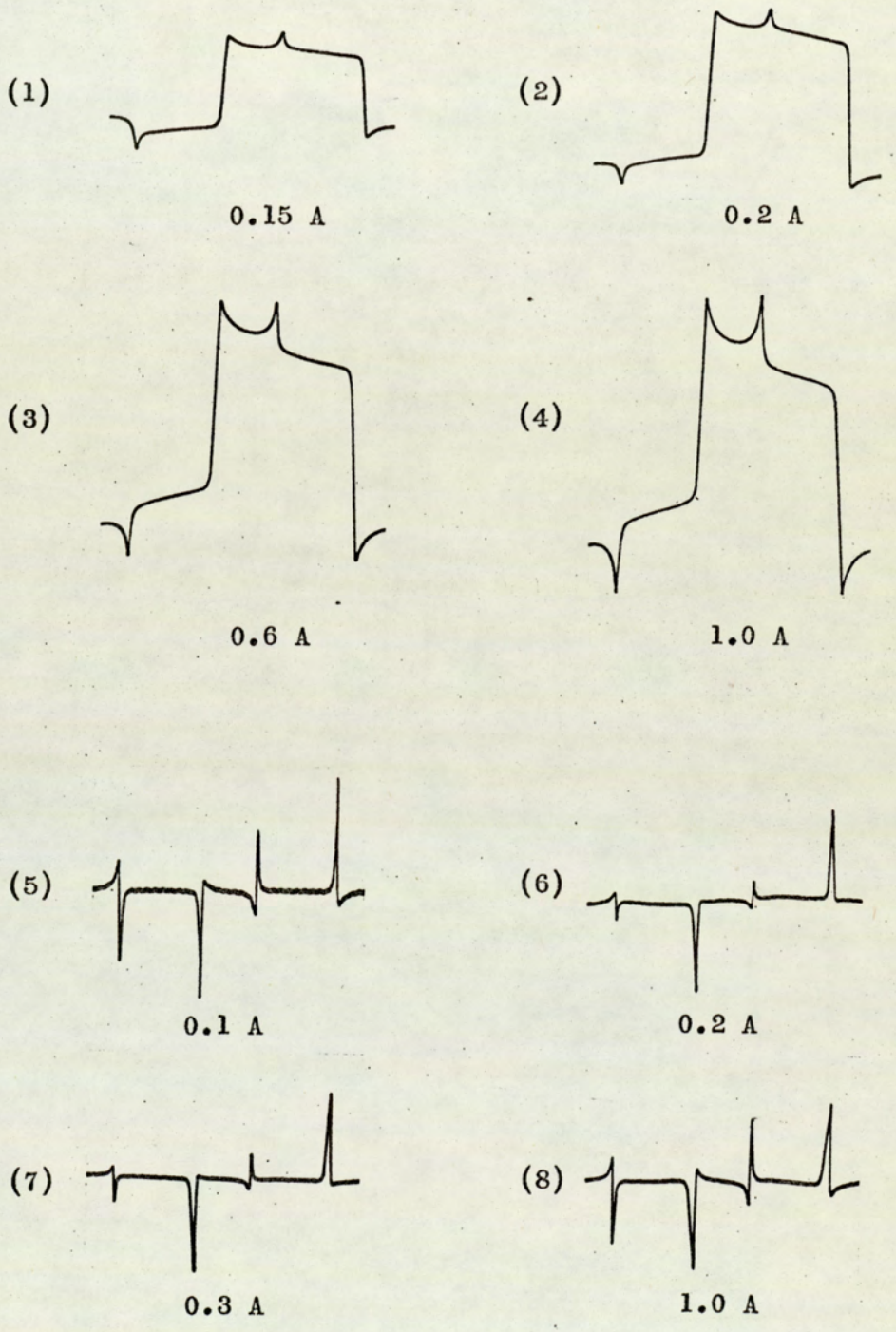

Time - integrated B_θ and $\triangle B_r$ in the Vicalloy annulus

Fig. 3.10

APPENDIX VIII

SPECIMEN COMPUTER RESULTS FOR FLUX DENSITY AND POWER FLOW

These are given on pages 222 to 224 for the external rotor surface at excitation currents 0.1 A, 0.3 A and 1.0 A.

RESULTS FOR CALCULATION OF FLUX DENSITY AND POWER FLOW - FIELD THEORY APPROACH

THIN ROTOR External SURFACE EXCITATION = 0.1 A

RADIUS FOR CALCULATIONS,R (M) = 0.0408877

ANGLE (DEG)	RAD.FLUX DENSITY (TESLA)	TAN.FLUX DENSITY (TESLA)	RESULTANT (TESLA)	PHASE ANGLE (DEGREES)	MAG.POTENTIAL- AT RAD.R (AMP)	POYNTING VECTOR -SHAPE OF
0.0	-1.0034& -2	-2.1277& -2	2.3525& -2	-154.75	-4.6872& 2	3.3189& 0
20.0	-1.0838& -2	-2.1258& -2	2.3861& -2	-152.98	-2.2726& 2	3.5817& 0
30.0	-1.1833& -2	-2.1232& -2	2.4307& -2	-150.87	-1.0659& 2	3.9057& 0
40.0	-1.3705& -2	-2.1256& -2	2.5291& -2	-147.19	1.3990& 1	4.5288& 0
47.0	-1.8071& -2	-2.1142& -2	2.7812& -2	-139.48	9.8102& 1	5.9391& 0
49.0	-2.0685& -2	-2.1441& -2	2.9792& -2	-136.03	1.2209& 2	6.8946& 0
50.0	-2.2520& -2	-2.2140& -2	3.1580& -2	-134.51	1.3444& 2	7.7508& 0
51.0	-2.4935& -2	-2.3744& -2	3.4431& -2	-133.60	1.4747& 2	9.2038& 0
52.0	-2.9054& -2	-2.5366& -2	3.8569& -2	-131.12	1.6132& 2	1.1457& 0
53.0	-3.4872& -2	-2.9438& -2	4.5636& -2	-130.17	1.7682& 2	1.5959& 0
54.0	-4.1909& -2	-3.9212& -2	5.7393& -2	-133.10	1.9575& 2	2.5547& 1
55.0	-4.8401& -2	-5.2938& -2	7.1729& -2	-137.56	2.2253& 2	3.9831& 1
56.0	-4.7497& -2	-4.4047& -2	6.4777& -2	-132.84	2.5094& 2	3.2523& 1
58.0	-3.4107& -2	-2.9367& -2	4.5008& -2	-130.73	2.9084& 2	1.5571& 1
60.0	-1.9694& -2	-2.3289& -2	3.0500& -2	-139.78	3.2025& 2	7.1300& 0
70.0	1.0284& -5	-1.9159& -2	1.9159& -2	179.97	4.3301& 2	-3.0628& -3
80.0	-1.0482& -5	-1.9092& -2	1.9092& -2	-179.97	5.4156& 2	3.1109& -3
90.0	1.2109& -5	-1.9131& -2	1.9131& -2	179.96	6.5013& 2	-3.6016& -3
100.0	-1.3721& -5	-1.9107& -2	1.9107& -2	-179.96	7.5867& 2	4.0756& -3
110.0	1.5560& -5	-1.9118& -2	1.9118& -2	179.95	8.6724& 2	-4.6244& -3
120.0	-1.8958& -5	-1.9131& -2	1.9131& -2	-179.94	9.7578& 2	5.6380& -3
125.0	-7.1132& -5	-1.9979& -2	1.9979& -2	-179.80	1.0304& 3	2.2093& -2
126.0	9.4001& -5	-2.1770& -2	2.1770& -2	179.75	1.0422& 3	-3.1812& -2
127.0	7.0694& -5	-2.3993& -2	2.3993& -2	179.84	1.0551& 3	-2.6367& -2
128.0	4.9698& -3	-2.2645& -2	2.3184& -2	167.62	1.0691& 3	-1.7495& 0
129.0	1.3527& -2	-4.4970& -4	1.3534& -2	91.90	1.0763& 3	-9.4563& -2
130.0	2.3098& -2	1.5165& -2	2.7631& -2	56.71	1.0712& 3	5.4453& 0
131.0	2.9068& -2	1.8765& -2	3.4599& -2	57.15	1.0614& 3	8.4798& 0
132.0	3.2559& -2	2.0056& -2	3.8241& -2	58.37	1.0503& 3	1.0151& 1
135.0	2.8796& -2	2.1669& -2	3.6038& -2	53.04	1.0139& 3	9.7002& 0
140.0	1.9156& -2	2.1495& -2	2.8792& -2	41.71	9.5262& 2	6.4010& 0
150.0	1.3190& -2	2.1297& -2	2.5051& -2	31.77	8.3130& 2	4.3669& 0
158.0	1.1567& -2	2.1292& -2	2.4231& -2	28.51	7.3454& 2	3.8286& 0
159.0	1.1424& -2	2.1286& -2	2.4158& -2	28.22	7.2245& 2	3.7802& 0
160.0	1.1275& -2	2.1295& -2	2.4095& -2	27.90	7.1036& 2	3.7323& 0
161.0	1.1163& -2	2.1277& -2	2.4027& -2	27.68	6.9827& 2	3.6922& 0
162.0	1.1033& -2	2.1294& -2	2.3982& -2	27.39	6.8618& 2	3.6521& 0
165.0	1.0769& -2	2.1271& -2	2.3841& -2	26.85	6.4993& 2	3.5608& 0
180.0	1.0034& -2	2.1277& -2	2.1277& -2	25.25	4.6872& 2	3.3189& 0

POWER FLOW(IN SYN. WATTS) = 2.441745& -1

TORQUE EQUIVALENT TO POWER FLOW (N-M) = 0.0497428

ORDER OF HARMONIC = 199 NUMBER OF HARMONICS = 100

RESULTS FOR CALCULATION OF FLUX DENSITY AND POWER FLOW - FIELD THEORY APPROACH

THIN ROTOR External SURFACE EXCITATION = 0.3 A

RADIUS FOR CALCULATIONS,R (M) = 0.0408877

ANGLE (DEG)	RAD.FLUX DENSITY (TESLA)	TAN.FLUX DENSITY (TESLA)	RESULTANT (TESLA)	PHASE ANGLE (DEGREES)	MAG.POTENTIAL-AT RAD.R (AMP)	POYNTING VECTOR -SHAPE OF
0.0	-2.8946& -2	-3.4504& -2	4.5038& -2	-140.01	-6.8633& 2	1.7091& 1
20.0	-3.0758& -2	-3.4505& -2	4.6224& -2	-138.29	-2.9418& 2	1.8161& 1
30.0	-3.2371& -2	-3.4509& -2	4.7316& -2	-136.83	-9.8147& 1	1.9116& 1
40.0	-3.7395& -2	-3.4431& -2	5.0831& -2	-132.64	9.7565& 1	2.2030& 1
45.0	-4.5274& -2	-3.5438& -2	5.7494& -2	-128.05	1.9559& 2	2.7455& 1
47.0	-5.3102& -2	-4.0762& -2	6.6943& -2	-127.51	2.3819& 2	3.7040& 1
49.0	-6.8719& -2	-5.3420& -2	8.7040& -2	-127.86	2.9098& 2	6.2819& 1
50.0	-7.9758& -2	-6.0658& -2	1.0020& -1	-127.25	3.2343& 2	8.2789& 1
51.0	-9.5117& -2	-6.8283& -2	1.1709& -1	-125.67	3.6005& 2	1.1114& 2
52.0	-1.1880& -1	-7.5040& -2	1.4052& -1	-122.28	4.0063& 2	1.5256& 2
53.0	-1.4790& -1	-8.5049& -2	1.7061& -1	-119.90	4.4618& 2	2.1526& 2
54.0	-1.7755& -1	-9.9125& -2	2.0335& -1	-119.17	4.9742& 2	3.0117& 2
55.0	-2.0369& -1	-1.3636& -1	2.4512& -1	-123.80	5.6437& 2	4.7529& 2
56.0	-2.0636& -1	-1.2973& -1	2.4373& -1	-122.16	6.4281& 2	4.5805& 2
58.0	-1.5651& -1	-8.5287& -2	1.7824& -1	-118.59	7.6030& 2	2.2842& 2
60.0	-9.3081& -2	-6.4719& -2	1.1337& -1	-124.81	8.4495& 2	1.0309& 2
70.0	5.9469& -4	-2.1454& -2	2.1463& -2	178.41	1.0631& 3	-2.1833& -1
80.0	9.2050& -4	-1.1669& -2	1.1706& -2	175.49	1.1472& 3	-1.8381& -1
90.0	3.1541& -4	-1.1699& -2	1.1703& -2	178.46	1.2137& 3	-6.3143& -2
100.0	-1.6673& -3	-1.1411& -2	1.1532& -2	-171.69	1.2797& 3	3.2557& -1
110.0	-2.7013& -3	-1.2949& -2	1.3228& -2	-168.22	1.3460& 3	5.9857& -1
120.0	-1.0902& -3	-2.6107& -2	2.6130& -2	-177.61	1.4480& 3	4.8706& -1
125.0	1.4407& -3	-5.2705& -2	5.2725& -2	178.43	1.5513& 3	-1.2994& 0
126.0	4.5431& -3	-6.3317& -2	6.3480& -2	175.90	1.5842& 3	-4.9225& 0
127.0	1.0400& -2	-8.1296& -2	8.1959& -2	172.71	1.6252& 3	-1.4469& 1
128.0	2.5122& -2	-5.6694& -2	6.2010& -2	156.10	1.6682& 3	-2.4372& 1
129.0	4.3483& -2	7.6154& -3	4.4145& -2	80.07	1.6811& 3	5.6666& 0
130.0	6.2267& -2	2.8454& -2	6.8460& -2	65.44	1.6691& 3	3.0318& 1
131.0	7.5076& -2	3.3158& -2	8.2072& -2	66.17	1.6514& 3	4.2598& 1
132.0	7.8329& -2	3.4453& -2	8.5571& -2	66.26	1.6321& 3	4.6180& 1
135.0	7.3389& -2	3.5043& -2	8.1326& -2	64.48	1.5728& 3	4.4009& 1
140.0	2.4801& -2	3.4406& -2	4.2413& -2	35.79	1.4706& 3	1.4602& 1
150.0	3.6181& -2	3.4611& -2	5.0070& -2	46.27	1.2754& 3	2.1430& 1
158.0	3.2322& -2	3.4613& -2	4.7358& -2	43.04	1.1182& 3	1.9144& 1
159.0	3.2058& -2	3.4585& -2	4.7157& -2	42.83	1.0985& 3	1.8972& 1
160.0	3.1636& -2	3.4588& -2	4.6873& -2	42.45	1.0789& 3	1.8724& 1
161.0	3.1304& -2	3.4627& -2	4.6679& -2	42.11	1.0592& 3	1.8549& 1
162.0	3.0871& -2	3.4556& -2	4.6337& -2	41.78	1.0396& 3	1.8255& 1
165.0	2.9970& -2	3.4616& -2	4.5787& -2	40.88	9.8065& 2	1.7753& 1
180.0	2.8946& -2	3.4504& -2	4.5038& -2	39.99	6.8633& 2	1.7091& 1

POWER FLOW(IN SYN. WATTS) = 1.751832& 0

TORQUE EQUIVALENT TO POWER FLOW (N-M) = 0.3401515

ORDER OF HARMONIC = 199 NUMBER OF HARMONICS = 100

RESULTS FOR CALCULATION OF FLUX DENSITY AND POWER FLOW - FIELD THEORY APPROACH

THIN ROTOR External SURFACE EXCITATION = 1.0 A

RADIUS FOR CALCULATIONS,R (M) = 0.0408877

ANGLE (DEG)	RAD.FLUX DENSITY (TESLA)	TAN.FLUX DENSITY (TESLA)	RESULTANT (TESLA)	PHASE ANGLE (DEGREES)	MAG.POTENTIAL- AT RAD.R (AMP)	POYNTING VECTOR -SHAPE OF
0.0	-9.6751& -2	-8.0774& -2	1.2604& -1	-129.86	-1.7854& 3	1.4295& 2
20.0	-9.9664& -2	-8.0698& -2	1.2824& -1	-129.00	-8.6996& 2	1.4712& 2
30.0	-1.0605& -1	-8.0575& -2	1.3319& -1	-127.23	-4.1263& 2	1.5631& 2
40.0	-1.1863& -1	-9.0488& -2	1.4920& -1	-127.34	6.4098& 1	1.9635& 2
45.0	-1.4404& -1	-1.1060& -1	1.8160& -1	-127.52	3.4388& 2	2.9140& 2
47.0	-1.6528& -1	-1.2295& -1	2.0600& -1	-126.65	4.7606& 2	3.7173& 2
49.0	-2.0248& -1	-1.3699& -1	2.4446& -1	-124.08	6.2314& 2	5.0736& 2
50.0	-2.2561& -1	-1.4444& -1	2.6789& -1	-122.63	7.0278& 2	5.9609& 2
51.0	-2.5465& -1	-1.5208& -1	2.9660& -1	-120.85	7.8727& 2	7.0838& 2
52.0	-2.8432& -1	-1.6464& -1	3.2854& -1	-120.07	8.7660& 2	8.5624& 2
53.0	-3.1407& -1	-1.7857& -1	3.6129& -1	-119.62	9.7364& 2	1.0259& 3
54.0	-3.4157& -1	-2.8047& -1	4.4197& -1	-129.39	1.0970& 3	1.7524& 3
55.0	-3.5659& -1	-4.0466& -1	5.3935& -1	-138.61	1.2983& 3	2.6395& 3
56.0	-3.3523& -1	-3.5547& -1	4.8861& -1	-136.68	1.5198& 3	2.1798& 3
58.0	-2.3032& -1	-2.3137& -1	3.2647& -1	-135.13	1.8430& 3	9.7477& 2
60.0	-1.2943& -1	-1.7754& -1	2.1972& -1	-143.91	2.0725& 3	4.2036& 2
70.0	2.5308& -3	-7.0753& -2	7.0798& -2	177.95	2.7149& 3	-3.2754& 0
80.0	4.1406& -3	-3.0832& -2	3.1109& -2	172.35	2.9916& 3	-2.3352& 0
90.0	2.4955& -3	-1.0968& -2	1.1249& -2	167.18	3.1039& 3	-5.0069& -1
100.0	-1.0455& -3	-2.5641& -3	2.7690& -3	-157.82	3.1372& 3	4.9034& -2
110.0	-2.8239& -3	-2.3897& -2	2.4063& -2	-173.26	3.1840& 3	1.2344& 0
120.0	1.5022& -3	-8.5972& -2	8.5985& -2	179.00	3.4667& 3	-2.3624& 0
125.0	1.8402& -2	-1.9933& -1	2.0018& -1	174.73	3.8366& 3	-6.7096& 1
126.0	3.7261& -2	-2.5769& -1	2.6037& -1	171.77	3.9665& 3	-1.7564& 2
127.0	8.6236& -2	-1.8244& -1	2.0179& -1	154,70	4.1027& 3	-2.8778& 2
128.0	1.4596& -1	2.8150& -3	1.4599& -1	88.90	4.1505& 3	7.5157& 0
129.0	1.9068& -1	6.4548& -2	2.0131& -1	71,30	4.1265& 3	2.2514& 2
130.0	2.2262& -1	7.7076& -2	2.3559& -1	70.90	4.0852& 3	3.1387& 2
131.0	2.3935& -1	7.8847& -2	2.5200& -1	71.77	4.0411& 3	3.4521& 2
132.0	2.4187& -1	8.0904& -2	2.5504& -1	71.51	3.9954& 3	3.5794& 2
135.0	2.2480& -1	8.2933& -2	2.3961& -1	69.75	3.8567& 3	3.4103& 2
140.0	1.6193& -1	8.1882& -2	1.8145& -1	63.18	3.6224& 3	2.4253& 2
150.0	1.1908& -1	8.0972& -2	1.4400& -1	55.78	3.1609& 3	1.7637& 2
158.0	1.0909& -1	8.0674& -2	1.3568& -1	53.52	2.7938& 3	1.6099& 2
159.0	1.0838& -1	8.0753& -2	1.3516& -1	53.31	2.7479& 3	1.6009& 2
160.0	1.0759& -1	8.0775& -2	1.3454& -1	53.10	2.7021& 3	1.5897& 2
161.0	1.0686& -1	8.0652& -2	1.3388& -1	52.96	2.6562& 3	1.5765& 2
162.0	1.0613& -1	8.0853& -2	1.3342& -1	52.70	2.6104& 3	1.5696& 2
165.0	1.0395& -1	8.0605& -2	1.3154& -1	52.21	2.4728& 3	1.5327& 2
180.0	9.6751& -2	8.0774& -2	1.2604& -1	50.14	1.7854& 3	1.4295& 2

POWER FLOW(IN SYN.WATTS) = 1.116862& 1

TORQUE EQUIVALENT TO POWER FLOW (N-M) = 2.0974980

ORDER OF HARMONIC = 199 NUMBER OF HARMONICS = 100

APPENDIX IX

DIGITAL COMPUTER PROGRAMMES FOR FIELD PLOTS

The programme for the calculation of field components is given on page 226, while that used for the field plot in the z - plane is given on pages 227 and 228.

```
'BEGIN' 'COMMENT' EEPSF088 BHARGAVA FLUX DENSITY PLOT;                                    BPL  100.
'PROCEDURE' POLAR(X,Y,R,PHI);                                                            POL  100
'VALUE' X,Y;  'REAL' X,Y,R,PHI;                                                          POL  200
'BEGIN' R:= SQRT(X*X + Y*Y);                                                             POL  300
        PHI:= 'IF' X=0 'THEN' 90*SIGN(Y) 'ELSE' 57.295779513*ARCTAN(Y/X) +               POL  400
              ('IF' X 'GE' 0 'THEN' 0 'ELSE' 'IF' Y 'GE' 0 'THEN' 180 'ELSE' -180);      POL  500
  'END' POLAR ;                                                                          POL  600
'PROCEDURE' QUPER(KC,K);                                                                 QPK  100
'VALUE' KC;  'REAL'  KC,K;                                                               QPK  200
'BEGIN' 'IF' KC=0 'THEN' 'BEGIN' K:= 1.5707963; 'GOTO' LC; 'END' 'ELSE'                  QPK  300
'BEGIN' 'REAL' P,Q; 'INTEGER' M,N; 'ARRAY' A,B,M1[0:4];                                  QPK  400
        A[0]:= 1.38629436112; A[1]:= 9.6663442599&-2; A[2]:= 3.590092383&-2;             QPK  500
        A[3]:= 3.7425637133&-2; A[4]:= 1.4511902123&-2; B[0]:= 0.5;                      QPK  600
        B[1]:= 0.1249859397; B[2]:= 6.8802485763&-2; B[3]:=3.328355346&-2;               QPK  700
        B[4]:= 4.4178701283&-3; M1[0]:= 1.0; M1[1]:= 1-KC*KC;                            QPK  800
        'IF' M1[1]<1.0 & -8 'THEN' 'BEGIN' NEWLINE(1);                                   QPK  900
        WRITETEXT ('(' QUARTER%PERIOD%INFINITE ')'); NEWLINE(1);                         QPK 1000
        M1[1]:= 1.0 & -8; 'END';                                                         QPK 1100
        'FOR' M:= 2,3,4 'DO' 'BEGIN' N:= M-1; M1[M]:= M1[1]* M1[N]; 'END' ;              QPK 1200
        P:=Q:=0; 'FOR' M:= 0,1,2,3,4 'DO'                                                QPK 1300
        'BEGIN' P:= A[M]* M1[M]+ P; Q:= B[M]* M1[M]+ Q; 'END' ;                          QPK 1400
        K:= P+Q * LN(1/M1[1]); 'END';                                                    QPK 1500
  LC : 'END' QUPER ;                                                                     QPK 1600
'REAL' A,A1,A2,A3,C,CA,HR,HT,K,K1,K2,MA,PA,R,R1,R2,R3,SA,X,Y,D,K3,HRR;                   BPL  200
'INTEGER' M,MM,N,NN;                                                                     BPL  300
WRITETEXT('(''('2C')'DATA%FOR%FIELD%PLOT'('2C')'HR%ON%THE%POLE%SURFACE,                  BPL  400
HR= '('1S')'')') ;  PA:= 53.00*0.0174532925/2; K:= SIN(PA)/COS(PA);                      BPL  500
K1:=K*K; K2:=K1*K1; K3:=SQRT(1-K2); QUPER(K3,HR); PRINT(HR,0,6);                         BPL  600
WRITETEXT ('(''('20S')' HRR='('1S')'')'); QUPER(K1,HRR); PRINT(HRR,0,6);                 BPL  700
M:= READ; 'FOR' MM:= 1 'STEP' 1 'UNTIL' M 'DO' 'BEGIN'                                   BPL  800
WRITETEXT ('(''('10C3S')' RADIUS '('9S')' ANGLE '('12S')' RADIAU%COMP. '('5S')'          BPL  900
TAN.%COMP. '('6S')' RESULTANT '('5S')' PHASE%ANGLE '('2C')'')') ;                        BPL 1000
R:= READ ; N:= READ; 'FOR' NN:= 1 'STEP' 1 'UNTIL' N 'DO' 'BEGIN'                        BPL 1100
MA:= READ; A:= 0.0174532925 * MA; CA:= COS(A); SA:= SIN(A); X:= R*CA; Y:= R*SA;          BPL 1200
POLAR(Y-1,X,R1,A1); POLAR(Y+1,X,R2,A2); R3:= R1/(K*R2); R1:= R3*R3;                      BPL 1300
A3:=(A1-A2-90)*0.0174532925; A1:=2*A3; X:= R1*COS(A1); Y:= R1*SIN(A1);                   BPL 1400
POLAR(1-X,-Y,R2,A2); R2:=SQRT(R2); A2:=0.5*A2; POLAR(1-K2*X,-K2*Y,R1,A1);                BPL 1500
R1:=SQRT(R1); A1:=0.5*A1; R2:=2*K*R2*R1; A2:=A2 + A1; X:=R3*COS(A3); Y:=R3*SIN(A3);      BPL 1600
POLAR(1+K*Y,-K*X,R1,A1); R1:=R1*R1; A1:=2*A1; R1:=R2/R1;                                 BPL 1700
A1:=(A2-A1)*0.0174532925; C:=R1*COS(A1); D:=R1*SIN(A1); X:=C*C + D*D;                     BPL 1800
X:= 'IF' X<1.0 & -45 'THEN' 1.0 & 45 'ELSE' 1/X; HT:= X*(C*CA-D*SA);                     BPL 1900
HR:=X*(C*SA+D*CA); POLAR(HR,HT,C,D); NEWLINE(1); PRINT(R,0,4); SPACE(3);                  BPL 2000
PRINT(MA,3,2); SPACE(10); PRINT(HR,0,4); SPACE(3); PRINT(HT,0,4); SPACE(3);              BPL 2100
PRINT(C,0,4); SPACE(3); PRINT(D,3,2);                                                    BPL 2200
'END' ; 'END' ; 'END' ;                                                                  BPL 2300
```

```
'BEGIN' 'COMMENT' EEPSF088 BHARGAVA FIELD PLOT;                                  FPT 100
'PROCEDURE' POLAR(X,Y,R,PHI);                                                    POL 100
'VALUE' X,Y; 'REAL' X,Y,R,PHI;                                                   POL 200
'BEGIN' R:= SQRT(X*X + Y*Y) ;                                                    POL 300
        PHI:='IF' X=0 'THEN' 90*SIGN(Y) 'ELSE' 57.295779513 * ARCTAN(Y/X) +      POL 400
             ('IF' X 'GE' 0 'THEN' 0 'ELSE' 'IF' Y 'GE' 0 'THEN' 180 'ELSE' -180); POL 500
'END' POLAR ;                                                                    POL 600
'PROCEDURE' QUPER (KC,K);                                                        QPK 100
'VALUE' KC; 'REAL' KC,K;                                                         QPK 200
'BEGIN' 'IF' KC=0 'THEN' 'BEGIN' K:= 1.5707963; 'GOTO' LC; 'END' 'ELSE'          QPK 300
'BEGIN' 'REAL' P,Q; 'INTEGER' M,N; 'ARRAY' A,B,M1[0:4];                          QPK 400
        A[0]:= 1.38629436112; A[1]:= 9.66634425%-2; A[2]:= 3.590092383%-2;       QPK 500
        A[3]:= 3.742563713%-2; A[4]:= 1.451196212%-2; B[0]:= 0.5;                QPK 600
        B[1]:= 0.12498593597; B[2]:= 6.88024857%-2; B[3]:= 3.328355346%-2;       QPK 700
        B[4]:= 4.417870123%-3; M1[0]:= 1.0;  M1[1]:= 1-KC * KC;                  QPK 800
        'IF' M1[1]<1.0%-8 'THEN' 'BEGIN' NEWLINE (1);                            QPK 900
        WRITETEXT('('QUARTER%PERIOD%INFINITE')'); NEWLINE(1); M1[1]:=1.0%-8; 'END'; QPK 1000
        'FOR' M:=2,3,4 'DO' 'BEGIN' N:= M-1; M1[M]:= M1[1]* M1[N]; 'END';        QPK 1100
        P:=Q:=0; 'FOR' M:= 0,1,2,3,4 'DO'                                        QPK 1200
        'BEGIN' P:=A[M]* M1[M]+ P; Q:=B[M]* M1[M]+ Q; 'END' ;                    QPK 1300
        K:=P + Q*LN(1/M1[1]); 'END';                                             QPK 1400
LC : 'END' QUPER;                                                                QPK 1500
'PROCEDURE' SNCNDN(X,MC,SN,CN,DN);                                               SCD 100
'VALUE' X,MC;  'REAL' X,MC,SN,CN,DN;                                             SCD 200
'BEGIN' 'REAL' A,B,C,CA,D,PIBY; 'INTEGER' I,L; 'BOOLEAN' BO; 'ARRAY' M,N[0:12];  SCD 300
        MC:= 1-MC;   'IF' MC 'NE' 0 'THEN'                                       SCD 400
        'BEGIN' CA:= 1.0%-4; PIBY:= 1.5707963; BO:=MC<0; 'IF' BO 'THEN'          SCD 500
        'BEGIN' D:= 1-MC; MC:= -MC/D; D:= SQRT(D); X:= D*X; 'END'; DN:=A:=1;     SCD 600
        'FOR' I:= 0 'STEP' 1 'UNTIL' 12 'DO'                                     SCD 700
        'BEGIN' L:= I; M[I]:= A; N[I]:=MC:= SQRT(MC); C:=(A + MC)/2;             SCD 800
        'IF' ABS(A-MC) 'LE' CA*A 'THEN' 'GOTO' L1; MC:= A*MC; A:=C;  'END' ;     SCD 900
    L1: X:=C*X; SN:= SIN(X); CN:= SIN(PIBY - X);                                 SCD 1000
        'IF' SN=0 'THEN' 'GOTO' L2; A:= CN/SN; C:= A*C ;                         SCD 1100
        'FOR' I:= L 'STEP' -1 'UNTIL' 0 'DO'                                     SCD 1200
        'BEGIN' B:= M[I]; A:= C*A; C:= DN*C; DN:=(N[I] + A)/(B+A); A:= C/B; 'END' ; SCD 1300
        A:= 1/SQRT(C*C+1); SN:='IF' SN<0 'THEN' -A 'ELSE' A; CN:= C*SN;          SCD 1400
    L2: 'IF' BO 'THEN' 'BEGIN' A:= DN; DN:= CN; CN:= A; SN:= SN/D; 'END'; 'END' 'ELSE' SCD 1500
        'BEGIN' D:= EXP(X); A:=1/D; B:= A+D; CN:=DN:=2/B;                        SCD 1600
        'IF' ABS(X)<3.0%-1 'THEN'                                                SCD 1700
        'BEGIN' D:= X*X*X; SN:=CN * (D*(1/3+D*X*3.96825397%-4) + SIN(X));        SCD 1800
        'END' 'ELSE' SN:=(D-A)/B; 'END' ;                                        SCD 1900
'END' SNCNDN ;                                                                   SCD 2000
'PROCEDURE'  SNC(X,Y,KC,A,B);                                                    SNC 100
'VALUE' X,Y,KC; 'REAL' X,Y,KC,A,B;                                               SNC 200
'BEGIN' 'REAL' KD,DD,SX,CX,DX,SY,CY,DY;                                          SNC 300
        KC:= KC*KC; KD:= 1-KC; SNCNDN(X,KC,SX,CX,DX);                            SNC 400
        SNCNDN(Y,KD,SY,CY,DY); KD:= SY*DX; DD:= 1-KD*KD;                         SNC 500
        A:= 'IF' DD<1.0%-20 'THEN' 1.0%20 'ELSE' (SX*DY)/DD;                     SNC 600
        B:= 'IF' DD<1.0%-20 'THEN' 0.0    'ELSE' (CX*CY*KD)/DD;                  SNC 700
'END' SNC ;                                                                      SNC 800
```

```
'PROCEDURE' SALPOL(U,V,K,X,Y);                                                    FPT  200
'VALUE' U,V,K;  'REAL' U,V,K,X,Y;                                                 FPT  300
'BEGIN' 'REAL' K2,P,Q,R,S,T,W; K2:= SQRT(K); SNC(U,V,K,P,Q); P:= K2*P; Q:= K2*Q;  FPT  400
        POLAR(1-Q,P,R,S); POLAR(1+Q,-P,T,W); P:=R/T;                              FPT  500
        Q:= 0.0174532925* (S-W); X:=P*SIN(Q); Y:=P*COS(Q);                        FPT  600
'END' SALPOL ;                                                                    FPT  700
'PROCEDURE' COMP(ML,MU,NL,NU,KC,KCC,K);                                           FPT  800
'VALUE' ML,MU,NL,NU,KC,KCC,K; 'REAL' KC,KCC,K; 'INTEGER' ML,MU,NL,NU;             FPT  900
'BEGIN' 'REAL' P,Q,X,Y; 'INTEGER' M,N;                                            FPT 1000
        'FOR' M:= ML 'STEP' 1 'UNTIL' MU 'DO' 'BEGIN' P:= M*KC ;                  FPT 1100
        'FOR' N:= NL 'STEP' 1 'UNTIL' NU 'DO' 'BEGIN' Q:= N*KCC;                  FPT 1200
        SALPOL(P,Q,K,X,Y); NEWLINE(1); PRINT(M,4,0); PRINT(N,4,0); SPACE(2);      FPT 1300
        PRINT(X,0,4); SPACE(2); PRINT(Y,0,4); 'END'; 'END';                       FPT 1400
'END' COMP ;                                                                      FPT 1500
        'REAL' A,K,KC,KCC,K1; A:= 53.00 * 0.0174532925/2; K:= SIN(A)/COS(A);      FPT 1600
        K:= K*K; QUPER(K,KC); K1:= SQRT(1-K*K); QUPER(K1,KCC);                    FPT 1700
        KC:= 0.05 *KC; KCC:= 0.05*KCC;  COMP(0,20,0,10,KC,KCC,K);                 FPT 1800
        COMP(0,20,0,0,KC,KCC,K); COMP(20,20, 0,10,KC,KCC,K);                      FPT 1900
'END' ;                                                                           FPT 2000
```

LIST OF SYMBOLS

A	Leading pole tip of the field system
B	Lagging pole tip of the field system
B	Flux density*
$\hat{B}$, B_m, B_{max}	Maximum value of flux density
B_r	Radial flux density component
B_θ	Peripheral or tangential flux density component
ΔB_r	'Difference' output from the full pitch coils
e	Induced electromotive force (e.m.f.)
E	Electric field intensity
E_z	Axial component of electric field intensity
F, f	Force
H	Magnetising force
$\hat{H}$, H_m, H_{max}	Maximum value of magnetising force
H_r	Radial component of magnetising force
H_θ	Tangential component of magnetising force
I	Excitation current
J	Magnetic current density
l	Axial length of the machine

---

*Vector quantities are denoted by a $-$ above the appropriate letter, as $\bar{B}$, or associated with unit vectors, as $B\bar{i}_n$, $B\bar{i}_r$, $B\bar{i}_\theta$, $B\bar{i}_z$.

M_A	Applied magnetomotive force (m.m.f.)
M_R	Rotor m.m.f.
M	Rotor magnetisation vector
$\mathcal{M}$	Magnetic dipole moment
N	Speed
n	Order of harmonic
P	Power
R,r	Radius
r	General suffix in radial direction
S	Surface
S	Poynting vector
S_r	Poynting vector in radial direction
S_0	Poynting vector in peripheral direction
T	Torque
T_s	Maxwell tensile stress
W_h	Alternating hysteresis loss
$\mathcal{z}$	General suffix in the axial direction

α	Angle of incidence of resultant flux density on rotor surface
α'	Angle of refraction of resultant flux density on rotor surface
α', α'', β', β''	Magnetic surface current elements
Δ	Incremental value

δ	'Load' angle of the machine
θ	Angular distance
θ	General suffix in the peripheral direction
μ_r	Relative permeability
ϕ	Scalar magnetic potential
φ	Magnetic flux
Ψ	Conjugate scalar magnetic potential
ω	Angular speed of rotation

$$\overline{\overline{\nabla}} \equiv \bar{i}_r \frac{\partial}{\partial r} + \bar{i}_\theta \frac{1}{r} \frac{\partial}{\partial \theta} + \bar{i}_z \frac{\partial}{\partial z}$$

REFERENCES

1 Warburg, E. ANN. PHYSIK 3 , Vol. 13, pp 141 - 64
1881 Magnetic investigation. [2]*

2 Ewing, J.A. Proc. Roy. Soc., Vol. 34, pp 39 - 45
1882,83 On effects of retentiveness in the magnetisation of iron and steel. [2]

3 Rowland, H.A. Phil. Mag., Vol. 46, pp 140 - 59
1873 On magnetic permeability, and the maximum of magnetism of iron, steel, and nickel. [2]

4 Ewing, J.A. Brit. Assoc. Rep., pp 402 - 4
1883 On the magnetic susceptibility and retentiveness of soft iron (and steel). [2]
Phil. Trans. Roy. Soc., Vol. 176, Pt. II, pp 523 - 640
1885 Experimental researches in magnetism. [2]

5 Ewing, J.A. Proc. Roy. Soc., Vol. 48, pp 342 - 58
1890 Contribution to the molecular theory of induced magnetism. [2]

6 Rayleigh, J.W. (Lord)
Phil. Mag., Vol. 22, Series 5, pp 175 - 83
1886 On the energy of magnetized iron. [2]

7 Fleming, J.A. The Electrician, Sept. 14, p 586
1888 Note on magnetic hysteresis. [2]

---

*Numbers in brackets refer to the page numbers in the thesis where the references appear.

8 Swinburne, J. Industries, Vol. 9, Sept. 19, p 289
1890 The electrical papers at the British Association. [3]

9 Baily, F.G. Brit. Assoc. Rep., pp 576 - 77
1894 On hysteresis in iron and steel in a rotating magnetic field. [3]

10 Ferraris, G. Atti. dello R. academia d scienze, Vol. 23, pp 360 - 75
1888 Rotazioni electrodinamiche prodotte per mezzo di correnti alternate. [3]

11 Ferraris, G. The Telegraphic Journal and Electrical Review, Vol. 22, Feb. 3, pp 111 - 13
1888 On the difference of phases of currents, on the retardation of induction, and on the dissipation of energy in transformers - Experimental and theoretical researches. [3]

12 Ewing, J.A. Jour. I E E, Vol. 24, pp 398 - 431
1895 A magnetic tester for measuring hysteresis in sheet iron. [4,41]

13 Steinmetz, C.P. Theory and Calculation of Alternating Phenomena, [Book]
1897 Pub: W.C.Johnstone.
(III Ed. 1900, pp 293 - 96). [4]

14 Steinmetz, C.P. Theory and Calculation of Electrical Apparatus, [Book] , Ch. 10, pp 168 - 71
1917 Pub: McGraw Hill Book Co. [4]

15 Zipp, H. Elekt. und Masch., Vol. 26, pp 443 - 50
1908 Hysteresis loss in polyphase induction motors

near the speed of synchronism. [5]

16 Lehmann, T. E.T.Z., Vol. 31, pp 1249 - 53
1910 The sudden change of power of induction motors on passing through synchronism. [5]

17 Vallauri, G. Elekt. und Masch., Vol. 30, pp 1061 - 67
1912 Phenomena accompanying the passage of induction motors through synchronism. [5]

18 Smith, C.F. Jour. I E E, Vol. 39, pp 437 - 83
1907 The experimental determination of the losses in motors. [6]

19 Robertson, D. Electrician, Vol. 68, pp 12 - 14
1911 Rotor hysteresis in polyphase induction motors. [6]

20 Holmes, W. and Grundy, E.
Jour. I E E, Vol. 77, pp 379 - 99
1935 Small self-starting synchronous time motors. [7]

21 Teare, B.R. Trans. A I E E, Vol. 59, pp 907 - 12
1940 Theory of hysteresis motor torque. [7,15]

22 Jaeschke, H.E. Elekt. und Masch., Vol. 60, pp 176 - 88
1942 The hysteresis motor. [8]

23 'S.Smith & Sons', U.K.
1944 British Patent 576 249. [9]

24 Roters, H.C. Trans. A I E E, Vol. 66, pp 1419 - 30
1947 The hysteresis motor - Advances which permit economical fractional horse power ratings. [9,15,23]

25 Hysteresis Motor Research Inc., U.S.A.
1962 British Patent 935 583. [10]

26 Parker, R.J. Gen. Elec. Review, Vol. 52, pp 16 - 20
1949 Permanent magnets in drag devices and torque-transmitting couplings. [11,31]

27 Copeland, M.A. and Slemon, G.R.
Trans. I E E E (P A S), Vol. 82, pp 34 - 42
1963 An analysis of the hysteresis motor: I-Analysis of the idealized machine. [12,13,14,17,19]

28 Copeland, M.A. and Slemon, G.R.
ibid., Vol. 83, pp 619 - 25
1964 An analysis of the hysteresis motor: II-The circumferential-flux machine. [12,13,14,17,19]

29 Larionov, A.N. et.al.
Electrichestvo, No. 7, pp 1 - 6
1958 General problems of the hysteresis motor theory. [12,14,18,19,21]

30 Miyairi, S. and Kataoka, T.
Elect. Eng. in Japan, Vol. 85, (10), pp 41 - 50
1965 A basic equivalent circuit of the hysteresis motor. [12,13,14,17,19]

31 Wakui, G. and Kusakari, Y.
ibid., Vol. 85, (6), pp 31 - 42
1965 Synchronous pull-out torque of hysteresis motor. [13,14,15,17,21]

32 Miyairi, S. and Kataoka, T.
ibid., Vol. 86, (6), pp 67 - 77
1966 Analysis of hysteresis motors considering eddy current effect. [13,14,15,17,18,19]

33 Stoma, S.A. Elec. Tech., U.S.S.R., Vol. 4, pp 15 - 27
1968 Effect of a non-sinusoidal magnetic field in the gap on the starting torque of a hysteresis motor. [13,14,21]

34 Robertson, S.D.T. and Zaky, S.Z.G.
Trans. I E E E (P A S), Vol. 88, pp 474 - 83
1969 Analysis of the hysteresis machine - Pt. I. [13,14,15,17,18,19,21]

35 Langen, A.M. Elect. Tech., U.S.S.R., Vol. 2, pp 107 - 18
1969 Theory of ideal hysteresis motors. [13,14]

36 Nakamura, S. et.al.
Elect. Eng. in Japan, Vol. 88, (6), pp 11 - 20
1968 Design of hysteresis motors. [13,14,22]

37 Olsen, E. Applied Magnetism : a study in quantities. [Book], Ch. 7, pp 54 - 55
1966 Philips Technical Library. [14,100]

38 Rahman, M.A. et.al.
Trans. I E E E, (P A S), Vol. 88, pp 954 - 61
1969 An analysis of the hysteresis motor: III- Parasitic losses. [14,18]

39 Miyairi, S. and Kataoka, T.
Elect. Eng. in Japan, Vol. 83, (2), pp 1 - 10
1963 Airgap flux density distribution in hysteresis motors. [14,20]

40 Takahashi, T. ibid., Vol. 89, (7), pp 78 - 87
1969 Calculation of rotor input power for hysteresis motor running at synchronous speed. [14,21]

41 Wakui, G. ibid., Vol. 86, (11), pp 95 - 105
1966 Optimum conditions in the design of hysteresis motors. [14,16,22]

42 Mishkin, E. Quart. Jour. Mech. Appl. Math., Vol. 7, Pt. IV, pp 472 - 87
1954 Theory of the squirrel-cage induction machines derived directly from Maxwell's field equations. [15]

43 Du Bois, H. The Electrician, Vol. 40, pp 218,316;511,652, 814, Vol. 41, pp 108 - 10
1897 On magnetic shielding. [16]

44 Lommel, J.M. Jour. App. Phy., Vol. 35, (3), pp 970 - 71
1964 Rotational hysteresis in Tungsten and in hysteresis motors. [22]

45 Wakui, G. Elect. Eng. in Japan, Vol. 90, (4), pp 85 - 93
1970 Alternating hysteresis and rotational hysteresis in the hysteresis motor. [22]

46 Young, D.G. Jour. I E E, Vol. 9, pp 437 - 39
1963 The hysteresis clutch. [31,42]

47 Medley, E. Mach. Design, Vol. 38, (Aug), pp 165 - 67
1966 The polarized hysteresis motor. [42]

48 Winston, J. Elec. Mfg., Vol. 60, (Dec), pp 114 - 27
1957 Design and application of hysteresis clutches. [42]

49 Yermolin, Yu.A. Electrichestvo, No. 8, pp 63 - 66
1971 The magnetic field in the airgap of a hysteresis coupling with cylindrical rotor. [42]

50 Ampex Corpn., U.S.A.

1963 British Patent 999 708. [42]

51 Apperson, J.W. and Hansen, E.F.
Gen. Elec. Review, Vol. 53, (Oct), pp 35 - 40
1950 An instrument for measuring magnetic hysteresis. [42]

52 Perry, C.C. and Lissner, H.R.
The Strain Gage Primer. [Book],
Ch. 3, pp 51,52 and Ch. 11, pp 230 - 32
1962 Pub: McGraw Hill Book Co. [43]

53 Crouzet Co. Ltd., France.
1966 British Patent 1 046 016. [52]

54 Rayleigh, J.W. (Lord)
Phil. Mag., Vol. 23, Series 5, pp 225 - 45
1887 The behaviour of iron and steel under the operation of feeble magnetic force. [99]

55 Kadkin, V.A. Phys. Metals Metallugr., Vol. 20, (1), pp 143 - 45
1965 Upper limits of the magnetic hysteresis of certain ferromagnetics. [109]

56 Kornetzki, M. and Lucas, I.
Zeitschrift fuer Physik, Vol. 142, pp 70 - 82
1955 On the theory of hysteresis losses in a rotating magnetic field. [139]

57 Hiecke, R. Electrotechn. Zeitschr., Vol. 23, pp 142 - 43
1902 Hysteresis in a rotating field. [139]

58 Brailsford, F. Jour. I E E, Vol. 83, pp 566 - 75
1938 Rotational hysteresis loss in electrical sheet steels. [139]

59 Stoner, E.C. and Wohlfarth, E.P.

Trans. Roy. Soc., Vol. 240, Series A, pp 599 - 644

1948 Mechanism of magnetic hysteresis in hetrogenous alloys. [139]

60 Poynting, J.H. Phil. Trans. Roy. Soc., Vol. 175, Pt. II, pp 343 - 61

1885 On the transfer of energy in the electromagnetic field. [149]

61 Slepian, J. Trans. A I E E, Vol. 61, pp 835 - 41

1942 Energy flow in electric systems - the V-I energy-flow postulate. [149]

62 Nesbitt, E.A. Trans. A I M M E, Vol. 166, pp 415 - 25

1946 Vicalloy - A workable alloy for permanent magnets. [175]

63 Hibbard, Jr.W.R.

Jour. of Metals, Trans. A I M E, pp 962 - 67

1956 Preferred orientations and magnetic properties of rolled and annealed permanent magnet alloys. [175]

64 Luzhinskaya, M.G. and Shur, Ya. S.

Fiz. Metal. Metalloved., Vol. 13, pp 49 - 53

1962 The nature of the magnetic anisotropy in Vicalloy. [175]

65 Cronk, E.R. Trans. I E E E, (Mag), (Sept), pp 268 - 69

1968 Progress in permanent magnet materials development. [175]

66 Fountain, R.W. and Joseph, F.L.
Trans. A I M E, (Feb), pp 349 - 56
1953 Development of mechanical and magnetic hardness in 10 pct. V-Co-Fe alloy. [175,181]

67 Martin, D.L. and Geisler, A.H.
Trans. A S M, Vol. 44, pp 461 - 83
1952 Constitution and properties of cobalt-iron-vanadium alloys. [175]

68 Karplus, W.J. Analog Simulation. [Book], Ch. 5 , pp 127 - 29
1958 Pub: McGraw Hill Book Co. [198]

69 Vitkovitch, D. Field Analysis : Experimental and Computational Methods. [Book], Ch. 5 , pp 199 - 203
1966 Pub: Van Nostrand Co. [198]

70 Abramowitz, M. and Stegun, I.A. (Editors)
Handbook of Mathematical Functions with Formulas, Graphs and Mathematical Tables.
pp 590 - 92
1965 Pub: Dover Publications Inc. [201]

71 Bulirsch, R. Numerische Mathematik, Vol. 7, pp 78 - 90
1965 Numerical calculation of elliptic integrals and elliptic functions. [201]

ACKNOWLEDGEMENTS

The author acknowledges with deep gratitude the excellent supervision and encouragement by

Dr. M.J.Jevons,

Senior Lecturer in electrical engineering, and helpful discussion and advice by

Prof. E.J.Davies,

Professor of electrical engineering (heavy current) at the University.

The author is thankful to the technical staff of the department of electrical engineering, especially to Mr. J.Partlow for the assistance in machining requirements.

Thanks are also due to Mr. J.T.Whittle of the University library for the production of Xerox copies of the thesis.

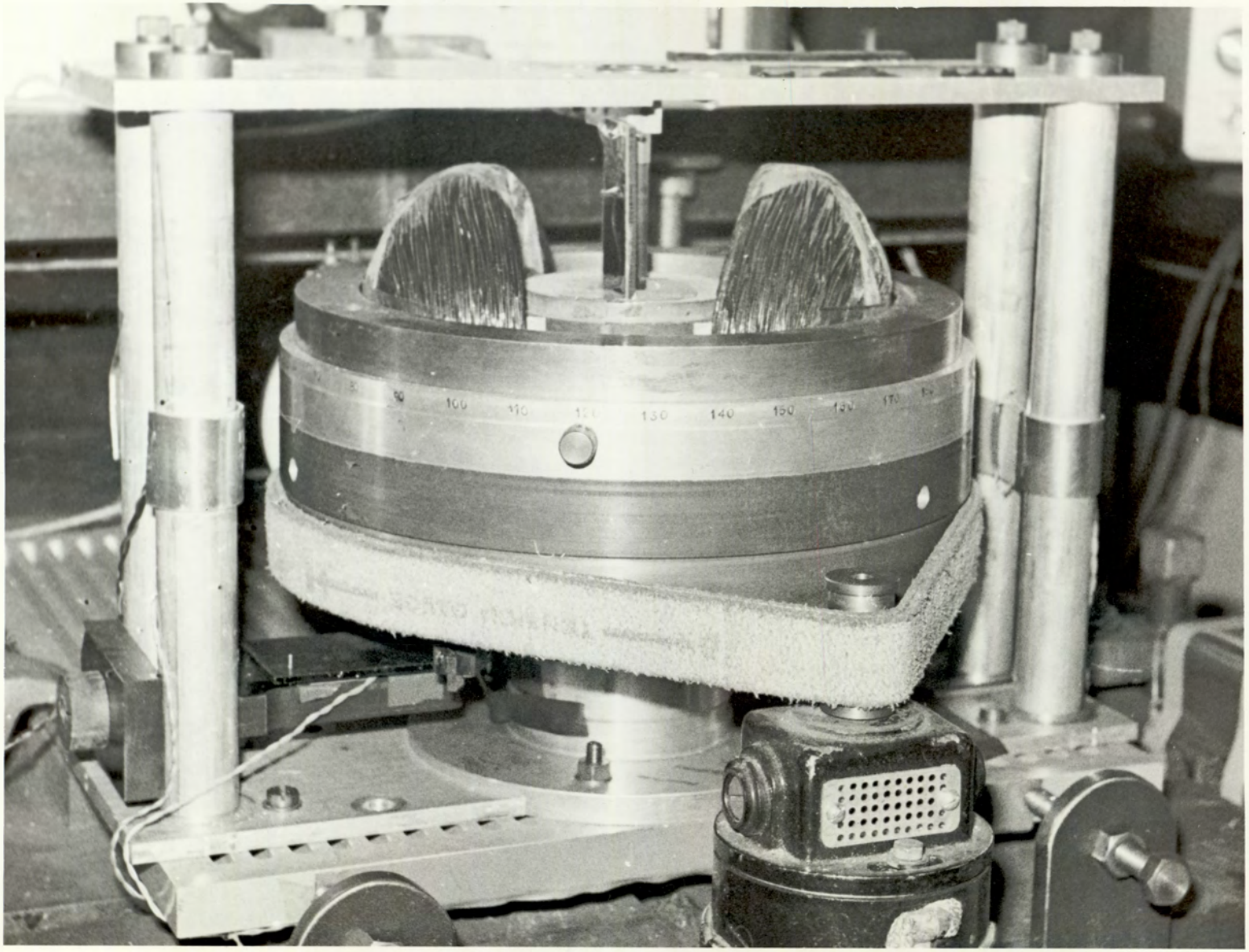

PLATE 2.1

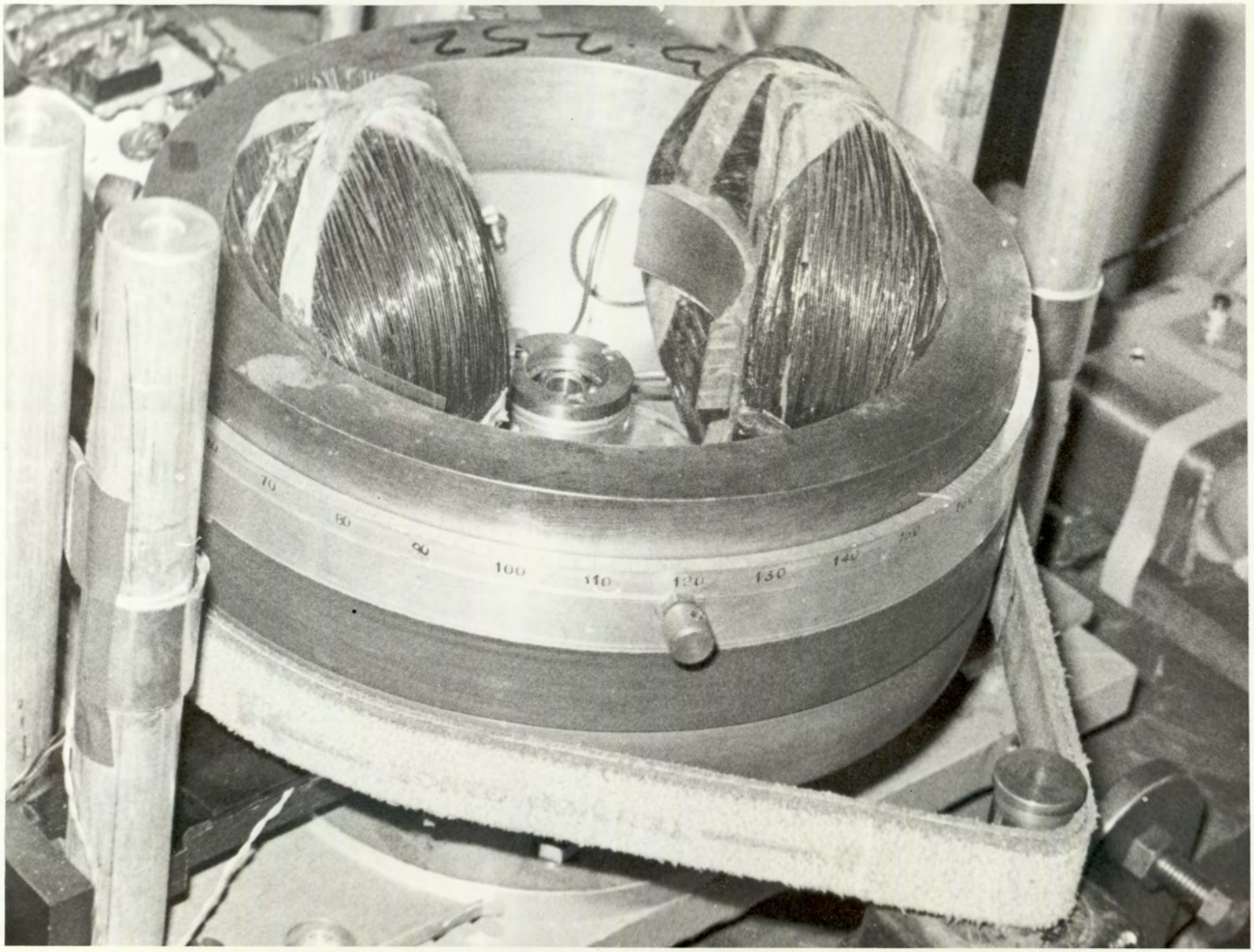

PLATE 2.2